



HAL
open science

Transparent electrodes based on silver nanowire networks : electrical percolation, physical properties, and applications

Thomas Sannicolo

► **To cite this version:**

Thomas Sannicolo. Transparent electrodes based on silver nanowire networks : electrical percolation, physical properties, and applications. Electric power. Université Grenoble Alpes, 2017. English. NNT : 2017GREAI073 . tel-01716842v2

HAL Id: tel-01716842

<https://theses.hal.science/tel-01716842v2>

Submitted on 19 Mar 2018

HAL is a multi-disciplinary open access archive for the deposit and dissemination of scientific research documents, whether they are published or not. The documents may come from teaching and research institutions in France or abroad, or from public or private research centers.

L'archive ouverte pluridisciplinaire **HAL**, est destinée au dépôt et à la diffusion de documents scientifiques de niveau recherche, publiés ou non, émanant des établissements d'enseignement et de recherche français ou étrangers, des laboratoires publics ou privés.

THÈSE

Pour obtenir le grade de

DOCTEUR DE LA COMMUNAUTE UNIVERSITE GRENOBLE ALPES

Spécialité : **Matériaux, Mécanique, Génie Civil, Electrochimie**

Arrêté ministériel : 25 mai 2016

Présentée par

Thomas SANNICOLO

Thèse dirigée par **Daniel BELLET** et **Jean-Pierre SIMONATO**
Co-encadrée par **Caroline CELLE**

Préparée au sein du **Laboratoire de Synthèse et d'Intégration des
Nanomatériaux (CEA-Liten)** et du **Laboratoire des Matériaux et du
Génie Physique (Grenoble INP-CNRS)**
Dans l'École Doctorale I-MEP2

Transparent Electrodes based on Silver Nanowire Networks: Electrical Percolation, Physical Properties, and Applications

Thèse soutenue publiquement le **30 Octobre 2017**
Devant le jury composé de :

Monsieur Yves BRECHET

Professeur, SIMaP, Grenoble INP-CNRS, Grenoble, Président du Jury

Monsieur Philippe POULIN

Directeur de recherche, CRPP, Univ. Bordeaux-CNRS, Bordeaux, Rapporteur

Monsieur Dominique VUILLAUME

Directeur de recherche, IEMN, Univ. Lille 1-CNRS, Lille, Rapporteur

Madame Lavinia BALAN

Chargé de recherche, IS2M, Univ. Haute-Alsace-CNRS, Mulhouse, Examineur

Monsieur Mathieu CREYSSELS

Maître de conférences, MFAE/LMFA, Ecole Centrale de Lyon, Lyon, Examineur

Monsieur Lionel FLANDIN

Professeur, LEPMI, Univ. Savoie MB-CNRS, Le Bourget-du-Lac, Examineur

Monsieur Jean-Pierre SIMONATO

Directeur de recherche, CEA-Liten, Grenoble, Directeur de thèse

Madame Caroline CELLE

Ingénieur de recherche, CEA-Liten, Grenoble, Co-encadrante de thèse



Acknowledgments / Remerciements

Je remercie chaleureusement mes directeurs de thèses, Daniel Bellet et Jean-Pierre Simonato, ainsi que mon encadrante de thèse, Caroline Celle. Daniel, tu auras été pour moi l'élément déclencheur d'une nouvelle marche en avant. Tu m'as donné pleinement confiance en moi dès le premier jour. Merci pour ta Science. Merci pour ta passion. Merci aussi pour ta bienveillance, si précieuse pour avancer « droit » jour après jour. Caroline, Jean-Pierre, grâce à vous, j'ai eu la chance d'évoluer au CEA dans les meilleures conditions. Merci pour vos conseils, vos encouragements, et pour la confiance sans faille que vous avez toujours placée en moi.

Je remercie Yves Bréchet, sans qui mon travail n'aurait pu voir le jour. Merci Yves d'avoir cru en ce projet et d'avoir permis sa réalisation dans ce contexte spécial, partagé entre le CEA-Liten et le LMGP. J'ai évolué dans un cadre optimal. Je t'en serai toujours reconnaissant.

Je remercie l'ensemble des membres du Jury pour l'investissement qu'ils ont bien voulu consacrer à mes travaux, à la fois en amont lors de la lecture du manuscrit, mais également lors de la soutenance. Merci pour la qualité de vos interrogations qui nous donnent, à moi et mes encadrants, des idées précieuses pour l'avenir des nanofils d'argent.

Je remercie la direction du LMGP. Franz, Carmen, je vous le répète. Quelle chance a le LMGP d'avoir une équipe de direction aussi investie et dévouée. Ce fut un plaisir de travailler « chez vous ». J'adresse également des remerciements spéciaux à Mélanie Lagrange et David Muñoz-Rojas. Merci David pour ta générosité et ta vivacité d'esprit sans égal. Merci Mélanie pour ta gentillesse, ta curiosité et ton enthousiasme. Ce fut un plaisir de « prendre la relève ».

Je remercie les stagiaires que j'ai eu la chance et le privilège d'encadrer, et qui auront considérablement contribué (et plus encore) à l'avancée de ces travaux. Merci Shujun. Merci Silas. Merci Dorina. Je te renouvelle mes encouragements pour ta nouvelle thèse qui commence !

Je remercie toutes celles et ceux qui ont accepté de collaborer avec nous sur ce sujet. Merci pour votre expertise et votre énergie qui auront donné lieu, le plus souvent, à des résultats d'intérêt majeur. Merci en particulier à Ngoc Duy Nguyen de l'université de Liège. Merci à Stéphane Moreau et Denis Mariolle du Leti. Merci à Romain Soulas et Nathalie Péliissier du Liten. Merci à Laetitia Rapenne, Béatrice Doisneau et Mikhail Anikin du LMGP. Merci à Francine Roussel du CMTC. Merci à Alejandro Niembro, Philippe Ferrari et Tan Phu Vuong de l'IMEP-LaHC. Merci enfin à Nicolas Charvin et Lionel Flandin du LEPMI.

Je remercie toutes celles et ceux, au CEA comme au LMGP (ils se reconnaîtront), qui auront rythmé et enrichi chaque jour mon parcours de thésard... pour m'emmener souvent bien au-delà des frontières de la Science. On s'est bien amusé. L'histoire, pour beaucoup d'entre vous, ne s'arrête pas là.

Je remercie ma Mère.

Abstract

Transparent electrodes attract intense attention in many technological fields, including optoelectronic devices (solar cells, LEDs, touch screens), transparent film heaters (TFHs) and electromagnetic (EM) applications. New generation transparent electrodes are expected to have three main physical properties: high electrical conductivity, high transparency and high mechanical flexibility. The most efficient and widely-used transparent conducting material is currently indium tin oxide (ITO). However the scarcity of indium associated with ITO's lack of flexibility and the relatively high manufacturing costs have prompted search into alternative materials. With their outstanding physical properties, silver nanowire (AgNW)-based percolating networks appear to be one of the most promising alternatives to ITO. They also have several other advantages, such as solution-based processing, and compatibility with large area deposition techniques. First cost estimates are lower for AgNW based technology compared to current ITO fabrication processes. Unlike ITO, AgNW are indeed directly compatible with solution processes, never requiring vacuum conditions. Moreover, due to very large aspect ratio of the NWs, smaller quantities of raw materials are needed to reach industrial performance criteria.

The present thesis aims at investigating important physical assets of AgNW networks – unexplored (or not explored enough) so far – in order to increase the robustness, reliability, and industrial compatibility of such technology. This thesis work investigates first optimization methods to decrease the electrical resistance of AgNW networks. *In situ* electrical measurements performed during thermal ramp annealing and/or chemical treatments provided useful information regarding the activation process at the NW-NW junctions. At the scale of the entire network, our ability to distinguish NW areas taking part in the electrical conduction from inactive areas is a critical issue. In the case where the network density is close to the percolation threshold, a discontinuous activation process of efficient percolating pathways through the network was evidenced, giving rise to a geometrical quantized percolation phenomenon. More generally, the influence of several parameters (networks density, applied voltage, optimization level) on the electrical and thermal homogeneity and stability of AgNW networks was investigated via a dual approach combining electrical mapping techniques and simulations. A thermal runaway process leading to a vertical crack and associated to electrical failure at high voltage could be visually evidenced via *in situ* electrical mapping of AgNW networks during voltage plateaus. Moreover, many efforts using Matlab and Comsol softwares were devoted to construct reliable models able to fit with experimental results. Due to the increasing demand for portable and wearable electronics, preliminary tests were also conducted to investigate the stretching capability of AgNW networks when transferred to elastomeric substrates. Finally, integrations of AgNW networks in several devices were performed. Specifically, studies were conducted to understand the mechanisms leading to failure in AgNW-based transparent film heaters, and to improve their overall stability. Preliminary investigations of the benefits of incorporating of AgNW networks into electromagnetic devices such as antennas and EM shielding devices are also discussed at the end of the manuscript.

Résumé

L'intérêt suscité par les électrodes transparentes (TEs) concerne un large spectre de domaines technologiques, tels que les dispositifs optoélectroniques (cellules solaires, LEDs, écrans tactiles), les films chauffants transparents, ou les applications électromagnétiques. Les TEs de nouvelle génération auront à combiner à la fois un très haut niveau de conduction électrique, de transparence optique, mais aussi de flexibilité mécanique. L'oxyde d'Indium dopé Etain (ITO) domine actuellement le marché des matériaux transparents conducteurs (TCMs). Cependant, la rareté de l'Indium, combinée à ses faibles performances en flexion mécanique et ses coûts de fabrication élevés ont orienté les recherches vers des TCMs alternatifs. Les réseaux percolants de nanofils métalliques, en particulier les nanofils d'argent (AgNWs), se sont imposés comme l'une des alternatives les plus sérieuses à l'ITO, en raison de leurs propriétés physiques très attractives. Ces réseaux interconnectés offrent également la possibilité d'utiliser des méthodes de synthèse en voie chimique et d'impression bas coût, sur de grandes surfaces. De manière générale, les premières estimations concernant les coûts de fabrication sont inférieures à celles de l'ITO. De plus, grâce au très haut facteur de forme des nanofils et à la nature percolante des réseaux, les besoins en matières premières nécessaires pour atteindre un haut niveau de performance demeurent faibles.

Ce travail de thèse s'intéresse à l'étude des propriétés physiques fondamentales – inexplorées ou non encore suffisamment étudiées – des réseaux d'AgNWs, afin de mieux comprendre leurs propriétés et d'améliorer la fiabilité et la compatibilité de ces électrodes vis-à-vis des critères de performance industriels. La première partie est consacrée à l'étude des méthodes d'optimisation utilisées pour diminuer la résistance électrique des électrodes. Les mesures électriques *in situ* effectuées au court d'un recuit thermique et/ou après traitement chimique fournissent de précieuses informations concernant les mécanismes d'activation au niveau des jonctions entre nanofils. A l'échelle du réseau, notre capacité à distinguer les zones qui participent efficacement à la conduction électrique de celles qui seraient potentiellement inactives est un défi majeur. Pour les réseaux dont la densité en nanofils est proche du seuil de percolation, un processus d'activation discontinu de chemins efficaces de percolation à travers le réseau a pu être mis en évidence. De manière générale, l'influence de plusieurs paramètres sur l'homogénéité et la stabilité électrique et thermique des électrodes a été étudiée, à l'aide de techniques de cartographie électrique et de simulations. A tension élevée, la formation et la propagation d'une fissure à travers un réseau d'AgNWs soumis à des plateaux de tension croissants ont pu être détectées visuellement. Des modèles de simulation via les logiciels Matlab et Comsol ont aussi été construits afin de confirmer, voire anticiper, les phénomènes observés expérimentalement. Par ailleurs, encouragés par la demande croissante pour les dispositifs électroniques portatifs, des tests préliminaires ont permis d'observer le comportement des réseaux d'AgNWs sous contrainte d'étirement mécanique lorsqu'ils sont transférés sur des substrats élastiques. Ce travail de thèse a également concerné l'intégration de réseaux d'AgNWs au sein de dispositifs. Des études ont été menées afin d'améliorer la stabilité des films chauffants transparents à base d'AgNWs et de mieux appréhender les mécanismes favorisant l'émergence de défauts. L'utilisation des réseaux d'AgNWs pour des applications électromagnétiques (antennes, blindage) a également fait l'objet de tentatives préliminaires dont les résultats sont commentés à la fin du manuscrit.

Table of Contents

Introduction	1
Chapter 1. Introduction to transparent electrodes based on metallic nanowire percolating networks	5
1.1. Metallic nanowire networks: Synthesis, Fabrication and Physical Properties	5
1.1.1. Synthesis of Metallic Nanowires (MNW) and Network Fabrication	5
1.1.2. Properties of individual MNWs: size effects.....	7
1.1.3. Influence of interconnections and network density on the optical and electrical properties.....	8
1.1.4. Light scattering of MNW networks.....	11
1.1.5. Flexibility of MNW Networks.....	12
1.1.6. Stability issues and hybrid nanocomposites based on MNWs	13
1.2. Integration of metallic nanowire networks for different applications.....	15
1.2.1. Photovoltaic Applications.....	15
1.2.2. Lighting (Organic LEDs).....	17
1.2.3. Transparent Film Heaters.....	19
1.2.4. Smart Windows and Displays	22
<i>1.2.4.1. Electrochromic and Polymer-Dispersed Liquid Crystal Devices.....</i>	<i>22</i>
<i>1.2.4.2. Touch Screens</i>	<i>23</i>
1.2.5. Electromagnetic Devices.....	24
<i>1.2.5.1. Electromagnetic Shielding</i>	<i>24</i>
<i>1.2.5.2. Radio Frequency Antennas</i>	<i>26</i>
1.3. Concluding remarks	28
Chapter 2. Optimization of the AgNW networks electrical performances.....	29
2.1. Impact of thermal annealing and acid treatment	30
2.1.1. Thermal annealing and acid treatment: protocols and set-up.....	30
<i>2.1.1.1. Thermal annealing set-up</i>	<i>30</i>
<i>2.1.1.2. Acid treatment protocols.....</i>	<i>30</i>
2.1.2. Description of the results	31
<i>2.1.2.1. Impact of thermal annealing and acid treatments on Seashell AgNWs.....</i>	<i>32</i>
<i>2.1.2.2. Impact of thermal annealing and acid treatments on Liten NWs</i>	<i>35</i>

2.1.2.3. <i>Other optimization techniques</i>	38
2.2. Nano-characterization of the phenomena taking place at the NW-NW junctions .	41
2.2.1. Morphological impact of thermal annealing: nanoscale characterization ..	42
2.2.2. Morphological impact of acid treatment: nanoscale characterization	45
2.2.3. Exploration of the internal structure of NW-NW junctions: preliminary results	47
Chapter 3. Description of the modelling tools developed during this thesis.....	51
3.1. Brief introduction to the percolation theory	51
3.2. Generation of random networks via Matlab-based Monte Carlo simulations	52
3.3. Electrical and thermal simulations using Comsol	57
3.3.1. Network geometry exportation from Matlab to Comsol.....	57
3.3.2. Materials properties used in the model.....	58
3.3.3. Boundary conditions for electrical simulations.....	58
3.3.4. Boundary conditions for thermal simulations.....	62
3.3.5. Geometrical meshing of the specimen.....	64
3.3.6. Calculation of the network resistance	65
3.3.7. Comsol-based simulations: positive and negative aspects.....	67
Chapter 4. Electrical distribution in AgNW Networks	71
4.1. The case of low density networks: geometrical quantized percolation	71
4.1.1. Introduction to geometrical quantized percolation phenomenon	71
4.1.2. Analysis of quantized percolation using lock-in thermography	73
4.1.2.1. <i>Lock-in thermography technique</i>	73
4.1.2.2. <i>Experimental results</i>	76
4.1.2.2.1. <i>Activation and detection of efficient percolating pathways (EPPs)</i>	76
4.1.2.2.2. <i>Discussion about partially highlighted EPPs</i>	77
4.1.2.2.3. <i>Influence of the electrode geometry: lightning rod effect</i>	77
4.1.3. Impact of the AgNW diameter on geometrical quantized percolation	78
4.1.4. Introduction to “anti-percolation” phenomenon	81
4.1.5. Concluding remarks	82
4.2. The parameters that influence the electrical homogeneity and stability of AgNW networks.....	84
4.2.1. Impact of the network density on the electrical homogeneity	84

4.2.1.1.	<i>Electrical and thermal mapping of AgNW networks with different network density</i>	84
4.2.1.2.	<i>Correlation with simulation models</i>	89
4.2.2.	Impact of the junction efficiency on the electrical homogeneity	90
4.2.2.1.	<i>Experimental analysis using lock-in thermography</i>	90
4.2.2.2.	<i>Correlation with simulation models</i>	91
4.2.3.	Optimization and failure dynamics of AgNW networks under electrical stress	92
4.2.3.1.	<i>Evolution of the electrical behavior of standard AgNW network under electrical stress</i>	93
4.2.3.2.	<i>Description of the mechanisms involved in the electrical breakdown of AgNW networks at high voltage</i>	95
4.2.3.3.	<i>“Life in the crack”</i>	100
4.2.4.	Conclusion and outlooks	102
Chapter 5. Stretching properties of AgNW-PDMS composites: preliminary results...		105
5.1.	Fabrication, properties and applications of AgNW-PDMS stretchable conductors: short state-of-the-art	105
5.2.	Protocols	108
5.2.1.	AgNW-PDMS composites preparation	108
5.2.2.	Stretching tests presentation	109
5.3.	Impact of the NW density on the stretching properties	111
5.4.	<i>In situ</i> characterization of the mechanical deformations	113
5.5.	Outlooks	116
Chapter 6. Applications		117
6.1.	AgNW-based transparent film heaters (TFHs)	118
6.2.	AgNW-based antennas and transmission lines: preliminary attempts	122
6.2.1.	Antenna fabrication and measurement procedure	123
6.2.2.	Performance of AgNW-based antennas	125
6.2.3.	Transmission lines	127
6.3.	AgNW networks for transparent electromagnetic shielding	130
6.3.1.	Measurement of the shielding effectiveness of AgNW networks	131
6.3.1.1.	<i>Description of the experimental setup</i>	131
6.3.1.2.	<i>Impact of the AgNW network density on the shielding properties</i>	132

6.3.1.3. <i>Impact of environmental ageing, thermal annealing, substrate, and deposition technique</i>	133
6.3.1.4. <i>Comparison with thin silver films and thin silver wire mesh screens</i>	135
6.3.2. EM shielding outlooks	139
Conclusion and future works	141
Appendix A: physical equations solved in Comsol simulations using the finite element method	147
Appendix B: calculation of the AgNW network areal mass density	148
References	149

Introduction

« Là où croît le péril, croît aussi ce qui sauve »
Friedrich Hölderlin, **Patmos** (1808)

Transparent electrodes (TE) play a pivotal role in many modern devices such as solar cells, displays, touch screens or transparent heaters.^[1] The strong demand for transparent conductive materials (TCMs) has led engineers and scientists to search for possible solutions involving indium tin oxide (ITO) replacement, which has been the most efficient and widely used TCM up to now. This is motivated by both economic and physical considerations: despite its very good optoelectronic properties, ITO is likely to become increasingly expensive due to the scarcity of indium.^[2,3] Moreover, its brittleness is not compatible with the strong demands for flexible electronics.

In this context, nanostructured transparent conducting materials^[4-11] such as metal grids, conductive polymers, carbon nanotubes, graphene and especially metallic nanostructures, have been thoroughly explored and have attracted much attention in the past few years thanks to their promising properties and applications.^[9,12,13] In particular, metallic nanowire (MNW) based percolating networks have been found to successfully combine high flexibility, high optical transparency and high electrical conductivity. These networks are made of randomly interconnected nanowires, playing the role of conductive medium, and allowing electrical current to flow through the electrode. Thanks to the very high aspect ratio of metallic nanowires, such networks can exhibit optoelectronic performances similar to ITO-based electrodes while consuming a substantially lower quantity of raw material: in order to reach optimized electrical resistance and optical transparency, the required quantity of indium is generally much higher in an ITO electrode than the quantity of silver required in a silver nanowire (AgNW)-based electrode. This latter quantity was measured as only several tens of mg m^{-2} .^[14,15] Moreover, AgNW networks have been shown to be compatible with solution-based processing, low cost and large area deposition techniques.

Transparent conducting thin films are mainly used in optoelectronic devices, either to collect charges from nearby functional layers (solar cells) or to supply them with charge carriers (light emitting diode displays) while allowing light either to enter or escape the device. However, MNW networks are also attractive for a wider range of applications, including transparent heaters.^[14,16,17] In addition, MNW networks were also found promising for electromagnetic applications such as stretchable radio frequency antennas^[18,19] and transparent electromagnetic shielding.^[20,21]

Due to the wide diversity of possible applications, it appears unlikely that just one type of transparent electrode will be superior than the other TEs: each target market requires an appropriate trade-off between the material's physical properties (electrical, optical, mechanical), stability (thermal, electrical, mechanical, chemical), sustainability, and, finally, certain technical and economic constraints regarding the available processing methods (synthesis, deposition, post-deposition treatments, etc.).

However, the technology of innovative flexible transparent conducting materials based on MNWs - and especially silver nanowire (AgNW) networks - is gaining increasingly in maturity. The latter have indeed been the most studied and mastered type of metallic nanowire network so far. More efforts in fundamental research are essential for understanding the scope and limitations of the materials, and continuing to develop advanced alternatives to existing technologies. At the same time, integrating MNWs into functional devices has already proved to be efficient in many demonstrations, as described below, and paves the way for various industrial applications in the foreseeable future.

This thesis project follows on from three previous thesis contributions recently conducted in Grenoble Alpes University within the frame of transparent electrodes based on AgNW networks. Céline Mayousse contributed in the optimization of both the synthesis of AgNWs and the performances of the resulting transparent electrodes. Several proof of concepts regarding the integration of the AgNW networks into functional devices (organic solar cells, capacitive touch sensors or transparent film heaters) also resulted from her thesis contribution. This thesis was conducted at CEA-Liten, directed by Jean-Pierre Simonato and Caroline Celle, and defended in September 2014.^[22] Daniel Langley's thesis work was dedicated to the understanding of AgNW networks physical properties via a dual approach combining simulations and experiments: by the mean of a 2D stick percolation modelling approach, he studied the impact of the NW's length distribution, NW's angle distribution, or NW shapes on the percolation threshold. On the other hand, experimental efforts were mainly focused on the physical understanding of mechanisms involved in the optimization of AgNW networks via thermal annealing. This thesis was conducted at LMGP and Université de Liège, directed by Daniel Bellet and Ngoc Duy Nguyen, and defended in October 2014.^[23] Finally, Mélanie Lagrange deeply studied the impact of network density and nanowire dimensions on the optoelectrical properties of AgNW networks effects via experimental and modelling approaches. Strong efforts were also devoted to the optimization of transparent film heaters made of AgNW networks, as well as to the deep analysis of their physical limitations (instability problems, electrical failure, etc.). This thesis was conducted at LMGP, directed by Daniel Bellet and Yves Bréchet, and defended in October 2015.^[24]

These three fruitful contributions were very inspiring in the sense they helped overcoming plenty of scientific and technological issues and answering several physical and chemical inquiries regarding the AgNW synthesis and the optimization of the overall performances of AgNW networks. However there are still challenges to tackle so that this technology can be more mature and better mastered to fulfill industrial requirements.

This thesis is divided into 6 specific chapters. Prior to the meticulous description of experimental work and analysis performed within the frame of this thesis, this PhD manuscript starts with a "state-of-the-art" (**Chapter 1**), which consists of an overview of the physical and chemical basics associated with transparent electrodes made of percolating metallic nanowire networks, and then provides several examples of successful integration into functional devices.

As already mentioned, it is still highly recommended to continue making efforts to investigate the physical properties of such percolating networks from a fundamental and multi-scale point of view. For this reason, a deep investigation of the physical mechanisms involved in the

physico-chemical treatments used for optimizing the optoelectrical properties of such networks was conducted, with special emphasis on thermal and acid treatments which seem to be the most efficient and relevant techniques. This work has been conducted by the mean of *in situ* electrical measurement and powerful scanning electron microscopy tools. The main results are reported in **Chapter 2** of the present thesis.

Besides, it is highly necessary for future device integration to get feedback about electrical distribution in such percolating networks when subjected to electrical bias. The literature is quite poor about this issue. In this regard, AgNW network based TE are very different compared to transparent conductive oxides. While the latter are homogeneous polycrystalline thin layers, the formers are by nature non-homogeneous layers and therefore electrical current is not supposed to flow identically in all network locations; this gives rise to potential local failures. Thus, it is of main importance to detect and potentially control which of the nanowires are effectively taking part to the electrical conduction. Electrical distribution, or more generally “electrical percolation” in AgNW percolating networks, constitutes the main objective of this thesis and is deeply analyzed in **Chapter 4**. The latter is divided into 2 sections. The first section (4.1) focuses on the onset of electrical percolation in rather sparse AgNW networks. We show that the activation process of efficient percolating pathways via thermal/current annealing is geometrically quantized and we use Lock-in Thermography (LiT) to highlight the phenomenon. The last three sections (4.2.1, 4.2.2, and 4.2.3) discuss the impact of network density, NW-NW junction efficiency, and electrical instabilities on the electrical distribution of standard AgNW networks. Such work was carried out via a threefold approach combining electrical measurements, electrical/thermal mapping techniques (one-probe voltage mapping, LiT), and simulation tools, which are carefully introduced in **Chapter 3**, prior to their practical use in Chapter 4.

Matlab and Comsol softwares indeed revealed to be very powerful not only to generate numerically 2D-stick percolating networks, but also to calculate their intrinsic electrical/thermal properties (individual current density in each of the sticks, overall network electrical resistance, local temperature, etc.). In particular, such simulation tools allowed us to generate either electrical or thermal maps associated to AgNW networks under bias. They revealed very convenient for the analysis of the phenomena related to electrical distribution issues reported in Chapter 4. From an applicative point of view, such modeling tools would also be beneficial for selecting the best combination of AgNW network parameters (NW dimensions, network density and dimensions) and external parameters (substrate, input voltage, environment), according to the target application.

Still from an applicative point of view, the trend for autonomic and portative devices make the flexibility and conformability of the materials used a highly desired asset. One of the main technological interests in finding a replacement to ITO actually concerns the research of flexible and stretchable transparent conductive materials. Touch Displays Research Inc. forecasts that the non-ITO transparent conductor market will reach up to \$13 Billion by 2023.^[25] Several studies have already shown the convenience of using AgNW networks for fabricating either flexible^[26,27] or stretchable^[28,29] devices. However, the stretchability of AgNW networks has not been deeply studied from a fundamental point of view in the literature. **Chapter 5** reports

preliminary results obtained during this thesis about this issue. Emphasis is put on the impact of the network density on the stretching properties, while *in situ* scanning electron microscopy characterization performed under mechanical stress helps visualizing the defects induced by high stress level and understanding the limitations of this material in terms of stretchability.

Finally, examples of device integration are provided and discussed in the final chapter of the manuscript (**Chapter 6**). While many integration works have already been performed in Grenoble labs by the past (organic solar cells,^[30] touch panels,^[26] transparent heaters,^[14]), the applicative contribution of this thesis is mostly dedicated to the followings. The first applicative angle tackled in the present work concerns the understanding of mechanisms leading to failure in AgNW-based transparent heaters. Given that most of the experimental works and analysis were carried out by former PhD student Mélanie Lagrange in 2015 and recently published by the team,^[31] only a very short part (6.1) will summarize the most significant achievements related to this topic. Second, the ability to integrate AgNWs into radio-frequency (RF) devices has been tested in collaboration with IMEP-LaHC laboratory (Grenoble). The corresponding work is developed in sections 6.2 and 6.3. First attempts associated to RF antennas and transmission lines are reported first, while emphasis is put on electromagnetic (EM) shielding thereafter.

Chapter 1. Introduction to transparent electrodes based on metallic nanowire percolating networks

Much of the content developed in this initial chapter appeared as a review article in *Small* journal,^[30] in collaboration with CEA-Liten and LMGP laboratories. This review was written during the thesis and consists of a deep investigation of the state-of-the-art related to metallic nanowire networks. The present chapter aims at overviewing the main applications for which the integration of MNW-based percolating networks is relevant. The important features and properties of such networks are reported in part 1.1. The main published results and future prospects are then discussed in detail in part 1.2 for each of the selected applications.

1.1. Metallic nanowire networks: Synthesis, Fabrication and Physical Properties

1.1.1. Synthesis of Metallic Nanowires (MNW) and Network Fabrication

The growth of metallic nanowires has already been described and reported by many groups.^[32–40] Several MNWs, such as silver, copper, gold, or cupronickel, have been synthesized in solution and deposited in the form of networks with promising properties. However, silver nanowire (AgNW) networks have so far been the most commonly studied.^[13,41–43] This stems from both the excellent physical properties of bulk silver, which is the most electrically conductive material at room temperature, and has rather straightforward synthesis scalability and reproducibility.

MNWs are mainly synthesized using the polyol process, but other methods, such as hydrothermal synthesis, may be preferred, notably for copper-based NWs.^[44–46] In the case of the polyol process, AgNWs are usually synthesized by reducing the Ag nitrate in the presence of polyvinylpyrrolidone (PVP) in ethylene glycol.^[34,47,48] PVP is the most widely-used capping agent and is responsible for anisotropic surface passivation. It is preferentially adsorbed along the (100) surfaces of the growing AgNW while the (111) surfaces are free to grow. The lateral growth is then prevented thanks to this anisotropic adsorption. **Figure 1a** shows a typical AgNW observed by Transmission Electron Microscopy (TEM) revealing the presence of an amorphous thin layer (mostly seen as the PVP shell) surrounding the (100) AgNW surfaces. This type of synthesis generally yields MNWs with a typical diameter ranging from 20 to 150 nm and lengths from few to several tens of μm . The AgNW synthesis is a scalable process (gram-scale synthesis), which is now well mastered. Several industrial providers such as “Blue nano”, “ACS Materials”, “Cambrios”, “BASF” (former AgNW activity developed by “Seashell Technology”), have already proposed commercial MNWs in solutions, specifically AgNWs and to a lesser extent CuNWs.

MNWs can be dispersed in many solvents, usually water or alcohols. Inks can be formulated to be suitable for various solution-based processing techniques in order to manufacture films with

randomly-oriented NWs. Of these methods, spin coating,^[49,50] spray coating,^[51] drop casting,^[52–54] doctor blade casting,^[55] dip-coating,^[56] Mayer rod coating,^[57–59] screen printing (serigraphy),^[60,61] vacuum filtration^[41,62,63] or brush coating,^[64,65] are the most reported in the literature. Figure 1b shows a typical, dense AgNW network sprayed on to a polyethylene naphthalate substrate (PEN). The network is dense enough to provide many electrical percolating pathways, while the free areas between the metallic NWs allow the light to go through, and the resulting film to exhibit high optical transparency.

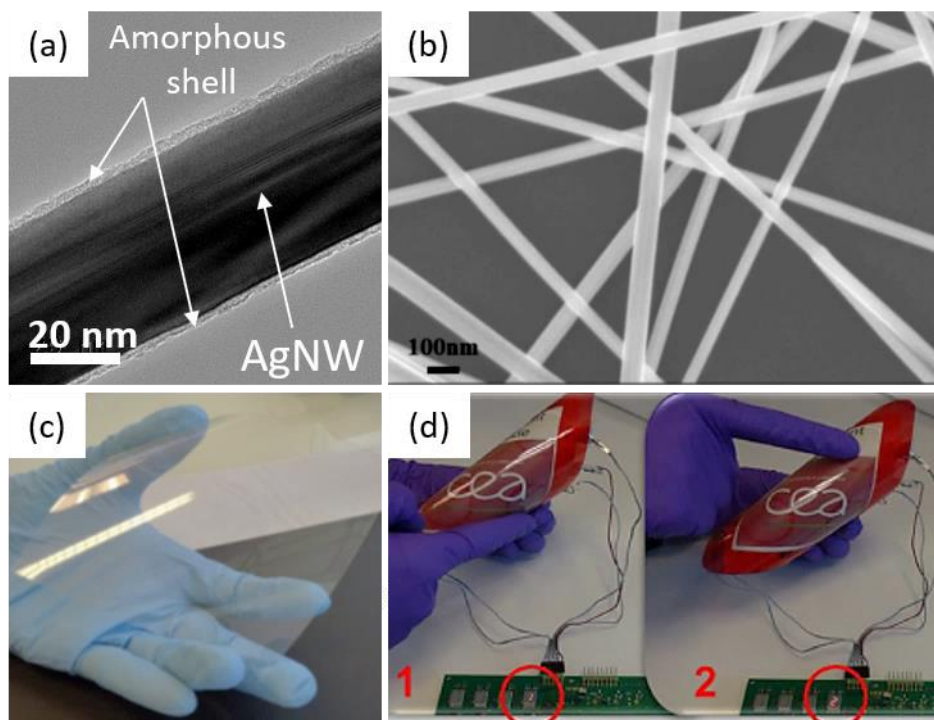


Figure 1. a) TEM image of a single AgNW showing the amorphous layer surrounding the NWs. This shell is assumed to be PVP. b) Plane-view SEM picture of an AgNW network. c) Typical flexible TE fabricated with MNW network. d) Flexible device (touch sensor) using MNW-based flexible TE.^[67]

As pointed out by Scardaci et al.^[51] or Cao et al.,^[43] either for MNWs or carbon nanotubes (CNTs), the choice of network fabrication method, as well as the experimental conditions, has a strong influence on the properties of the network. A trade-off often needs to be considered. For instance, for the spray method, the substrate should be heated high enough to allow the droplets to dry fast and prevent coalescence into larger droplets before drying. However the heating temperature should be adapted to the type of substrate, remaining moderate for polymer substrates for example.^[51,66] In addition, certain techniques, such as spin coating or vacuum filtration, can only be effective for fabricating films on small area substrates. The spray technique is compatible with up-scaling, as well as being cheap and providing fast deposition of uniform MNW films on either rigid or flexible substrates (see Figure 1c-d). This is why most of the samples studied within the frame of this thesis have been prepared using a spray-coating set-up (ExactaCoat Benchtop Ultrasonic Spraying System, from Sono-Tek Corp.). However, one possible limitation arises from the difficulty of spraying long MNWs as they tend to break in the ultrasound nozzle or become stuck and clog the spray.

1.1.2. Properties of individual MNWs: size effects

Individual MNWs have very good electrical and thermal conductivity: silver is the most efficient electrical conductor, and gold, copper and even alloys such as Cu-Ni are also highly conductive. Even for small NW diameters, i.e. typically from 20 to 150 nm, the electrical conductivity is still very high. It decreases for diameters approaching the mean free path of electrons in bulk metals (about 40 nm for Ag or Au). Bid et al., for instance, measured at both low and room temperature the electrical resistivity of AgNW and CuNW.^[68] These authors showed that when the NW diameter approaches the mean free path of electrons in the bulk material, the electrons surface scattering increases, leading to an increase in NW resistivity. Such a behavior was experimentally demonstrated and can be well described by Equation 1.1:^[68]

$$\rho_{NW}^{Ag} = \rho_{bulk}^{Ag} \left(1 + \frac{\Lambda}{2D_{NW}} \right) \quad (1.1)$$

With ρ_{NW}^{Ag} the resistivity of silver nanowire, ρ_{bulk}^{Ag} the resistivity of bulk silver, D_{NW} the nanowire diameter and Λ the electrons mean free path. For instance, at room temperature, the electrical resistivity of a 30 nm diameter AgNW is 25% higher than for a diameter of 100 nm.^[68] A similar trend is observed for CuNWs. However, this increase still appears reasonable for efficient integration, but could play a negative role when stability under high current density or rather high temperatures is required.^[50]

From an optical point of view, a low diameter is beneficial for increasing the transmittance and decreasing the proportion of photons scattered by the NW.^[69-71] Larger NW diameters are also associated with higher roughness, which often needs to be reduced for most optoelectronics devices, especially when very thin layers are concerned, such as in organic solar cells or OLEDs for instance.

Long MNWs help to reach electrical percolation at a lower network density (the latter is simply defined as the number of AgNWs per unit area). Indeed, as described in §1.1.3, the critical density, associated with the percolation occurrence probability of 50% and defined as n_c , is inversely proportional to the square of the NW length. Hence, the use of high aspect ratio nanowires appears of interest since it allows a decrease of the number of resistive junctions involved in the electrical percolating network. Meanwhile, it increases the optical transparency of the network. Several studies recently reported major advances in the synthesis of very high aspect ratio (>1000) silver nanowires,^[72-75] suitable for fulfilling the industrial criteria of optoelectronic performances. However, it is rather challenging trying to maintain the integrity of very long NWs as they tend to break during the dispersion or deposition processes (especially when ultrasounds are used). Finally, a compromise needs to be found for the choice of the most suitable NW dimensions in relation to target applications. The ability to control the dimensions of nanowires (both average values and size distribution^[76]) during synthesis remains a crucial issue and a challenge for future prospects for metallic nanowire networks.

1.1.3. Influence of interconnections and network density on the optical and electrical properties

The interconnections between MNWs play a key role, strongly influencing the properties of the network.^[77–79] Just after deposition, the electrical resistance in the MNW network is often high. This can be attributed to the non-efficient contacts between NWs, and to the presence of organic residue such as the PVP shell at the contact points. This feature is similar to CNT based networks, but MNWs appear much more prone than CNTs to creating efficient interconnections: the network's electrical resistance can be drastically reduced thanks to methods such as thermal annealing (see **Figure 2a** and **Figure 2b**),^[42,80] chemical treatments,^[49] laser sintering,^[81] light-induced plasmonic nano-welding (see **Figure 2c** and **Figure 2d**),^[82,83] or mechanical pressing (see **Figure 2e** and **2f**).^[54] Many papers report that such methods can lead to a dramatic decrease in sheet resistance from 10^4 or 10^5 to about $10 \Omega \text{ sq}^{-1}$.^[42,50,54] A decrease of this type can be attributed to the activation of surface diffusion phenomena, leading to local sintering at the junctions between neighboring NWs. Bellew et al.^[78] and Nian et al.^[79] have recently been able to measure the electrical resistance of NWs and certain individual junctions after post-deposition treatments. Both investigations show that for optimized networks, the junctions do not seem to predominantly impact the network's electrical resistivity any more.

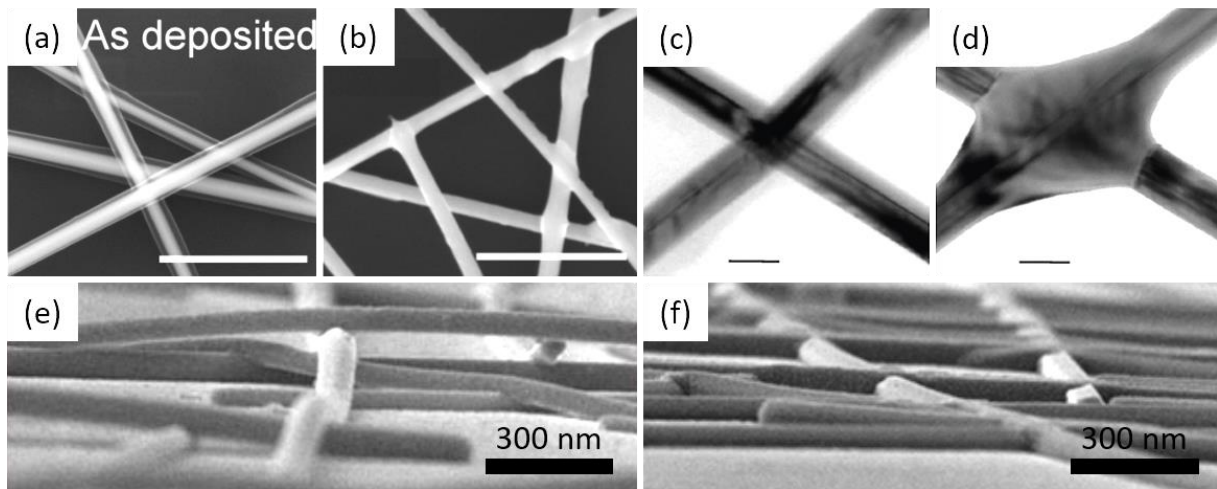


Figure 2. *a,b*) SEM images of an as-deposited sample (a) and of a specimen annealed for 10 minutes at 300 °C (b). Scale bar is 1 μm.^[42] *c,d*) TEM images of silver nanowire junctions before (c) and after (d) optical welding. Scale bar is 50 nm. Reproduced with permission.^[83] *e,f*) SEM images of AgNW electrodes before (e) and after (f) mechanical pressing at 25 MPa for 5 s.^[54]

Network density, defined as the number of nanowires per unit area, is also of primary importance. It may also be useful to consider the areal mass density (amd) simply expressing the metal mass per unit area in mg m^{-2} .^[41,50] This parameter has a strong influence on the optoelectronic properties of the network. For instance, optical transparency often appears to decrease linearly with network density,^[69,84] while sheet resistance R_{sh} is linked to the density as follows:

$$R_{sh} \propto (n - n_c)^{-\gamma} \quad (1.2)$$

where n_c is the critical density and γ is the percolation exponent.^[85] This is well-demonstrated by the experimental measurements depicted in **Figure 3a**. Increasing the network's *amd* leads to a linear decrease in optical transmittance and a power-law decrease in electrical resistance (linked to a non-linear increase in efficient electrical pathways available through the whole network). Moreover, such experimental measurements can be well fitted by relatively simple modeling approaches.^[50] As shown first by De et al. and then by Lagrange et al., percolation theory dominates the electrical behavior of networks associated with low density.^[41,50]

It is necessary to search for a trade-off in network density. A network that is too sparse does not provide enough efficient pathways for electrons in the network to reach low sheet resistance values, while one that is too dense conducts efficiently but becomes too opaque. For many applications, network density should lead to high light transmittance (~90%), associated with low electrical resistance (~10-100 $\Omega \text{ sq}^{-1}$) through the whole electrode area. To efficiently assess the effects of network density, figures of merit (*FoM*) are often used. A classic *FoM* for considering TE performances is Haacke's *FoM* defined as:

$$FoM = \frac{Tr^{10}}{R_{sh}} \quad (1.3)$$

where Tr is optical transmittance (often considered at 550 nm) while R_{sh} is sheet resistance.^[86] This *FoM* is used to assess performance of a TE specifically for comparing different TEs, with a higher value corresponding to a better trade-off between transmittance and sheet resistance. For the AgNWs presented in Figure 3a, the *FoM* is bell-shaped. The best *amd* appears to be close to 130 mg m^{-2} .^[50] This value depends on how the network is manufactured, and the dimensions of the MNWs. Other values have been reported in the literature, for instance 40 mg m^{-2} by Celle et al.,^[14] (*in supplementary material section*), 70 mg m^{-2} for De et al.,^[41] and 331 mg m^{-2} for Göbelt et al., who used AgNWs of rather large diameters and small lengths.^[87] Most of these values show that considering an *amd* range of values of 40-200 mg m^{-2} (compatible with the literature^[50,79]) corresponds to an equivalent material quantity of a homogeneous thin Ag layer that is 4-20 nm thick. To obtain similar optoelectronic performances, the usual thickness range associated with conventional ITO-based electrodes is 150-200 nm.^[88] Given that In_2O_3 represents roughly 90 wt% in ITO, the corresponding indium *amd* range is roughly 750-1050 mg m^{-2} , much higher than the required Ag *amd* in AgNW networks. Knowing that the price per unit mass of In and Ag are of the same order of magnitude, this shows that integrating MNW networks as TEs in devices can be an interesting cost-efficient replacement for the conventional ITO or Ag grids used in solar cells.^[87,89] Therefore regarding the costs associated to raw materials, AgNWs appear more competitive than ITO. Moreover, ITO is fabricated using an expensive high vacuum physical phase deposition process, whereas AgNW-based electrodes are compatible with low-cost solution-based deposition processes. It is actually difficult to compare fairly the final overall costs for various processes including all production costs (capital expenditure, operating expense, raw material prices, etc.). It is beyond the scope of this thesis, however some information dedicated to this specific point is available elsewhere.^[90]

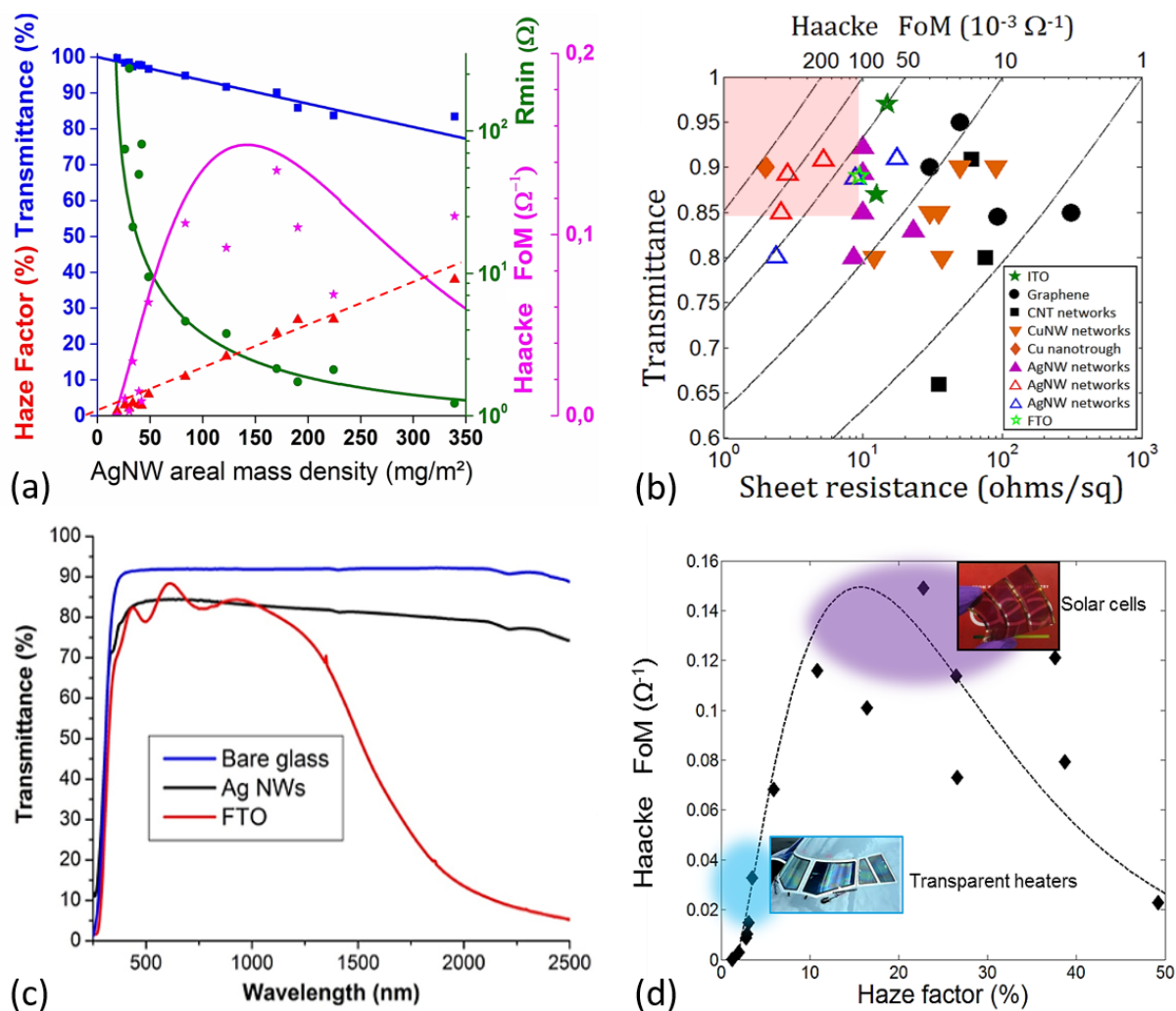


Figure 3. a) Dependence of the experimental values of optical transmittance, electrical resistance, haze factor, and Haacke's FoM of AgNW networks versus their areal mass density (amd). The continuous lines are associated with fits extracted from physical modeling by Lagrange et al.^[50] b) Transmittance versus sheet resistance diagram for comparison between various TCMs: ITO,^[3,41] graphene,^[3,91–93] CNTs,^[3,41,94] CuNWs,^[38,57,82,95] Copper nanotrough,^[96] AgNWs,^[3,50,54,97–99] FTO.^[100] The dashed lines correspond to different iso-values of Haacke FoM: 200, 100, 50, 10, 1 with units $10^{-3} \Omega^{-1}$. c) Comparison of optical total transmittance in the UV-VIS-NIR region for a bare glass substrate (blue), AgNW network (black) and fluor-doped tin oxide (FTO, in red) which exhibit similar sheet resistance of about $11 \Omega \text{ sq}^{-1}$. MNW networks are still transparent in the NIR region. d) Calculated Haacke FoM (from experimental values) of AgNW networks versus their experimental haze factor. The dashed line is associated with a fit extracted from physical modeling by Lagrange et al.^[50] Areas of interest are roughly represented for two applications which require either low or high haze factor values.

Figure 3b shows the characteristics (Tr vs R_{sh}) of several transparent conducting materials including ITO, FTO (Fluorine doped Tin Oxide), CNTs, graphene, copper and silver nanowire networks. The discontinuous lines plotted in Figure 3b are associated with several iso-values of the Haacke FoM. Obviously, the target is in the top left corner of Figure 3b. By using adequate

post-deposition treatments, many research groups have reported metallic NW networks with optical transmittance of 90% and sheet resistance of less than $10 \Omega \text{ sq}^{-1}$,^[50,79] showing that metallic nanowire networks can exhibit more competitiveness than other TCMs in terms of trade-off between transparency and electrical performances. Finally, when compared to other conventional TCMs, MNW networks benefit from interconnections that enlarge the wavelength range for which the optical transparency is very high. For instance, Figure 3c shows the optical transmittance of an AgNW network and one typical Transparent Conductive Oxide (TCO), i.e. Fluor-doped Tin Oxide (FTO). Both films have similar physical properties, a sheet resistance of $10 \Omega \text{ sq}^{-1}$ and an optical transparency of 90% at 550 nm once the glass substrate background has been removed. An interesting feature for the AgNW network is the high transmittance values in the near Infra-Red region (NIR) which is a relevant asset for certain applications, especially photovoltaic systems.

1.1.4. Light scattering of MNW networks

Another important parameter which needs to be considered for applications where TEs are involved is the haze factor (or haziness). This is an optical parameter that quantifies the amount of transmitted light scattered by the TE and is simply defined as the ratio between the diffuse part and total transmittance. Requirements regarding haziness depend greatly on the applications. For instance, touch panels and transparent heaters placed on windscreens or visors need a low haze factor (typically below 3%) to ensure comfort for the human eye, and to prevent blurred viewing, while the performance of solar cells is enhanced by a high haze factor associated with the TE used.^[101,102] Scattering light enhances the optical path length of photons in solar cells, increasing their probability of being absorbed by the active area of the cell and then generating charge carriers.^[103]

The haziness of MNW networks has thus been the subject of several studies.^[69,70] Experimental data show a linear increase in haze factor with network density, as is clearly shown in Figure 3a. In a similar way, the haze factor decreases in a linear manner as T_r increases.^[50,69,84] Moreover, the haze factor depends significantly on the dimensions of the NW. For instance, Araki et al.^[69] showed that using very long AgNWs (20-100 μm) helps to decrease the haze factor, in agreement with Chang et al.^[104] In the same vein, Preston et al.^[70] observed that AgNWs with higher diameters lead to a higher haze factor in the visible range.

Unfortunately, the literature has not yet provided many detailed investigations capable of explaining these tendencies. Interestingly, Khanarian et al. reported that AgNW diameter appears to be the most important parameter morphologically, determining both the transmission and haze of AgNW networks.^[105] As discussed below, MNWs can be mixed with other materials to produce hybrids. A good example for varying haziness is the controlled incorporation of ZnO nanopylamids into an MNW network film which makes possible highly tunable control of the scattering properties of this type of TE.^[106]

Figure 3d shows the behavior of the AgNW networks' FoM against the haze factor. Each experimental point is related to one specific value of areal mass density. The FoM is bell-

shaped. **Figure 3d** can be seen as a guideline for selecting the most appropriate density value compatible with the target application, as well as the associated constraints regarding the haze factor.^[50] Defining a new *FoM* taking into account the haziness of the MNW-based TCM studied would be very useful for selecting the appropriate physical parameters for each specific application.

1.1.5. Flexibility of MNW Networks

Mechanical flexibility is one of the featured characteristics of MNW networks, paving the way for flexible electronics. Unlike ITO and many other TCMs, their electrical conductivity is not affected much when subjected to bending tests (see **Figure 4a**) and they also show good responses in the case of stretching.

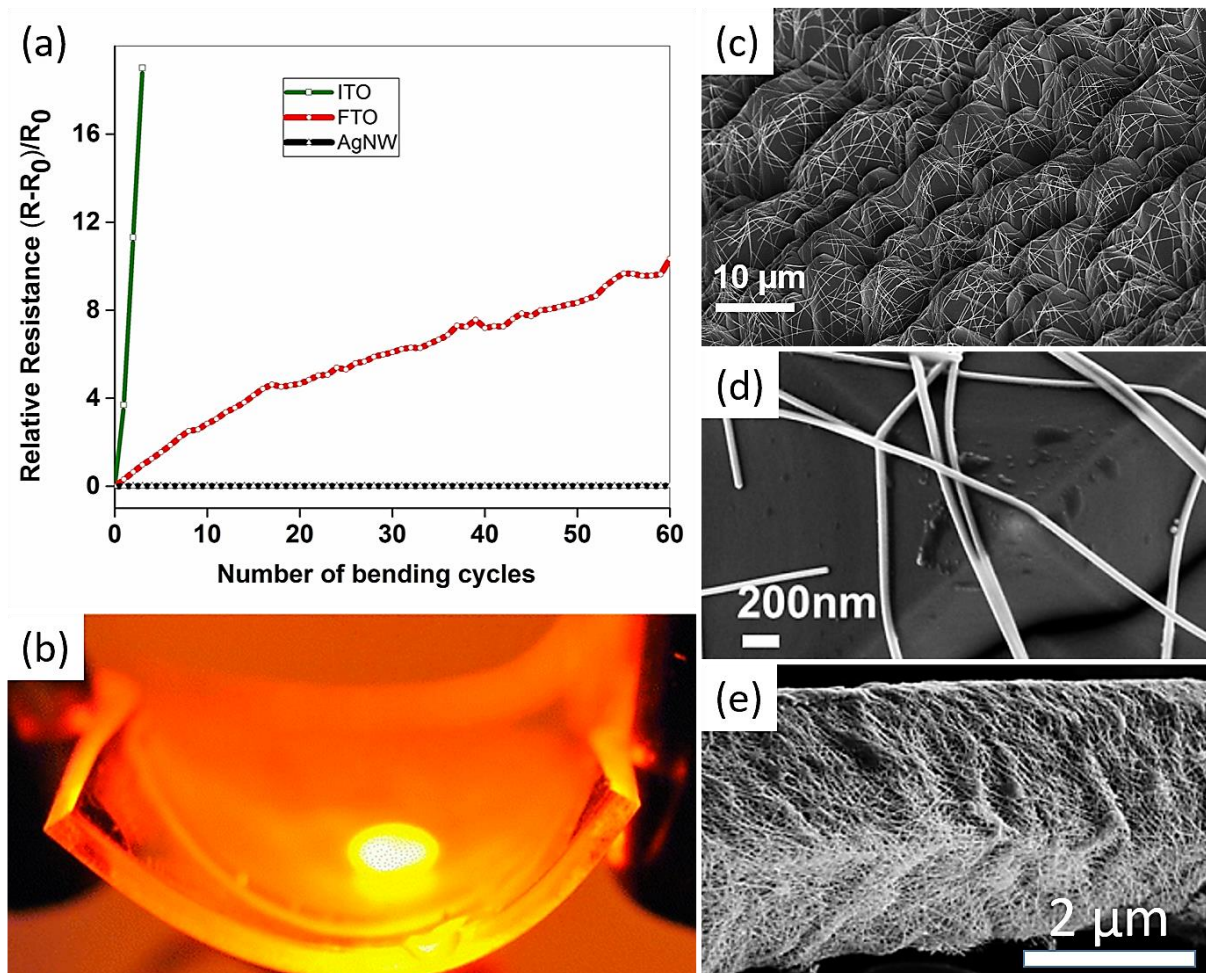


Figure 4. a) Comparison of the relative electrical resistance of different types of TE under mechanical bending. The radius of curvature used was 5 mm.^[9] b) Flexible light-emitting electrochemical cell using an AgNW network embedded in a polyurethane optical adhesive as a TE.^[27] c,d) SEM images of AgNWs coated on textured Si surfaces. The nanowires can perfectly fit the shape of this uneven surface. e) SEM image of coated AgNWs on a polyester/rubber thread.^[107]

For instance, Miller et al. reported that AgNW networks can withstand up to 76% tensile strain and 250 bending cycles of 15% strain with negligible increase in electrical resistance.^[27] When AgNW networks are embedded in a transparent polyurethane optical adhesive and inserted into a flexible light-emitting electrochemical cell, the latter devices continue to emit light under bending, even with a radius of curvature of 1.5 mm (see **Figure 4b**).^[27] Many other examples are provided in the applications sections, showing that MNW networks can be efficiently assimilated into a wide range of flexible devices. Finally, another very significant advantage of MNW networks is their ability to conform to non-planar surfaces. This may be useful in various applications involving highly roughened surfaces. For instance, Figure 4c and Figure 4d show that AgNWs are very ductile and are able to fit closely to the shape of a textured silicon surface, the latter being often used in the Si-based solar cell industry. Figure 4e is another example, showing the conformability of AgNWs for smart conductive textile applications.^[107]

As already mentioned in the introduction, not only the flexibility but also the stretchability is an important asset for next generation transparent electrodes. Given that one chapter of the present thesis specifically discusses the stretching properties of composites made of interconnected AgNWs deposited on elastomeric substrates, the corresponding state-of-the-art about stretchability is available in the very first section (5.1) of dedicated Chapter 5.

1.1.6. Stability issues and hybrid nanocomposites based on MNWs

The stability of MNW networks has been mentioned as a possible limitation for their integration into devices. Stability in relation to different stresses is worth considering: thermal, chemical, electrical. When submitted to high temperatures and/or current conditions, MNW networks can have early failure rates^[108] caused for instance by surface diffusion^[42,109] and/or electromigration processes and/or modifications of surface chemistry. **Figure 5a** presents the morphology of an AgNW network after exposure to high temperatures. Plateau-Rayleigh instability occurs, leading to spheroidization, which is associated with a drastic increase in electrical resistance of several orders of magnitude. Figure 5b shows an AgNW network after exposure to electric stress.^[110] The combination of high relative humidity and high temperature appears critical as well^[111,112], while humidity-assisted annealing at low temperatures appears to act favorably on lowering electrical resistance in AgNW networks.^[113] Reports in the literature on MNW stability issues appear controversial and this can be explained by the different experimental conditions used, either for NW synthesis, solvent purity, network fabrication, post-deposition treatment or storage.^[112,114] All these parameters can have a strong impact on network stability.

For instance, Mayousse et al. showed that the sheet resistance of AgNW-based electrodes was insignificantly degraded after two years of storage in the dark and in air.^[111] On the contrary, Jiu et al. observed high degradation of naked AgNW networks (day light, in air) after only two weeks. When storing the samples in air, but in the dark, the increase in resistance was less than a factor of 5 over 30 days, meaning that natural light might accelerate the degradation of

AgNWs.^[112] Depending on the research groups, the environmental stability of AgNW networks is then very different, and can vary from several days up to years. Given that investigations of MNW networks are relatively new, more background regarding environmental stability (relative humidity, natural light, storage) is still required. An important point that needs to be taken into account for MNW integration is that their stability will have to be studied in the final product, after encapsulation. As discussed in more detail below, the use of nanocomposites can drastically improve the stability of NW networks.

The thermal stability of MNWs can be improved by increasing their diameters: the thinner they are, the lower the temperature associated with the nanowire's thermal instability.^[50] However, it seems that using hybrid materials combining MNWs and thin layers of other materials is a much more promising way of drastically decreasing the effects of such instability. For instance, the use of reduced graphene oxide with either AgNWs^[115] or CuNWs^[116] has been shown to increase the robustness and stability of the resulting TE.

Embedding AgNW with either ZnO nanoparticles^[117] or a TiO₂ layer^[118] was found to significantly improve the thermal stability. More specifically, using atomic layer deposition (ALD) makes possible the deposition of very conformal and homogeneous thin protecting layers (just a few nm) without significantly impacting the transparency of the resulting TE, while improving the contact between the MNW network and the underlying substrate at the same time (see Figure 5c).^[87]

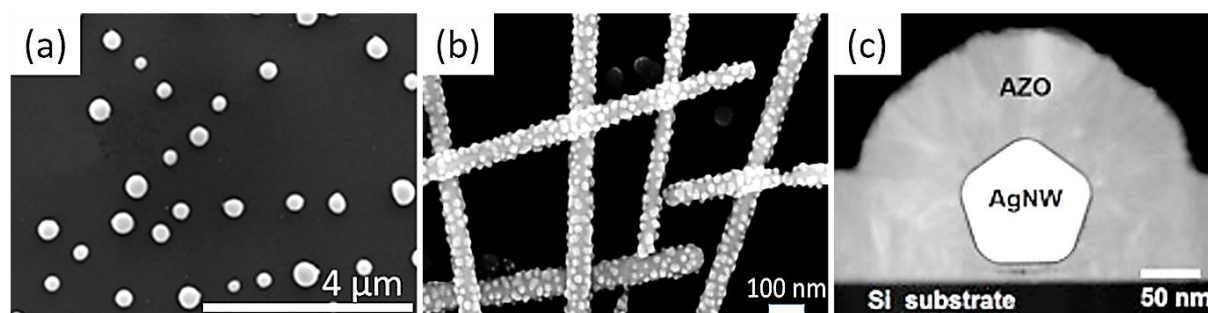


Figure 5. a) SEM observation of AgNWs after thermal annealing up to 350°C.^[42] b) Deterioration of AgNWs on a PEN substrate when submitted to electrical stress (constant current flow for two weeks). Induced modification of surface chemistry might also play a critical role in degradation. c) Scanning Electron Microscopy cross sectional image of an AgNW after encapsulation by a 100 nm thick layer of Aluminum-doped Zinc Oxide (AZO).^[87]

From an applicative point of view, the use of hybrid materials combining MNW with either graphene, conductive polymers, carbon nanotubes, TCOs or other materials can improve the performances of the final devices they are used in. Several examples given in the applications section are dedicated to hybrid materials which have several assets, as a result of taking advantage of improved stability as well as interface properties (adhesion, roughness, balance of the work functions, etc...). Many studies report enhanced performances for devices when hybrids are used instead of bare MNW networks.^[87,117,119] For instance, highly stretchable and

transparent conductors were obtained by combining the mechanical compliance of small CNTs and the high conductivity of AgNWs.^[120] Another recent example is the use of atomic layer deposition of aluminum-doped zinc oxide on AgNWs leading to a very efficient nanocomposite-based transparent electrode used on top of Si-solar cells.^[87] Other studies also considered hybrids between MNWs and other materials, such as graphene or conducting polymers, which pave the way for many possibilities in terms of architecting nanocomposites: hybrids should provide future innovations in terms of enhanced properties and integration into devices.

1.2. Integration of metallic nanowire networks for different applications

The main properties and challenges linked to MNW networks were presented in the last section and we will now address how to integrate them into real devices. Every application has its own peculiarities, is subject to various problems and requires different properties of the MNW networks. The applications of MNW networks are addressed in the six following categories: first the field of photovoltaic systems, second that of lighting, focusing on OLED devices, and third the field of transparent film heaters. The first three fields of application reviewed here are the main studies reported that deal with the integration of MNW networks into devices. We continue by reviewing the field of smart windows and displays, especially electrochromic and Polymer Dispersed Liquid Crystal (PDLC) devices, as well as touch screens, and then the field of electromagnetic devices, in particular RF antennas and electromagnetic shielding. Beyond a simple list of the different applications that have been studied in the literature, this section aims to emphasize the advantages of using MNWs in such devices and highlight future prospects for integrating MNW-based transparent electrodes into next-generation flexible devices.

1.2.1. Photovoltaic Applications

Photovoltaic systems, among other sustainable green energy technologies, have been developed to offer an alternative to fossil fuel energy. Efforts are made, for instance, for reducing costs, improving efficiency and using abundant materials.^[121] Light obviously needs to enter a solar cell while the latter also requires transparent contacts to collect the photo-generated charge carriers. Transparent electrodes are a key component in solar cells, directly influencing photo-conversion efficiency. Generally speaking, the materials chosen must have several properties:^[122] high electrical conductivity, high transparency, as well as band alignments, and the work function should be considered when the TEs are used as efficient ohmic contacts.^[123] For many decades, transparent conductive oxides (TCO) such as ITO, AZO or FTO have been used for solar cell applications.^[8] For these materials, light absorption is associated with free carrier inter-band processes, resulting in a trade-off between conductivity and light transmission which both strongly depend on doping level: significant doping results in better electrical conductivity but in lower light transmittance. This type of trade-off should not be considered when dealing with MNW networks as their transparency versus wavelength dependency

appears as a rather monotonous function (at least above 400 nm),^[124] as shown in Figure 3c. However there is still, as for all applications implying transparency and conductivity, a trade-off between electrical resistance and optical transmission: for TCOs this is controlled by the film's thickness, for metallic NW networks, the key parameter is network density (or areal mass density), as developed in §1.1.3.

One of the main topics that has attracted interest recently is the development of flexible solar cells with the use of simple and low cost methods of cell printing.^[125,126] Unlike ITO, AgNW networks are flexible and retain their electrical properties intact when bending, as seen earlier. Andrés et al. have recently synthesized high aspect ratio AgNWs, seen to be a low-cost alternative to ITO in organic solar cells (OSC) whereas they induce only a small decrease in the power conversion efficiency.^[125] Guo et al. obtained conversion efficiency up to 5.81% by using AgNWs as the top electrode in tandem OSCs.^[126] Using AgNWs now appears compatible with the development of solar cells that can be fully printed. For instance, Angmo et al. fabricated single and tandem cells almost entirely in ambient conditions compatible with the roll-to-roll method, which is an easily scaled up deposition method for flexible substrates.^[127] Other reported works have also proved that AgNW networks can be used effectively as the transparent top electrode in OSCs^[60,98,128] with excellent bending capacities within this application.^[129] These results show that AgNW networks can compete with ITO in terms of photovoltaic performances, but have much greater flexibility.

In addition to high transparency, low electrical resistance and excellent flexibility, another asset of AgNW networks is their haziness. Scattering light increases the efficiency of the solar cells by increasing the length of the photon pathways within the cell, making possible a higher probability of photon absorption. This feature was already studied in 2008 by Lee et al. for example, and AgNW networks were integrated for this purpose into organic solar cells with good performances compared to when TCOs were used.^[130]

As depicted in **Figure 6a-c**, AgNW-based electrodes were also used to fabricate polymer solar cells that are semi-transparent in the visible region^[131–133] (for example, 66% transparency at 550 nm^[134]). While semi-transparent in the visible range, the cell is nevertheless highly absorbent in the IR range. As seen previously, AgNW networks, unlike TCOs, are highly transparent in this region (see Figure 3c), allowing the cell to be very efficient by absorbing in the IR and being semi-transparent for the human eye. While this approach is of interest, integration of such electrodes into windows can be delicate because of the haziness which needs to remain low.

A recent investigation also reported the use of AgNW networks as front electrodes for a fully roll-to-roll processed flexible ITO-free organic photovoltaic cell.^[135] The stability of the devices was tested and it was shown that replacing the PEDOT:PSS as the front electrode with an AgNW network increased operational stability by up to 1000%.^[135] Finally, the use of sort of MNWs other than Ag has also been reported by Wiley's group. They successfully integrated entirely solution-processed CuNi NW based-films as anode in OPV devices exhibiting efficiencies of 4.9%.^[49] Generally, the integration of other MNWs than Ag ones as transparent electrodes with good properties and high stability still remains a challenge in front of photovoltaic applications.

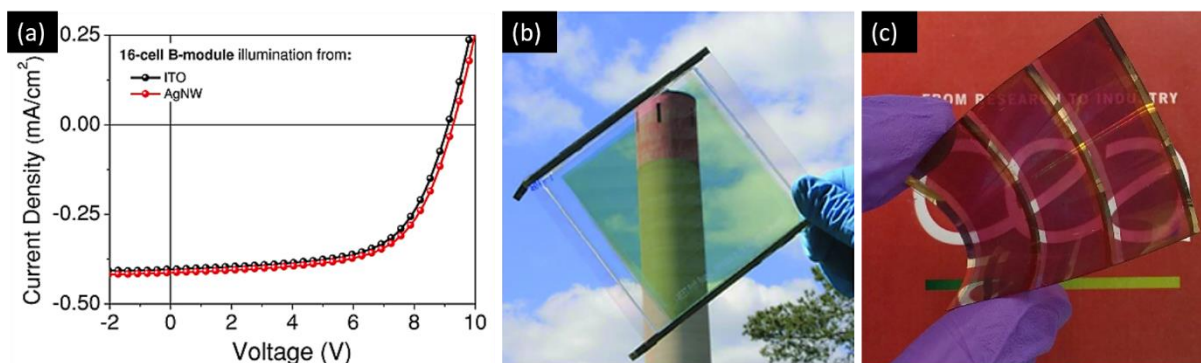


Figure 6. a) *J-V curves of a 64 cm² 16-cell module with illumination from both the bottom ITO and top AgNW electrodes.*^[133] b) *Photograph of a semi-transparent module with an active area of 64 cm².*^[133] c) *Semi-transparent module with an AgNW top electrode and an active area of 11 cm².*

1.2.2. Lighting (Organic LEDs)

The vast majority of lighting devices using MNW network transparent electrodes concerns organic light-emitting diodes. For this reason, this application will be investigated in depth in this section. In organic or polymer-based Light-Emitting Diodes (LEDs), the global architecture has similarities with that of solar cells. The active layer is sandwiched between two electrodes, at least one of which is transparent. Contrary to solar cells, charge carriers are not extracted but driven to the active layer, which is responsible for the recombination of electron-hole pairs to produce photon emission. The use of organic component (OLEDs) or polymers (PLEDs) as the active layer paves the way for the production of flexible light-emitting devices compatible with an entirely solution-based and low cost process. In order to offer appropriate solutions for the target applications, e.g. portable electronic rollable displays or conformable lighting panels, not only the active layer but also the interfaces and especially the transparent conducting layer have to be highly flexible. Large angle bending cycles with no alteration in conductivity, transparency or light emission properties are essential. All these needs can be fulfilled by using MNW-based electrodes.

In the very first studies examining silver nanowire-based OLEDs, good electroluminescent properties were reported.^[80,136–140] Zeng et al. replaced the commonly used Glass/ITO layer with an AgNW/PVA (polyvinyl alcohol) mixture in the architecture of the OLED device.^[136] In order to prevent electrical leakage and to adjust the anode work function to enhance hole injection, a buffer layer of PEDOT:PSS a few nanometer thick was deposited between the AgNW network and the active layer. Gaynor et al. were able to produce very efficient ITO-free white OLEDs using an AgNW/PMMA (poly(methyl methacrylate)) composite electrode.^[140] The whole device showed one of the highest levels of luminous efficacy reported so far for an ITO-free white OLED, i.e. over 30 lm W⁻¹ at a brightness of 1000 cd m⁻², and exhibited two other major optical characteristics: color-independent emission while increasing the viewing angle (see **Figure 7a**) and an almost perfect Lambertian emission.

Another key challenge is the ability of the AgNW-based OLED devices to keep their electroluminescent performances unaffected when exposed to deforming strains, which has

been dealt with remarkably by Pei's group.^[28] Both stretchability (see Figure 7b, and Figure 7d-e) and bendability (see Figure 7c) of elastomeric polymer light-emitting diodes (EPLEDs) with a rubbery AgNW/PUA (poly(urethane acrylate)) composite as the transparent electrode were studied in depth. The resulting stretched device was found to withstand strain up to 120% while displaying fairly uniform light emissions across the entire luminous area. It also showed significantly improved efficiency in the stretched state. A module of 5×5 EPLED-based pixels was fabricated for the first time, showing the ability of this kind of architecture to face the technical challenges required for stretchable OLED displays.

As mentioned above, lowering the work function, avoiding potential current leakage with the active layer, and enhancing the flexibility are some of the key challenges that need to be faced when integrating a MNW-based transparent electrode into an OLED device. In order to eliminate the energy level mismatches that occur with the adjacent layer, a n-type hole injection layer (HIL) can be inserted between the AgNW-based transparent electrode and the hole transport layer (HTL). In the case of MNW-based electrodes, this process makes it possible to smooth the surface of the electrode at the same time, which is necessary to avoid short circuits. Using this process, Lee et al. manufactured a phosphorescent OLED device with promising performances such as a very low turn-on voltage (3.6 V) and very high current and power efficiencies (44.5 cd A⁻¹ and 35.8 lm W⁻¹ respectively).^[99]

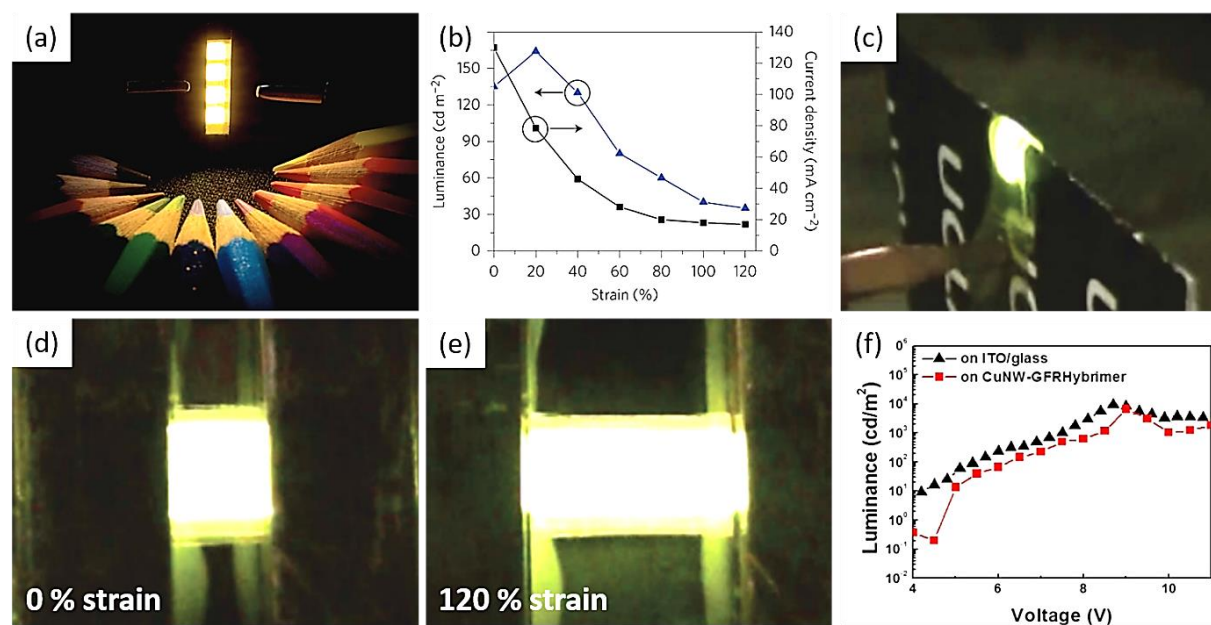


Figure 7. a) Photographic image of four functioning white tandem OLEDs at 1000 cd m⁻².^[140] b-d) Current density and luminance characteristics of an elastomeric polymer light-emitting diode (EPLED) device working at 12 V with increasing strain (b). Image of an EPLED (original emission area of 3.0×7.0 mm², biased at 12 V) wrapped around the edge of a piece of 400 μm thick cardboard (c). Photographs of an EPLED (original emission area, 5.0×4.5 mm²) biased at 14 V at 0% (d) and 120% strains (e).^[28] f) Demonstration of a flexible OLED on a CuNW-GFRHybrimer film: plotting luminance vs voltage (L-V). A reference OLED device on ITO/glass was tested for comparison.^[141]

Very few examples of CuNW integration into OLED applications have been reported so far. For instance, Im et al. embedded CuNWs into a Glass Fabric Reinforced plastic film (GFRHybrimer film) and the resulting platform was successfully integrated for the very first time into a flexible OLED device with performances almost identical to those of the ITO based-reference device (see Figure 7f).^[141] Proper encapsulation is a crucial point when trying to integrate CuNWs in general, as copper is readily prone to oxidation, leading to degradation of the electrode's performances. This was achieved by manufacturing stable core-shell nanowires, i.e. Cu@Cu₄Ni nanowires, used in a transparent elastomeric form for segments of the external circuits of OLEDs.^[142]

1.2.3. Transparent Film Heaters

Transparent film heaters (TFHs) are transparent conducting films that can heat by voltage application.^[143] They make possible a variety of possible applications, for instance in defrosting or defogging vehicle windows,^[144] outdoor panel displays^[146] or more generally devices exposed to temperature variations. Historically, TFHs were one of the first applications envisaged for transparent conducting materials (TCM). They were used to de-ice aircraft windscreens during World War II, enabling the aircraft to fly at much higher altitudes.^[147] After extensive studies based on TCOs, TFHs made from emerging nanomaterials have started to arise in the past few years. The use of carbon-based nanostructures such as graphene^[148] and carbon nanotube^[149] (CNT) networks, metallic nanowires (MNWs) as well as hybrid materials^[150,151] has recently been reported. The reasons for this development are the same as for other TE applications: to reduce fabrication costs, extend to large surfaces, increase flexibility and, in this special case, give the possibility for heating at low voltages.

MNW networks are among the most promising materials for TFH applications. In the literature, AgNW networks have been the main sort of MNW networks proposed for TH applications in the last years.^[14,152,153] They are able to increase their temperature by several tens of degrees using an operating voltage of less than 12 V, which is convenient for most devices.^[14,16,154] as well as producing large-area uniform heating^[143] and a fast thermal response.^[14,17] They do not show any significant resistance change when subjected to bending.^[155] Furthermore, they can be used for surfaces with complex geometries and shapes (helmet visors, windscreens...), as the processes can lead to conformable depositions. In addition to the previous criteria (heating properties, transparency and flexibility), the development of future electronic devices will possibly require high stretchability for wearable electronics.^[154]

The first report of AgNW networks used as transparent heaters from Celle et al.^[14] studied the temperature elevation of the films while applying different voltages, as reported in **Figure 8a**. A thermochromic display was also designed by coupling AgNWs used as transparent heaters with a thermochromic ink (see Figure 8b-c). The power dissipated in the material (V^2/R) is directly related to the steady-state temperature by means of a balance between the Joule effect and heat loss: conduction to the substrate, convection to the surrounding air and radiation from the hot surface.

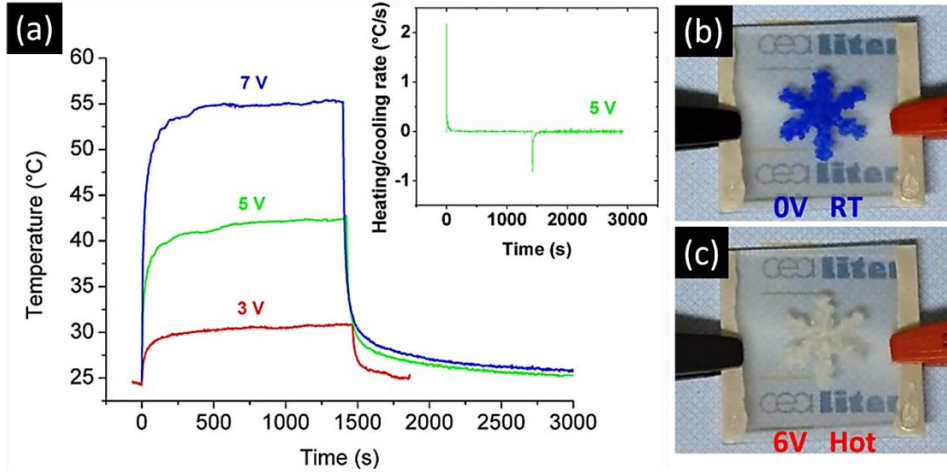


Figure 8. a) Temperature achieved by an AgNW-based transparent heater (TH) with $R_s = 33 \Omega \text{ sq}^{-1}$ at various voltages (on PEN substrate). Insert: heating and cooling rate at 5 V.^[14] **b,c)** Simple thermochromic device composed of an AgNW network: (b) at room temperature, (c) when a voltage of 6 volts is applied between opposite electrodes.

Sorel et al.^[16] described the theory of Joule heating in a TFH composed of AgNWs. Considering that the temperature is uniform over the whole sample, the energy balance can be written as follows (conduction losses to external parts of the system being neglected):

$$I^2R = mC \frac{dT(t)}{dt} + A(h_1 + h_2)(T(t) - T_0) + \sigma A(\varepsilon_1 + \varepsilon_2)(T(t)^4 - T_0^4) \quad (1.4)$$

The term on the left is the power input to the TFH. The first term on the right is the heat that is responsible for the temperature elevation of the sample of mass m and specific heat C , the second term represents the heat losses by convection (A and h are respectively the specimen area and the convective heat-transfer coefficients) and the third one the heat losses by radiation (1 and 2 design the MNW network and the substrate, respectively). At low temperature ranges, as in the experiment presented in Figure 8a, the radiation term can be linearized and then this energy balance has the following analytical solution, demonstrated in Sorel's paper:^[16]

$$T(t) \approx T_0 + \frac{1}{\alpha} \frac{I^2R}{A} \left[1 - \exp\left(-\frac{\alpha}{mC/A} t\right) \right] \quad (1.5)$$

with α the heat transfer constant, which is related to the time constant σ equal to $mC/\alpha A$. This solution shows that there is indeed a transitional state at small t , and then a steady-state temperature is achieved, which depends on the voltage and resistance of the sample. This approach is validated by the results displayed in Figure 8a. The steady-state temperature is thus directly proportional to the applied power density, $\frac{I^2R}{A}$, as observed experimentally.^[17]

The key parameters in TFHs are therefore the steady-state temperature T_{stab} , which needs to be high while applying an operating voltage as low as possible, and response time, which needs to be as short as possible. Response time is considered as the time needed to achieve 90% of T_{stab} . The phenomena limiting these key parameters are heat loss (convection, conduction and radiation), which also tend to increase with temperature.^[16,148,155]

One of the major problems of MNWs is their low adherence to substrates and their thermal and electrical stability during TFH operations.^[42,108] To address this issue, Li et al.^[155] for instance created a polymer composite resisting temperatures as high as 230 °C, while allowing adhesion that could pass the tape test. Ji et al.^[17] also coated AgNW networks with PEDOT:PSS for the same reasons of thermal stability and improved adhesion, and Zhang et al. with graphene microsheets.^[151] The latter shows that temperatures as high as 230 °C can be reached in a reproducible manner.

Another drawback that has been identified for MNW networks in TFH applications is their high degree of haziness, especially when dense networks are considered, as haziness increases with network density.^[50,69] This can be a problem for applications for window defrosting, as the user needs a clear view of the outside. One of the solutions for reducing haziness is hybridization of the AgNW based heaters with CNTs.^[150] As already mentioned in the introduction, using AgNWs with low diameters was also proved to be beneficial for reducing the Haze factor,^[70,156] as well as by using long NWs,^[69,104] to a lesser extent.

Spatial uniformity is also an essential requirement for preventing hot spots in TFHs, especially in applications such as car and aircraft windscreens. Solutions have been proposed for this problem: the work of Kim et al., as shown in **Figure 9a-b**, has made possible good spatial uniformity over the entire metallic network area thanks to the use of clay platelets.^[152]

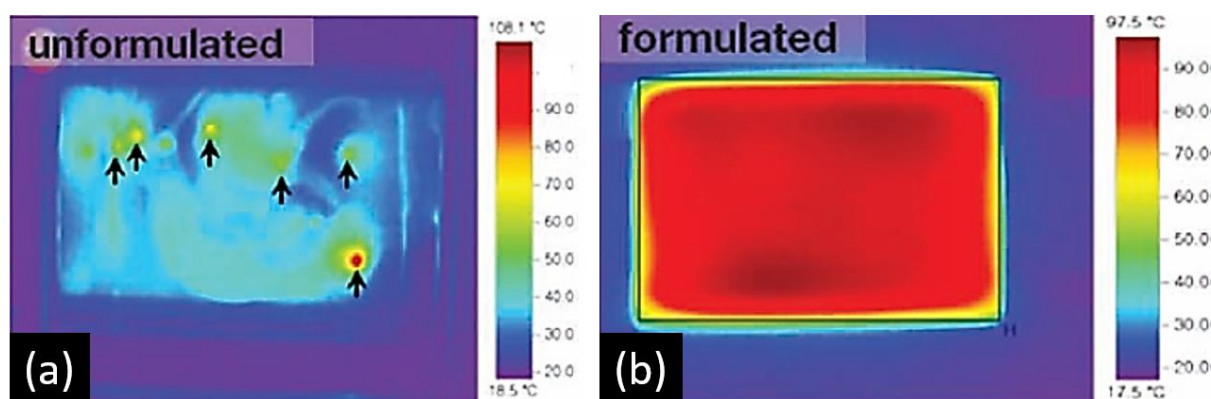


Figure 9. Infrared images of AgNW-based film heaters ($50 \times 75 \text{ mm}^2$) exhibiting hot spots due to the self-aggregated nanowires within the network (a), while uniform heat distribution can be obtained thanks to the use of exfoliated clays, leading to improved spatial network uniformity (b).^[152]

In conclusion, while several interesting studies have been reported since the first manufacture of TFH composed of AgNW networks in 2012,^[14] there is still some need to enhance electrical/thermal stability and to ensure the homogeneity of the heating surface. TFHs that are simultaneously transparent, non-hazy, flexible, stretchable, stable, and with a short reaction time, are the object of ongoing research. An important target is the possibility of covering non planar substrates, even with a complex relief, as this would be a clear breakthrough. Associated with flexibility, this will offer possibilities for combining new design properties. This is particularly interesting in textile and medical applications.

1.2.4. Smart Windows and Displays

The aim of this part is to review the use of MNW networks as transparent electrodes in display applications and for controlled-transmittance windows, often called “smart windows”. In this section we mention recent results first on electrochromic and Polymer-Dispersed Liquid Crystal (PDLC) devices, and then on touch screens.

1.2.4.1. Electrochromic and Polymer-Dispersed Liquid Crystal Devices

“Electrochromic” stands for materials with the ability to modify their optical properties in a long-term and reversible way by changing their oxidation states when subjected to electrical fields. Either metal oxides (WO_3 , NiO) or polymers can be convenient.^[157,158] In PDLC devices, electrical fields allow the liquid crystals droplets - dispersed in a solidified polymer matrix - to align so that the device is in its transparent configuration. Otherwise, the random dispersion of the droplets results in a scattering of the incident light as a result of the mismatch of the refractive indices at the boundaries of the droplets:^[159] the device then turns opaque.

Both electrochromic and PDLC devices can be used in a wide variety of optical switchable technologies,^[157] such as information displays, electronic paper-like displays, anti-reflectance mirrors and smart windows. The latter help improve energy efficiency, safety and personal comfort in buildings, vehicles or aircraft by regulating incident energy and harsh lighting. This technology is getting closer and closer to households and which has already been developed by several companies.^[160–162]

Both devices require transparent electrodes, either to change the oxidation level of the electrochromic material or to apply voltage and align the liquid crystals in the case of PDLCs. Here again, ITO is the most commonly used transparent electrode. But the need for highly flexible displays and smart windows able to conform to complex non-planar surfaces has encouraged research into cheap and flexible alternatives to ITO. Moreover, it seems that ITO degrades when subjected to voltammetry cycles in electrochromic cells which is, of course, a serious issue regarding the aging of devices.^[163]

Here again, AgNW networks seem to be promising candidates. For instance, Yan et al. successfully integrated stretchable conductors made of AgNW/PDMS elastomer matrix into a WO_3 electrochromic display device.^[164] The final device could sustain considerable stretching, twisting and folding stress without being damaged. **Figure 10a** shows the final device being stretched up to 50% strain in both colored and bleached states. The use of AgNW-based electrodes in PDLCs was also recently investigated. Hosseinzadeh Khaligh et al. sandwiched PDLC layers between either AgNWs embedded in poly(ethylene terephthalate) PET or ITO electrodes with similar sheet resistance ($50 \Omega \text{ sq}^{-1}$).^[165] Pictures of the resulting smart windows using AgNW networks are provided in Figure 10b (“on state”) and Figure 10c (“off state”). Despite the fact that the conduction level of both the ITO and AgNW-based electrodes was similar, the final AgNW-based smart window could be modulated over a larger transparency range and at lower voltage supply when compared to the similar ITO-based architecture.^[165]

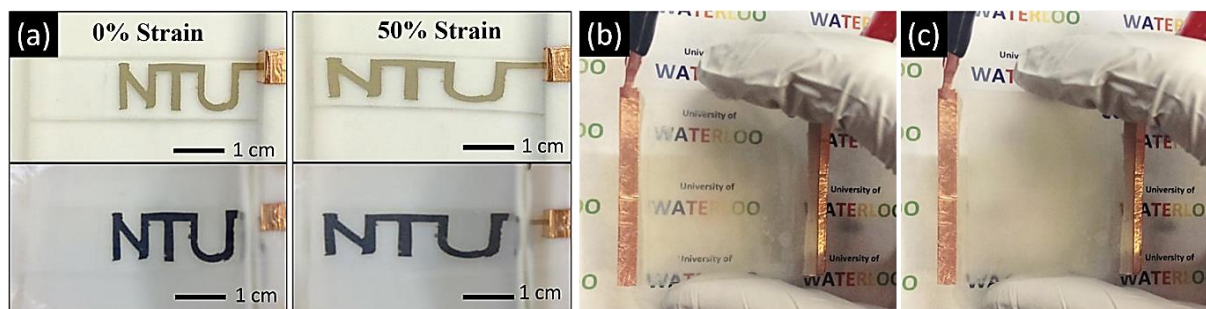


Figure 10. a) Electrochromic display devices - in both colored and bleached state - using an AgNW/PDMS matrix as the elastic electrodes. The device has high resistance to stretching stress.^[164] b,c) Example of a PDLC smart window using silver nanowire-based electrodes in the “on state (85 V)” (b) and “off state (0 V)” (c).^[165]

1.2.4.2. Touch Screens

Smart phones, tablets and notebooks have become ubiquitous in our day lives at home or at work. Worldwide market forecasts estimate that the surface area of manufactured touch screens will double between 2014 and 2025, representing more than 80 km² in 2025.^[166] Moreover, the touch screen market is increasing ten times faster than other displays. This field of research is strongly correlated to market trends for flexible displays. A lot of advertisements on this subject from Apple,^[167] Samsung,^[168] LG, Toshiba, Lenovo, etc.^[25] are strong indicators for this trend. To address the flexibility issue, technological interest in finding a replacement for ITO is focused on research into flexible transparent conductive materials. Touch Displays Research Inc. forecasts that the non-ITO transparent conductor market will reach up to \$13 Billion by 2023.^[25]

Korean research institutes (KAIST and KETI) are heavily involved in the integration of MNWs into flexible touch screens (see **Figure 11a-b**). Most of the papers reported focus on capacitive sensing related to the change in capacitance when fingers interact with the electrode. Beyond resistive sensing which makes possible low costs and high resolution, capacitive detection can also ensure both multi-touch features and durability.^[168] Depending on the technology involved, capacitive touch sensors can be made up of one or two transparent and conductive layers for respectively single^[26,169] or double-sided sensors.^[170,171] The former requires resolution at the millimeter scale whereas the latter is down to hundreds of microns. For AgNW networks, caution should be taken to prevent the divergence of the electrical properties in narrower lines (<250 μm in width) because orientation and alignment will also in this case govern the properties of percolative networks (not only random NW distribution).^[170,172] AgNW patterning (line/column, see Figure 11c) is of prime importance for high performance touch screens.

Capacitive touch modules using AgNW transparent conductive films, manufactured in a real production environment and with both high manufacturing yields (over 90%) and high reliability in various environments (temperature, relative humidity and power), were reported in a very relevant paper by Fried et al.^[173] Pei et al. published interesting results on healable touchscreens in which AgNWs are embedded into a thermally-stable thin layer on a healable

polymer substrate.^[171] For reading applications, the integration of very low haze electrodes is mandatory. The use of small diameter (and to a less extent, high length) MNW-based electrodes should be considered to reduce the haze factor.^[71,174,175]

However, despite the promising results reported for AgNW-based touch panels, emulation of new, fully flexible or rollable touch screens is time-to-market dependent on our ability to make the external parts of the entire device, such as the electrical circuits and the battery, flexible as well.

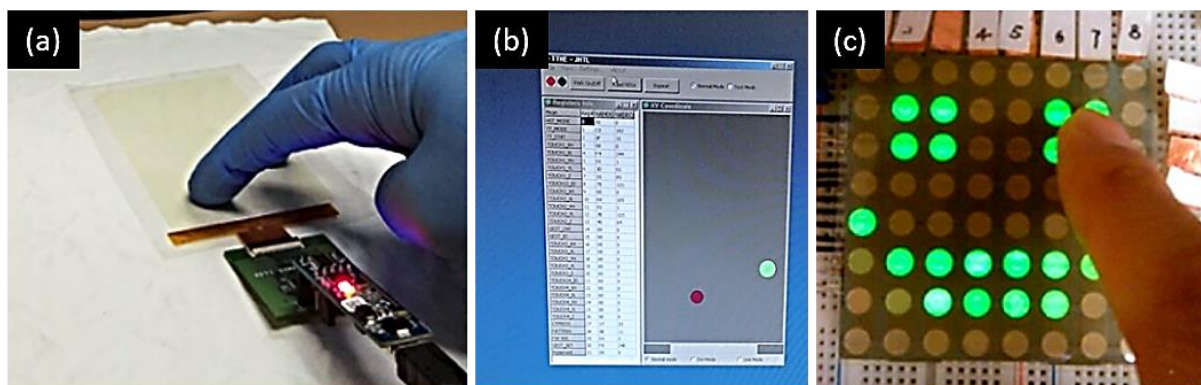


Figure 11. a,b) Highly flexible AgNW-based multi-touch panel developed at the KETI Institute.^[169] c) AgNW-based capacitive sensing films overlaid on a LED display for Smiley face drawn by finger touch on real device.^[171]

1.2.5. Electromagnetic Devices

1.2.5.1. Electromagnetic Shielding

Metallic nanowire (MNW) networks also attract intense attention for electromagnetic applications. In this section, we focus on the ability of MNW electrodes to efficiently attenuate electromagnetic (EM) waves. The shielding effect can originate from reflection of EM waves at the surface of the shielding materials (reflection losses), from absorption of EM waves (absorption losses), and from multiple reflection losses taking place inside the shielding material itself. A major challenge is to reduce the EM interference (EMI) that is likely to cause a noise signal in electrical circuits or even the malfunction of the latter. EM shielding also finds markets in reducing the risks of hacking at home, as well as for companies or military purposes. The limiting factors for some of these new markets with regard to integrating them into transparent surfaces such as windows are the material costs and the low optical transparency. In addition, the market wants to orient toward light materials. Interest in 1D nanoparticle-based materials has thus grown for EM shielding applications. The use of MNW percolating networks seems to be a promising route for fulfilling these requirements and offering appropriate shielding devices likely to be integrated into transparent windows, touchscreens or even windscreens.

Gelves et al. first demonstrated the ability of CuNWs to efficiently shield electromagnetic signals.^[176] They prepared cell-like CuNW networks embedded into a polystyrene matrix and found the EMI shielding effectiveness (SE) of the resulting nanocomposite to be higher than 20 dB in the range of 8-12 GHz and at a relatively low concentration of copper nanowires (1.3 vol%, i.e. roughly twice the percolation threshold). By putting a smartphone inside a paper box reshaped with a thin layer of AgNWs, Yang et al. also evidenced the ability of the box to shield the RF signal from the smartphone when dialing a number (see **Figure 12a**).^[177]

Yu et al. studied the impact of silver content on the ability of AgNWs/PVA and AgNWs/epoxy films to efficiently shield radio-frequency (RF) signals and made the comparison with films made of silver nanoparticles (AgNPs).^[178] AgNWs were found to be more effective at low material content, compared to nanoparticles, considering that lower resistances could be achieved with a smaller amount of Ag as predicted by the percolation theory. By using AgNPs instead of AgNWs, the amount of Ag needed to achieve shielding effectiveness of more than 20 dB (>99%) for all the frequency ranges (from 3 to 17 GHz) was multiplied by four.^[178]

Hu et al. also performed EM shielding tests on poly(ethersulfones) PES/AgNW/PET sandwich-structured films with good flexibility and transparency properties.^[179] By varying the density of the AgNW network, they obtained several films with different optoelectrical performances leading to specific EMI shielding performances (see Figure 12b). While increasing the density of the network, the transparency gradually decreased and the sheet resistance dropped (down to $1.8 \Omega \text{ sq}^{-1}$) while providing satisfying EMI shielding properties – more than 25 dB at a frequency of 8 GHz. The optical transparency of the associated films was not affected too much and remained reasonable (at least 70% at the wavelength of 550 nm).

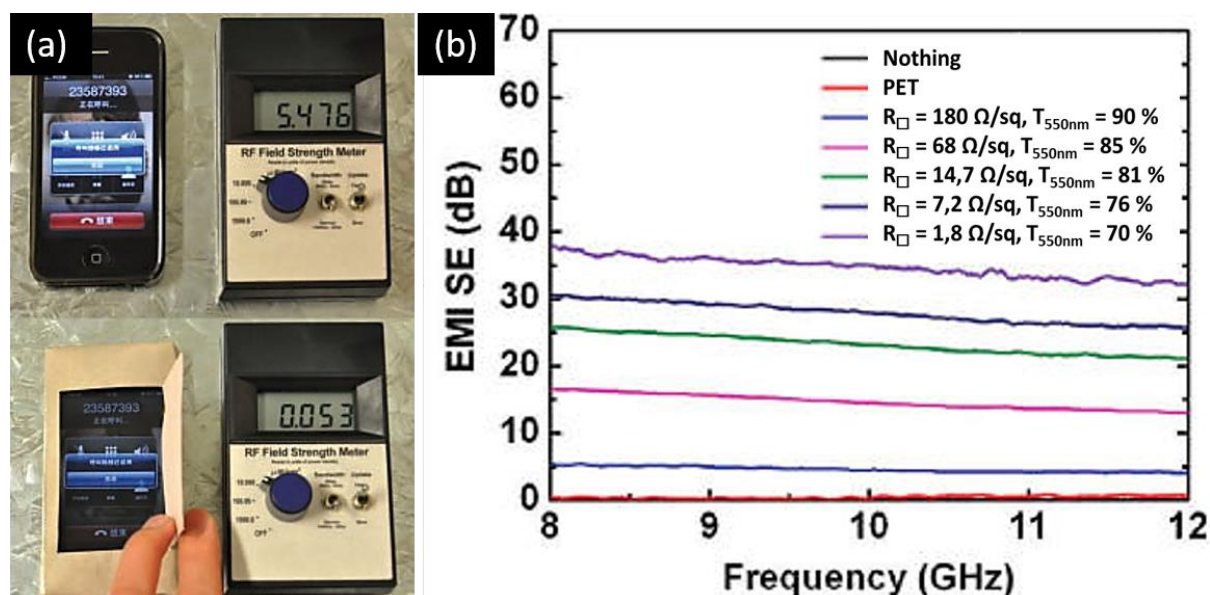


Figure 12. a) Photographic comparison of the radio frequency (RF) field strength when dialing an Apple iPhone 4 smartphone. Top: normal (no shielding); bottom: the cell phone is shielded with a piece of single-sided, AgNW-covered Fuji Xerox paper and grounded by the zinc plate substrate.^[177] b) Electromagnetic interference shielding effectiveness of PES/AgNW/PET sandwich-structured films with different associated AgNW network sheet resistance and transparency.^[179]

Using MNWs to efficiently shield EM waves has already been demonstrated by several research teams. The main advantages of MNWs over materials such as metallic nanoparticles,^[178,180] CNTs^[181–183] and graphene^[184] rely on the smaller amount of material required to efficiently shield the signals, the high level of transparency and finally the flexibility. Due to the original architecture of MNWs, the exact nature of the interaction between the incident EM waves and MNWs has still not yet been fully understood. Fundamental approaches might be required to better control the shielding performances of the final devices and to fabricate more complex architecture dedicated to specific applications such as transparent Frequency Selective Surfaces (FSS),^[185] or optimization of RF signal transmission through double glazed windows with reinforced thermal insulation. Finally, the shielding behavior of MNW networks under mechanical stress (stretching, bending, etc.) still need to be studied further.

1.2.5.2. Radio Frequency Antennas

AgNW networks have also been studied over recent years as a means of developing flexible radio frequency (RF) antennas, which can be integrated into many devices such as smartphones, automotive navigation systems, wireless network systems, wearable systems for detecting motion and health monitoring, or radio frequency identification (RFID) systems. One of the most well-known flat surface RF antennas, patch antennas, is generally made of thin metallic films. Replacing these films with a percolating MNW network would: i/ drastically decrease the amount of metal required for the electrode (thus lowering the manufacturing costs), ii/ induce an increase in the flexibility of the device (useful for improving the antenna's portability) and iii/ increase transparency in the visible range. However, although flexible and even stretchable RF antennas based on MNW networks have already been fabricated, most research reported so far has not dealt with the optical transparency of the resulting antenna. The MNW networks used for this application are also subject to the trade-off between transparency and conductivity imposed by the AgNW network density, as the electrical level is directly related to the EM performances of the resulting devices. Reaching high transparency levels without affecting the EM performances of the resulting device seems to be a serious challenge.

Several teams have already examined the possibility of using AgNW-based materials as the radiating elements in antennas. For instance, Yang et al. integrated a pair of AgNW-based RFID tags on to a battery-powered LED device and showed that the electrical resistance of the whole AgNW network is a critical parameter that directly influences the read range distance.^[177] Moreover, it has been demonstrated by Komoda et al. that the morphology of the antenna and especially the smoothness of its surface is a crucial parameter that has a significant influence on the signal losses of the antenna at high-frequency radio.^[186,187] They succeeded in printing an AgNW paste-based antenna measuring 3 cm in length with low signal loss, on to a flexible PET film. This antenna was integrated into a radio-controlled car (see **Figure 13a**) and could be controlled efficiently within a distance of 10 m. When their resistivity, surface roughness and thickness are optimized, AgNW-based mixtures can be used efficiently as the building blocks for RF antennas with low return losses. However, the literature has not yet provided much information regarding the radiation performances (gain and radiation pattern) of

transparent electrodes composed of solely MNW percolating networks, which is of great importance for obtaining feedback on the electromagnetic limitations of MNWs and therefore learning how to use them properly in RF applications.

The flexible and stretchable properties of AgNW-based materials make it possible to control the frequency response of antennas by changing the dimensions of the radiating element's structure, paving the way for wireless strain sensing applications. Rai et al. were the first to elaborate a stretchable RF antenna with PDMS as the dielectric substrate and an AgNW network as the radiating element.^[188] More recently, Song et al. studied the stretchable and reversible properties of such AgNW/PDMS antennas in depth: for this purpose, a 3-GHz-microstrip patch antenna and 6 GHz-2 element patch arrays were fabricated and tensile strains from 0% to 15% were applied to the antennas leading to a linear shift in the resonant frequency as the strain was increased (see Figure 13b).^[189] The reversibility of the deformation of these antennas could be demonstrated and their spectral properties were found to be almost the same both before and after deformation tests such as bending, twisting and rolling. Finally, Kim et al. recently managed to enhance the stretchability and resistance to cycling deformation tests of such antennas by using wavy AgNW networks.^[29] This technique made it possible to reduce the quantity of AgNWs used, resulting for the first time in the fabrication of an optically transparent RF antenna (see Figure 13c) with reasonable radiation performances.^[29]

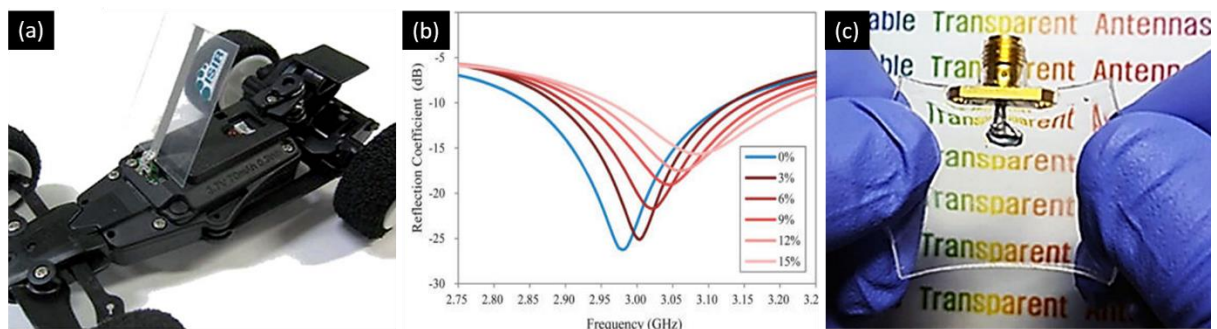


Figure 13. a) A commercialized radio-controlled car with a printed AgNW paste monopole antenna on a PET substrate.^[186] b) Measured frequency response of reflection coefficient for the AgNW/PDMS microstrip patch antenna for various tensile strains.^[189] c) Photograph of a stretchable transparent RF antenna based on wavy AgNWs.^[29]

To conclude, using flexible MNW-based materials in RF applications seems promising. In order to use them appropriately as radiating elements in RF devices, better understanding of the EM behavior of MNWs in this range of frequencies is required, for instance evaluating both dielectric and conduction losses. More in-depth studies relying on transmission lines made of MNWs might help obtain this precious information. In addition, detailed study of the MNW network density necessary for achieving reasonable radiating performances is still essential. This would be helpful for assessing the potential MNWs have (and their limitations) for being efficiently integrated into flexible and transparent RF antennas, while transparent antennas made of MNWs still remain a serious challenge.

1.3. Concluding remarks

The aim of this initial chapter was to demonstrate the considerable potential of MNW networks and their promising integration into devices in various fields of application such as energy, lighting, thin film heaters, etc. Beyond their excellent optical and electrical properties, these networks may present high flexibility, the ability to be conformably deposited and even stretchability, all of which are breakthrough aspects for the development of many innovative devices. The nanowires (NWs) can be produced at large scale in solution, and processed at room temperature and ambient pressure using large area printing techniques. This gives access to low-cost fabrication processes. Further studies are still ongoing to maximize electrode efficiency and reduce their costs.

The most significant research carried out during this PhD is reported in the 5 following chapters. To starts with, efforts devoted to describe the impact of physico-chemical treatments such as thermal annealing or acid treatment on the local morphology of the nanowires as well as on the overall optoelectrical properties of resulting networks are discussed in Chapter 2, thereafter.

Chapter 2. Optimization of the AgNW networks electrical performances

As mentioned in section 1.1.3, the electrical resistance of as-deposited AgNW networks is often high. This can be attributed to the presence of organic residues or PVP that is surrounding silver nanowires after synthesis. PVP is highly necessary for the unidimensional synthesis of the wires. It also acts as a very powerful dispersing agent in solution, preventing the NWs from agglomerating. However, it also consists of a thin insulating polymer layer leading to non-efficient contacts between nanowires after deposition. In most cases, post-deposition treatments are required for activating AgNW networks and create efficient interconnections.

During his PhD at LMGP, Daniel Langley deeply studied the impact of thermal annealing on commercial AgNWs purchased from Seashell Technology (*N.B.* Seashell Technology announced acquisition of AgNW product lines by BASF in March 2015).^[23,42] In order to answer the industrial demand for full solution-based processing of AgNW networks, Céline Mayousse looked for alternative methods of networks activation during her PhD at CEA. More specifically, nitric acid-based chemical treatment, performed either before or after deposition was found quite promising in offering a simple and free energy activation method.^[22] Finally, Mélanie Lagrange's work on optimization at LMGP was mainly focused on the optimization of thermal annealing procedure by performing "stopped heating ramp". She also explored the effects of pre-annealing treatments, network density, and kinetics associated to either isothermal or thermal ramp annealing.

Given that this thesis was conducted conjointly between LMGP and CEA-Liten, both thermal annealing and acid treatment were deeply explored. Their impact on reducing the electrical resistance of AgNW networks is reported in section 2.1. More specifically, their effects were evaluated on both commercial AgNWs (purchased from Seashell Technology) and AgNWs synthesized at CEA-Liten. Examples of SEM images associated to Liten AgNW networks are reported in **Figure 14** thereafter.

In order to find the best treatment combination leading to the lowest resistance achievable, the combination between them was also evaluated. This work was conducted in collaboration with Mélanie Lagrange at the end of her thesis. Alternative techniques such as mechanical pressing or laser annealing were also investigated in the frame of a European collaboration, and compared to classic thermal and acid treatments performed in Grenoble. The corresponding results are briefly discussed at the end of section 2.1. Given that the NW-NW junctions are definitely the critical entities responsible for the optimization of AgNW networks, section 2.2 reports the most significant work performed during this thesis about nano-characterization of the physical and chemical phenomena taking place at the NW-NW junctions during either thermal or acid treatments.

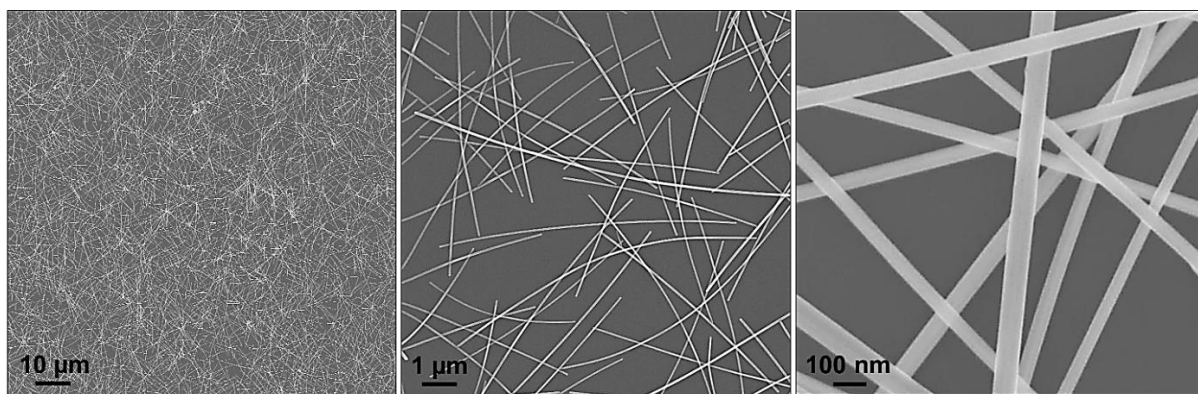


Figure 14. SEM images of AgNWs synthesized at CEA-Liten, and deposited on glass by spray-coating. Their average diameter and length are 60 nm and 10 μm , respectively.

2.1. Impact of thermal annealing and acid treatment

2.1.1. Thermal annealing and acid treatment: protocols and set-up

2.1.1.1. Thermal annealing set-up

The thermal annealing set-up was designed to perform thermal annealing of various sorts as well as for evaluating *in situ* the impact of thermal annealing on the electrical resistance of AgNW networks. For this purpose, the sample is deposited on a hot plate whose elevation temperature is set by a temperature controller (see **Figure 15a**). It is possible to program the controller so that either isothermal or ramp annealing, with various duration and temperature increasing rates, can be performed. The experimental temperature of the hot plate is measured using thermal probes directly connected to a computer responsible for collecting the data (LabVIEW program). On the other hand, silver paint-based contacts are deposited at each end of the network so that a two-point probe system using a Keithley 2400 source meter can perform *in situ* measurement of the electrical resistance while thermal annealing is on-going. Setting of parameters used for measuring the network electrical resistance (applied voltage, slot-time between two successive measurements, number of measurement) as well as data collection is driven and performed by the Labview program.

2.1.1.2. Acid treatment protocols

As investigated by Céline Mayousse during her PhD, acid treatment performed after NW synthesis is likely to improve the overall electrical performance of the resulting networks. Such a treatment can be performed either to the NW solution before deposition, or to the NW electrode after deposition (see Figure 15b). The associated protocols are reported thereafter:

(i) Acid treatment of the AgNW solution^[22]

- In every centrifugation tube, 8 mL of AgNWs dispersed in Methanol (MeOH) solution are mixed with DI H₂O and HNO₃ (5%), in ratio of 1:2:1.2.
- After 5 min of manual agitation, tubes are centrifuged at 2500 rpm during 15 min.
- In order to remove any trace of residual acid, an additional cleaning step is performed: after removing supernatant, tubes are filled out with fresh MeOH and centrifuged one more time in the same conditions as previous step.
- Finally, supernatants are removed and pellets are dispersed in 40 mL each of fresh MeOH.

(ii) Acid treatment of the AgNW electrode^[22]

- Whatever the substrate, the AgNW electrode is immersed in HNO₃ acid bath (5% in DI H₂O solvent) during 15 min.
- The electrode is then rinsed in EtOH bath and finally dried on a hot plate at 60 °C.

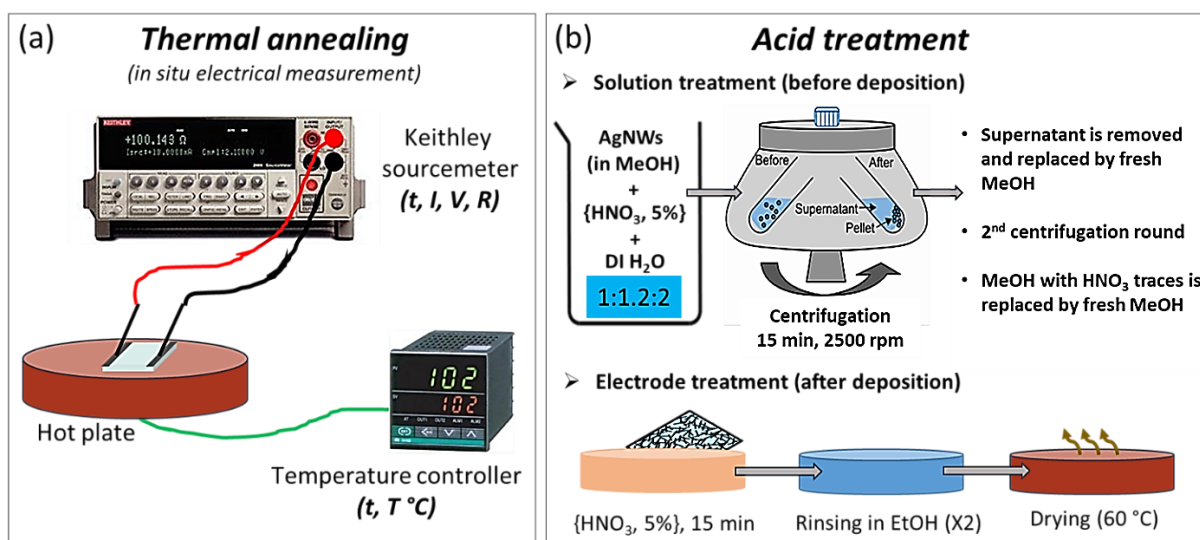


Figure 15. a) Schematic representation of the thermal annealing set-up with in-situ electrical measurement. b) Schematic representation of the protocols followed when performing acid treatment of the AgNW solution (before deposition), or the AgNW based electrode (after deposition).

2.1.2. Description of the results

The impact of thermal and acid treatments are reported in the present section using different types of AgNWs. It has indeed been noticed that such activation treatments do not have exactly the same impact depending on the AgNWs used. This suggests that even though the polyol process technique used for synthesizing AgNWs is quite well mastered and reproducible (see

section 1.1.1), it might exist slight differences in the way the synthesis is performed from one research team to another, leading to distinctive features in the resulting behavior of the NWs in terms of electrical performance as well as environmental ageing (see section 1.1.6). This is why two different types of NWs were investigated in this thesis: commercial AgNWs purchased from Seashell Technology, associated with an average diameter and length of 45 nm and 14 μm , respectively, and AgNWs synthesized at CEA-Liten, associated with an average diameter and length of 60 nm and 10 μm , respectively. The impact of thermal annealing and acid treatment on these two types of AgNWs is investigated thereafter. The impact of other activation methods (mechanical pressing, laser annealing) is also briefly reported at the end of this section.

2.1.2.1. Impact of thermal annealing and acid treatments on Seashell AgNWs

For the purpose of this study, AgNW networks were fabricated by Mélanie Lagrange using the LMGP spray deposition set-up. Silver paint-based contacts were then deposited at the extremities of the samples to perform *in situ* 2-probes electrical measurements. Four of these samples were subjected to thermal ramp annealing at $2\text{ }^\circ\text{C min}^{-1}$. Prior to thermal treatments, two samples were subjected to post-deposition acid treatment. The results are reported in **Figure 16a**.

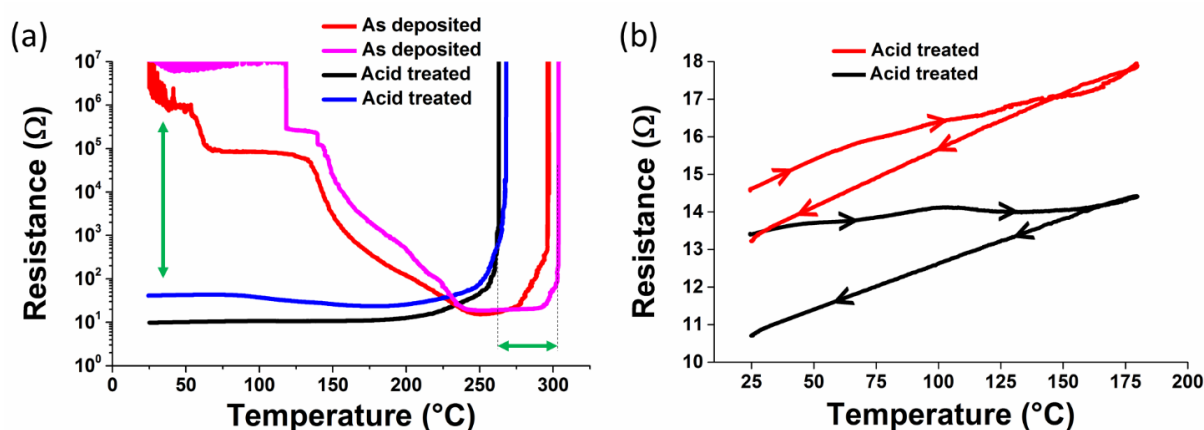


Figure 16. a) Evolution of the electrical resistance of Seashell AgNW networks during a full thermal ramp annealing of $2\text{ }^\circ\text{C min}^{-1}$. The networks are either “as deposited” or “acid treated” before thermal treatment. b) Evolution of the electrical resistance of Seashell AgNW networks during a “ramp & stop” thermal annealing of $2\text{ }^\circ\text{C min}^{-1}$ up to $180\text{ }^\circ\text{C}$. The two samples were subjected to post-deposition acid treatment before thermal annealing.

The impact of thermal annealing on as-deposited networks is clearly visible. The initial resistance of the corresponding samples (red and pink curves) is higher than $10^5\text{ }\Omega$, while it is decreased down to 10-20 Ω at 250 °C (minimum resistance achieved for these two samples). Such a decrease in resistance is attributed to the evaporation of organic residues in a first time

(70 – 150 °C thermal range) and then to the local sintering of the NW junctions at higher temperature (150 – 250 °C thermal range).^[42] More details and nanoscale information about the physical mechanisms involved in the sintering of the junctions are provided in section 2.2.1. At higher temperature (275 – 300 °C thermal range), the NWs start being destabilized and tend to spheroidize in order to reduce their surface energy (Plateau-Rayleigh instabilities), leading to loss of the network percolating nature. This phenomenon is associated with a high increase in electrical resistance near 300 °C.

On the other hand, it can be noticed that the initial resistance associated with the two acid treated samples is already very low, i.e. close to 40 Ω and 10 Ω , for the blue and black curves respectively (see Figure 16a). As a consequence, acid treatment performed after deposition has a tremendous impact in helping Seashell AgNWs to have good quality contacts between them. The nature of PVP layer is likely to be modified due to acid treatment. However, the nanoscale mechanisms involved in the improvement of the electrical performances of AgNW networks still remain unclear in some points. Specific investigations about this issue are reported in section 2.2.2.

Moreover, it seems that acid treatment also has an impact in the spheroidization temperature. In Figure 16a, the blue and black curves (acid treated samples) start diverging around 260 °C while the pink and red curves start diverging around 290-300 °C. Two kinds of explanation might be brought face to such a difference. First, the PVP layer might act as a stabilization barrier at high temperature, in favor of the postponing of Plateau-Rayleigh instabilities. In the case the PVP layer is destabilized by acid treatment, the NWs might be subjected to earlier spheroidization process at high temperature. Second, it has been demonstrated that the spheroidization temperature of AgNWs is highly dependent on the AgNW diameter.^[50] The lower the diameter, the lower the spheroidization temperature. This can be explained by surface effects enhancement which occurs for small AgNW diameters. Since it is well known that silver should be attacked by nitric acid when mixed together, it can be imagined that the PVP does not prevent the HNO₃ from reacting with AgNWs during acid treatment, leading to the reduction of AgNW diameter. However, nano-characterization analysis performed on AgNWs after acid treatment did not reveal convincing enough conclusion regarding the reduction on the AgNW diameter. Hence, the first hypothesis seems to be the most probable.

In order to evaluate further the impact of combining acid and thermal treatments in the electrical optimization of Seashell AgNW networks, two samples acid treated after deposition were finally subjected to “ramp & stop” thermal annealing (see Figure 16b). It consists of cutting the network into two equivalent parts, performing full thermal ramp annealing (until spheroidization) to the first part so that the temperature at which the minimum resistance is reached can be collected, and then performing thermal ramp annealing to the second part up to the temperature that minimizes the electrical resistance (around 180 °C in the present case). Finally, the sample is cooled down to room temperature in order to compare the electrical resistance before and after optimization.

The electrical behavior of the two samples during heating and cooling process is clearly different. Even though the initial resistance (after acid treatment) of the samples is already very low (14.6 Ω and 13.4 Ω), the shape of the curves during heating reveals that the networks have

not been entirely optimized yet. Instead of increasing linearly with the temperature (classic metallic behavior), the electrical resistance increases more slowly and irregularly, showing that there are still optimization process like sintering of the junctions taking place in the networks. On the contrary, once the optimization temperature has been reached and the cooling process has started, the electrical resistance exhibits a perfect linear behavior against the temperature. This shows that once the sintering of the junctions has been completed, AgNW networks behave as classic metallic component against the temperature. This increase in the electrical resistance with temperature due to phonon-induced scattering can be modeled as follows:

$$\rho(T_0 + \Delta T) = \rho_0(T_0)(1 + \beta_R \Delta T) \quad (2.1)$$

Where β_R is the temperature coefficient of resistivity and is equal to $3.8 \times 10^{-3} \text{ K}^{-1}$ for bulk silver.^[190] In the present case, by fitting the experimental data associated with cooling process in Figure 16b, β_R was calculated to be $2.43 \times 10^{-3} \text{ K}^{-1}$ and $2.49 \times 10^{-3} \text{ K}^{-1}$, for black and red curves, respectively. According to Lagrange et al., the difference between bulk silver and AgNW networks might arise from the presence of junctions between AgNWs which could behave differently, as well as defects such as grain boundaries or twins present in AgNWs.^[50]

In order to get more robust knowledge of the impact of acid treatment and thermal annealing on the optimization of AgNW networks, the same type of treatments have been reproduced on several different samples. The results associated with three more samples are reported in **Figure 17**. Contrary to previous graphs, electrical performance was measured using a four pin probe with a Loresta EP resistivity meter. Each value reported in Figure 17 consists of the sheet resistance's mean value extracted from 5 different measurements at various locations across the sample. Hence, it also gives rise to a first evaluation of the electrical homogeneity.

As already reported above, the sheet resistance R_{sh} is very high after deposition (blue columns). It is always higher than the measurement limit of the resistivity meter (i.e. higher than $10^6 \text{ } \Omega \text{ sq}^{-1}$). For the three samples reported here, R_{sh} is dramatically reduced after acid treatment (red columns). The average value after acid treatment is indeed $24 \pm 4 \text{ } \Omega \text{ sq}^{-1}$, which confirms that acid treatment is really powerful in reducing the NW junction resistance and activating the overall AgNW networks made of Seashell NWs.

The main advantage of such an activation technique is that it is fully compatible with low cost solution-based processing of AgNW transparent electrodes. However, as already mentioned above, additional thermal treatment can help completing the optimization of AgNW networks. Here, the three samples were subjected to additional isothermal annealing at $150 \text{ } ^\circ\text{C}$ during 1h (green columns), after acid treatment. R_{sh} was found to decrease a little bit more after additional thermal treatment. The average value reported is indeed $16 \pm 1 \text{ } \Omega \text{ sq}^{-1}$, in accordance with the results depicted Figure 16b. Contrary to acid treatment which is believed to be only responsible for making adjacent AgNWs in very close contact, the sintering process of the junctions induced by thermal annealing helps having optimized contacts between adjacent NWs. A deeper analysis of the physico-chemical phenomena involved in the optimization process of AgNW networks via acid or thermal treatment is provided in section 2.2.

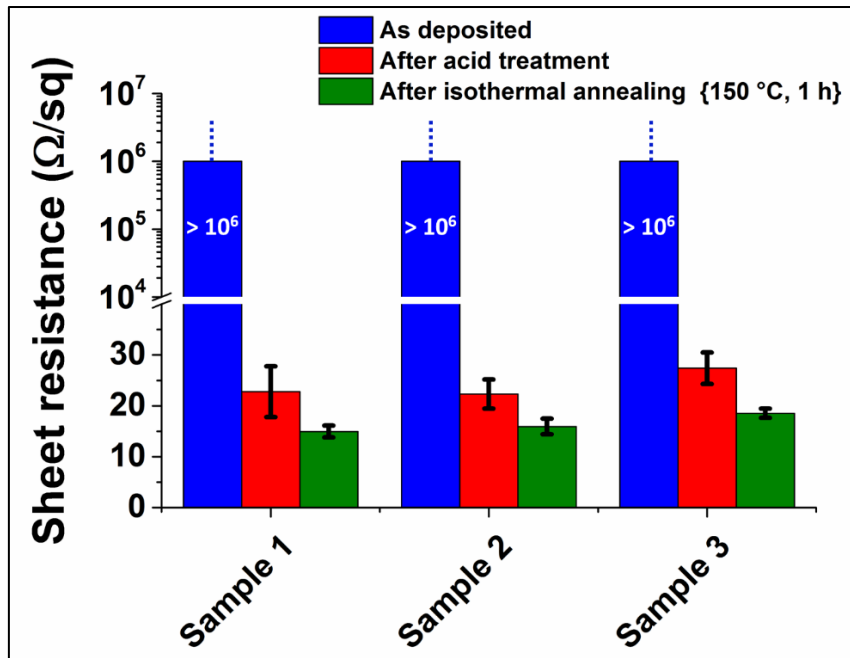


Figure 17. Evolution of the sheet resistance of AgNW networks, fabricated with Seashell AgNWs. The sheet resistance measured after deposition (blue) are all higher than the detection limit of the 4 probe system (over load). Measurement are repeated again after post-deposition acid treatment (red) and finally after additional isothermal annealing at 150 °C during 1h.

Finally, the standard deviation when measuring R_{sh} is significantly decreased after thermal annealing (see Figure 17). It switches from $4 \Omega \text{ sq}^{-1}$ after acid treatment, down to $1 \Omega \text{ sq}^{-1}$ after additional thermal treatment. This feature suggests that the overall electrical homogeneity of the samples is increased. From a morphological and statistical point of view, the sintering process of the junctions is likely to favor an increase of the number of AgNWs participating to the current distribution. This is a first interesting indication about electrical distribution in AgNW networks, which will be investigated in detail in Chapter 4.

2.1.2.2. Impact of thermal annealing and acid treatments on Liten NWs

For the sake of comparison, the impact of thermal annealing and acid treatment has also been investigated using AgNWs directly synthesized at CEA-Liten. Performing such a study on Liten AgNWs was mandatory since a large majority of the samples studied within the frame of this thesis were fabricated using Liten AgNWs. The average diameter and length of the NWs reported in this section are 60 nm and 10 μm , respectively. The NWs were synthesized by polyol process. Compared to Seashell NWs, there are three main differences in the post-synthesis process that should be taken into account for analyzing the results associated with Liten NWs. First the nanowires are dispersed in Methanol instead of isopropanol (IPA) for Seashell NWs. Methanol was indeed found to be the best dispersing agent for AgNWs by Mayousse et al.^[22] Second, an additional decantation step is performed after synthesis in order

to remove as much as non-nanoscale silver contents from the solution (the first decantation step consists simply of removing the reducing agent Ethylene Glycol (EG) from the solution and replacing it by a dispersing agent such as MeOH. Thanks to the second decantation step, which was patented by Simonato et al.,^[191] the selectivity of the solution in NW contents is increased, which is favorable for reducing the need for raw material (silver), as well as minimizing the quantity of unwanted silver micro-particles in the resulting AgNW networks. Finally, the NWs are usually acid treated directly in solution before being spray-deposited (see Figure 15b). In that way, Liten AgNW networks have proved to be very performant just after deposition.

For the purpose of this study, 6 samples were fabricated by spray-coating according to the protocol described above. The electrical and optical performances are reported in **Figure 18**. The conduction and transparency levels exhibited by the samples are already high after deposition. The sheet resistance of the samples is around $10 \Omega \text{ sq}^{-1}$, while the optical transparency is around 90% (at $\lambda = 550 \text{ nm}$, without the glass substrate contribution). *N.B. unless otherwise specified, the values of optical transmittance provided in the entire manuscript consist of “total” transmittance.* This suggests that contrary to the vast majority of the AgNW networks reported so far in literature, Liten AgNWs do not require any post-deposition treatment for achieving an electrical and optical trade-off as high as $\{10 \Omega \text{ sq}^{-1}, 90\%$ in performance. Such performance level is compatible with most of the optoelectronic applications for which the use of transparent electrodes is required.

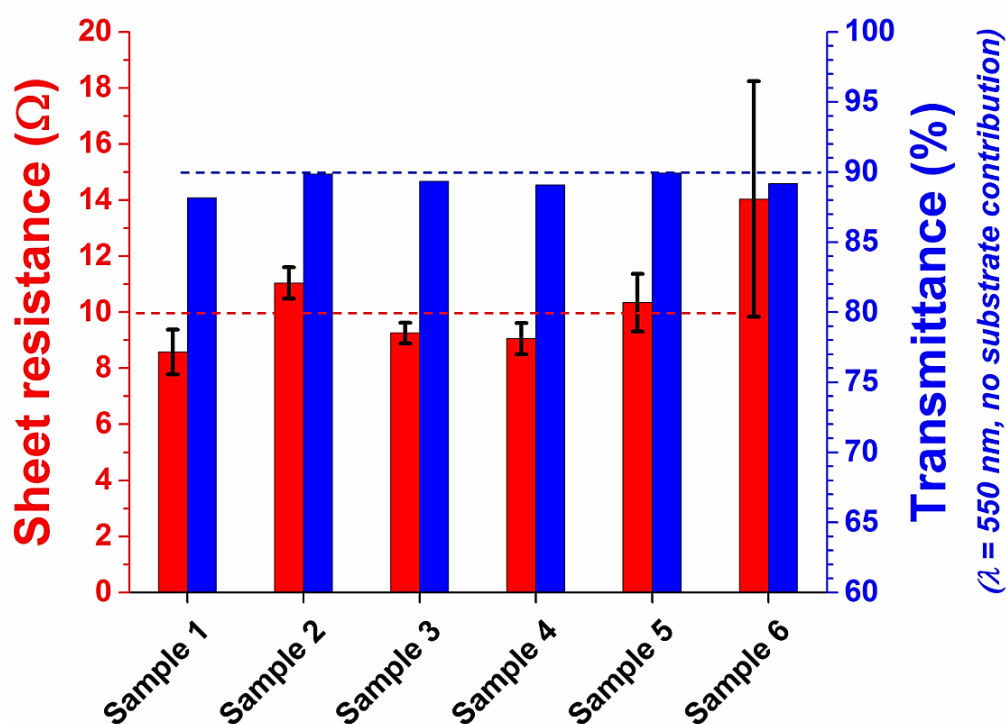


Figure 18. Electrical and optical performance of spray-coated AgNW networks fabricated with Liten NW, acid treated in solution prior to deposition.

Four more samples were also subjected to additional “ramp & stop” annealing ($2\text{ }^{\circ}\text{C min}^{-1}$, up to $170\text{ }^{\circ}\text{C}$) after deposition in order to evaluate the impact of combining acid and thermal treatments on Liten AgNWs. In **Figure 19a**, it can be noticed that similarly to Seashell AgNWs, the resistance (two probe) of the samples can be slightly decreased thanks to additional thermal annealing. The evolution of the resistance during “ramp & stop” annealing is also reported in Figure 19b. The shape of the curve is similar to the one depicted in Figure 16b. During the heating process, optimization mechanisms take place leading to a nonlinear increase of the resistance against the temperature. On the contrary, during cooling process, the decrease in resistance is perfectly linear, which suggests that the optimization of AgNW networks has been completed. In order to test the robustness of metallic behavior obtained after optimization, each sample was subjected to a 2nd “ramp & stop” process (see short dotted blue and red lines in Figure 19b) and finally to a last 3rd round (see short dashed blue and red lines in Figure 19b). The same “metallic” evolution of the resistance against the temperature was obtained during the 2nd and 3rd rounds. For the sake of comparison with Seashell networks studied in previous section, here the temperature coefficient of resistivity β_R was measured to be $2.35\times 10^{-3}\text{ K}^{-1}$, $2.36\times 10^{-3}\text{ K}^{-1}$, and $2.35\times 10^{-3}\text{ K}^{-1}$ for the 3 rounds of samples 1, respectively (blue curves), and $2.38\times 10^{-3}\text{ K}^{-1}$, $2.39\times 10^{-3}\text{ K}^{-1}$, and $2.36\times 10^{-3}\text{ K}^{-1}$ for the 3 rounds associated with sample 2, respectively (red curves). Such values are very similar to the ones reported when using Seashell NWs. As a consequence, once optimization has been completed, both Seashell and Liten exhibit the same metallic electrical behavior, at least from a macroscale point of view (network scale).

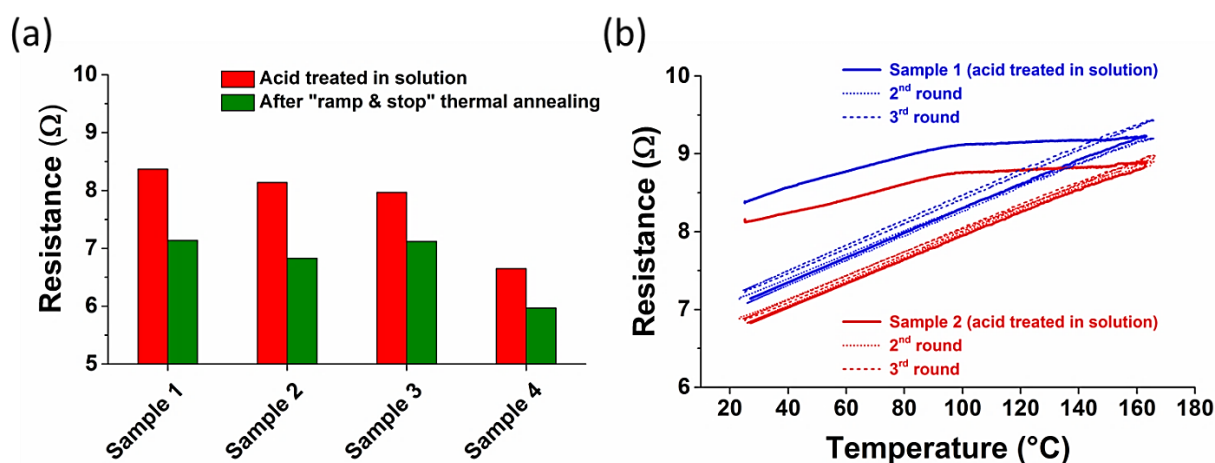


Figure 19. a) Electrical resistance associated with AgNW networks made of Liten NWs, acid treated in solution before deposition (red curves).

Finally, it has to be mentioned that a cautious description of the electrical performance of Liten Networks without any acid treatment is missing. Within the frame of this thesis, acid treatment performed in solution before deposition was considered as the standard process to follow for preparing AgNW networks. This is why in this section, all the samples were fabricated with AgNWs already acid treated before deposition. However, according to Mayousse et al.,^[22] AgNW networks fabricated with Liten NW can sometimes exhibit very good electrical

properties (as high as $R_{sh} = 23 \Omega \text{ sq}^{-1}$, and $T_r = 91\%$) even without acid treatment, while some others (although supposed to be similar) are not conductive without acid treatment.

Such an unreproducible result might originate from the amount of residual organic material in the networks that is likely to vary from one sample to another one.^[22] In any case, it was found that performing acid treatment helped preventing such fluctuations, leading to the efficient activation of networks in any case. However, it seems that for now, the vast majority of the AgNWs synthesized at CEA-Liten do not require any acid treatment for having the resulting AgNW networks activated. As a consequence, most of the samples fabricated with Liten AgNWs are not acid treated anymore. Surprisingly, from the time when Céline Mayousse performed AgNW synthesis (thesis defended in 2014) up to now, the synthesis protocol has not changed. Hence it is quite difficult to explain why the electrical behavior of “as-synthesized” AgNWs has changed.

2.1.2.3. *Other optimization techniques*

In order to try the influence of optimization techniques other than thermal annealing and acid treatment and compare all the available techniques together, a non-formal European collaboration initiated by Mélanie Lagrange was created between LMGP (thermal annealing), CEA-Liten (acid treatment), Univ. of Konstanz (mechanical pressing), and Univ. of Catania (laser annealing). The results dealing with thermal annealing and acid treatments have already been deeply discussed in previous section. Here, we briefly present the results associated with the optimization of AgNW networks by either mechanical pressing or laser annealing.

(i) Optimization by mechanical pressing

Samples prepared at LMGP by Mélanie Lagrange using Seashell NWs, as well as samples prepared at CEA using Liten NWs, were sent to Konstanz University to perform several mechanical pressing tests. Experiments were carried out by Julian Reindle. The protocol for pressing the samples is as follows: first, the AgNW network on glass substrate is placed on top of a defect free PDMS layer and a polished Cu plate. PDMS is used to ensure that pressure is uniformly applied to the sample during pressing, and for preventing the glass substrate from breaking when high mechanical pressure is applied. Then, a smooth Silicone layer (treated with Silane) is placed upside-down on the AgNW network. Finally mechanical pressure is applied to the entire structure by the mean of a press, during 2 min.

Mechanical pressing on Seashell AgNW networks revealed very powerful for decreasing the sheet resistance of the samples. One sample of the series was mechanically pressed at 12.5 MPa. The two other samples were pressed at 17 MPa (see **Figure 20A**). In any case, the sheet resistance was decreased from very high value (i.e. higher than $10^6 \Omega \text{ sq}^{-1}$) down to values close to $10 \Omega \text{ sq}^{-1}$. Hence, mechanical pressing was very suitable in making good contacts between adjacent AgNWs. Besides, using 12.5 MPa for the process was found suitable enough to optimize the samples. However, it has to be mentioned that the quality of the PDMS layer used

is very critical for the efficiency of such treatment. For instance, the presence of residual air bubbles inside the PDMS layer is likely to cause not uniform pressing of the network, leading to electrical inhomogeneities through the sample. From an optical point of view, a slight decrease in optical transparency of about 1% at $\lambda = 550$ nm could be measured after mechanical pressing. This decrease in optical transmittance might originate from the pressing-induced flattening of NWs, causing a very slight increase of the NW surface coverage in the network.

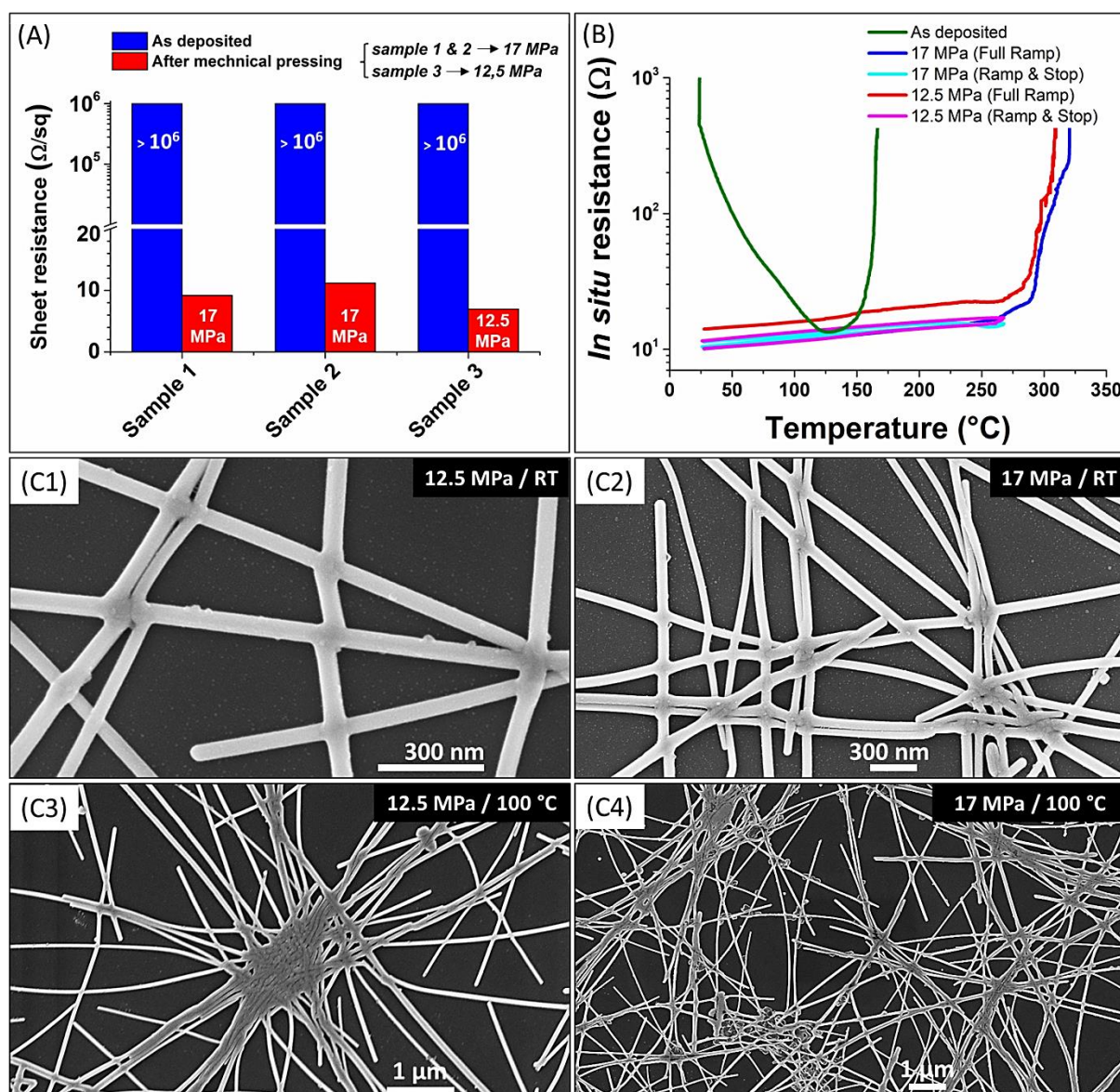


Figure 20. (A) Impact of mechanical pressing on the sheet resistance of “as-deposited” Seashell AgNW networks. Sample 1 and 2 were subjected to 17 MPa during 2 min, while sample 3 was subjected to 12.5 MPa during 2 min. (B) Evolution of the electrical resistance of Seashell AgNW networks before (green curve) and after mechanical pressing, during additional thermal annealing: full ramp (blue and red curves) or “ramp & stop” (cyan and purple curves). (C) SEM images showing the morphology of Liten AgNW networks after mechanical pressing in the following conditions: (C1) 12.5 MPa at room temperature, (C2) 17 MPa at room temperature, (C3) 12.5 MPa at 100 $^{\circ}\text{C}$, and (C4) 17 MPa at 100 $^{\circ}\text{C}$.

In order to evaluate the rate of optimization completion after mechanical pressing, the impact of additional “ramp & stop” thermal annealing was tested on the samples (see Figure 20B). Contrary to “ramp & stop” process performed after acid treatment, here the resistance of the sample could not be decreased further. The samples exhibited a linear increase of the resistance with the temperature during the heating process, meaning that the optimization of AgNWs had already been completed.

Mechanical pressing on Liten AgNW networks was also investigated. However, since the NWs had been acid treated in solution, the sheet resistance of the samples after deposition was already very low. No significant additional decrease in resistance could be noticed after mechanical pressing. However, the impact of mechanical pressing on the sintering of the junctions is very clear on the SEM collected after treatment (see Figure 20C1-C2). Hence it was expected that optimizing the shape of the junctions would influence positively the overall conduction level of the sample. This result suggests that the contact resistance between adjacent AgNWs is not substantially influenced by the shape of the junctions. As a consequence, the quality of the interface between the bottom and top NWs is likely to be the critical element for good conduction while the global shape of the junction seems less crucial than believed.

Finally, combining heating and mechanical pressing was also tested on Liten AgNW networks. The pressing plates were heated up to 100 °C while performing mechanical pressing. Here again, the resistance of the samples was not significantly impacted. However, some large stacked NW clusters could be detected when pressing at 100 °C (see Figure 20C3-C4). Such clusters revealed larger and exhibited stronger damaged when 17 MPa stress was applied to the network (C4), leading to a substantial decrease in optical transmittance. The latter was decreased down to 80% ($\lambda = 550$ nm, without substrate contribution) while it was close to 90% before pressing. Generally speaking, the sample pressed at 12.5 MPa at room temperature was the only one having its optical transparency almost unaffected by the process. This suggests that performing mechanical pressing at high pressure and high temperature is not necessarily beneficial to AgNW networks. At the end, {12.5 MPa, room temperature} were found to be the most suitable parameters for the two sorts of AgNW networks (Seashell and Liten).

Generally speaking, mechanical pressing revealed quite promising for optimizing AgNW networks. However, the process was found more complicated than either thermal or acid treatment, as well as leading to less reproducible results in general. Moreover, it was not found to be more efficient than the optimization techniques commonly used in Grenoble. Hence, the huge majority of the samples studied within the frame of the thesis were only activated by acid treated (in solution), and further optimized by thermal treatment when needed. However, from an applicative point of view, mechanical pressing could be of great interest for reducing the surface roughness of the AgNW electrode before integration into devices such as organic solar cells to prevent short circuit with the active layer, or in RF antennas for improving the radiation efficiency.^[189] It was indeed evidenced by Tokuno et al. that mechanical pressing can reduce the surface roughness of AgNW networks to one third of the initial value.^[54]

(ii) Optimization by laser annealing and other post-deposition treatments

Several samples prepared at LMGP (Seashell NWs) or at CEA (Liten NWs) were sent to Stefano Boscarino from the University of Catania to investigate the impact of laser annealing on AgNW networks. Laser irradiations were performed by a pulsed (10 ns) Nd:yttrium aluminum garnet (YAG) laser operating at {532 nm – 10 Hz}. The samples were entirely or partially scanned by the laser beam. In most cases, a total area of $1.5 \times 1.5 \text{ cm}^2$ was irradiated. Several laser power values were tried [1 mW- 532 mW], and various number of pulses (1 pulse up to 500 pulses) were performed in each spot in order to find the most suitable combination of experimental parameters.

When using Liten AgNWs, it was found that whatever the number of pulses, the NWs get always spheroidized if the power is set to be higher than 50-100 mW, while no morphological impact on the wires can be detected below 50 mW. Moreover, applying 500 pulses at 50 mW in each spot did not yield any change in the electro-optical properties of AgNW networks. Here again, acid treatment performed before deposition might have almost completed the optimization process.

When using Seashell AgNWs, no damage process of the NWs was detected for power values lower than 300 mW. It implies that Seashell NWs could sustain higher laser-induced heating load than Liten NWs. This might originate from the acid treatment systematically performed when using Liten NWs, in accordance with the lower spheroidization temperature observed in the case of acid treated samples in Figure 16a. Finally, when applying 500 pulses at 50 mW in each spot, the resistance of Seashell networks could be decreased by 2-3 orders of magnitude (from $R > 10^6 \Omega$ down to $\approx 10 \text{ k}\Omega$) without inducing any morphological change to the networks.

As a conclusion, laser annealing did not reveal as efficient as other optimization techniques previously reported in this section. However, this technique should be investigated further in order to reach higher optimization levels. Finally, optimization tests based on IR and UV-flash annealing were also tried at CEA within the frame of this thesis, without leading to reliable nor convincing results.

2.2. Nano-characterization of the phenomena taking place at the NW-NW junctions

Given that NW-NW junctions and especially the quality of the interface between adjacent NWs have proved to play a pivotal role in the overall electrical performance of AgNW networks, many efforts have been devoted to the characterization of the junction morphology evolution when optimization techniques such as thermal annealing or acid treatment are performed. For this purpose, several nanoscale characterization techniques (SEM, TEM, and Ultramicrotomy) were used within the frame of this thesis. SEM and TEM revealed to be efficient enough for analyzing the physical mechanisms involved in the optimization of junctions by thermal annealing (see section 2.2.1).

On the other hand, the physico-chemical phenomena responsible for the junction activation by acid treatment could not be easily detected and interpreted (section 2.2.2). At least some of the hypothesis previously proposed as a piece of explanation to why such treatment can efficiently activate AgNW networks could be tested and unfortunately not validated. It was found highly necessary to explore directly the internal structure of the junctions before and after treatment. Ultramicrotomy technique revealed quite efficient and helpful for this purpose. Preliminary results about this technique and associated nanoscale analysis are reported in section 2.2.3.

2.2.1. Morphological impact of thermal annealing: nanoscale characterization

In order to explore the effect of thermal annealing on the morphology of NW junctions, AgNWs were spray-deposited directly onto copper-based TEM grids filled with an amorphous holed carbon matrix. Before TEM observation, some grids were thermally annealed at 180 °C during 1h using a hot plate. TEM images corresponding to “as deposited” and thermally treated AgNW grids are reported in **Figure 21A** and Figure 21B, respectively. More specifically, (A1) and (A2) are associated with junctions made of Liten and Seashell AgNWs, respectively, and (A3) is a zoom of the bottom-right corner of the junction in (A2). As in Figure 1a, it can be noticed that “as-deposited” AgNWs are always surrounded by an amorphous shell that is probably PVP. The shape of as-deposited junctions look perfectly straight and regular. At least the top-view TEM images reported here suggest that AgNWs are not in intimate contact with each other.

On the contrary, it can be clearly detected in Figure 21B1-B3 that atomic diffusion process are activated by thermal energy near the junctions, leading to the morphological reorganization of the junctions. Local sintering process is indeed clearly visible in (B1) and (B2) and the junctions tend to minimize their surface energy. As reported by Langley et al. thermal annealing is responsible for the optimization of junctions in two distinct steps: first, the desorption of organic residues such as residual solvents at low temperature (around 100 °C), second the local sintering of junctions at higher temperature (150-250 °C).^[42] Residual solvents might consist of either Ethylene Glycol (EG) used for reducing silver during the synthesis, or dispersing agents such as Methanol (MeOH) or Isopropanol (IPA), depending on the type of AgNWs considered. Of course, the kinetics of thermal annealing might influence a lot the temperature at which these two steps occur.

According to these TEM observations, the surrounding carbonaceous shell is still on the AgNW surface after thermal annealing. Its chemical nature might have changed but its morphology and aspect when observed in TEM remain unchanged. As a consequence, thermal annealing does not seem to be responsible for removing PVP. When describing mechanisms involved in thermal annealing, a strong distinction should be made between the organic residues mentioned above and the organic PVP shell surrounding the nanowires.

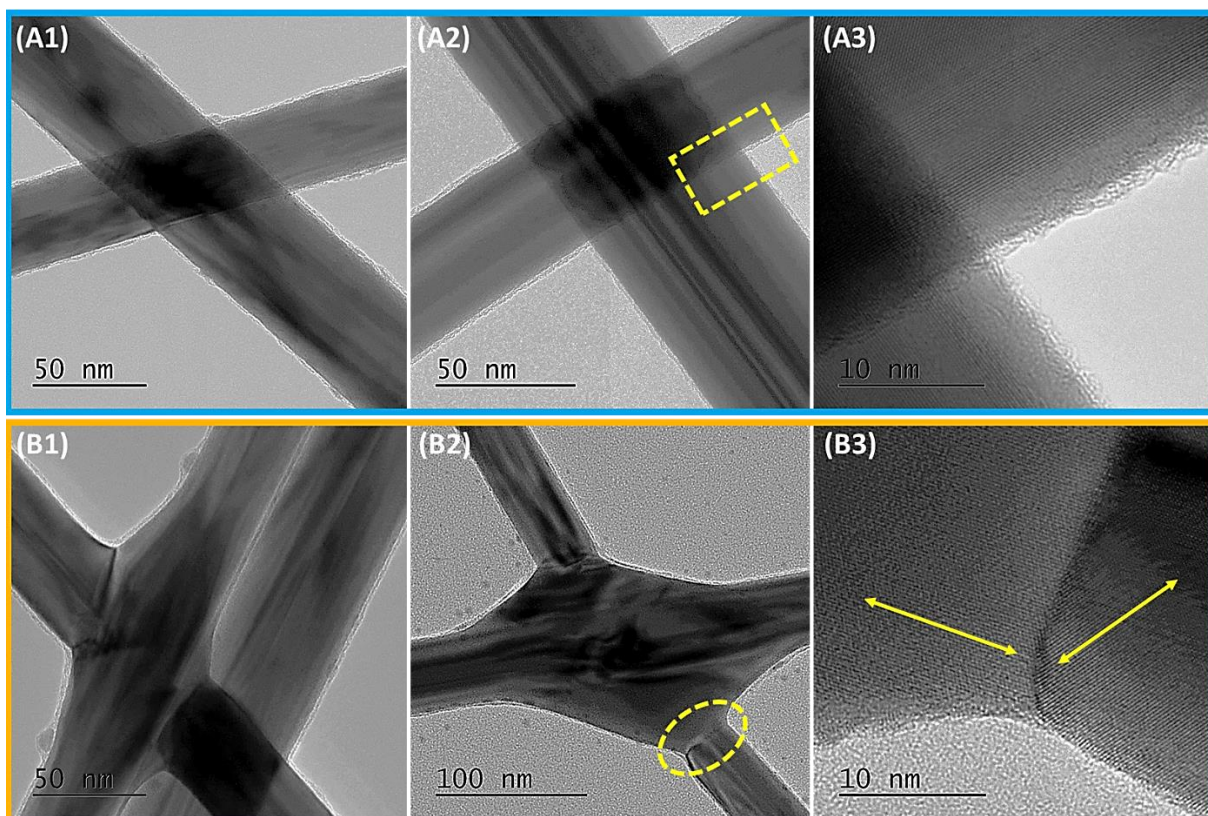


Figure 21. A1-A3) TEM images of « as deposited » AgNWs (without any optimization treatment). The NWs were spray-coated directly on a TEM grid for top-view observation. A NW-NW junction made of Liten AgNWs is depicted in (A1), while (A2) shows a Seashell AgNW junction. (A3) is a zoom of the bottom-right area of (A2) junction. B1-B3) TEM images showing the morphology of Liten AgNW junctions after isothermal annealing on a hot plate at 180 °C during 1h. (B3) is a zoom in the grain boundary circled at the bottom of (B2) junction.

Besides, after annealing, the amorphous shell is surrounding not only the NWs, but also the sintered junctions themselves. Hence, the atomic diffusion process does not concern only silver atoms but also the polymer chains that PVP is made of. The diffusion process of PVP is well visible when looking at two lined-up AgNWs (see **Figure 22A1-A2**). At 180 °C, PVP glass transition is overtaken. According to Buera et al.,^[192] glass transition in PVP (Mw= 40 000 g mol⁻¹) is indeed close to 140 -150 °C. Hence PVP diffusion process is likely to be facilitated at temperature higher than 150 °C. However, such merging of PVP at the extremities of two lined-up NWs was also observed on unheated NWs (see Figure 22A3). This suggests that slimming of PVP layer at the interface of two adjacent NWs is likely to be encouraged first by chemical attraction and the weight of top NW, and second by the PVP diffusion at temperature higher than glass transition. Once the adjacent NWs are in physical contact, the sintering process associated with lateral silver diffusion can begin. A schematic representation of the physico-chemical mechanisms involved in thermal annealing from room temperature up to optimization temperature is reported in Figure 22C. Here again the temperature values depicted in the schema should be considered with caution since they are highly dependent on the thermal annealing kinetics, as well as on the NW dimensions.

Finally, even though the junctions depicted in Figure 21B1-B2 are good examples of the sort of junctions that can be considered as “optimized”, it has to be noted that two grains boundaries are still facing each other. Figure 21B3 is a zoom in the bottom grain boundary. Atomic planes with different orientation on each side of the grain are clearly visible. The central part of the junction looks perfectly crystalline. Hence the main contribution to the junction resistance after optimization might originate from the face-to-face grain boundaries that are systematically observed after having completed thermal annealing. Such junction morphology after optimization was taken into account when building up the simulation models (see Chapter 3). This has a strong influence on the way optimized junctions behave from an electrical point of view. The presence of crystalline mismatches and perhaps dislocations also imply that it might still be possible to optimize further the junction even after having completed thermal annealing. For instance, additional electrical annealing could be investigated as a way to favor electron wind-induced re-organization of crystal planes near the junctions.

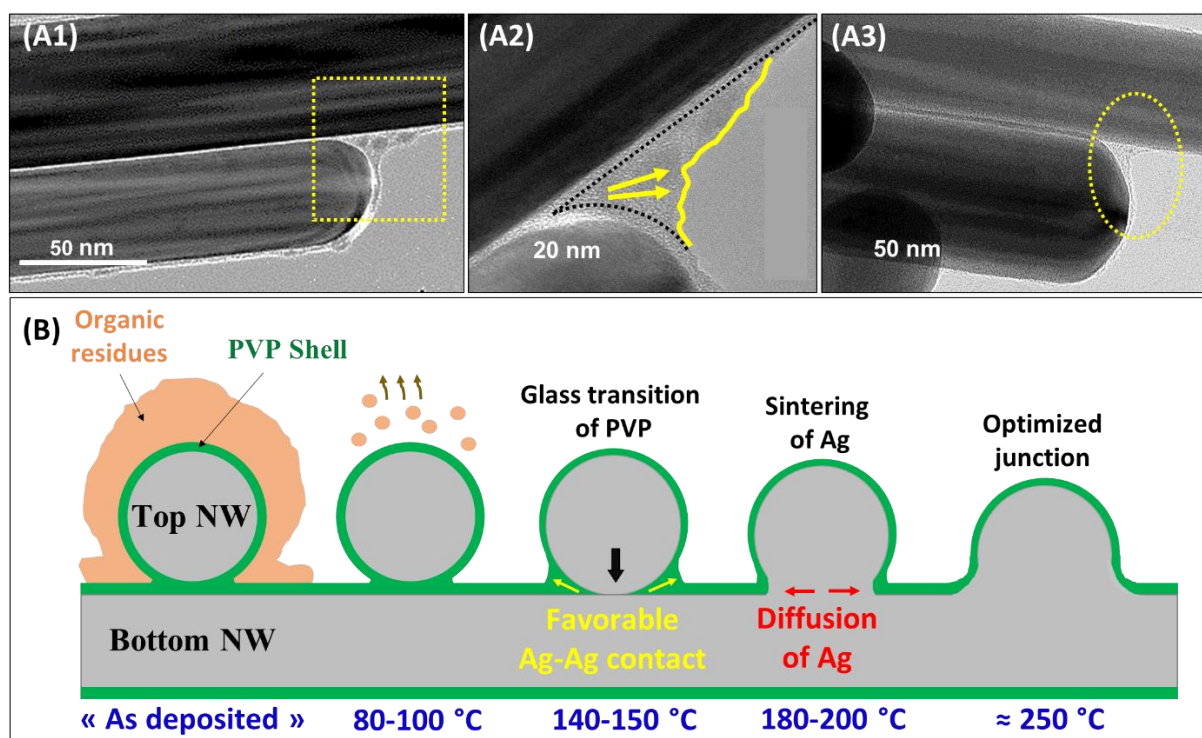


Figure 22. A1-A3) TEM images of lined-up AgNWs after isothermal annealing at 180 °C (A1-A2), and without any thermal treatment (A3). (A2) is a zoom in the yellow dashed square in (A1). In both cases, diffusion of PVP is well visible. B) Schematic representation of the successive mechanisms involved in the reduction of junction electrical resistance by thermal annealing. Temperature values depicted here are highly dependent on the kinetics of thermal annealing and on the NW dimensions. Therefore they should be considered with caution.

2.2.2. Morphological impact of acid treatment: nanoscale characterization

As already mentioned in section 2.1.2, the efficiency of acid treatment on the optimization process of AgNW networks depends on the type of AgNWs used as network building-blocks. The latter has proved to be very efficient on Seashell NWs (see Figure 16a and Figure 17). Regarding Liten AgNWs, as reported by Céline Mayousse in her PhD manuscript, the activation level of as-deposited AgNW networks (without any acid treatment) used to be subjected to statistical fluctuations. By performing acid treatment in any case, such statistical fluctuations regarding the activation of as-deposited AgNW networks could be discarded. As a consequence, acid treatment was implemented as regular step of Liten AgNW networks fabrication protocol.

It was first believed that acid treatment was responsible for entirely removing the PVP layer surrounding the networks. Mayousse et al. did performed X-ray Photoemission Spectroscopy (XPS) on several Liten AgNW networks to compare the amount of PVP before and after acid treatment.^[22] Surprisingly, by analyzing XPS pics associated to Carbon (C1s) and Nitrogen (N1s), it was concluded that the amount of PVP adsorbed in the surface of AgNWs was exactly the same with or without acid treatment.^[22] As a consequence, it was secondly believed that instead of literally removing PVP, HNO₃ action consisted of destabilizing and “de-wetting” the PVP shell, as a way to favor intimate contact between adjacent NWs (see schematic representation in **Figure 23A**).

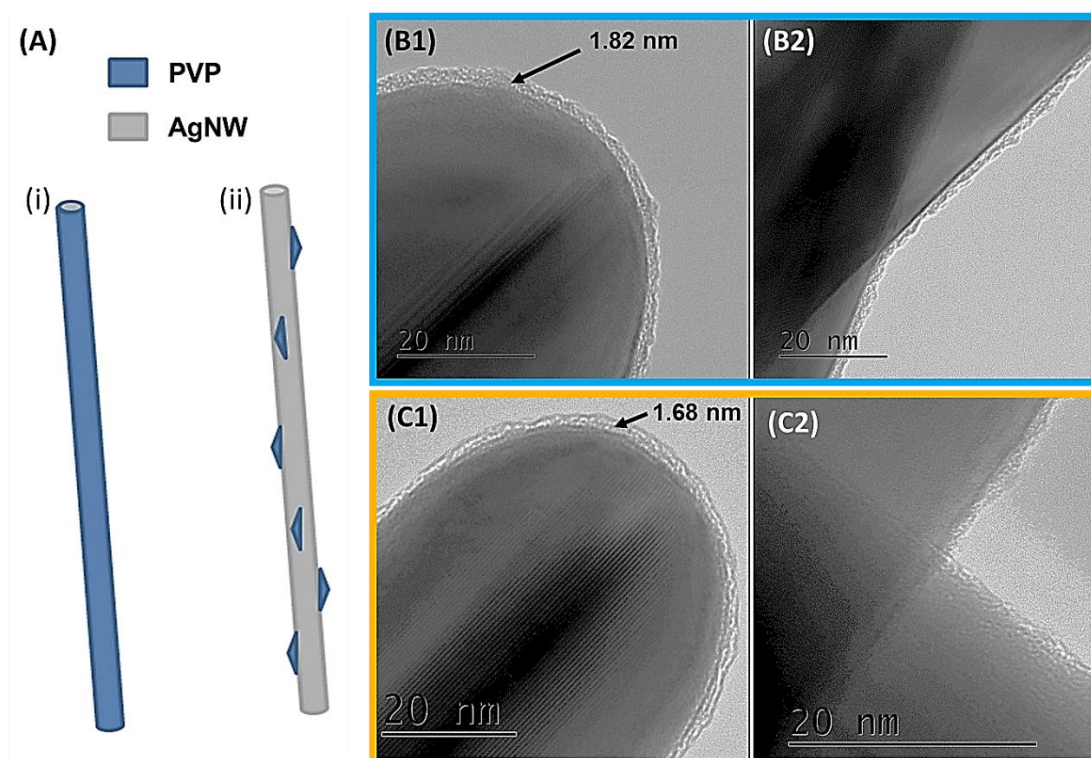


Figure 23. A) Schematic of an AgNW: (i) untreated with a thin continuous PVP shell (blue), (ii) acid treated in solution which induces a de-wetting of the PVP shell. Reproduced from ^[22]. B) TEM images of untreated Liten AgNWs: (B1) at a NW extremity, (B2) near a NW junction. C) TEM images of Liten AgNWs acid treated in solution: (C1) at a NW extremity, (C2) near a NW junction.

In order to confirm or infirm such hypothesis, several TEM images of Liten AgNWs before and after acid treatment were captured (see Figure 23B and Figure 23C, respectively) within the frame of this thesis. In any case, it seems that carbonaceous layer surrounding the NWs is always present and continuous. Measurements of the shell thickness with or without treatment do not lead to any reliable conclusion regarding the impact of HNO₃ in the potential reduction of the carbonaceous shell. As a consequence, comparing simply top-view TEM images did not yield any straightforward conclusion regarding the physico-chemical mechanisms involved the reduction of AgNW contact resistance. At least it was helpful for discarding the “de-wetting” hypothesis.

Similarly to thermal treatment, the thickness and morphology of carbonaceous shell remains the same after acid treatment. However, once acid treated, AgNW solutions exhibit several material aggregates after a couple of days. It is well known that PVP acts as powerful surfactant agent, favoring the proper dispersion of AgNW in solution. Hence, the presence of aggregates in solution after acid treatment suggests that even though the morphology of PVP is not affected by acid treatment, its chemical nature might be. In order to get further information about the chemical nature of the carbonaceous shell with and without treatment, preliminary analysis based on Electron Energy Loss Spectroscopy (EELS) were performed in order, first, to validate that the carbonaceous shell corresponds to PVP, and second to see whether the chemical nature of such layer is modified by acid treatment. Unfortunately, the signature of PVP could not be strictly validated by EELS. The absorption pic of azote (N), which is the critical element to validate the presence of PVP, is indeed covered by the one of silver. Hence only silver, carbon, and oxygen elements could be detected by EELS in a reliable way. PVP monomer chemical formula is depicted in **Figure 24A1**. According to Gao et al. PVP is attached to AgNWs via Oxygen-Silver links.^[193] This would lead to the linking scenario reported in Figure 24A2.

Figure 24B reports the results associated with an untreated Liten AgNW junction. The area selected for analysis corresponds to the yellow dashed square area visible in the TEM image (B1). The entire chemical map is provided in (B2) for Ag, C, and O components. The results corresponding to the yellow line-cross in (B2) are reported in (B3). As expected, the amorphous shell is mostly composed of carbon. The barrier between carbon-based shell and Ag-based core is well visible too. On the other hand, the intensity of Oxygen is very low since its content in the PVP monomer is very low (1 over 17 atoms), as compared with Carbone content (6 over 17 atoms). However, it can be detected that Oxygen intensity is slightly increased once reaching the AgNW. This suggests that Oxygen is located at the surface of AgNWs and is likely to make the link between silver and PVP, in accordance with Gao et al.

The same type of analysis was performed on acid treated Liten, resulting in the same kind of observations. Hence, it was not possible to detect any change in the chemical nature of the amorphous shell surrounding the NWs by the mean of EELS. At least the resolution associated to this spectroscopy technique did not yield any significant results. In order to get further information about the mechanisms taking place at interface of adjacent NWs, it was then found necessary to explore the internal structure of the junctions. Ultramicrotomy technique was found suitable for studying AgNW-AgNW cross-section. The corresponding results are reported in section 2.2.3.

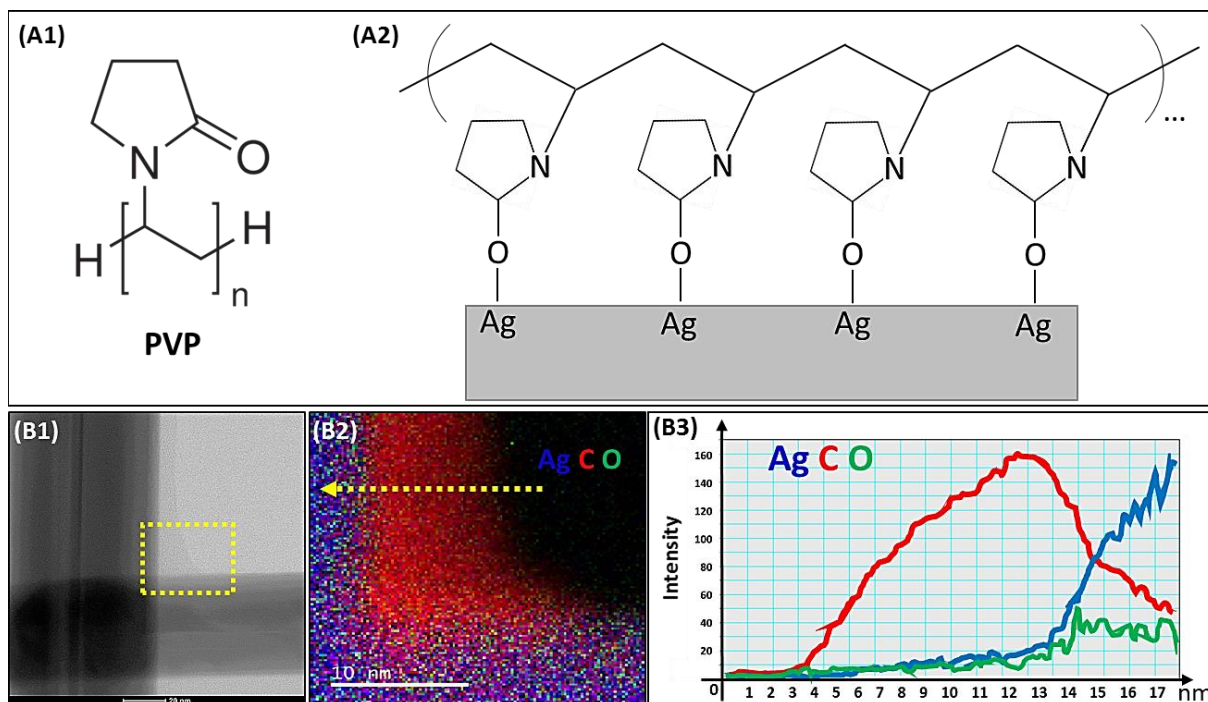


Figure 24. (A1) Chemical formula of PVP monomer. (A2) Possible linking scenario between PVP and AgNWs. B1-B3) EELS analysis of untreated Liten NWs showing: (B1) TEM image of the scanned junction area, (B2) EELS-based chemical map of the area (red: carbon, blue: silver, green: oxygen), (B3) EELS results associated with the line cross (yellow arrow) in (B2).

2.2.3. Exploration of the internal structure of NW-NW junctions: preliminary results

Given that the morphology of AgNW junctions is very sensitive to thermal energy, cutting methods commonly used in nanotechnology field such as Focused Ion Beam (FIB) were considered as inappropriate for maintaining the NW junctions safe during cutting process. On the contrary, ultramicrotomy technique does not require any thermal energy. While it is mostly used for biological observations, it revealed suitable for exploring the internal structure of NW-NW junctions. The ultramicrotomy protocol is as follows: AgNWs in high quantity are spray-deposited onto a 5×5 mm² PEN substrate. The sample is then vertically fixed in a cylindrical capsule, which is filled out with a mounting epoxy resin. Such epoxy resin is highly necessary for maintaining the sample fixed during the cutting process. The extremity of the capsule is cut to give the desired pyramidal form with a truncated extremity, which consists of the surface about to be cut. Finally, very thin slices of the capsule content are cut using an ultramicrotome machine fitted with a diamond knife.

The resulting specimen consists of very thin slices (50-90 nm) of the successive layer present in the capsule {PEN, AgNWs, epoxy resin}, ready to be observed in TEM (see **Figure 25a**). For proper cutting, hardness of the selected substrate has to be similar to the one of epoxy resin. First tests using Silicon substrate yielded a lot of damage during the cutting process, while PEN was found appropriate for this purpose. Contrary to FIB technique, it is not possible to target one specific junction during cutting. Each specimen obtained by ultramicrotomy comprises all

the metallic entities contained in the corresponding cross-sections of the initial AgNW-PEN sample. When scanning the specimens under TEM, most of the detectable metallic compounds consist of single NW cross-sections (see Figure 25a). Longer entities, much less numerous, correspond to the less probable case where NWs are cut along their length. In this study, we focused on the NW intersection (see Figure 25b-c), where such longer entities are in close contact with NW cross-sections.

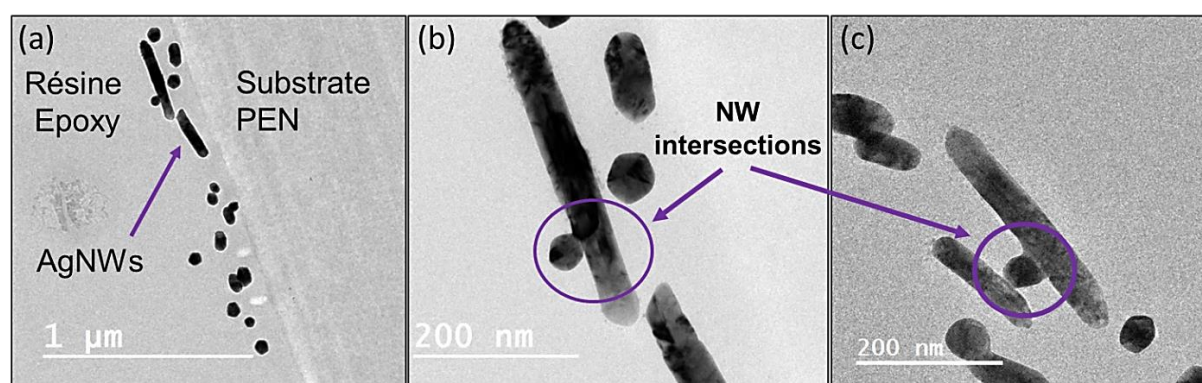


Figure 25. a) TEM images of an ultramicrotomy strip showing the epoxy resin, PEN substrate, and cross-section of AgNWs all together. b-c) Zoom in AgNW intersections.

Only two sorts of AgNWs have been investigated using the ultramicrotomy technique so far: “as-deposited” Seashell NWs, and acid treated Liten NWs. The latter were acid treated twice, in solution and after deposition (see Figure 15b), while the former were not subjected to any acid nor thermal treatment. These two sorts of NWs correspond to the two extreme cases in terms of AgNW network electrical performance evaluated after deposition. Untreated Seashell NW network are indeed highly resistive while acid treated Liten AgNW networks offer very low electrical resistance after deposition (see Figure 16a and Figure 18, respectively). TEM images of the junctions cross-sections obtained by ultramicrotomy and associated with these two sorts of NWs are reported in **Figure 26A** and Figure 26B, respectively. Whatever the sort of NWs investigated, or the treatment performed on them, the morphology of the junctions is subjected to statistical fluctuations. Hence, the images shown in Figure 26 reflect a general tendency only, which should be further checked and confirmed.

The NWs belonging to the untreated Seashell NW junction (A1) are not in intimate contact with each other. When zooming in the interface (A2), it seems that there is a small amorphous gap between them, which is likely to be composed of organic residues and/or PVP. On the other hand, the NWs belonging to acid treated Liten NW junction are in very close contact (B1). EELS analysis performed on the same area (B2) suggests that there is a carbonaceous content increase along with a silver content decrease at the interface. However, even without any thermal treatment, silver atoms could diffuse to create a physical link between the adjacent NWs. The difference in contact quality observed between these two junctions might originate from a change in the PVP surfactant behavior after acid treatment, leading a drastic change in the overall AgNW networks resistance measured after deposition.

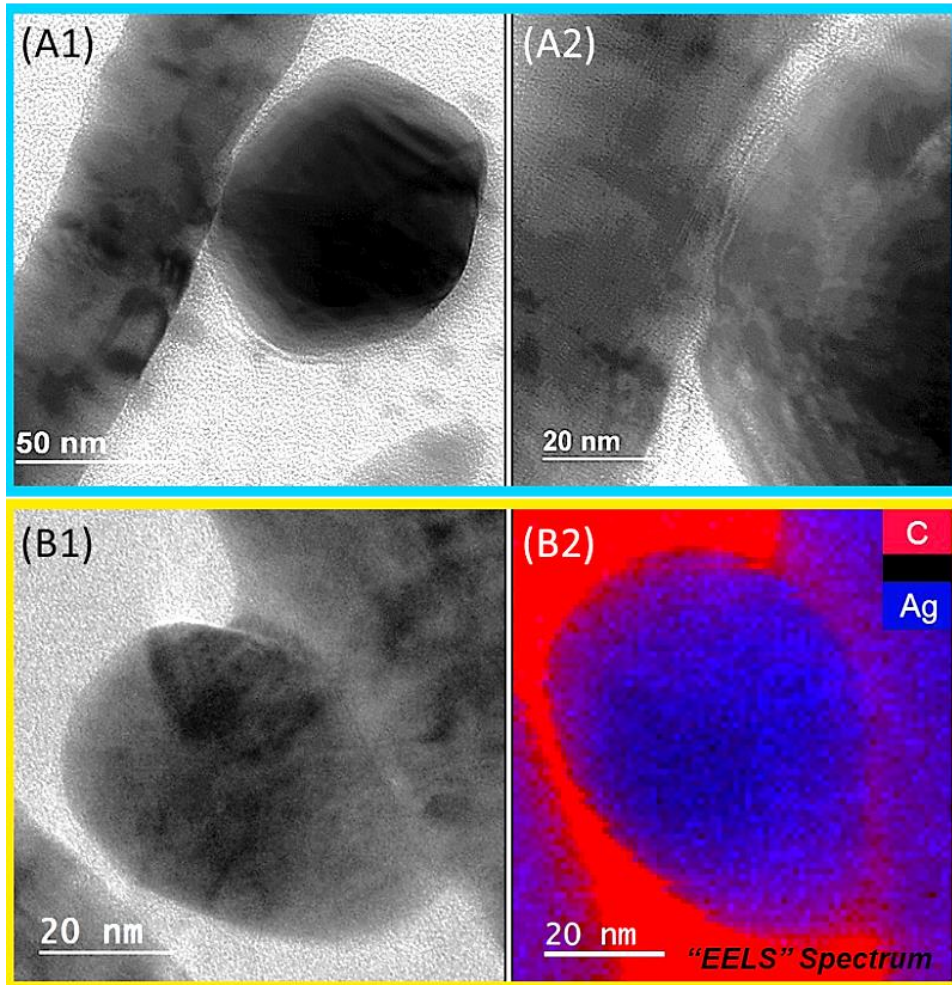


Figure 26. A1) TEM images showing an ultramicrotomy strip associated with “as-deposited” Seashell AgNW junction. A2) Zoom in the interface of the junction in (A1). B1) TEM images showing an ultramicrotomy strip associated with an “acid-treated” Liten AgNW junction. B2) EELS-based chemical map of the same junction as in (B1).

These results still constitute a preliminary study. Further ultramicrotomy specimen should be prepared and analyzed in order to complete this study about the physico-chemical phenomena involved in the optimization of contact quality between adjacent AgNW junctions. In particular, observations of untreated Liten NW junction, as well as thermally treated junction should be performed to complete the series. Apart from the physico-chemical treatments performed before or after deposition, other experimental parameters might influence the NW junction contact quality after deposition: even slight differences in the synthesis protocol and the purification methods, as well as the sort of dispersing solvent used might influence the behavior of resulting AgNWs. Deposition technique and associated protocol are also likely to influence the contact nature of adjacent NWs. For instance, Lee et al. suggested, based on TEM observations, that the PVP layer had its thickness slightly decreased by performing numerous methanol cleaning of the AgNW solutions.^[194] The same authors reported that the spray deposition technique was favorable for curving and even for partially fusing adjacent NWs, due to their high spray-induced kinetic energy during deposition.

Chapter 3. Description of the modelling tools developed during this thesis

Improvements in the integration of AgNW networks as transparent electrodes into functional devices require having a deeper knowledge and understanding of their electrical and thermal properties. Under such consideration, the main questions and challenges to tackle are: how electrical current is distributed over the network when voltage is applied? And considering the stability of the AgNWs, what is the local (AgNWs) and global (substrate) temperature elevation of the electrode induced by Joule effect after certain duration? Due to the high complexity of the network architecture, experimental approaches have provided fruitful but still incomplete results so far.

Another approach to collect further information is to perform “realistic” simulations of the AgNW network properties. For this purpose, Matlab and Comsol softwares have been the simulation tools mostly used and developed within the frame of this thesis. More specifically, this chapter introduces the generation of random 2D-stick networks by Monte-Carlo simulations using Matlab, as well as the simulation of electrical and thermal properties of AgNW networks via finite element method using Comsol. This chapter aims at presenting and describing in details the approach and methodology adopted for constructing the simulation models developed during this thesis, while their practical use for characterizing AgNW networks is mostly reported in Chapter 4.

3.1. Brief introduction to the percolation theory

Percolation phenomenon deals with the concept of interconnection between neighbouring entities of small dimension, and with their ability to form larger clusters over a surface large enough so that any potential boundaries effect can be considered as negligible, and thus yielding macroscopic properties and behaviour.^[195] Stick percolation theory has been widely studied over the last decades^[195,196] and has recently attracted renewed interest as an efficient tool to describe both the architecture and the physical properties of either carbon nanotube or metallic nanowire-based networks.^[197,198]

By considering single silver nanowires as 1D sticks, the specific case of AgNW networks can be treated as a 2D percolation model. Percolating pathways originates from the interconnections between the wires allowing the electrons to travel from one side to the other side (see **Figure 27**). These pathways usually intercept with each other, leading to a complex combination of series and parallel resistances. Therefore, the total resistance of the network is directly influenced by the number and the shape of these pathways.

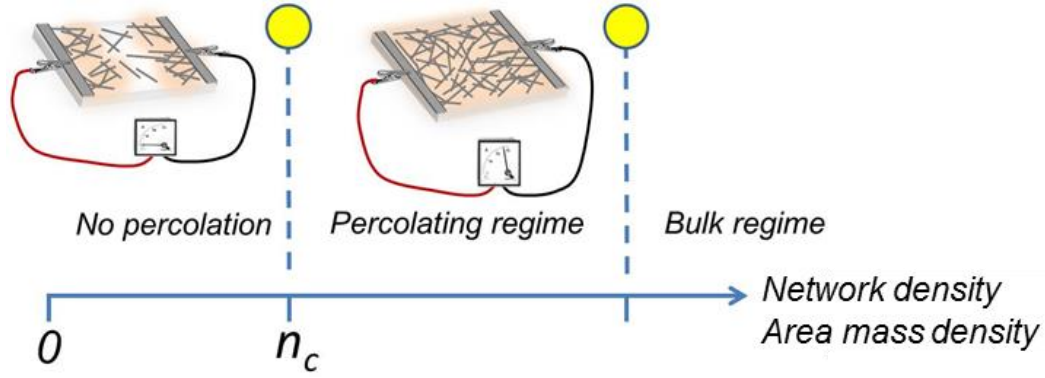


Figure 27. Schematic representation of the three different regimes while the network density (or areal mass density) is increased.

During his thesis, D. P. Langley studied deeply the 2D stick percolation problem by simulating the network generation (under Matlab) via the Monte-Carlo method.^[23] It was found that for an ideal system in which all the sticks are (i) perfectly straight, (ii) have the same length and (iii) are randomly deposited inside a square frame, the number of wires N_c associated to the percolation threshold n_c depends on the ratio between the stick length L_{NW} and the length of the square system L_s as follows:

$$N_c = n_c * S = 5.6373 \frac{L_s^2}{L_w^2} + \frac{L_s}{L_w} + 5.5 \quad (3.1)$$

With S the surface area of the network. If angular anisotropic distribution is taken into account, which corresponds, for example, to the case where the wires are deposited by spin-coating, then the required network density to ensure percolation increases. Indeed, the more anisotropic the sticks, the higher the amount of wires required for reaching percolating, no matter the sticks are arranged longitudinally or transversely.^[23] Finally, it has to be mentioned that the convergence of N_c as defined in Equation 3.1 can be achieved only in the case where a substantial number of simulations are performed. According to D. P. Langley, performing 10^5 simulations is considered sufficiently high to result in the convergence of N_c for all calculations.^[23]

3.2. Generation of random networks via Matlab-based Monte Carlo simulations

The algorithm developed in the team by D. P. Langley during his thesis to generate a random stick network and to distinguish the percolation cluster is illustrated in **Figure 28a**. It has been partly inspired from principles presented by Newman and Ziff.^[199,200] To start with, a square frame in which all the wires are about to be generated is defined, symbolizing the substrate in the real world. The top and bottom boundaries correspond to the two silver paste electrodes in real samples. Wires are added into the frame step by step, with randomly distributed (x,y) coordinates and a randomly generated angle θ , as shown in Figure 28a-A. This is achieved by using the command *rand*, which generates a set of random numbers between 0 and 1 uniformly. One can also control how many wires are generated at one time.

After the generation of each wire, all of them are assigned to a “serial number” as an initial “cluster number”. The count of serial number starts from 1. Then, if the program detects that a wire intercepts with others, all the wires involved in the intersection will be assigned to the minimum cluster number available among them (Figure 28a-B and C). As a simple example, in Figure 28a-C, there are three different clusters, represented by three different colors (red, black and blue). Particularly, the top and bottom “electrode” wires are assigned to a cluster number of -2 and -1, respectively, and any wire lately generated, and intercepting one of the two boundaries, will automatically have its cluster number assigned to these specific cluster numbers as well (-2 or -1). At the end, when the cluster number of the bottom boundary wire switches to -2, meaning that there is at least one pathway connecting the two electrodes together, the network reaches its percolation state. Figure 28b shows a typical percolation network generated using this algorithm in Matlab. The “system size” is 25 mm², the NW length is 37.5 μm, while the network density is n_c (percolation threshold). The wires that are recognized as part of the percolation network appear blue, while others are black.

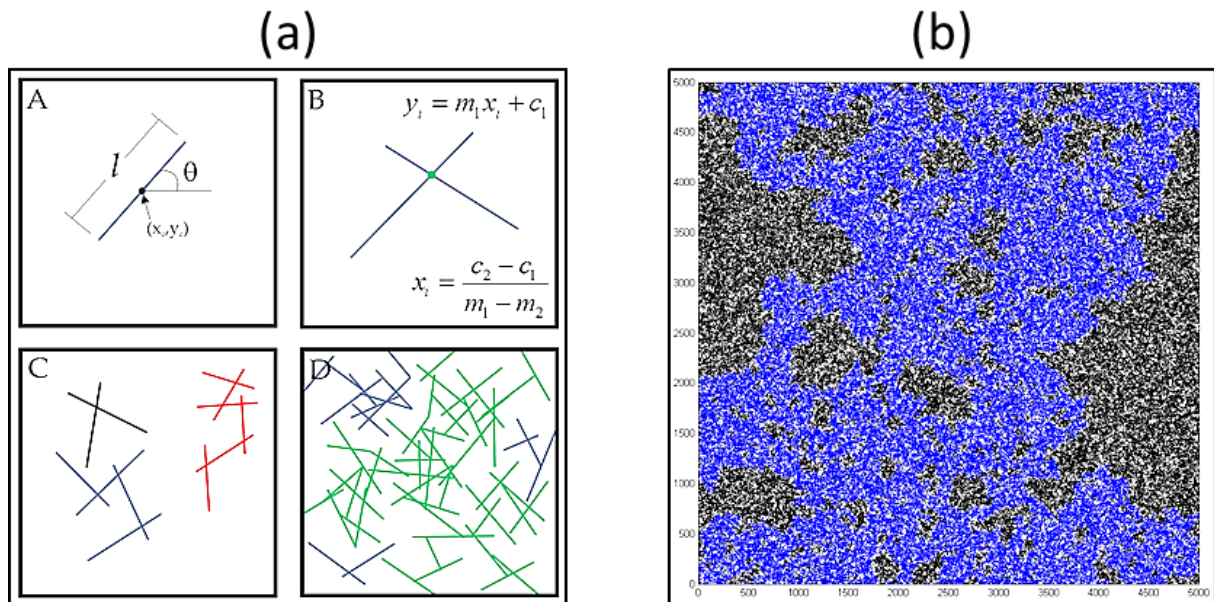


Figure 28. a) A schematic illustration of the successive steps involved in the generation of new wires and in the determination of the different clusters. b) A typical network generated in Matlab (Area: 25 mm² network, NW length: 37.5 μm, Network density: n_c). The wires that are recognized as part of the percolation network appear blue, while others are black

This algorithm developed by D. P. Langley has several advantages. Firstly, a random and percolating network can efficiently be generated inside a frame whose size can vary. Moreover, detailed information regarding the wires is provided, such as their position and the cluster they belong to. Last but not least, it distinguishes the not percolating wires from the percolating ones. However, there is still some space for improvement. At the end of the simulation, the wires are considered as percolating when their cluster number is equal to -2. However, such criteria might be fulfilled in the two following circumstances: (i) the wires are part of the percolating cluster, (ii) the wires intercept one of the two electrodes but do not actively participate to the percolation

cluster. As depicted in **Figure 29a**, it's not suitable to classify the wires in case (ii) as percolating ones since they don't conduct the current to the bottom electrode. From a strict electrical point of view, such wires do indeed not participate to electrical conduction. However, they might still contribute to the carrier collection efficiency in the case of TEs for solar cells, or still contribute to thermal diffusion in the case of transparent heaters. Hence, their potential influence should be discussed depending on the target application.

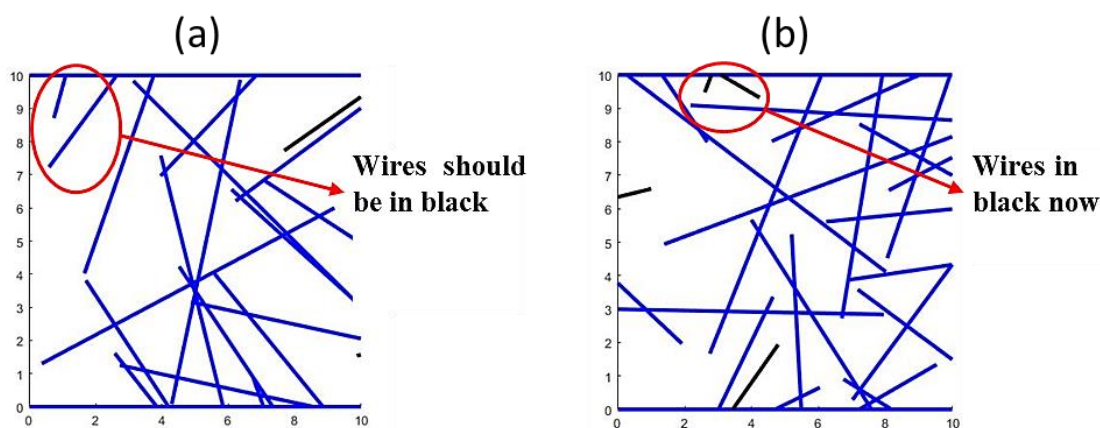


Figure 29. a) A schematic illustration of the two cases where wires are classified as part of the percolation network. b) Elimination of case (ii) in the new code.

During the present thesis, a strategy was developed to avoid such situation (ii). The latter is described by a schematic illustration in **Figure 30**. Instead of using only one cluster number, the improved code assigns three cluster numbers to each of the generated nanowires, depicted as C_1 , C_2 and C_3 in Figure 30. Similarly, C_1 means the same as the original cluster number used in the code developed originally by D. P. Langley et al. It tells which cluster the wires belong to. However, the information regarding the potential connection with the bottom and top electrodes is no longer stored in C_1 but separately stored in C_2 and C_3 . The C_2 (C_3) value of the wires is equal to -1 if they are linked to the bottom (top) electrode, otherwise it is 0. Each cluster is then considered as percolating only in the case where C_2 and C_3 are equal to -1 at the same time. In this way, case (ii) is eliminated from the percolating wire collection (see Figure 29b).

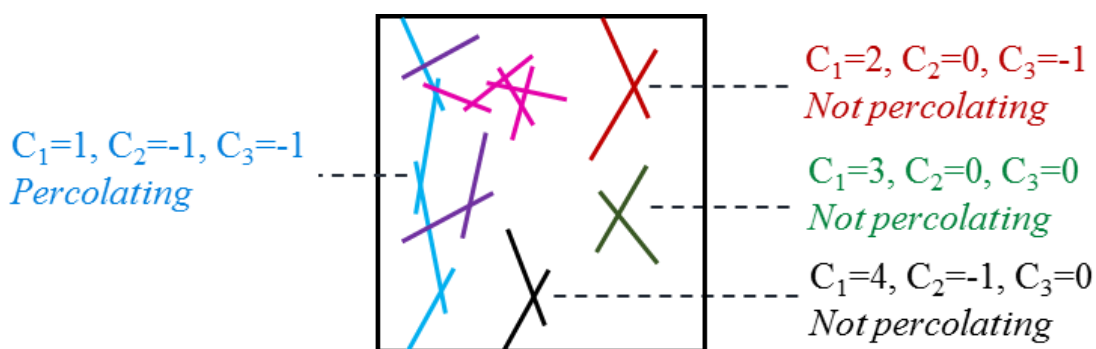


Figure 30. Illustration of the strategy to exclude case (ii) from the physical percolating cluster.

In real world, even a small size network (1 cm²) is composed of millions of wires since the average length of the nanowires used is only several microns. According to Equation (3.1), the simulation of a 1 cm² AgNW network (with $L_{NW} = 10 \mu\text{m}$, and $n = 5n_c$, which roughly corresponds to the density limit above which AgNW networks are suitable for the vast majority of applications), requires the generation of 2.8×10^7 wires. Dealing with such enormous number of entities in the simulation is extremely time consuming. To address this problem, we first need to reduce the system to a reasonable size so that the network contains a smaller but still acceptable amount of wires, without impacting the network physical properties due the smaller size. This strategy is necessary and effective: according to D. P. Langley's work, the influence of the system size on the percolation threshold becomes insignificant when L_s/L_{NW} is larger than 5. If L_s/L_{NW} reaches 10, the system size has no influence from a statistical point of view (see **Figure 31**).^[23] Given that the length of most of the AgNWs used in the experiments is maximum 10 μm , the system size was chosen to be 50 μm in most of the simulation tests so that L_s/L_{NW} can reach the critical value of 5. In the case of a dense network ($n \approx 8n_c$), it represents approximately 1300 wires, which is still within the calculation capability of the software. Moreover, when working on homogeneous square networks, the electrical resistance does not depend on the size of the network in first approximation. As a consequence, it seems acceptable in first approximation to compare the behavior of small size-simulated networks with much bigger experimental networks fabricated for real experiments.

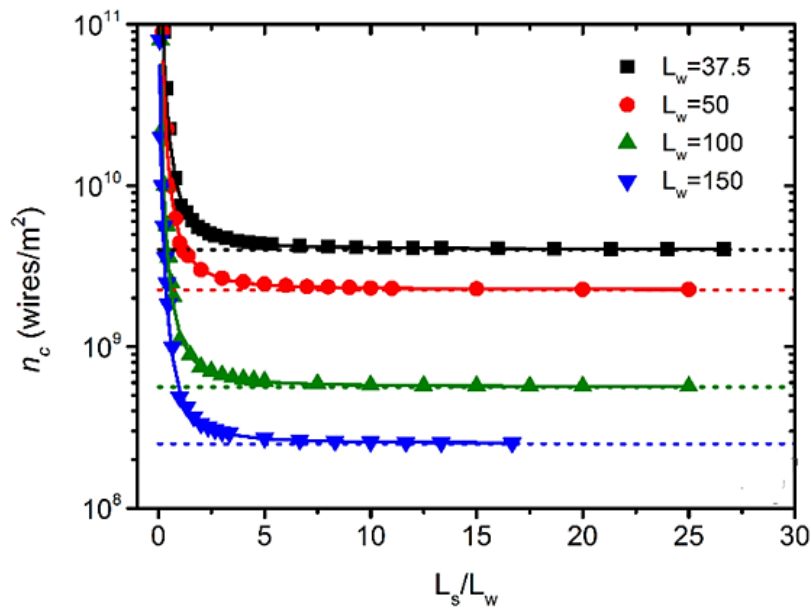


Figure 31. Graph showing the percolation threshold as a function of the system size divided by the nanowire length.^[23]

In order to decrease even more the number of entities the software has to deal with, we also tried to get rid of all the wires that do not take part in the “electrical percolating cluster”. Indeed, even though some of the wires are connected to the physical percolating cluster, they cannot participate to the current flow since they are located in “dead branches” (see the purple wires

in Figure 30). As they have no influence on the electrical properties of the network, they can be removed from the simulation in order to save some calculation time. The process to exclude these wires is explained in **Figure 32**. To start with, an “intersection matrix” records the coordinates of all the intersection points and detects the wires involved in each of the intersection. It is then possible to count the number of intersections each wire is involved in. The wires involved in only one intersection constitute “dead branches” (see Figure 30) that cannot participate to the electrical current flow. Therefore, they are removed from the percolating cluster in order to save time for future electrical simulations. Once these wires have been excluded, their adjacent wires have one intersection point less. The detection of wires involved in only one intersection is carried out again until all the percolating wires intercept at least two other wires.

Such an approach is very helpful in removing several dead branches from the percolating cluster. However, it is not powerful enough for eliminating all the dead branches, especially when the architecture of the latter is too much complex (see the case of pink nanowires in Figure 30), which form a complex dead branch that cannot be removed by the mean of this method). Finally, trying to eliminate as much dead branches as possible is only suitable in the case we focus on the electrical properties of studied networks. On the contrary, when thermal properties are considered, such dead branches are likely to participate to thermal diffusion process and therefore should not be removed from the network.

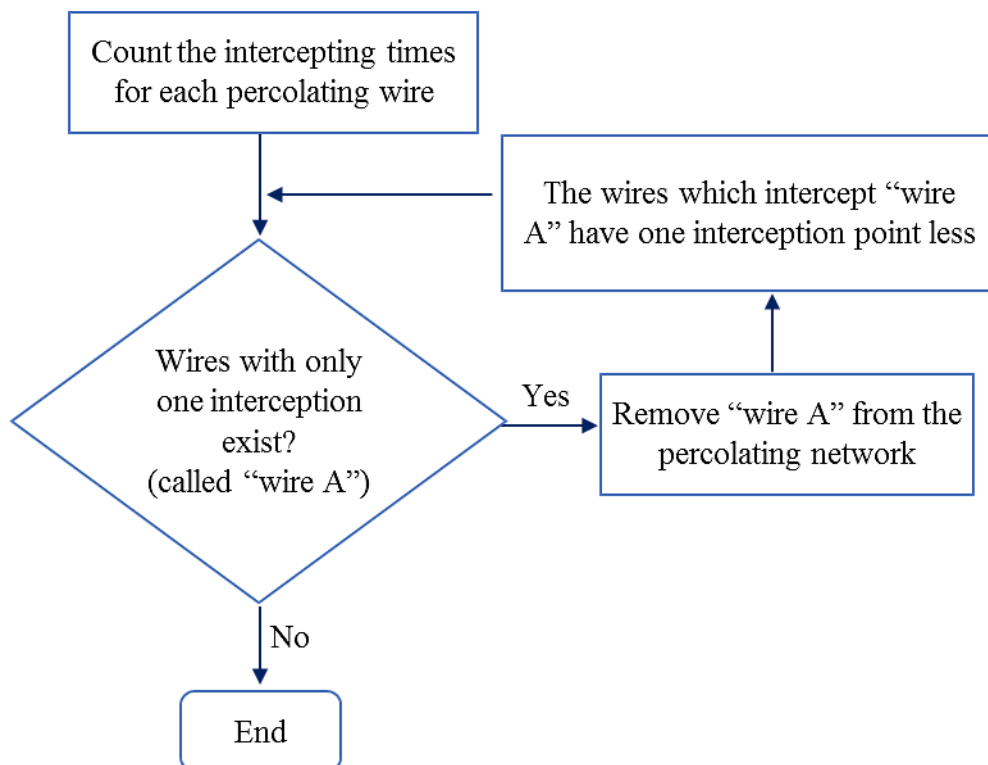


Figure 32. A schematic illustration of the process to remove the dead end wires from the electrical percolation network.

3.3. Electrical and thermal simulations using Comsol

In order to simulate the physical properties of AgNWs, it is necessary to switch from Matlab to Comsol. Comsol is a very powerful software for performing the simulations accounting for coupled or multi-physics phenomena. By applying the finite element method, it can solve the physical equations numerically and provide local and displayable results. For the simulation of the electrical and thermal properties of AgNW networks, Maxwell's and heat transfer model are the equations solved by Comsol (see Appendix A for more details). The present section deals with the construction of the Comsol model and the attribution of appropriate boundary conditions for either electrical or thermal simulations likely to mimic properly the physical phenomena taking place in the real world.

3.3.1. Network geometry exportation from Matlab to Comsol

To construct the simulation model in Comsol, the first step is to export the random network generated in Matlab to Comsol. For each of the sticks generated in Matlab, the information $\{x, y, \text{center coordinate}, \text{rotation angle } \theta\}$ are stored in the workspace as the “network matrix”. Thanks to this information, the wires can be automatically reproduced one by one in Comsol using the Livelink with Matlab, a specific simulation module that allows communication between Matlab and Comsol. The segment without width in Matlab is replaced by a rectangle in Comsol (see **Figure 33a**), with the desired diameter and length values. As the vast majority of the real nanowires used for experiments during this thesis had an average diameter of 60 nm, and a length of 10 μm , these dimensions are the ones used in this presentation chapter as example.

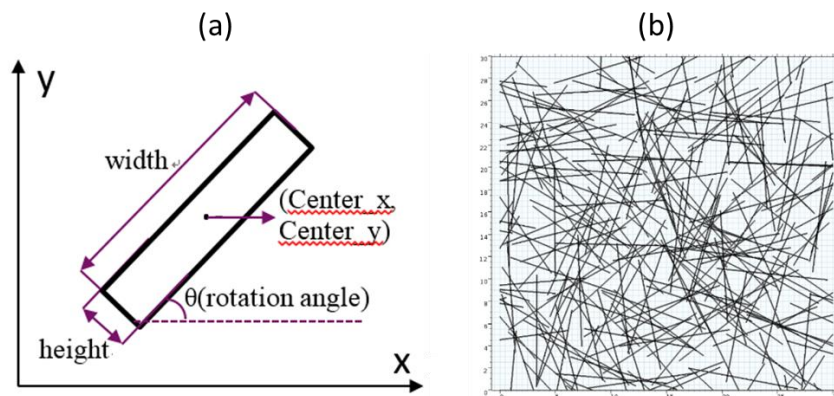


Figure 33. a) A schematic illustration of a rectangular wire generated in Comsol. b) A random network converted to Comsol from Matlab.

For the simulation of electrical properties, the insulating substrate can be ignored and a 2D network is sufficient since the electrical current is supposed to be homogeneously distributed along the z axis. This statement was confirmed by performing simulations on both 2D and 3D networks with the same geometry and same conditions, leading to the same simulation results.

However, when focusing on the thermal properties of AgNW networks, it is mandatory to work in 3D. Indeed, when AgNW networks are used in transparent heaters, the heat generated by Joule effect in the network diffuses through the substrate so that the transparent surface below (windscreen, helmet visor, etc.) can be heated as well. Since the substrate plays a critical role, it is necessary to simulate the thermal properties of AgNW networks using a 3D model.

3.3.2. Materials properties used in the model

The two materials used in the simulation are silver nanowires and polyethylene naphthalate (PEN) as the substrate (only when thermal simulations are considered). Their physical parameters are listed in **Table 1**. All the material properties of silver nanowires are the same as the ones of bulk silver except the electrical conductivity and the thermal conductivity. This is due to the decrease of the electron mean free path in conductive materials of small dimensions, as already mentioned in section 1.1.2. According to Equation 1.1, with λ equal to 50 nm, D_{NW} equal to 60 nm, the derived electrical conductivity value for AgNWs is $4.4 \times 10^7 \text{ S m}^{-1}$ (instead of $6.25 \times 10^7 \text{ S m}^{-1}$ for bulk silver). For similar reasons, it was measured by Cheng et al. that the thermal conductivity of the silver nanowires at 290 K is reduced by 55% from the corresponding bulk's value.^[201]

Table 1. The physical parameters used in the simulation in the case of PEN substrate, and AgNWs with the following dimensions: $D_{NW} = 60 \text{ nm}$ and $L_{NW} = 10 \mu\text{m}$

	Density (kg.m^{-3})	Thermal conductivity ($\text{W.m}^{-1}.\text{K}^{-1}$)	Heat capacity ($\text{J.kg}^{-1}.\text{K}^{-1}$)	Electrical conductivity (S.m^{-1})	Electrical Resistivity ($\Omega.\text{m}$)
Ag bulk	1.05×10^4	429	235	6.25×10^7	1.60×10^{-8}
Ag NWs	1.05×10^4	234	235	4.40×10^7	2.27×10^{-8}
PEN	1.36×10^3	0.15	1200	1.00×10^{-13}	1.00×10^{13}

3.3.3. Boundary conditions for electrical simulations

The bottom and top blue lines visible in **Figure 34a** represent the two silver paste electrodes to which voltage is applied. The outer physical boundary of the nanowires are automatically set as electrically insulating by Comsol, as shown in Figure 34b. In order to estimate the overall resistance of the simulated network, it is required to calculate the current density flowing through individual nanowires. In order to get realistic values for the current density flowing through the nanowires, as well as realistic values for the heat generated by the network, it is mandatory to select a realistic voltage value in the simulation process. Due to the low dimension of the simulated networks (in general $50 \times 50 \mu\text{m}^2$) as compared to real-size samples (generally $2.5 \times 2.5 \text{ cm}^2$), it is necessary to adapt the applied voltage value so that the simulation can provide realistic current values.

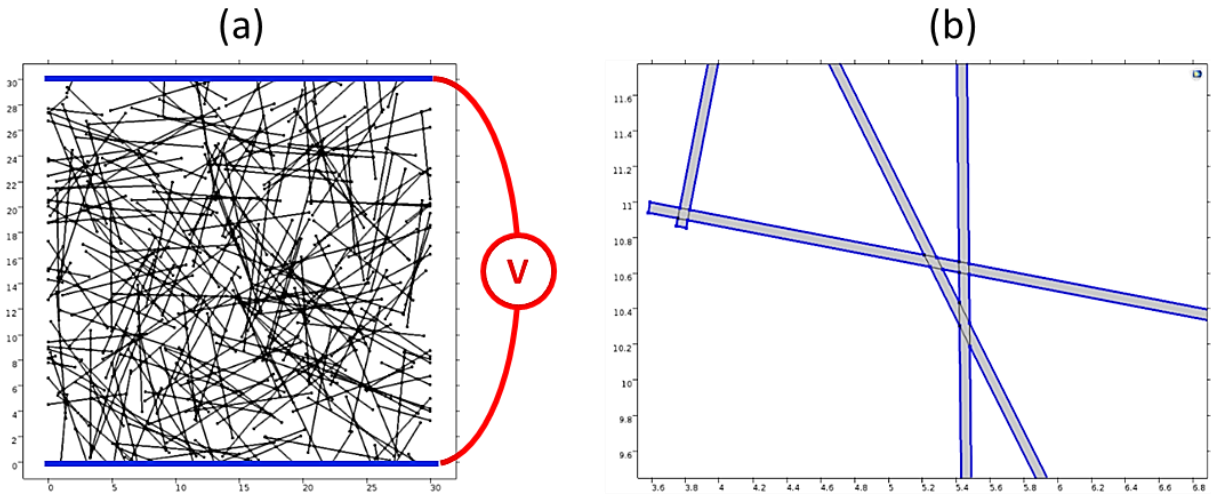


Figure 34. a) The two electrodes of the network (in blue). b) The outer physical boundary of the nanowires are automatically set as electrically insulating by Comsol in the outer boundary (represented by the blue line).

More specifically, when trying to mimic the electrical behavior of a real-life sample whose network length is L_n and the applied voltage is V_0 , then the corresponding “partial” voltage V_n to be applied to the simulated square network whose length is L_n can be calculated according to the following equation:

$$V_n = \frac{L_n}{L_0} * V_0 \quad (3.3)$$

Equation 3.3 can be interpreted as follows: first, the real large-size network (see **Figure 35a**) of resistance R_0 can be artificially divided into $n = L_0/L_n$ horizontal rectangles of same width, behaving as resistors in series (see **Figure 35b**) whose partial resistance is R_0/n . Therefore, each of the latter is subjected to partial voltage of V_0/n . Then, each horizontal rectangle can be further divided into n square resistors in parallel (see **Figure 35(c)**), one of which is studied in the simulation model. Thus, all these square resistors are subjected to the same partial voltage V_0/n . For example, the voltage to apply to a $50 \times 50 \mu\text{m}^2$ simulation network (equivalent to a voltage of 5 V applied to a $2.5 \times 2.5 \text{ cm}^2$ real network) should be 10 mV.

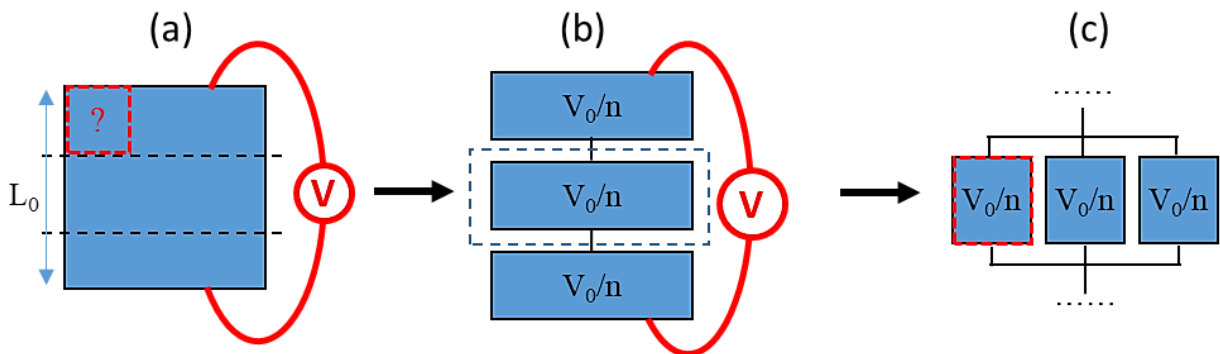


Figure 35. Schematic illustration for explaining Equation 3.3 in the case where $n = L_0/L_n = 3$.

According to experimental results (see section 1.1.3), the optimization level of the junctions plays a critical role in the electrical performances of AgNW networks. As already mentioned, as-deposited networks fabricated with commercial AgNWs are highly resistive (almost insulating). By performing very quick thermal or electrical annealing, it is possible to “activate” the networks. In that case, the junctions are not perfectly sintered but at least the adjacent AgNWs are in intimate contact with each other, allowing electrical current to flow.^[202] In this thesis, “active” networks are considered to have a two probe-resistance ranging from 100 Ω to 1 k Ω . Finally, when full sintering of the junctions is achieved (thanks to appropriate post-deposition treatments), the networks are considered as “optimized” and their two probe-resistance is in the range of 50 Ω in the case the AgNW density is high enough. All these variable features regarding the junction efficiency have to be taken into account in the model. This requires to assign specific material properties or boundary conditions to the junction areas (see **Figure 36**) to mimic the reality as much as possible.

For this purpose, it was first tried to attribute to all of the junctions an arbitrary resistivity value (ρ_j) 30 times higher than the one of individual silver nanowire (ρ_{NW}). Surprisingly, the simulation results show that the calculated equivalent resistance of the network remains only several Ohms no matter ρ_j is similar or 30 times higher than ρ_{NW} . This deviation from the experiment results may come from the inhomogeneous current concentration at the junctions in the simulation, as depicted in Figure 36a. It seems that in the Comsol model, the electrical current is indeed able to skip the high resistive junction area by passing through the connecting point between the two adjacent nanowires. As a result, the current concentrates in the corner of the wire and the influence of the junction resistivity becomes insignificant. Therefore, assigning high resistivity value to the junctions was not relevant and suitable enough for modeling properly the influence of the junction efficiency on the network resistance.

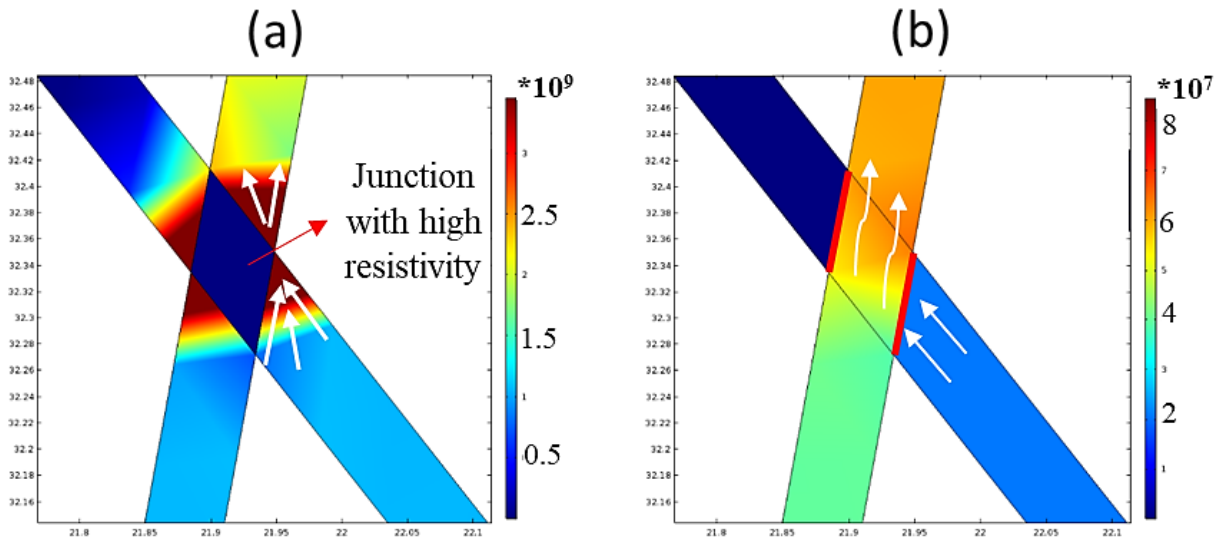


Figure 36. Comsol simulation results showing the local current density [$A m^{-2}$] near a NW-NW junction: a) when the common part (junction) between nanowires is set (numerical input) much more resistive than the nanowires, b) when both the nanowires and the common parts between them (junctions) are set to have the same resistivity but have resistive boundaries between them. “Contact impedance” (see red boundaries) is numerically assigned to 2 over the 4 junction boundaries in the Comsol model, as explained in next paragraph. The white arrows represent the direction of current.

By examining carefully the TEM images of perfectly sintered junctions (see **Figure 37a-b**), it can be noticed that the optimized junction is well crystallized while two parallel grain boundaries are systematically present. The occurrence of a perfectly well crystallized junction and two face-to-face grain boundaries has also been observed by Garnett et al.^[83] These observations indicate that the junction areas should in fact have a similar resistivity value as the nanowires. On the contrary, the grain boundaries will scatter the electrons and therefore, lead to a decrease of the current flow. Thus, it was decided to simulate the junction resistance by attributing an electrical contact impedance boundary condition to the junction boundaries. In the simulation model, two parallel borders are randomly chosen for each junction and assigned the contact impedance condition discussed above, as shown in Figure 36b and Figure 37c. The resistivity of the junction area is kept equal to the one of the nanowires for the sake of simplicity. In the case of “combined junctions”, i.e. when they intercept more than 2 wires, half of the junction boundaries are arbitrary assigned to the contact impedance condition discussed above while all the others are considered as perfect (no grain boundaries).

Bellew et al. recently succeeded in measuring the electrical resistance individual AgNW junctions R_j and they found the average value to be 11Ω for the “optimized junctions” (perfectly sintered), and 680Ω for the “activated junctions” (the nanowires are in close contact but the junctions are not perfectly sintered).^[202] Based on these experimental values, we implemented in our Comsol model the contact impedance (Z_c) of the junctions as follows:

$$R_j \approx R_{GB} = \frac{Z_c}{S_{GB}} \quad (3.4)$$

With R_j the measured junction resistance, R_{GB} the resistance of the grain boundary and S_{GB} the surface of the grain boundary, assimilated to the cross section of silver nanowires. Numerical application with $D_{NW} = 60 \text{ nm}$ yields contact impedance values Z_c equal to $3.96 \times 10^{-14} \Omega \cdot \text{m}^2$ for the “optimized” junctions and $2.38 \times 10^{-12} \Omega \cdot \text{m}^2$ for the “activated” ones. Using this contact impedance condition, the concentration of electrical current in the junction’s corner is relieved, leading to a much more homogeneous local current distribution (see Figure 36b). Moreover, the impact of the junction efficiency on the network electrical performances was found much more significant (see section 4.2.2).

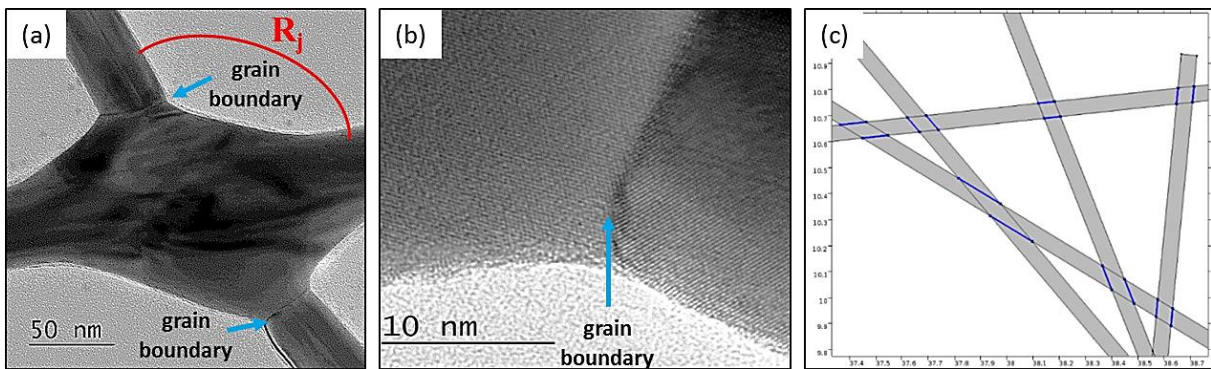


Figure 37. a) TEM image of an AgNW junction after annealing at 180°C for one hour. b) Zoom in the boundary of the junction depicted in (a). c) The random selection of junction boundaries (in blue).

3.3.4. Boundary conditions for thermal simulations

Simulating the thermal properties of AgNWs requires to input specific boundary conditions to the system so that the three main thermal losses mechanisms (conduction, convection and radiation losses) are appropriately implemented in the model. In this particular case, convection with air and radiation phenomena take place in all the outer faces of the geometry, while the boundary conditions related to the conduction losses phenomenon are restricted to the contact surface between the network and the substrate. In the simulation model, all these three mechanisms are taken into consideration except the conduction losses contribution due to the physical contact between the system and its environment (external circuit). The ambient temperature at which convection and radiation take place is set to be 293 K.

The influence of convective losses was recently estimated in the team thanks to the combination of experimental and modeling approaches. Considering the Joule heating in an AgNW network, the energy balance in the system {AgNW network, substrate} can be described as follows (conduction losses to external parts of the system are neglected):^[16,31]

$$I^2R = (m_1C_1 + m_2C_2) \frac{dT(t)}{dt} + A(h_1 + h_2)(T(t) - T_0) + \sigma A(\varepsilon_1 + \varepsilon_2)(T(t)^4 - T_0^4) \quad (3.5)$$

Where I is the electrical current in the network, m is the mass, C is the specific heat capacity, $T(t)$ is the instantaneous temperature, T_0 is the ambient temperature, h is the convective heat-transfer coefficient, A is the area of the film, σ is the Stefan-Boltzmann constant and ε is the emissivity. The indexes 1 and 2 refer to the network and substrate, respectively.

Equation 3.5 indicates that the heat generated by the Joule effect (the left term) is dissipated through the temperature elevation in the network and the substrate (the first term on the right), the heat losses by convection (the second term) and radiation (the third term). Lagrange et al. experimentally estimated the value h_1+h_2 to be $4.3 \text{ W.m}^{-2}.\text{K}^{-1}$.^[24] Such a value is the one implemented to the model for taking the convection losses into account. Regarding the emissivity (radiation losses), the value associated to the PEN substrate is very high, in the order of about 0.7 (value implemented to the model). To our knowledge, the emissivity of AgNWs has not been experimentally measured yet. Given that the emissivity of polished bulk silver varies between 0.01 and 0.02, the latter (0.02) is the value chosen for the AgNWs in the simulation. We believe that the order of magnitude should be appropriate even though this value might be a little bit either under or overestimated.

Regarding the conduction losses, the interface between the nanowires and the substrate introduces some perturbation of the heat transfer: a temperature drop is likely to be observed at the contact interface due to the not perfect adhesion of the wires to the substrate and to the discontinuity of the thermal conductivity. For this purpose, a thermal contact resistance ($R^{thermal}$) was introduced in the model at the interface between the nanowires and the substrate. Thermal contact resistance is defined as the ratio between this temperature drop and the average heat flow across the interface. The inverse parameter is named thermal contact conductance. It is the one required by Comsol in the simulation model.

The formula to calculate the thermal resistance associated to a flat-cylindrical contact surface with a certain surface area is deduced from Mcgee et al:^[203]

$$R^{thermal} = \frac{1}{2w\pi k_F} \ln\left(\frac{D}{\pi b}\right) \quad (3.6)$$

Where $2w$ is the contact length, D is the diameter of the cylinder, $2b$ is the contact width and k_F is the thermal conductivity of the flat surface. The contact geometry is shown in **Figure 38**, thereafter.

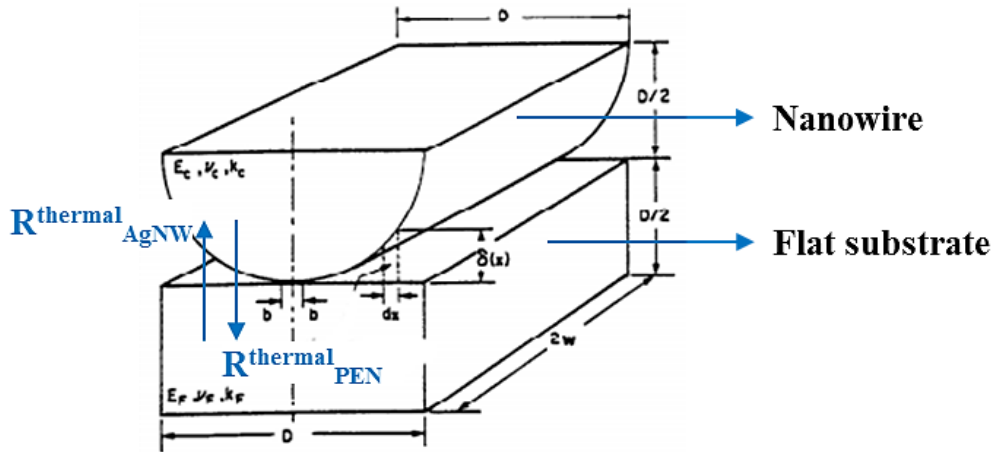


Figure 38. Schematic representation of a cylinder-flat contact geometry mimicking the contact surface between one single nanowire and the PEN substrate.^[203]

Theoretically, $R^{thermal}_{PEN}$ and $R^{thermal}_{AgNWs}$ should be both taken into account and summed together for estimating the total thermal contact resistance of the structure. However, as $k_f^{AgNWs} \gg k_f^{PEN}$, $R^{thermal}_{AgNWs}$ is neglected in the calculation. Moreover, the surface contact (“ $2b$ ”) between a single nanowire and the PEN is difficult to estimate. Since it has been proved that the silver nanowires have a pentagonal cross section,^[204] then for the sake of simplification, all the nanowires are considered as flatly deposited on one side of the pentagon, leading to perfectly flat-flat contact surface between the nanowires and the PEN substrate.

In the particular case where $L_{NW} = 10 \mu\text{m}$ and $D_{NW} = 60 \text{ nm}$, w is $5 \mu\text{m}$ (half of the AgNW length), D_{NW} is 60 nm (AgNW diameter), b is $0.294 \times D_{NW}$ (half of one side of the pentagonal AgNWs) and k_{PEN} is $0.15 \text{ W.K}^{-1}.\text{m}^{-1}$. Therefore, the calculated value for $R^{thermal}_{PEN}$ is 16873 K.W^{-1} . At last, the constriction conductance h_c (parameter input in the Comsol model) can be derived from:

$$h_c = \frac{1}{A * R^{thermal}} \quad (3.7)$$

With A the surface of the contact area. The calculated value of h_c is $1.68 \times 10^8 \text{ W m}^2 \text{ K}^{-1}$. All the boundary conditions used in the thermal simulation such as the electrical contact impedance, the radiation losses, the convection losses, and the constriction conductance, are summarized in **Table 2**, thereafter.

Table 2. List of the electrical and thermal parameters implemented into the simulation model, in the particular case where $L_{NW} = 10 \mu\text{m}$ and $D_{NW} = 60 \text{ nm}$.

	Electrical contact impedance		Surface emissivity		Heat transfer coefficient	Constriction conductance
	Optimized junction	Activated junction	ϵ			
Entities	Two parallel borders		PEN	AgNWs	All outer faces	Interface between AgNWs and PEN
Value	$3.96 \times 10^{-14} \Omega \text{ m}^2$	$2.4 \times 10^{-12} \Omega \text{ m}^2$	0.7	0.02	$4.3 \text{ W m}^{-2} \text{ K}^{-1}$	$1.68 \times 10^8 \text{ W m}^{-2} \text{ K}^{-1}$

3.3.5. Geometrical meshing of the specimen

The finite element method (FEM) is a numerical strategy used to compute approximate solutions to boundary value problems for partial differential equations. It subdivides the entities of interest into many smaller parts, called as finite elements or meshing. The equations are solved for these small elements and the solutions are then assembled together, giving the global solutions for the whole entities. The method has several advantages such as: good adaptation to complex geometry, ability to deal with discontinuous material properties and capture of local effects.^[204] As building block of the calculation method, the meshing quality has a critical impact on the accuracy of resulting solutions. Generally speaking, the smaller the element size, the more precise the solutions, but the longer it takes to solve the model at the same time. **Figure 39a** shows how the integrated current density at a certain network location changes as the element size becomes smaller.

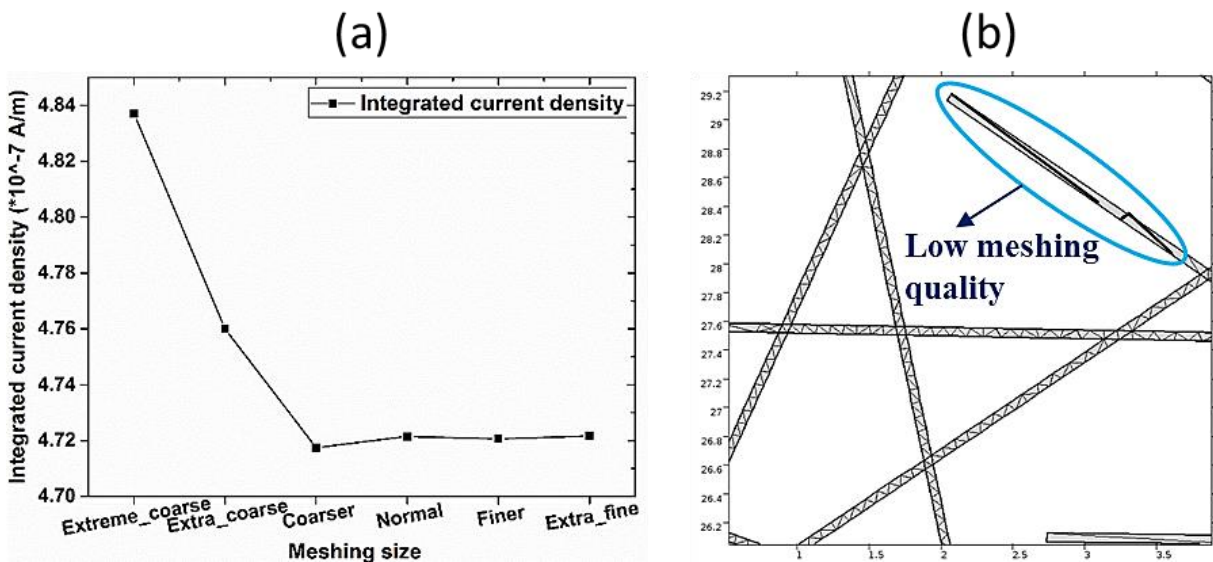


Figure 39. a) Calculation of the integrated current density in a selected AgNW network area as a function of the selected meshing element size. The maximum element size (in μm) for different meshing (extreme coarse, extra coarse, coarse, normal, finer, extra fine) is 16.6, 10, 6.5, 3.4, 1.9, and 1, respectively. b) Example of meshing elements with low quality.

As already illustrated in section 1.1.3, the NW-NW junctions have a strong impact on the network properties. To improve the accuracy of the model, it is then necessary to have a finer meshing at the junction areas, as shown in **Figure 40a**. In the 3D model, non-uniform meshing of the substrate can save a lot of computing resource due to its large volume. The volume near its top face should have a small finite element size since it reveals how the heat is transferred from the network to the substrate. On the other hand, the meshing can be coarser in the remaining volume of the substrate because the temperature there is quite homogeneous in the xy plane and its gradient along z axis is within $0.2 \text{ }^\circ\text{C } \mu\text{m}^{-1}$. Figure 40b is a typical example of how the meshing of the 3D architecture is set to be non-uniform, as a way to save calculation time without affecting the accuracy of the results.

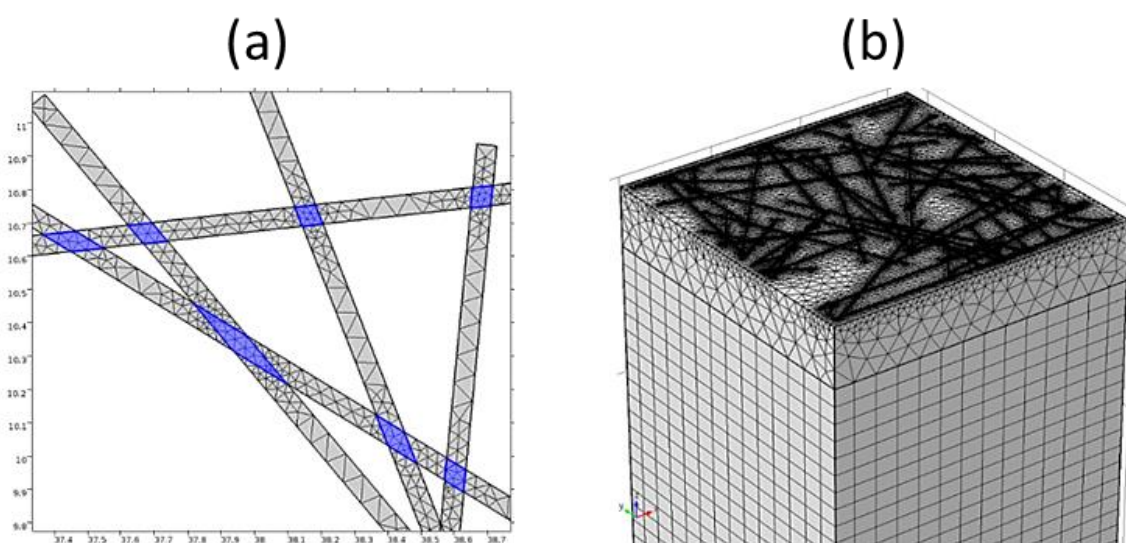


Figure 40. a) Interconnected AgNWs in Comsol model showing a smaller meshing element size at the junction areas. b) Meshing of the entire system (substrate, AgNWs) showing the finite element size non-uniform distribution in the substrate. The network size is $15 \times 15 \text{ } \mu\text{m}^2$, while the substrate's is $25 \times 15 \times 15 \text{ } \mu\text{m}^3$.

3.3.6. Calculation of the network resistance

The calculation of the network resistance (2-probe resistance between the two silver paste electrodes) is of major interest since this is one of the most significant parameter to characterize the electrical properties of AgNW networks. The process to extract this value is described as follows. When solving the model, Comsol can provide not only the current density in each location, but also the current density integrated along any specific cutline. When choosing a cutline that cross the entire network of width W (see **Figure 41**), the integrated current density j_{Σ} , calculated by Comsol, can be defined as $j_{\Sigma} = \int_0^W j * dx$. The value of j_{Σ} provided by Comsol is expressed in A m^{-1} instead of A m^{-2} , since the simulated AgNW network are described in 2D. The nanowires indeed consists of 2D rectangles with D_{NW} as the rectangle width.

As a consequence, the electrical current $I_{network}$ flowing the network, when switching from a 3D to a 2D problem can be expressed as described in Equation 3.8 thereafter:

$$\begin{aligned}
 I_{network} &\stackrel{3D}{\Leftrightarrow} \sum_1^N I_{NW} = \sum_1^N \left(\iint_{S_{NW}} j * dS \right) = \int_0^{D_{NW}} \int_0^W j(x, z) dx dz \\
 I_{network} &\stackrel{2D}{\Leftrightarrow} D_{NW} * \int_0^W j(x) dx \\
 I_{network} &= j_{\Sigma} * D_{NW}
 \end{aligned} \tag{3.8}$$

Where N is the number of wires intercepted by the cutline, I_{NW} is the intensity in each individual nanowires, j the local current density, W the width of the network, and S_{NW} the surface area of each cross section between the NWs and the cutline. S_{NW} equals $D_{NW} \times D_{NW}$ and is assumed to be the same for all nanowires (S_{NW} has no sense in 2D).

If the cutline intercepts the entire width of the network, the resulting j_{Σ} value provided by Comsol should theoretically be exactly the same whatever the location of the selected cutline. However slight differences can sometimes be noticed due to statistical fluctuations. As a consequence, calculation of j_{Σ} is performed on 6 different cutlines “ y_i ” ($i=1..6$), in different network locations, as described in Figure 41.

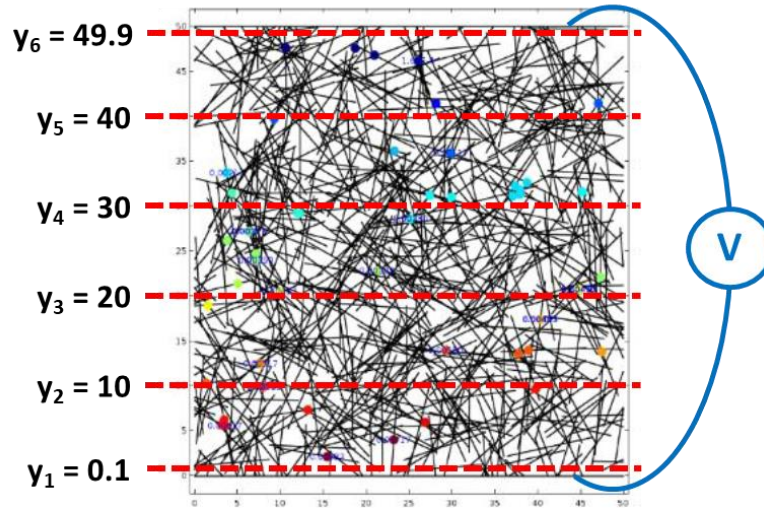


Figure 41. Simulated AgNW network in Comsol showing the cut lines (y_i , $i=1..6$) along which the current density is integrated (j_{Σ}). The y_i values are given in μm .

By multiplying the resulting mean value of j_{Σ} with the NW diameter (See Equation 3.8), the electrical current value can be deduced with a good approximation. So does the electrical resistance of the network. **Table 3** shows such calculation process for the specific case were $L_{NW} = 10 \mu m$, $D_{NW} = 60 nm$, $n = 5 n_c$, and when all the junctions are set as “optimized”.

Table 3. The calculation of the equivalent resistance for the specific case were $L_{NW} = 10 \mu\text{m}$, $D_{NW} = 60 \text{ nm}$, $n = 5 n_c$, and all the junctions are set as “optimized”.

Cutline location (μm)	j_{Σ} (A/m)	Ave(j_{Σ})	Std(j_{Σ})	I_{network} (A)	R_{network} (Ω)
y=0.1	13458	15962	1529	9.6×10^{-4}	10
y=10	17660				
y=20	17235				
y=30	15543				

3.3.7. Comsol-based simulations: positive and negative aspects

This work constitutes the first attempt to simulate the AgNW networks physical properties (electrical, thermal) using the FEM numerical method. To our knowledge, no other FEM based study has been reported so far in the literature dealing with AgNW networks. The models developed during this thesis were helpful for trying to make correlations with experimental results (see section 4.2). However they also have some drawbacks. The next paragraphs discuss the positive and negative aspects that are worth to be aware of when discussing results about Comsol-based AgNW network simulations.

(i) Electrical simulations

The simulation model developed using Comsol revealed to be quite powerful for generating electrical maps (more results will be presented in sections 4.2.1 and 4.2.2). Besides, the physical parameters extracted from the model have proved to be coherent with real-life measurements in many cases. As a first example here, **Figure 42a** reports the calculated resistance a simulated AgNW network (systemsize: $50 \times 50 \mu\text{m}^2$, $L_{NW} = 10 \mu\text{m}$, $D_{NW} = 60 \text{ nm}$), as a function of the areal mass density (amd), for the three level of junction optimization (“activated”, “half-optimized”, “optimized”). For the sake of comparison, experimental measurements performed by Lagrange et al. are also presented thereafter (see Figure 42b).

Even though the NW dimensions of simulated and experimental networks are not strictly the same, it can be noticed than the calculated resistance of the optimized simulated networks at $amd = 50 \text{ mg m}^{-2}$ is the same order of magnitude ($\approx 10 \Omega$) than the experimental one depicted in Figure 42b. As a consequence, the resistance values calculated from the model are compatible with values extracted from real life measurements performed on AgNWs. The model can then be considered as reliable here.

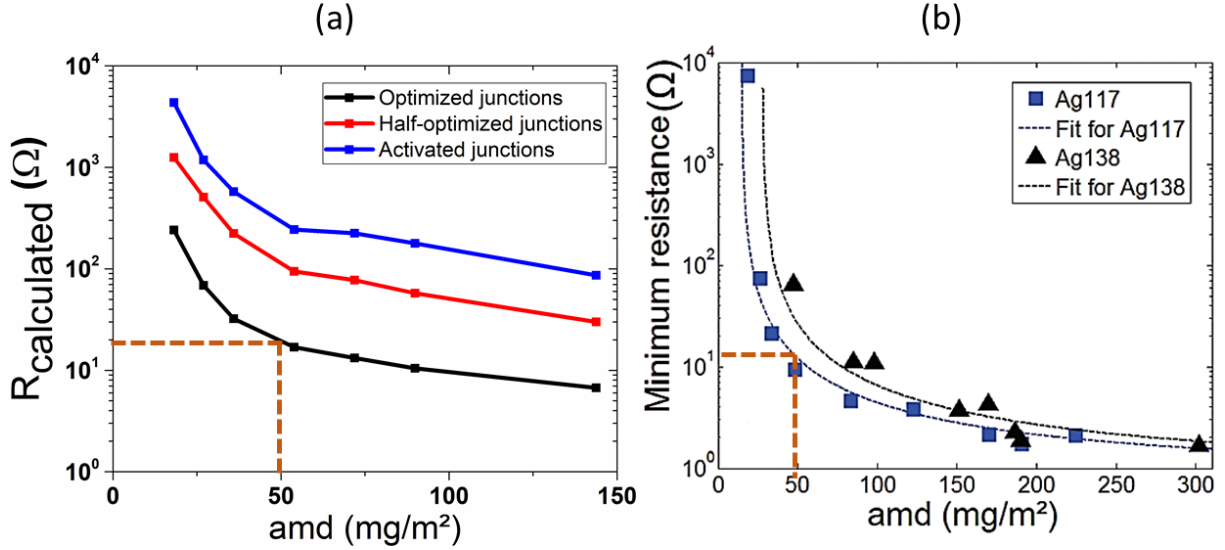


Figure 42. a) Calculated electrical resistance of a simulated AgNW network (system size: $50 \times 50 \mu\text{m}^2$, $L_{\text{NW}} = 10 \mu\text{m}$, $D_{\text{NW}} = 60 \text{ nm}$), as a function of the areal mass density, for three different levels of junction optimization (“activated”, “half-optimized”, “optimized”). b) Minimum experimental electrical resistance values achieved during a $2 \text{ }^\circ\text{C min}^{-1}$ ramp annealing of AgNW networks fabricated with nanowires of different dimensions (either $D_{\text{NW}} = 117 \text{ nm}$ and $L_{\text{NW}} = 43 \mu\text{m}$; or $D_{\text{NW}} = 138 \text{ nm}$ and $L_{\text{NW}} = 32 \mu\text{m}$), and with different areal mass densities.^[50]

In order to confront our model to the percolation theory at low density, $\log(R_{\text{calculated}})$ was plotted against $\log\left(\frac{n}{n_c} - 1\right)$ (see **Figure 43**). According to Equation 1.2 and the percolation theory, in the percolating regime, the conductivity and resistance of the network are indeed linked to the network density as follows:^[195]

$$\sigma \propto (n - n_c)^{4/3} \xrightarrow{\text{yields}} \rho \propto (n - n_c)^{-4/3} \xrightarrow{\text{yields}} R \propto (n - n_c)^{-4/3} \quad (3.9)$$

Therefore:

$$\log(R) = \text{cste} - \frac{4}{3} * \log\left(\frac{n}{n_c} - 1\right) \quad (3.10)$$

The results depicted in Figure 43 were linearly fitted for low densities ($n < 4n_c$). Coefficient of determination R^2 for the fitting curves was found over 0.97. The slopes of the fitting curves were found to be -1.01, -1.21 and -1.14 for the “optimized”, “half optimized” and “activated” cases respectively, slightly higher than the expected one, - 1.33. Such deviation might come from the small system size considered in the model ($50 \times 50 \mu\text{m}^2$) compared to an infinite system, as supposed theoretically. In the present case, L_s/L_w equals 5. As already discussed, in these conditions, the percolation threshold is almost no influenced anymore by the system size (see Figure 31, section 3.3.1). However, the overall electrical properties might still be under the influence of the size of the simulated networks. Moreover, the distribution of contact resistance at the NW junctions is set to be isotropic in the “activated” and “optimized” cases. Statistically, it is very probable that some of the junctions are not active in real networks even after optimization treatment (presence of defects, inhomogeneities, etc.). For low density and low

size networks, the presence of totally inactive junctions might substantially impact the overall network resistance. As a consequence, it has to be kept in mind that our model overestimates the electrical resistance of low density AgNW networks. A possible route to overpass this issue may consist of implementing contact resistance at the junctions according to a much wider value distribution.

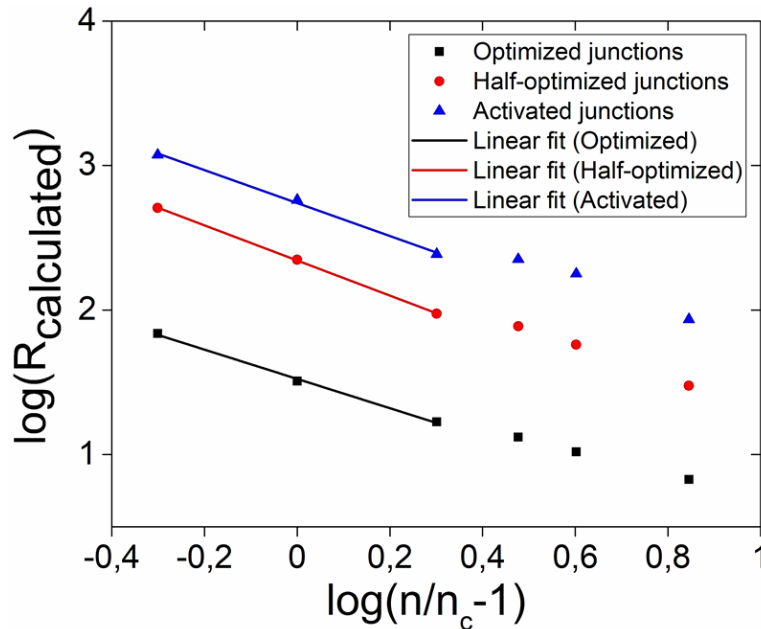


Figure 43. Logarithm of the calculated resistances depicted in Figure 42 (systemsize: $50 \times 50 \mu\text{m}^2$, $L_{\text{NW}} = 10 \mu\text{m}$, $D_{\text{NW}} = 60 \text{nm}$), as a function of the logarithm of “ $n/n_c - 1$ ” and for the three different levels of junction optimization (“activated”, “half-optimized”, “optimized”)

Finally, the main drawback of Comsol-based AgNW network simulations is the heaviness of the finite element method. The latter can indeed be very time-consuming, especially when the aspect ratio of the simulated entities is much higher than the meshing size. This is why the system size of the simulated networks was kept quite small so that the simulations can be performed in a reasonable time-slot. However, when trying to perform “dynamic” simulations of AgNW networks and tackle the instability issue under high current flow (see section 4.2.3), Comsol revealed not efficient enough because of its heaviness.

Another simulation model based on SPICE software is currently being constructed by Nicolas Charvin from the LMOPS team at LEPMI laboratory, with whom we are collaborating through the EARTH project funded by Labex CEMAM. When specifically focusing on the dynamic electrical behavior of AgNW networks at high voltage (i.e. close to electrical breakdown), ongoing work using this software might help performing simulations in a much faster and simple way (see **Figure 87**).

(ii) *Thermal simulations*

Preliminary simulation tests associated to AgNW network on PEN substrate were performed using the thermal model developed during this thesis (see examples in **Figure 44a-c**). However, due to the substantial time-consumption of Comsol when dealing with thermal simulation of AgNW networks, the system size was even more reduced to $15 \times 15 \mu\text{m}^2$. The applied voltage was set to be 3 mV in order to make the comparison with a real AgNW network of $2.5 \times 2.5 \text{ cm}^2$ subjected to an applied voltage of 5 V (see Equation 3.3). In the present case, the NW dimensions are the same in the three samples generated ($D_{\text{NW}} = 60 \text{ nm}$, $L_{\text{NW}} = 10 \mu\text{m}$), and the junction efficiency is set to correspond to the “optimized case”. The network density is the only varying parameter. The latter is set to be equal to $1.5 n_c$ (a), $3 n_c$ (b), and $4 n_c$ (c), respectively.

First of all, a higher temperature is calculated in the case of the densest network (c). The corresponding temperature of the substrate is calculated to be close to 57°C , whereas it is only 52°C and 29°C , respectively, for the lower network density. This is coherent with the simulation parameters. However, according to the relatively low density of simulated networks, the calculated temperatures are found higher than expected. This might originate from the fact that the lateral faces are thermally isolated, which is not the case for real networks. Moreover, in reality there are also much more losses due to the conduction losses contribution with the external part of the network (contact probes, temperature detector underneath the samples, etc.). The latter are not taken into account in the simulation model. Hence, in the simulation case, the heat that remains in the network and the substrate might be overestimated. As a consequence, the thermal model developed during this thesis provides interesting information but cannot be considered as realistic enough yet. Efforts have to be devoted to improve the description of losses mechanisms, especially with external part of the circuit and at the lateral faces of the substrate, as well as increasing the size of simulated systems. This should result in more realistic temperature distributions.

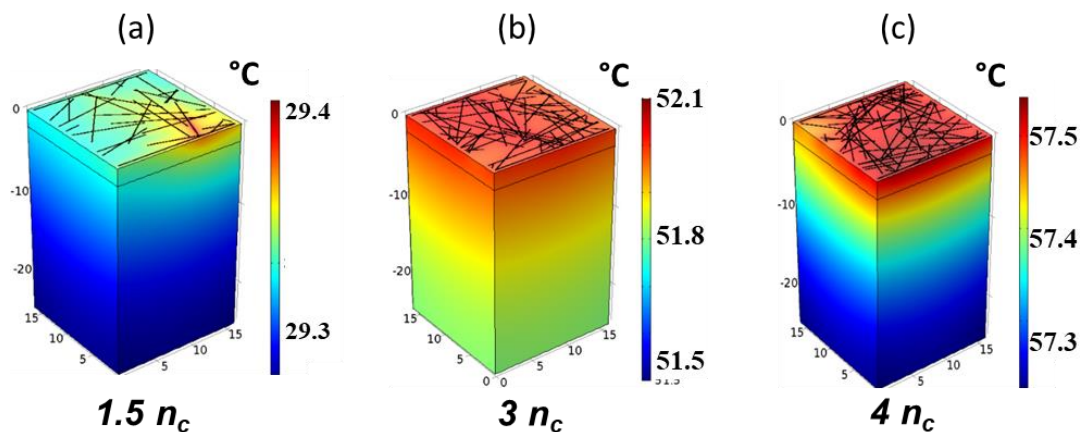


Figure 44. Comsol simulations showing the steady-state temperature distribution ($^\circ\text{C}$) through AgNWs and PEN substrate for three network densities: $1.5 n_c$ (a), $3 n_c$ (b), and $4 n_c$ (c).

Chapter 4. Electrical distribution in AgNW Networks

The present chapter discusses the physical parameters likely to influence the electrical distribution in AgNW networks. Unlike metal oxide-based transparent electrodes, AgNW-based electrodes consist of non-homogeneous material. Hence, electrical current may not flow identically in all network locations, leading to potential local failure, hot spots, or “inactive” areas across the network. From an applicative point of view, it is then mandatory to get information about the mechanisms impacting the electrical distribution, in order to increase the overall efficiency and reliability of resulting AgNW-based devices.

Section 4.1 deals with the onset of electrical percolation in low density networks when either thermal/electrical annealing is performed. Much of the content developed in this first section and dealing with the phenomenon of “geometrical quantized percolation” appeared as a research article in Nano Letters journal,^[205] through a collaboration between LMGP, CEA-Liten, CEA-Leti (Stéphane Moreau), and Liege University (Ngoc Duy Nguyen).

Section 4.2 explores the physical parameters likely to influence substantially the electrical distribution in AgNW networks, such as the network density or the conduction level of the junctions. Several electrical and thermal mapping techniques are combined together to provide visual evidence, while simulation techniques previously introduced in Chapter 3 are used to make correlation with experimental results. Section 4.2 also provides recent results about the optimization and failure dynamics of AgNW networks under electrical stress, which also give rise to substantial modifications of the electrical distribution. All the work reported in section 4.2 was conducted in collaboration with LMGP, CEA-Liten, and LEPMI (Nicolas Charvin, Lionel Flandin).

4.1. The case of low density networks: geometrical quantized percolation

4.1.1. Introduction to geometrical quantized percolation phenomenon

This section highlights the discontinuous activation of efficient percolating pathways (EPPs) for AgNW networks having densities slightly above the percolation threshold. Such networks exhibit abrupt drops of electrical resistance when thermal or electrical annealing is performed, giving rise to a “geometrically quantized percolation”. The conductive nature of these networks depends on two main factors. First, the networks have to be “physically” percolating, i.e. they have to contain at least one “physical” pathway between two opposite sides of the sample. Second, the percolating pathways have to be electrically “efficient”. As already mentioned in section 1.1.3, the junctions between neighboring nanowires often remain resistive after deposition due to the presence of a resistive polymer shell (polyvinylpyrrolidone, PVP) surrounding the nanowires as well as the very small contacts area between AgNWs. Physico-chemical treatments can be performed to reduce the electrical resistance of these junctions so that the physical percolating pathways get “activated”.^[42,54,83,206] One of these is thermal

annealing at low temperatures. **Figure 45a-c** shows TEM images of three typical junctions, as-deposited (a), and after thermal annealing at 180 °C for one hour (b,c). Thermal annealing results in the desorption of organic residues, which at first prevent neighboring nanowires from being in intimate contact with each other, and leads, in a second step, to local sintering at the junctions, which become increasingly efficient.^[109,207] Statistically, the shape of the resulting junctions indicates that the latter can be considered as “activated” (Figure 45b) or even “optimized” (Figure 45c) when the sintering has been completed.^[42,78]

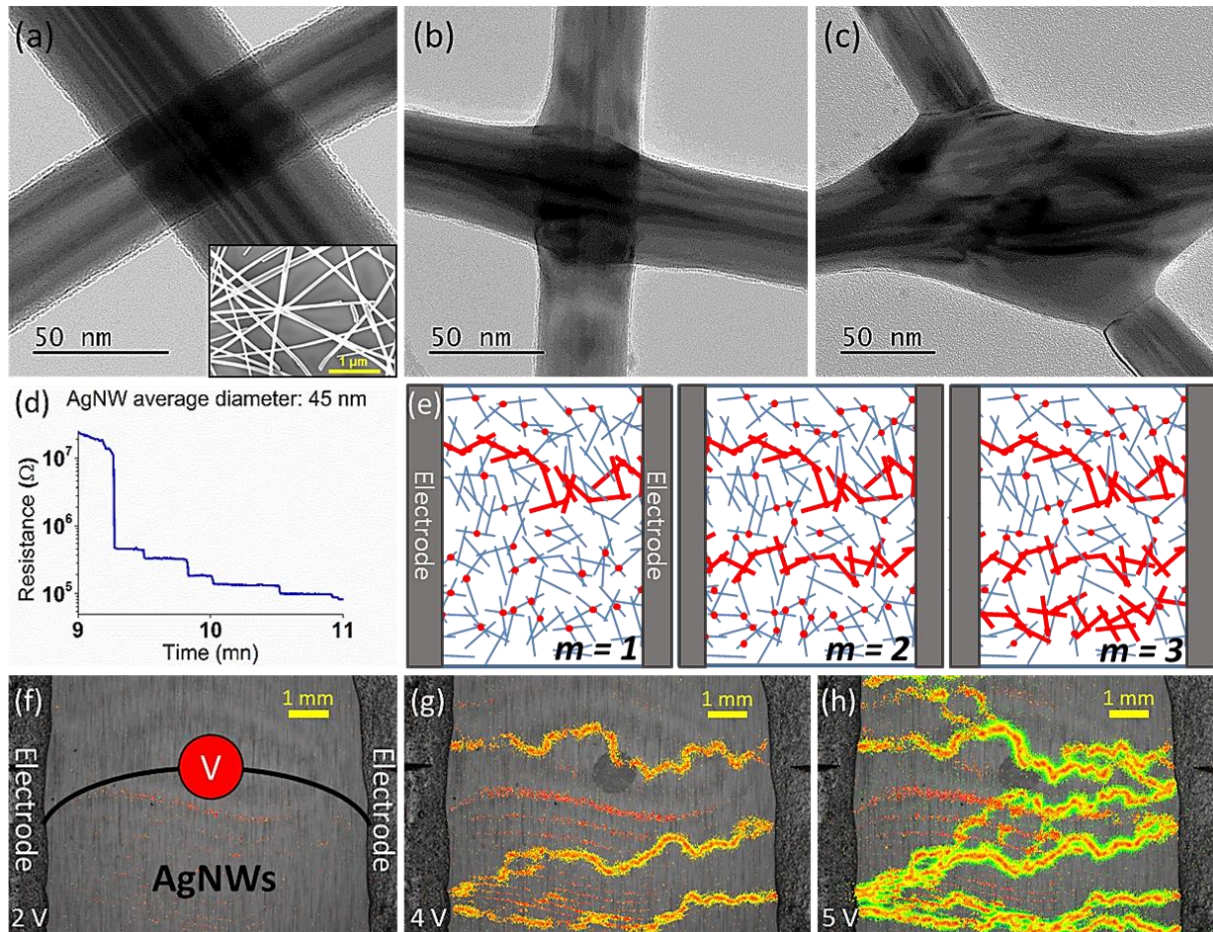


Figure 45. a) TEM image of an as-deposited junction. Insert is a SEM image of an AgNW network. b-c) TEM images of annealed junctions at 180 °C for 1h. The junction can be considered as “active” (b) or even optimized (c). d) Electrical resistance curve obtained for AgNW percolating networks with an average diameter of 45 nm while thermal annealing is performed (here the temperature was increased from 20 to 100 °C in 10 min and then maintained at 100 °C for one hour). e) Schematic representation of the activation of efficient percolating pathways (EPPs) via thermal annealing. Thermally activated junctions are drawn in red. f-h) Thermal Lock-in images of an AgNW network close to the percolation threshold and subjected to electric annealing: at 2 V (f), no EPPs can be detected. At 4 V (g), 3 individuals EPPs are clearly visible. At 5 V (h), 5 individual EPPs can be detected as well as interactions between them. Note that the red fringes appearing at the lower-left part of images f-h are frequency-independent artifacts due the non-perfect planarity of the sample during the acquisition, which is caused by the pressure of the probes on the flexible substrate as well as the vacuum suction system (dark circle in the center of g-h images) used to fix the samples.

Prior to this thesis work, the phenomenon of quantized percolation for networks whose density is slightly above the percolation threshold had already been reported by D.P. Langley et al. at LMGP.^[42] In such networks, the electrical resistance decreases by well determined single steps when subjected to a thermal/electric annealing (Figure 45d). In this previous work,^[42] a simple model was introduced to account for the quantized percolation phenomenon observed, in which each resistance drop would correspond to the activation of an EPP (see Figure 45e).

From a fundamental point of view, geometrical quantized percolation can be compared to quantized conduction phenomenon in 1D-ballistic conductors which was observed for the first time more than 25 years ago.^[208,209] The latter was studied because potential applications could result from the switching behavior that occurs when a device is moving between the different quantized conduction levels.^[210] Indeed, when charge carriers are confined in small constrictions, the conductance appears as a stepwise function of contact size and is a multiple of the quantum unit of conductance $G_0 = \frac{2e^2}{h}$. This result was first established by Landauer^[211] and has been experimentally demonstrated several times thereafter.^[212,213] Given that the Fermi wavelength is very short in metallic compounds (about 0.5 nm for silver), quantized conduction can only be observed in atomic-scale structures. In the case of AgNW networks, geometrically quantized percolation does not require quantum confinement conditions to be observed. It takes place at the scale of an entire AgNW network (several millimeters).

While the model gives satisfactory fittings, an experimental demonstration of the formation of such individual active pathways was not yet provided before the present thesis. Within the frame of the latter, Lock-in Thermography (LiT) has been used to visualize *in situ* the formation of active pathways for the first time and with a pertinent spatial resolution (Figure 45f-h). In a more general way, such technique can be used to map the heat generated locally by Joule effect across the network, revealing how electric current is distributed through the percolating pathways. LiT can be compared to the thermo-reflectance (TR) imaging technique which was also recently proved efficient for detecting hotspots in percolating nanocomposites.^[214] In this section, the effect of electrode geometry and the nanowire dimensions on the geometrical quantized percolation phenomenon is also evaluated. Finally, it is also demonstrated for the first time that the breakdown of the networks can also happen in a quantized manner.

4.1.2. Analysis of quantized percolation using lock-in thermography

4.1.2.1. Lock-in thermography technique

To validate the occurrence of geometrical quantized percolation in the onset of electrical percolation, lock-in thermography (LiT) measurements of AgNW networks close to the percolation threshold were performed. For this purpose, silver nanowires synthesized at CEA-Liten with an average diameter and length of 60 nm and 10 μm , respectively, were dispersed in methanol solution and deposited by spray-coating on $12 \times 10 \text{ mm}^2$ and 125 μm thick polyethylene naphthalate (PEN) substrates (Teijin DuPont Films - Teonex Q65HA).

The density of these spray-deposited AgNW networks was intentionally adjusted to just above the percolation threshold density n_c . Electrical resistance of the as-deposited samples was several mega-ohms ($M\Omega$), as measured by the two-point probe system. Silver paste-based contacts were manually deposited at opposite sides of the specimen. Electrical connection with the LiT set-up was ensured by two voltage probes in contact with the silver paste electrodes. The activation of the EPPs was driven by electrical annealing induced by the voltage application during the LiT experiments.

Several AgNW networks were analyzed in a thermal emission microscope (THEMOS-1000 from Hamamatsu). Such a thermal microscope can achieve high resolution thanks to an InSb camera with 640×512 pixels (pixel size: $15 \mu\text{m}$), and high sensitivity in the 3 to $5 \mu\text{m}$ wavelength region with a noise equivalent temperature difference (NETD) of 20 mK. Moreover, thermal “lock-in” measurement is used to drastically reduce the noise by synchronizing the image capture and the timing of power supply to the network (see **Figure 46**).

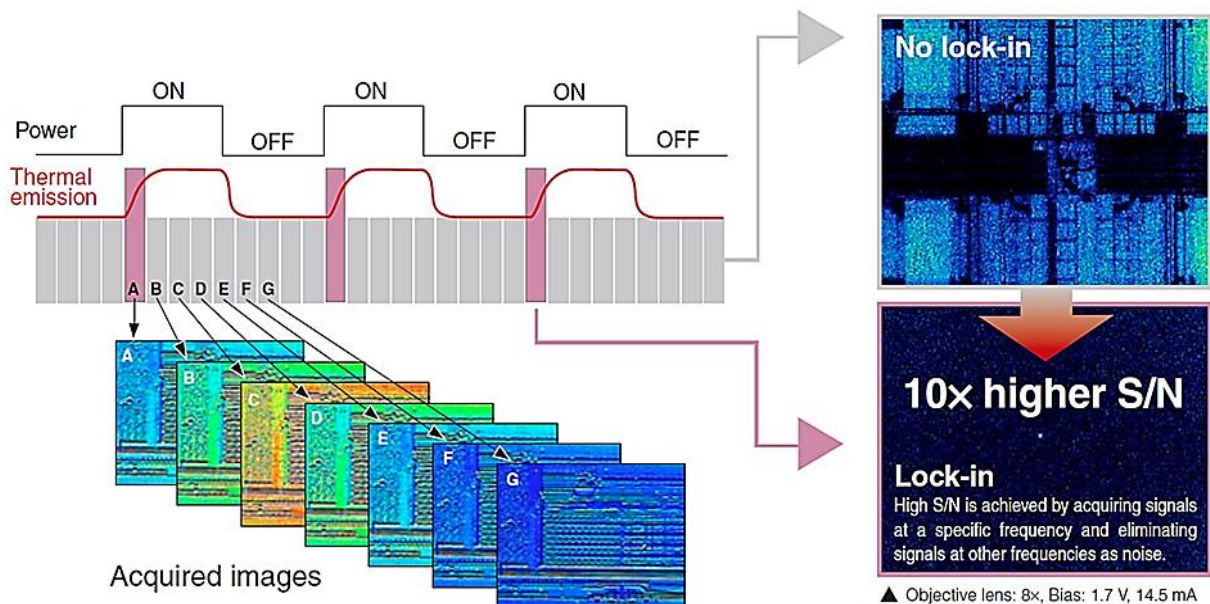


Figure 46. Working principle of Lock-In thermography. Courtesy of Hamamatsu Photonics K.K.

LiT is mostly dedicated to the detection of hot spots and failures in microelectronic devices.^[215,216] However, it was found to be very adapted to detect individual “illuminated” pathways associated to geometrical quantized percolation studied here. For each LiT image reported in this letter, the microscope objective magnification is $0.8\times$ (field of view: $12 \times 9.6 \text{ mm}^2$) and the signal frequency is 10 Hz, which means that the network was subjected to “On-Off” voltage cycles with a frequency of 10 Hz (square signal, duty cycle: 0.5). Here, the final images are captured after a constant acquisition time of 5 min and show the sum of all the photons, in the $\sim 3.7\text{-}5.2 \mu\text{m}$ wavelength range, collected during that period.

Such a thermal microscope can provide both amplitude (IR emission intensity map) and phase (heat timing map) information. More specifically, phase signals originate from the heat propagation process through the device, inducing a phase shift between electrical excitation and the detected IR response.^[216] Contrary to classic infrared thermography, no thermal calibration is available when using the LiT feature. As a consequence, the LiT images provided in this study do not include any numerical scale and physical unit.

In the case of amplitude images, the color scale represents the amount of IR photons collected during the entire LiT acquisition. In the case of phase images, the color scale quantifies the local phase shift between the different entities within the network, revealing which conductive clusters are emitting the faster. A low phase shift indicates a heat sources whereas a large phase shift indicates diffused heat (see **Figure 47**). The comparability across the different experiments is ensured by the fact that the color scale used is the same in each of the reported images. Further details on the LiT technique can be found in reference.^[215]

In this section, we mainly focus on phase images since we find that they reveal the discontinuous onset of activation in a clearer way, within a short acquisition time. Moreover, they are not affected by the local emissivity.

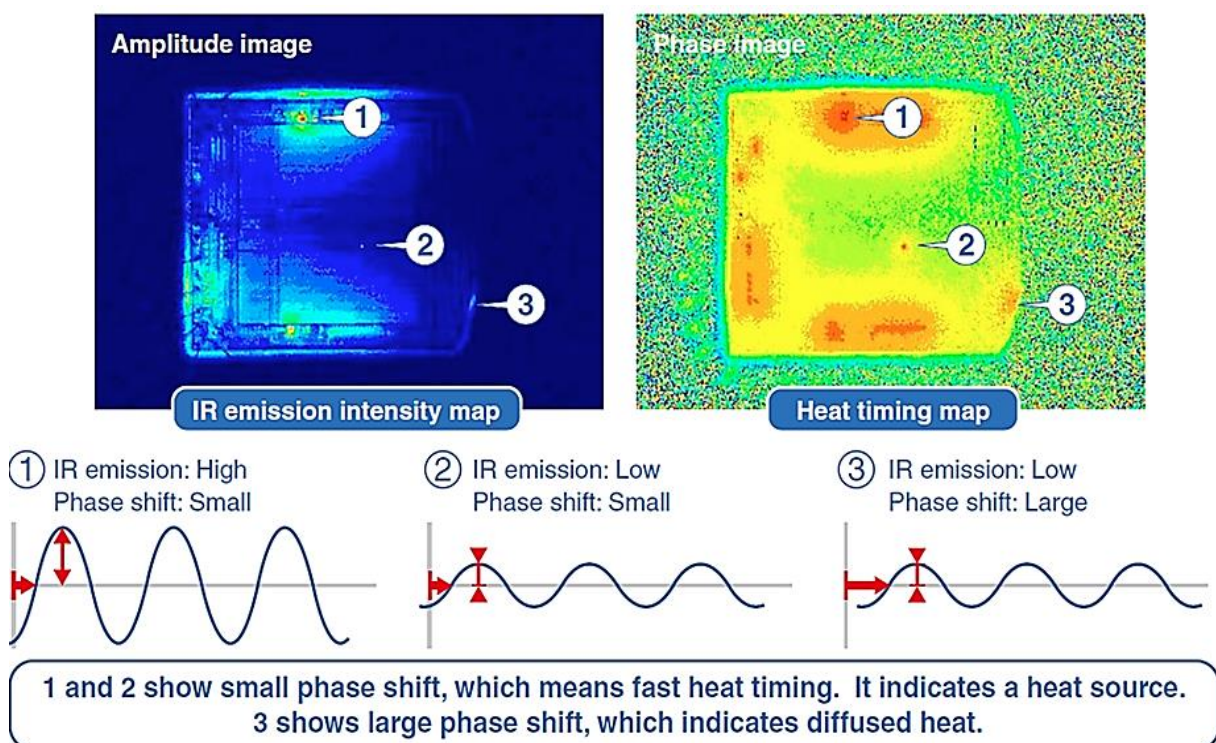


Figure 47. Meaning of the Lock-In phase imaging technique. Courtesy of Hamamatsu Photonics K.K.

4.1.2.2. Experimental results

4.1.2.2.1. Activation and detection of efficient percolating pathways (EPPs)

Thermal “lock-in” phase images of one dedicated sample subjected to different voltages ranging from 2 to 30 V are shown in **Figure 48A**. The onset of electrical activation is discontinuous. After 2 V, individual activated pathways can already be detected (see A2). After 4 V, at least 6 EPPs are highlighted and several ramifications can be detected between them (see A3) meaning that the EPPs start to interact with each other. Higher voltages (from 6 to 30 V) are then used in order to activate all the available efficient percolating pathways (see A4-A6).

Phase images associated to the same sample after switching the voltage down from 6 to 2 V (B1), and from 30 to 2 V (B2), respectively, are shown in Figure 48B. Even though the signal of the resulting images is significantly decreased, the electrical active skeleton remains the same. As a consequence, the onset of electrical percolation is a non-reversible phenomenon. Indeed, as depicted in TEM images of junctions in Figure 45a-c, the morphology of the network, especially in the vicinity of junctions, is non-reversibly modified when heated. In this series of experiments, the sintering of the junctions originates from the Joule heating induced by the bias during the LiT acquisition.

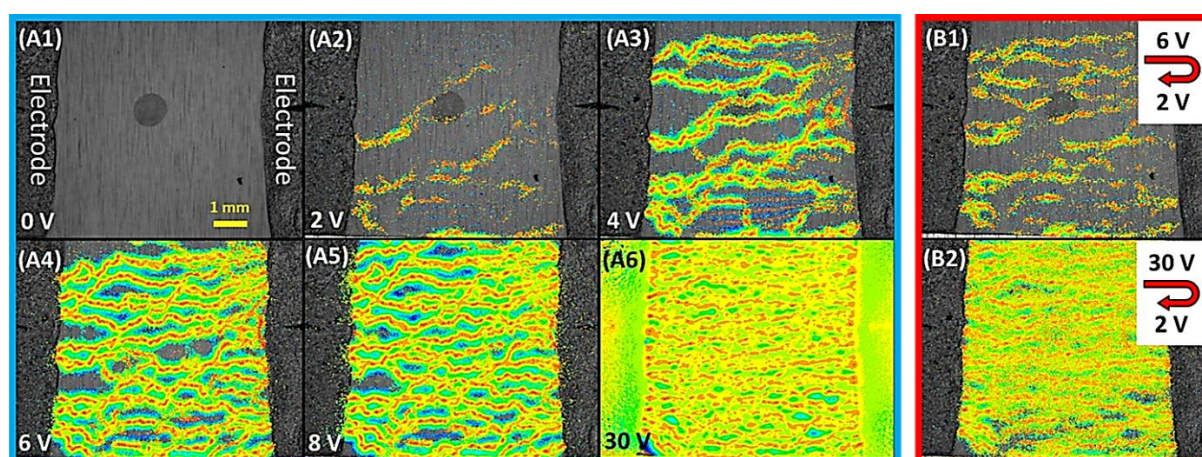


Figure 48. A1-A6) Thermal Lock-in images of a silver nanowire network close to the percolation threshold. Continuous On-Off (10 Hz) voltages were applied to the network during 5 min, from 2 V up to 30 V. Each image shows the phase signal resulting from all the IR radiations collected during the 5 min cycles at a given voltage. The electrical resistance of the silver nanowire network was measured before each LiT acquisition (except at 4V). The corresponding values are several M Ω (0 V), 39 k Ω (2V), 11 k Ω (8 V), 8.4 k Ω (10 V), 6.3 k Ω (20 V), and 3.5 k Ω (30 V). B1-B2) After 6 V (B1) and 30 V (B2), the applied voltage is decreased back to 2 V: all the percolating paths previously activated are still illuminated - with a lower intensity - which confirms that the activation process is not reversible.

4.1.2.2.2. Discussion about partially highlighted EPPs

In Figure 48A2, it can be noticed that some pathways are only partially highlighted. It means that at the stage of activation process (2 V), in some part of the EPPs, the power of the emitted IR signals originating from local Joule heating, is not detected within the acquisition time currently used. This can be interpreted as follows: the resistance of the network depicted in Figure 48A2 is still quite high, close to 40 k Ω . Hence the current density flowing inside the several EPPs is very low in the early stages of the onset of percolation, making the detection of IR emitted signals less efficient within a short time. Besides, the inhomogeneous emission level of IR signals along the same EPP (see Figure 48A2 or Figure 48B1) suggests that the width of EPPs might change along their length. Indeed, in some locations, the EPPs are statistically likely to organize in wider percolating “clusters”, involving several nanowires in the electrical conduction. These locations are characterized by a weaker local electric current density, which is associated with a broader spatial distribution of the electric power. As a consequence, the amplitude of the latter ones is below the detection limit within the acquisition time frame.

Additionally, the heat locally generated in the EPPs by Joule effect can also diffuse along neighboring transverse AgNWs. In Figure 48, Joule effect-induced heat sources are denoted by the red areas, highlighting what we call the EPPs. Conversely, the yellow, green, and blue areas (increasing phase shift) indicate thermal diffusion-induced emitting areas. IR signals originated from blue areas, localized far away from the EPPs, are emitted last. The intensity of the diffusion phenomenon depends on the local architecture of the network and the EPPs. Statistically, there might be locations where the transverse heat diffusion process is important, leading to a lower local temperature in the EPPs themselves. However, even though thermal diffusion along transverse nanowires might have an impact in the proper detection of the EPPs, especially in the early stages of the activation, one has to keep in mind that the data presented in this study are mostly dominated by changes in the electrical conductivity.

Finally, some pathways still appear partially activated in Figure 48B1, after having decreased the voltage from 6 V to 2 V, whereas they were entirely highlighted (i.e. entirely activated) at 6 V (see Figure 48A4). Given that the activation process is non-reversible, the morphology of the network and the electrical resistance of the EPPs are the same in (A4) and (B1). Hence the only parameter that changes is voltage, and apparently it induces a too low input power for appropriate detection at 2 V.

4.1.2.2.3. Influence of the electrode geometry: lightning rod effect

Figure 49 shows that the onset of percolation is significantly influenced by the shape of the electrodes. The influence of the electrode geometry on the conductivity level of AgNW networks has been indeed reported by Fairfield et al.^[217] Here, it is demonstrated that percolating pathways get preferentially activated in the areas where the distance between the electrodes is the lowest, in accordance with the lightning rod effect. It implies that the junctions located in places where the electrical field is the strongest are likely to be activated first. This

can be easily understood if one considers the expression of the local Joule heating: $P = \sigma \cdot E^2$ where P is the heat power generated per unit volume, σ is the electrical conductivity and E the electric field.

To summarize, the LiT analysis reported in this section suggest that it is possible to control the signature of the thermal and electrical maps of AgNW percolating sparse networks, by modifying either the shape of the electrodes or the voltage application level. It is demonstrated that the onset of percolation in sparse AgNW networks is a tunable phenomenon which paves the way to their use as adaptive macroscale system.

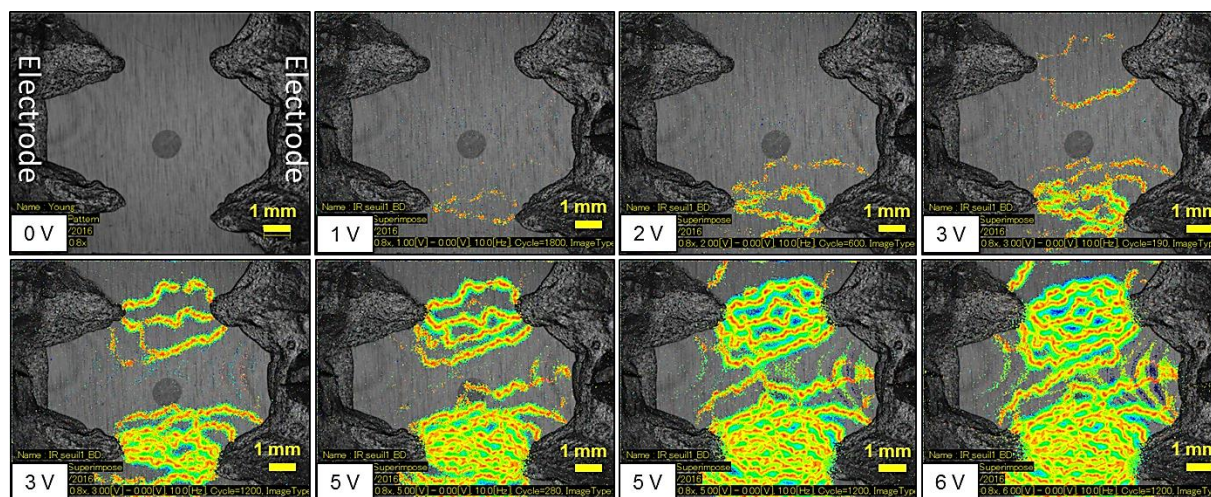


Figure 49. LiT phase images of AgNW networks slightly denser than the percolation threshold, showing preferential activation of efficient percolating pathways (EPPs) where the distance between the electrodes is the shorter (where the electrical field is the highest). Images are collected after voltage application of 0, 1, 2, 3 (twice), 5 (twice), and 6 V, during 5 min.

4.1.3. Impact of the AgNW diameter on geometrical quantized percolation

Once having validated the occurrence of geometrical quantized percolation experimentally, the model developed by D. Langley et al. was used to study the effect of NW diameter in the quantized percolation phenomenon. For this purpose, AgNWs with different morphologies were purchased from Seashell Technology, dispersed in isopropyl alcohol (IPA) and deposited by spin-coating at room temperature on 12.5×12.5 mm² Corning 1737 glass substrates. The AgNWs are referred in the current study as: “AgNW 45”, “AgNW 117” and “AgNW 138”, having an average diameter of 45, 117 and 138 nm, and an average length of 13.6, 42.9 and 32 μm, respectively. Silver paint-based contacts were deposited at two opposite sides of the specimen. A stamp was used to have the two contacts parallel and separated by a distance that was similar for all of the samples tested (7 mm). Thanks to a two-point probe system using a Keithley source meter, *in situ* measurement of the electrical resistance of the networks could then be performed during thermal annealing.

In this approach, the overall resistance consists of the initial resistance (very high) of the network before activation in parallel with the EPPs. Each EPP is indeed considered as a parallel resistance of value R_{EPP} . The estimation of R_{EPP} , based on Pouillet's law, is of crucial importance. R_{EPP} can vary from one EPP to another one. As already depicted by Langley *et al.*, in its simplest form, the equivalent resistance R_{eq}^m of the network after m plateaus can then be estimated using the formula:^[42]

$$\frac{1}{R_{eq}^m} = \frac{1}{R_S} + m * \left(\frac{1}{R_{EPP}} \right) = \frac{1}{R_S} + m * \left(\frac{\pi \cdot D_{NW}^2}{4K \cdot \rho(D_{NW}) \cdot L} \right) \quad (4.1)$$

R_S is defined as the resistance of the AgNW network before the activation of the first EPP while L is the distance between the two opposite straight electrodes, D_{NW} the average nanowire diameter and ρ the resistivity of the nanowires. The latter differs from the value for bulk silver due to the enhancement of the electron scattering on lateral surfaces of small dimension objects.^[218] According to Bid *et al.* ρ depends on the mean free path of the electron Δ and on the nanowire diameter D_{NW} as $\rho = \rho^{bulk} \cdot \left(1 + \frac{\Delta}{2 \cdot D_{NW}} \right)$.

Finally, K is a dimensionless parameter depending on the path length (considering the EPP tortuosity) and on the efficiency of the junctions involved. A value of 1 for K would correspond to the unlikely case where all junctions belonging to the EPP are strictly aligned and perfectly conductive. In practical cases, however, EPPs exhibit more tortuous shapes and junctions are not totally sintered at this stage of the annealing, which result in K values larger than 1.

It is worth mentioning that equation (4.1) is valid assuming that the two following conditions are fulfilled: first, each EPP would exhibit a rather similar shape and efficiency. Second, it is supposed that the EPPs belonging to the same network do not interact with each other. This is a substantial limitation that remains at least acceptable since we focus on the very first steps of the percolating process. This assumption is validated by the LiT images (Figure 45 and Figure 48) at least for the very first pathways activated. This simple modelling approach was found to yield good results in many cases, even for networks composed of different types of nanowires. **Figure 50a-c** show the electrical resistance curves obtained for three different AgNW average diameters (Ag45 (a), Ag117 (b) and Ag138 (c)). Here the temperature was increased from 20 to 100 °C in 10 min and then maintained at 100 °C for 1 h. These are good examples of what can be achieved when applying this model for fitting the experimental drops of resistance (see dashed red curves).

Our model suggests that geometrical quantized percolation phenomenon is impacted by the NW diameter. According to Equation 4.1, the calculated equivalent resistance is linked to the NW diameter via D_{NW}^2 and $\rho(D_{NW})$. The model predicts that the smaller the NW diameter, the higher the values of electrical resistance for which the plateaus can be observed. This is indeed in good agreement with Figure 50a-c. The reliability of the model is further confirmed by plotting $1/R_{eq}^m$ as a function of m (the plateau number). According to Equation 4.1, $1/R_{eq}^m$ depends indeed linearly on the number of plateaus. One expects that the associated slope is a function of the nanowire average diameter as well as of the K values attributed for each of the efficient pathways that belong to the percolating network. Figure 50d shows the corresponding

curves for the different diameters of 45, 117 and 138 nm. First, the linear behavior of $1/R_{eq}^m$ as a function of m is clearly demonstrated. This is in full agreement with equation (4.1) as well as with our model in general, emphasizing the relevance of assimilating the activated EPPs as a set of R_{EPP} resistances in parallel.

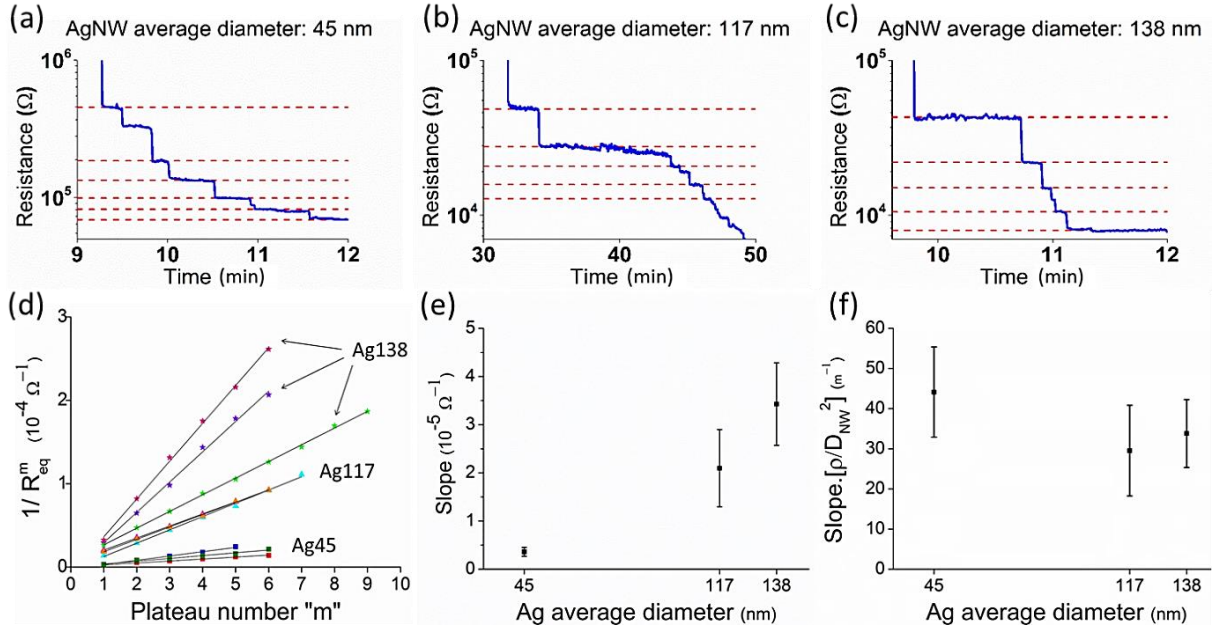


Figure 50. *a-c) Electrical resistance curves obtained for three AgNW percolating networks with AgNW average diameter of 45 (a), 117 (b) and 138 nm (c). The values associated to the plateaus calculated from the model are also pointed out (red dashed lines) leading to a good visual agreement. Here the temperature was increased from 20 to 100 °C in 10 min and then maintained at 100 °C for 1 h. d) Plots of the experimental values of $1/R_{eq}^m$ versus the plateau number m for various ‘Ag45’, ‘Ag117’, and ‘Ag138’ silver nanowire networks associated to an average diameter of 45, 117, and 138 nm, respectively. e) Plot of the slope values (extracted from the linear curves exposed in (d)) as a function of the diameter for AgNW networks associated with three different average NW diameters: Ag45, Ag117, Ag138. f) Plot of the associated Slope $\cdot (\frac{\rho}{D_{NW}^2})$ values as a function of the diameter. As expected from our model, a diameter-independent object is obtained.*

Furthermore, it is also obvious from Figure 50d that the associated slope values depend on the AgNW average diameter (see the difference between Ag45 on one side and Ag117 and Ag138). However, as depicted in Figure 50d, the samples show slight variations in the associated slope values (especially Ag138 samples). This is mainly due to statistical fluctuations in the level of nanowire density achieved during the deposition process. Since we focus on samples close to the percolation threshold, a slight difference in the network density is likely to induce a significant difference in the network conduction level. Besides, such statistical fluctuations are inherent to the geometrical quantized percolation phenomenon itself. Finally, Slope $\cdot (\rho(D_{NW})/D_{NW}^2)$ is supposed to remain constant as a function of the diameter. Quantitatively, it can be calculated that $\frac{Slope_{Ag138}}{Slope_{Ag45}} \approx 10$, whereas $\frac{Slope \cdot (\rho/D^2)_{Ag138}}{Slope \cdot (\rho/D^2)_{Ag45}} \approx 1.3$. As a consequence, by

multiplying *Slope* by $(\rho(D_{NW})/D_{NW}^2)$, a diameter-independent mathematical object can be obtained with a good approximation (Figure 50e-f). This is another experimental observation that is consistent with our model.

4.1.4. Introduction to “anti-percolation” phenomenon

As already mentioned, geometrical quantized percolation occurs at relatively low temperature (about 100 °C) at which the electrical properties of the junctions are not optimized yet. In general, the minimum and optimized resistance is reached for temperatures ranging from 200 to 300 °C, the exact value depending on the AgNW diameter.^[50] At higher temperatures (close to 300 °C), the morphology of the rod-like nanowires become instable by the Rayleigh instability that is driven by the reduction of the surface energy, leading to the spheroidization of the nanowires and eventually to the loss of the network percolating nature.^[109,207,219,220] In a very few cases, electrical resistance steps can also occur close to the spheroidization temperature, as shown in **Figure 51**. This discontinuous network collapsing process can be fairly well interpreted in terms of our model, as shown by the good agreement between the measured electrical resistance of the AgNW networks and the red dashed line calculated from equation (4.1). Since it can be understood as the opposite phenomenon to quantized percolation (i.e. it does not correspond to the onset of percolation but to the loss of the network percolating nature up to a state where only few EPPs are still existing and slowly being destroyed by the increase of temperature), we refer to this phenomenon as “anti-percolation”.

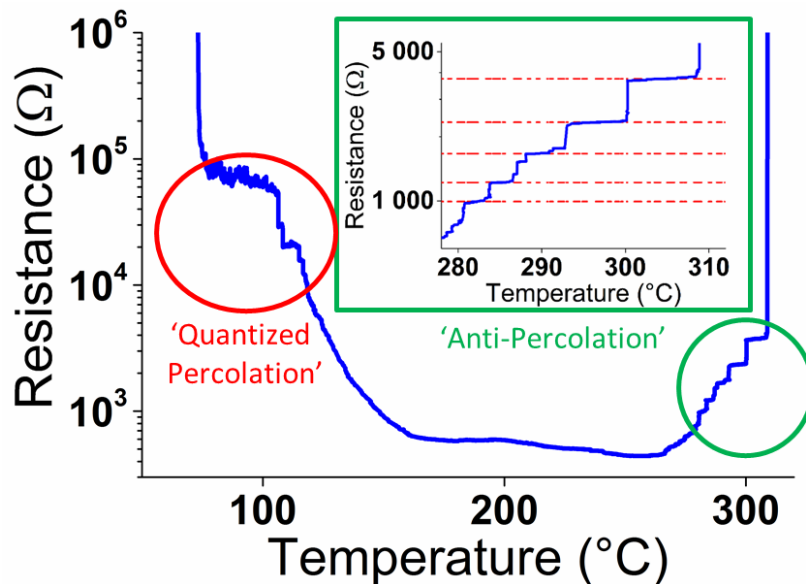


Figure 51. Electrical resistance of an AgNW network (average diameter: 117 nm), measured during a full thermal ramp annealing of 2 °C min⁻¹. In some cases, quantized steps related to the discontinuous loss of the network percolating nature can be observed beyond the minimal networks resistance. The related anti-percolation phenomenon can be described by a similar model, as shown by the red dashed lines of the inset.

Once all the junctions are totally sintered ($T \approx 200\text{-}250\text{ }^\circ\text{C}$), their morphology is roughly the same. However ‘anti-percolation’ highlights the fact that in very few cases, some “robust” efficient percolating pathways are able to resist a little bit longer than others to Rayleigh instabilities. It can be noticed in Figure 51 that the steps belonging to ‘anti-percolation’ are about one order of resistance lower than those belonging to the original quantized percolation. This can be explained by the width of the distribution of AgNW diameters: the onset of percolation (as shown in Figure 45d-f) mostly involves the thinnest AgNWs of the whole network since the smaller the diameter, the faster the sintering, while anti-percolation should be associated with the largest AgNWs.

This interpretation is compatible with the Gibbs-Thomson equation which predicts a monotonous increase of the spheroidization temperature while increasing the AgNW average diameter, as demonstrated by Lagrange *et al.*^[50] In the case of a wire diameter range of $117\text{ nm} \pm 35\text{ nm}$ (Ag117 networks), the computation of the equivalent resistances corresponding to the first EPP ($m=1$, see Equation 1) yields the following results: $R_{eq}(lowest) \approx 10^4\ \Omega$ and $R_{eq}(highest) \approx 10^3\ \Omega$, for the lowest and the highest diameter values of the range, respectively. This is in excellent agreement with the data shown in Figure 51. It has to be noted as well that the observation of the anti-percolation process requires that some of the EPPs are mainly made up of AgNWs with large diameters. Such configuration is highly subject to statistical fluctuations, and thus anti-percolation is rarely observed under the associated experimental conditions (only 4 occurrences could be observed in this study out of 95 studied specimens).

4.1.5. Concluding remarks

In this section, the occurrence of a geometrically quantized percolation phenomenon via thermal/electrical activation at the scale of the whole network (several millimeters) has been evidenced. Using lock-in thermography helped providing visual evidence of the discontinuous activation process of efficient percolating pathways (EPPs) through AgNW networks. It shows the validity of our model in the very first steps of activation. LiT images suggest that the thermal and electrical map associated to the onset of electrical percolation in AgNW percolating networks can be controlled by the voltage application level and by the shape of the electrodes as well. The relatively simple model proposed was found to be in fair agreement with the experiments reported in this section. In particular, the impact of the AgNW average diameter could be well demonstrated by the linear behavior of the inverse of the equivalent electrical resistance as a function of the plateau number m : the associated slopes were found to be substantially different according to the average diameter. The definition of the resistance (R_{EPP}) associated to the EPPs was found to be relevant as well. Furthermore, in some cases, similar but increasing steps of electrical resistance could be detected at higher temperature (around $300\text{ }^\circ\text{C}$) right before that all AgNWs would be spheroidized. These incremental resistance increases were interpreted as evidence of a discontinuous collapsing of the EPPs. We believe that quantized percolation and anti-percolation constitute key elements for the understanding of

nanoscale phenomena having directly measurable impact at the macroscopic scale. They could certainly be useful tools to tune and optimize adaptive material systems and devices based on MNW percolating network. We also believe that LiT is a very promising technique for the mapping of electrical clusters through thin layers made of interconnected conductive entities, which is of paramount importance for their integration in functional devices.

Given that this study was mainly dedicated to visualizing and describing geometrical quantized percolation, which is only detectable for low density networks, in this section we have mainly reported LiT analysis of AgNW networks whose density is close to the percolation threshold (n_c). However, LiT is also well adapted for characterizing “standard” density networks (i.e. whose NW density equals at least $5n_c$), which have been the most widely studied and integrated into functional devices so far. LiT is suitable for probing the electrical/thermal distribution in such standard density network (see sections 4.2.1 and 4.2.2), as well as for the detection of hotspots and failures when subjected to aggressive ageing stress (see section 4.2.3).

4.2. The parameters that influence the electrical homogeneity and stability of AgNW networks

In the present section, the analysis of electrical distribution also turns to denser AgNW networks (basically with n ranging from $3 n_c$ to $15 n_c$). Even though very sparse AgNW networks have recently attracted new applicative interest in antistatic applications or for highly transparent films heaters (very low haze factor), the vast majority of successful AgNW integrations in devices have indeed concerned this range of network density so far. It is then mandatory for industrial prospect to tackle the electrical distribution issue by investigating networks with higher density too. As a consequence a very large network density range is explored in this present section.

For this purpose, a threefold approach combining electrical measurements, electrical/thermal mapping techniques, and simulation tools, has been engaged. The influence of the NW density and the junction efficiency on the network electrical homogeneity is firstly investigated in sections 4.2.1 and 4.2.2, respectively, while section 4.2.3 highlights the dynamics of optimization and failure mechanism under electrical bias, as well as their influence on the electrical distribution.

All the results and discussions reported in this section 4.2 were conducted in collaboration with Nicolas Charvin and Lionel Flandin from LEPMI laboratory (LMOPS team, le Bourget-du-Lac) who have very pertinent tools for mapping the physical properties of AgNW networks: one-probe electrical mapping and infra-red (IR) imaging.

4.2.1. Impact of the network density on the electrical homogeneity

4.2.1.1. *Electrical and thermal mapping of AgNW networks with different network density*

Electrical mapping of AgNW networks at the macroscale was performed using a one-probe (“1P”) electrical measurement set-up, designed by Nicolas Charvin at LEPMI. Pictures of the set-up, as well as a schematic representation are provided in **Figure 52**. Silver paste is deposited at the network extremities to form contact electrodes. The sample is placed on a magnetic steel-based chuck. Left contact electrode is connected to ground, while electrical potential is applied to right electrode (usually 1 V). Voltage is applied by the mean of a SMU Keithley 2602 source meter. The mapping probe was purchased from Harwin (“ATE Spring Probe - P25-0423”) and was spring-loaded to avoid mechanical deterioration of the samples. The probe is moved by a customized computer numerical control (CNC) mill, driven by a LabVIEW software which: (i) sends G-code instructions to the system, (ii) controls the SMU acquisition. To start with, the probe approaches the network surface near the position $\{x = 0, y = 0\}$ (see Figure 52a). When $z = 0$, the probe is in intimate contact and the first measurement of the local electrical potential is performed. It has to be mentioned that electrical bias is applied to the sample only when the probe is in intimate contact with the surface, i.e. only when measuring the surface electrical

potential. Then, the probe raises up, moves in the x direction (0.5 mm), goes down again, perform a second measurement, and so on. The distance between 2 successive measurements is 0.5 mm (probing resolution). The trajectory followed by the probe is also depicted in Figure 52a. In these conditions the duration required for scanning a 25×25 cm² sample is about 15 min.

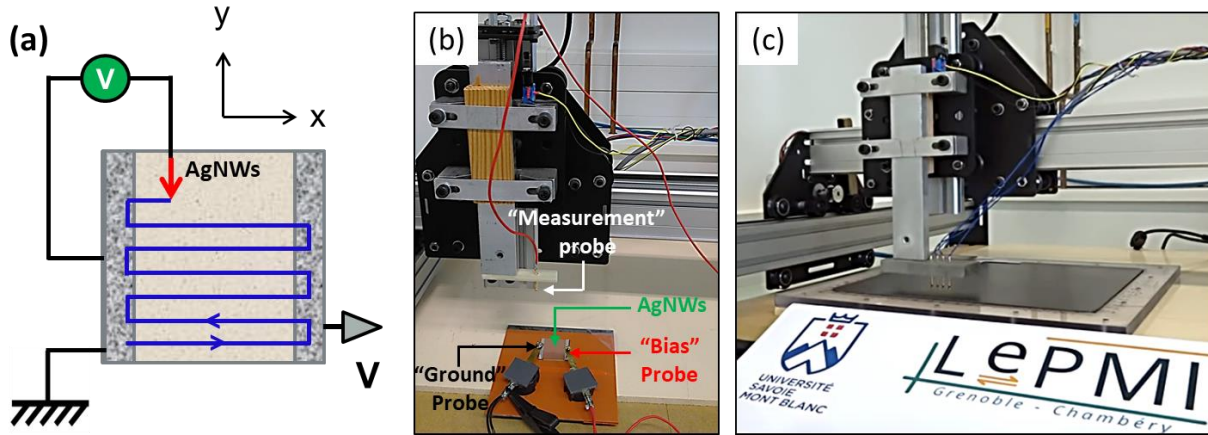


Figure 52. a) Schematic representation of the IP-electrical measurement set-up developed for macroscale electrical mapping of AgNW networks. b,c) Pictures of the IP mapping set-up designed by Nicolas Charvin at LEPMI.

In order to explore the influence of the NW density on the network electrical homogeneity, several samples with different densities were fabricated by spray-coating technique. The NWs used were synthesized at CEA-Liten ($D_{NW} = 79$ nm, $L_{NW} = 7$ μ m) via polyol process. By increasing the number of scans performed by the spray nozzle above the samples, the NW density could be increased as much as required for the experiments. The morphology of the fabricated samples was explored under SEM. **Figure 53A1-A3** reports the SEM images of 3 selected samples. It is well visible that the NW density is significantly different from one sample to another. More specifically, their change in density is highlighted by their electrical conduction level after deposition. The electrical resistance after deposition was measured to be 68 k Ω (A1), 329 Ω (A2), and 26 Ω (A3), for the three samples selected, respectively. In order to correlate the experimental results with the simulation results in next section, a careful calculation of their areal mass density (amd) was performed. First of all, the estimation of the “geometrical density” d_g , defined as the total NW length per unit area, is required. The calculation is based on ImageJ software analysis of SEM images associated to any AgNW network. The protocol and Image J script developed for calculating the geometrical density of any AgNW networks are reported in **Appendix B**. The corresponding value of amd can then simply extracted as follows: $amd = d_g * \left(\frac{\pi d_{Ag} D_{NW}^2}{4} \right)$, with d_{Ag} the density of silver, and D_{NW} the average NW diameter. In the present case, amd values were calculated to be 50 ± 4 mg m⁻² (A1), 63 ± 7 mg m⁻² (A2), and 86 ± 7 mg m⁻² (A3), respectively.

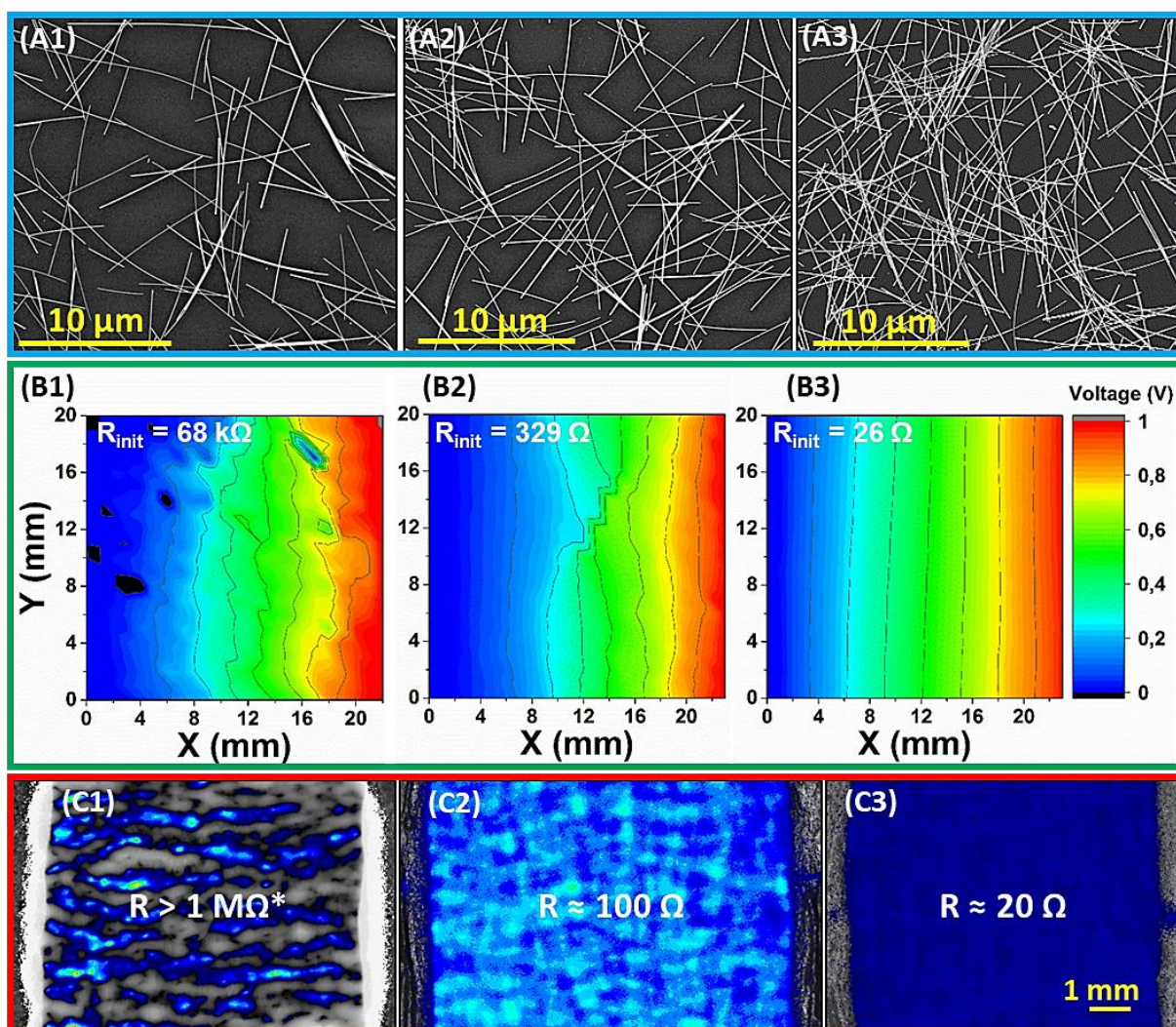


Figure 53. A1-A3) SEM images of AgNW networks with increased density. Their electrical resistance was measured to be 68 kΩ (A1), 329 Ω (A2), and 26 Ω (A3), respectively. B1-B3) IP-electrical maps associated with the samples depicted in (A1-A3). The left silver paste electrode is connected to ground (deep blue), while 1 V is applied to the right silver paste electrode (deep red). C1-C3) LiT acquisitions associated with three AgNW networks with increasing density. Their initial resistance was measured to be higher than 1 MΩ* (C1), around 100 Ω (C2), and around 20 Ω (C3), respectively. Images are collected after voltage application of 30 V, 2 V, and 0.5 V, respectively, and during 5 min each. (* the value provided here was measured just after deposition. Due the electrical activation process during the LiT acquisition, the electrical resistance of this sample could be decreased down to 3.5 kΩ.)

Electrical mapping of the three samples was performed thereafter. The results are depicted in Figure 53B1-B3. X and Y axis corresponds to the real X and Y sides of the samples (in mm), while the color scale represents the electrical potential values recorded when probing the network with the 1P-mapping set-up (deep blue indicates 0 V, while deep red indicates 1 V. Black areas indicate artefacts measurements recorded to be below 0). It is then possible to reconstruct the equi-potential lines across the network. It is well visible in Figure 53B1-B3 that the denser the network, the straighter the equi-potential lines. The equi-potential lines associated with the sparsest network (B1), are indeed very sinuous, while the ones associated

with the densest network (B3) are almost perfectly straight. These electrical maps evidence that, not solely the network density influences the overall conduction level of the network, but it also influences the local electrical distribution. The denser the network, the lower the fluctuations of the electrical potential, leading to a better electrical homogeneity. The level of electrical homogeneity could be quantitatively estimated by evaluating numerically the tortuosity of the equi-potential lines. Numerical simulations (Matlab and Comsol) are currently being developed to estimate the tortuosity of equi-potential lines and correlate them with the local statistical distribution of electrical resistance. Depending on the target applications, the level of homogeneity might be a further electrical parameter along with the overall conduction level. For instance a local area associated with a lower network density constitutes a potential hotspot for a transparent heater or will lower photovoltaics conversion efficiency (through a slight increase of the series resistance and therefore a lower form factor in the J-V curve).

In order either to save raw material when fabricating AgNW-based transparent electrodes, or to achieve very high level of transparency ($T_r > 95\%$) but maintaining a high conduction level at the same time, fabricating hybrids made of sparse AgNW networks mixed with other very thin conductive materials has been investigated. For instance, adding clay platelets was found very helpful for improve the thermal homogeneity of sparse AgNW-based transparent heaters.^[30,152] Depositing a very thin layer of PEDOT-PSS on top of sparse AgNW networks was also proved to decrease drastically the sheet resistance without affecting too much the transparency of the electrodes ($\approx - 2\%$).^[22] For this purpose, electrical mapping could also constitute a pertinent tool to assess the homogeneity of low density AgNW-based hybrid transparent conductors.

For the sake of comparison, LiT measurements were also performed on AgNW networks with different network density. The corresponding amplitude images are reported in Figure 53C1-C3. The initial electrical resistance of the samples was higher than $1\text{ M}\Omega$ (C1), close to $100\ \Omega$ (C2), and close to $20\ \Omega$ (C3), for the three samples respectively. The sample depicted in C1, very sparse, correspond to the same sample as in Figure 48A6, used for the geometrical quantized percolation study. After electrical activation, its resistance dropped down to $3.5\text{ k}\Omega$. Individual electrical pathways are highlighted in the corresponding thermal map (C1). In (C2), such individual pathways are not detectable anymore due to the increase in network density. However, the thermal map is not very homogenous and exhibits many distinct hotspots. Finally, at higher density (C3), the thermal map looks perfectly homogeneous.

In order to test the reproducibility of the 1P-mapping technique, several samples were subjected to exactly the same mapping experiment twice. **Figure 54A1-A2** reports the electrical potential map associated with a relatively low density network (initial resistance: $68\text{ k}\Omega$), after first and second 1P-mapping, while **Figure 54B1-B2** reports the same information for a higher density network (initial resistance: $133\ \Omega$). In both cases, the electrical potential maps collected after the first and second runs are very similar. However, in the low density case, more changes and fluctuations can be detected, as compared to the denser network case where the equi-potential lines have almost exactly the same shape. This is due to the drastic increase of the conduction level in the low density case, induced by the voltage application during 1P-mapping, when successive measurements of electrical potential are performed. The associated electrical resistance indeed switches from $68\text{ k}\Omega$ down to $5\text{ k}\Omega$, before and after the first mapping. It

shows that applying 1 V several times during the experiment has an impact in the sintering of junctions and in the activation of efficient pathways through the network. Such impact is less visible for denser networks since the optimization process is more “diluted” through the interconnected nanowires (a similar trend was already observed when investigating the effects of thermal annealing on AgNW networks: the denser the network the lower the influence of thermal annealing on the electrical properties.^[50] Hence, for testing the reproducibility of 1P-mapping in the case of sparse networks, it might be beneficial to apply a lower voltage (≈ 0.1 V) when probing the sample, so that the temperature elevation induced by Joule effect remains low and has a limited impact on the sintering of the junctions.

Anyway, in any cases the reproducibility of the technique can be considered as satisfying and the denser the network, the better the reproducibility. Observations with optical microscope after mapping revealed that repeated contacts between the probe and the sample are likely to induce some damages to the sample (see Figure 54C1-C2). However, when examining the successive 1P-mappings collected, especially the ones associated with high density networks, it seems that the resolution of the technique is not high enough to be influenced by such irreversible defects and such local modifications of the electrical field.

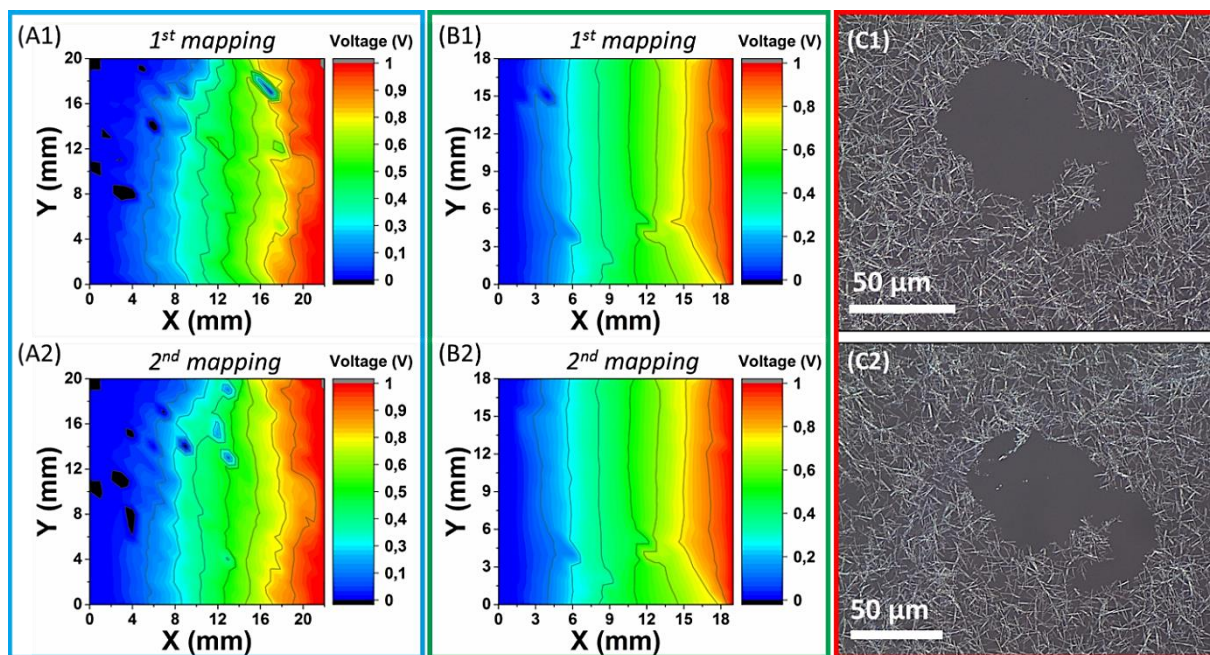


Figure 54. A1-A2) Two successive 1P-electrical maps associated with a low density AgNW networks in exactly the same experimental conditions. The electrical resistance of the sample before experiment was $68 \text{ k}\Omega$. It decreased down to $5 \text{ k}\Omega$ after the first mapping, and decreased even more down to $4.2 \text{ k}\Omega$ after the second mapping. B1-B2) Two successive 1P-electrical maps associated with a denser AgNW network in exactly the same experimental conditions. The electrical resistance before and after mapping remains the same and equals 133Ω . C1-C2) Optical microscope images of the same samples (in different locations) after 1P electrical mapping. Some defects can be detected all along the network as the signature pattern of the contact between the sample and the probe during the experiment.

1P-electrical mapping provides information regarding the electrical distribution in AgNW networks, while LiT provides information about the thermal distribution. LiT and 1P-mapping are complementary techniques since the thermal maps generated when performing LiT analysis originate from Joule heating that is induced by voltage application. Hence, the thermal and electrical information are intimately correlated.

However, these two techniques do not provide information with the same resolution. In 1P-electrical mapping, electrical potential data is collected every 0.5 mm, while the thermal microscope used in LiT can achieve very high resolution thanks to an InSb camera with 640×512 pixels (pixel size: 15 μm). Moreover, LiT can provide both amplitude and phase thermal images. Hence information regarding the thermal diffusion process (not only the Joule effect-induced heating) is also contained in the LiT phase images. However, the maximum field of view (FoV) in LiT is 12×9.6 mm² meaning that the maximum size network that can be observed with the minimum objective magnification available (×0.8) is 12×9.6 mm². On the contrary, 1P-mapping provides only electrical information but is not limited to small system-size, which is a major advantage. For instance, electrical mapping of samples as large as 5×5 cm² was successfully performed within the frame of this thesis.

4.2.1.2. Correlation with simulation models

For better understanding and demonstrating the tunable electrical properties of AgNW network the experimental results presented in previous section were confronted to the Matlab and Comsol-based simulation models introduced in chapter 3. More specifically, the network density of the three samples reported in Figure 53B1-B3 (1P-mapping), was firstly calculated by Image J analysis of the corresponding SEM images (see Appendix B). Three simulation samples with a similar network density as in the experiments were then generated using Matlab. Images of the three generated networks are reported in **Figure 55A1-A3**. The fictive corresponding *amd* are 50, 65, and 82 mg m⁻², which is very close to the experimental samples we make the comparison with (50 ± 4, 63 ± 7, and 86 ± 7 mg m⁻²).

Corresponding electrical potential maps were then extracted using Comsol (see Figure 55B1-B3). The same behavior regarding the impact of the network density on the electrical homogeneity was observed. The denser the network, the straighter the equi-potential lines. This confirms our conclusion on the impact of the network density on both the conduction level of AgNW networks and their electrical homogeneity. Second, it demonstrates the robustness of our modelling tools about electrical properties.

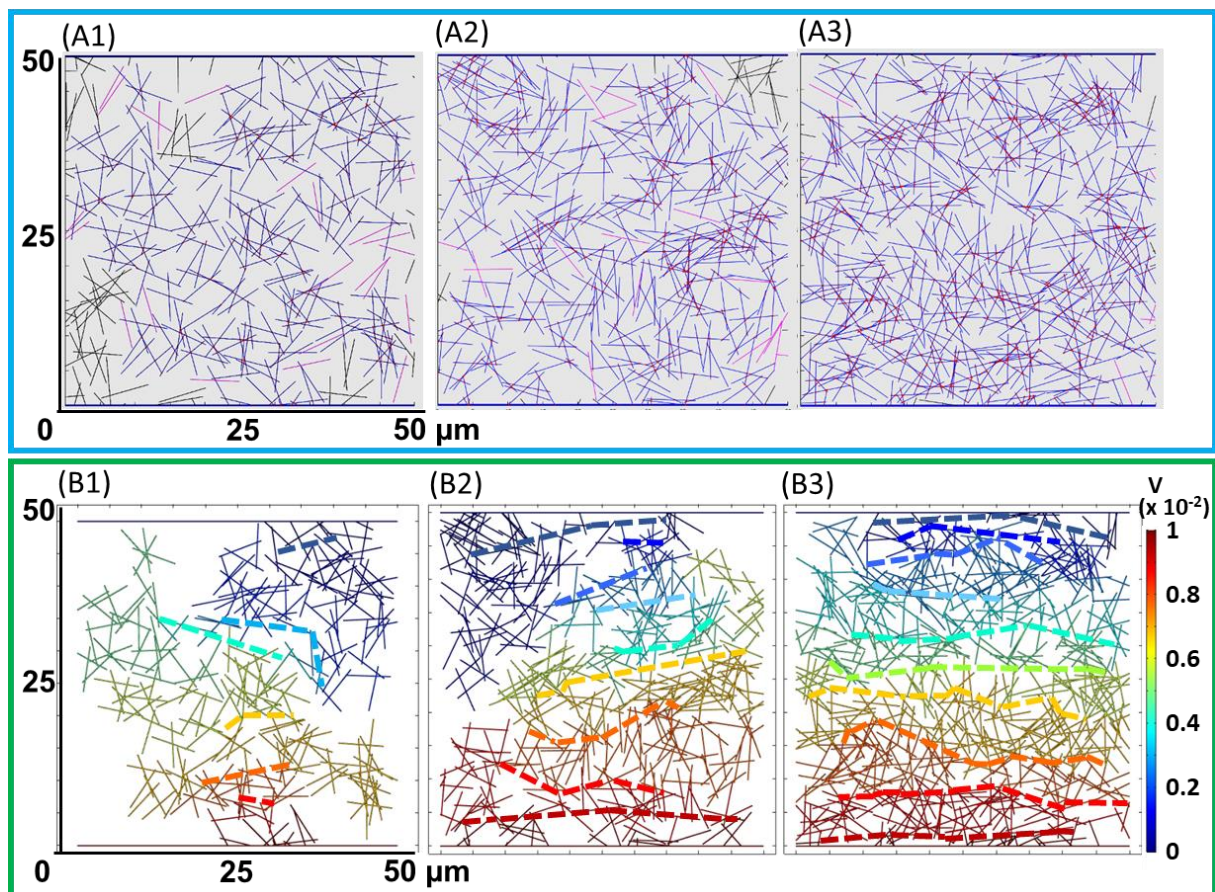


Figure 55. A1-A3) Images of virtual networks generated using Matlab. The network density values are set to be similar to the ones of real network presented in Figure 53A1-A, i.e. 50 (A1), 65 (A2), and 82 mg m⁻² (A3), which is very close to those of real AgNW networks. B1-B3) Electrical potential maps generated using Comsol electrical model, for the three networks generated in A1-A3).

4.2.2. Impact of the junction efficiency on the electrical homogeneity

4.2.2.1. Experimental analysis using lock-in thermography

Not only the network density but also the optimization level of the NW junctions is likely to increase the conduction level of the resulting AgNW networks. It has been demonstrated in chapter 2 and section 4.1 that post-deposition treatments such as thermal or current annealing can induce complete sintering of the junctions, resulting in the decrease of the individual resistance of the junctions, and finally to the decrease of the overall resistance of the network. Besides, it is also expected that such treatments help reducing the disparity in terms of conduction levels that might exist between the junctions when no optimization process is performed, leading to a higher electrical homogeneity at the same time. This section attempts to validate this hypothesis.

For this purpose, LiT analysis were conducted. **Figure 56a-b** shows LiT amplitude images of two standard AgNW networks associated with an electrical resistance of 31 and 11 Ω,

respectively. The first one (a) is “as-deposited”, whereas the other one (b) was subjected to thermal annealing prior to the LiT acquisition. Thermal treatment was performed at 150 °C during 1 h using a hot plate. In both cases, the LiT amplitude images were collected after 1 V was applied during 5 min. It can be noticed that the amplitude signals are much more homogeneous all over the sample after annealing. As mentioned above, this is due to the creation of well-sintered junctions as thermal annealing is performed. As a consequence, there are statistically many more junctions that participate efficiently in electrical conduction after annealing, and thus the electrical current is more homogeneously distributed over the AgNW electrode.

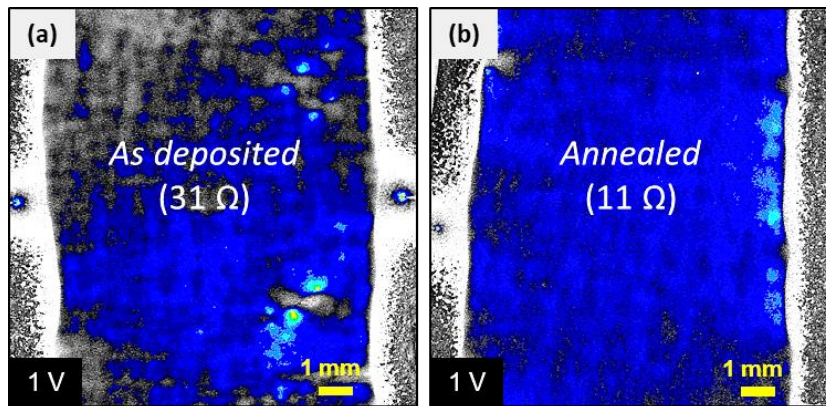


Figure 56. a-b) Influence of thermal annealing on the electrical distribution in “standard” density networks. LiT amplitude images of AgNW networks: (a) without thermal treatment, and (b) after thermal annealing at 150 °C for 1 h. Images were collected after voltage application of 1 V for 5 min.

4.2.2.2. Correlation with simulation models

Experimental results presented in the previous section were also confronted to the simulation tools developed during this thesis. As already mentioned in section 3.3.3, Bellew et al. were able to measure the electrical resistance of single NW junctions in the case the latter can be considered as “activated” ($R_{act} \approx 680 \Omega$) or fully “optimized” ($R_{opti} \approx 11 \Omega$).^[202] In order to take into account the optimization of AgNW junctions during thermal or current annealing, the value of contact impedance Z_c has to be implemented in Comsol software. The contact impedance value contains all the electrical information at the boundary between adjacent nanowires. Z_c can be adjusted according to the experimental values, for instance those measured by Bellew et al., and according to the NW diameter used in the simulation (see Equation (3.3)). In the simulation, apart from the “activated” et “optimized” cases, a third “half-optimized” case is studied, for which the resistance of the NW junctions is pseudo-randomly attributed as follows: $R_{half-opt} = R_{opt} + k(R_{act}-R_{opt})/4$, where $k = 0, 1, 2, 3$ or 4 .

Comsol electrical simulations were performed on networks with the same architecture – same network density ($n = 8n_c$), same AgNW diameter and length ($D_{NW} = 60 \text{ nm}$, $L_{NW} = 10 \mu\text{m}$) – but by implementing the junction efficiency according to the three different grain boundary conditions (“activated”, “half-optimized”, “optimized”). Their electrical resistance was

calculated to be 102 Ω , 28 Ω , and 7 Ω , respectively. As expected, in the case of optimized junctions, the network resistance is much lower.

In **Figure 57**, the corresponding equi-potential lines associated with the three networks are provided. In the case where the junctions are set as “optimized” (c) the equi-potential lines are quite smooth and the electrical distribution is very homogeneous. When the junctions are less optimized (b) the lines are more tortuous. In the “activated” case (a), there are very few elements exhibiting the same potential so that the equipotential lines cannot be drawn easily. Although the distribution of contact resistances is totally isotropic in both the “activated” and “optimized” cases, the resulting electrical map is much less homogeneous when the value of contact resistance is set high. Contrary to commonly used homogenous layers in which the current distribution is theoretically isotropic whatever the resistance of the material, in the case of interconnected networks, the local network architecture is likely to influence drastically the current distribution, especially when the contact resistance is much higher than the wire resistance (“activated case”).

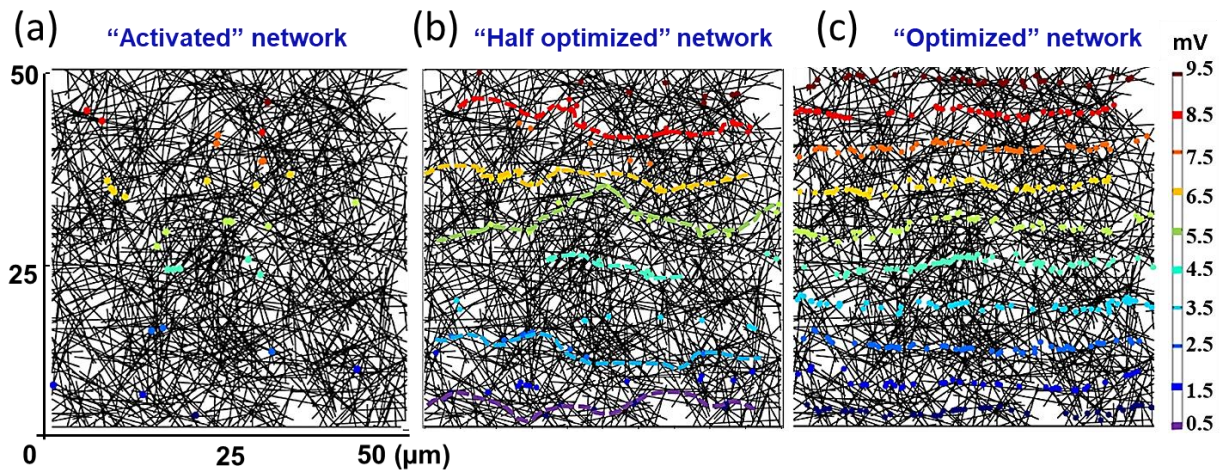


Figure 57. Voltage equi-potential lines of AgNW networks with the same architecture, associated with a network density, length, and diameter of 8 n_c , 10 μm and 60 nm, respectively, and for the three junction optimization levels: (a) “activated”, (b) “half optimized”, (c) “optimized”. The corresponding network electrical resistances were calculated to be 102 Ω , 28 Ω , and 7 Ω , respectively.

4.2.3. Optimization and failure dynamics of AgNW networks under electrical stress

As demonstrated in the previous section, by playing with parameters such as the network density and the junction efficiency, the electrical conduction level of AgNW networks as well as their electrical and thermal homogeneity can be drastically modified. For demonstrating the ability of AgNW networks to be safely integrated into functional devices, it is also mandatory to evaluate the electrical stability of AgNW networks under extended electrical bias. Electrical stress during extended time can be either beneficial or harmful for the AgNW-based electrodes in terms of performance. This is why the influence of electrical stress on the AgNW network integrity is investigated in this section. By using the electrical and thermal mapping technique (1P-potential mapping and LiT), some huge modifications of the active electrical percolating

cluster have been observed, especially when the networks are close to voltage breakdown. Hence, the present study also tackles the electrical homogeneity issue that is deeply discussed throughout the whole chapter 4.

4.2.3.1. Evolution of the electrical behavior of standard AgNW network under electrical stress

For characterizing the electrical behavior, reliability, and limitations of AgNW networks under electrical bias, several networks were subjected to increasing voltage plateaus. Measurement of the electrical resistance during the plateaus was performed by connecting the sample to a Keithley source-meter driven by a LabVIEW program. **Figure 58** reports the corresponding results for an AgNW network with an initial resistance of 33 Ω . The applied voltage was increased from 2V up to 20 V (breakdown), with a duration of 5 min for each of the plateaus. In parallel with electrical measurement, electrical/thermal mapping of the samples between each plateaus was performed via LiT analysis. LiT images were collected after voltage application of 0.5 V during 5 min. For the sake of simplicity, the samples were maintained fixed on the LiT metallic support (favorable for heat dissipation) during the entire experiment, which means that the external circuit (Keithley, PC) was directly connected to the sample, inside the LiT chamber.

First of all, the evolution of the electrical resistance of the AgNW network during the successive voltage plateaus is reported in Figure 58A. Each time the voltage is applied, the electrical resistance of the network starts increasing due to the elevation of the network temperature induced by Joule effect. The elevation of the temperature is getting more and more important as the voltage (i.e. the input electrical power) increases, according to Equation (3.5). So does the electrical resistance. Once the thermal equilibrium has been achieved, the resistance at steady-state is reached.

From 2V up to 10 V, the steady-state resistance is strictly constant (see Figure 58B1), which means that the network is not subjected to any optimization or damaging process. From a morphological point of view, until 10 V, the temperature of the network is not high enough to either encourage the sintering of the junctions (optimization) or induce spheroidization of the nanowires (damaging). At least, no positive nor negative influence of the temperature can be detected during the 5 min plateaus.

On the other hand, between 12 V and 16 V, the steady-state electrical resistance starts slightly decreasing during the plateau (see Figure 58B2). This can be interpreted as the Joule effect-induced optimization of the NW junctions. As a consequence, the overall resistance of the network at room temperature is decreased as well. This is clearly detectable in Figure 58A by following the decreasing shape of the green dashed-line. The latter fits the starting-point values of the electrical resistance in the early stage of each voltage plateau, i.e. when no influenced by Joule effect. Between 2 V and 10 V, the green dashed line is perfectly straight, meaning that the network is in a “stable state”, whereas from 12 V, the line starts falling down, meaning that the network is in a more “optimized state”.

At the end of the 18 V plateau, it can be detected that the steady-state electrical resistance starts increasing slightly (see Figure 58B3). This can be interpreted as the electrical signature of the early stages of a damaging process. The Joule effect-induced elevation of the network temperature starts getting so high that Plateau-Rayleigh instabilities are likely to appear, inducing the spheroidization of several junctions. At 20 V, the electrical resistance starts diverging only after one minute of voltage application; electrical breakdown of the sample has been achieved (see Figure 58B4). It has to be noted that the breakdown process is very quick. Moreover, it takes place at very high voltage as compared to the value already reported in the literature. For instance, voltage at breakdown were reported to be around 8 V by Lagrange et al.^[31] However, in the latter case the AgNW networks were not deposited on any support, whereas in the present case, the sample was placed on a metallic support, which is very convenient for diffusing efficiently the heat and thus reducing the elevation temperature. As a consequence, the electrical limitations of the sample were pushed back to higher voltage limits.

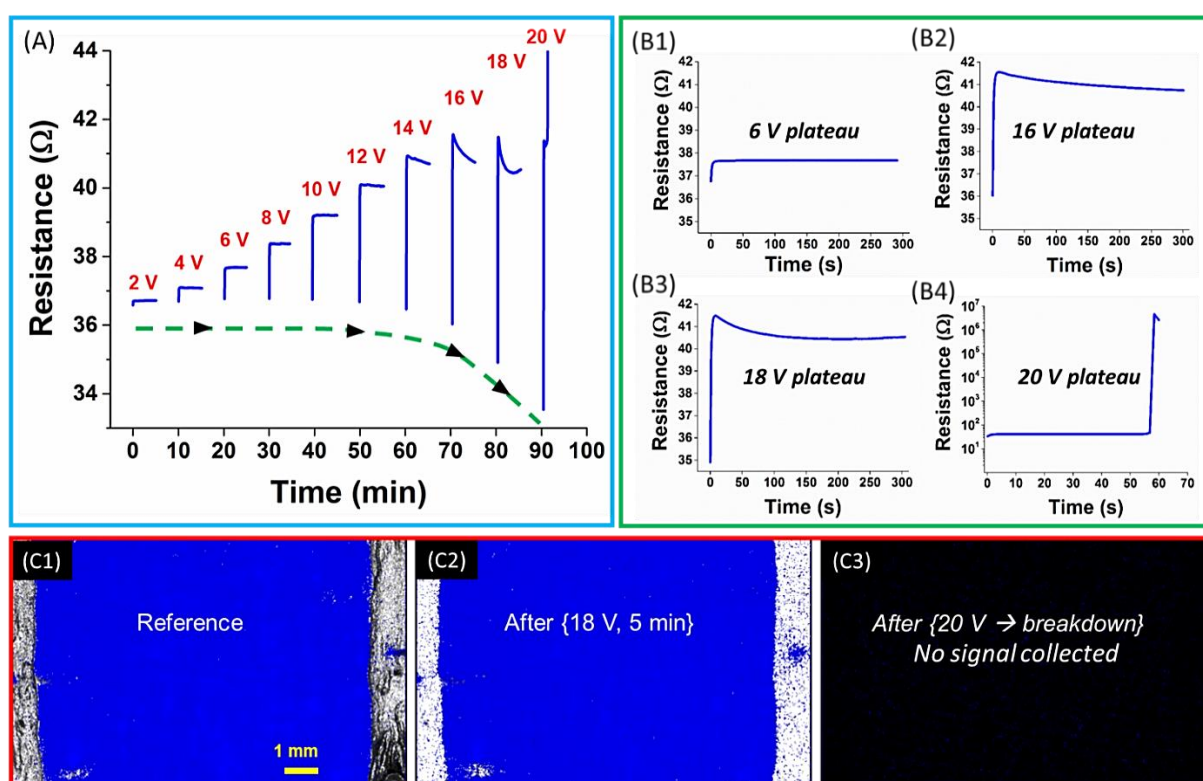


Figure 58. A) Electrical resistance of an AgNW network associated with an initial resistance of 33 Ω , deposited on a metallic support. The resistance is measured while voltage plateaus of 5 min each are successively performed from 2V, up to electrical breakdown at 20 V. Between each plateau, no bias is applied anymore (except when the sample is subjected to intermediate LiT acquisition). B1-B4) Zoom in the 6 V (B1), 16 V (B2), 18 V (B3), and 20 V (B4), voltage plateaus, respectively. C) Thermal lock-in images of the same AgNW network. Images are collected after on-off voltage application of 0.5 V for 5 min. Images were collected before starting the electrical plateau (C1), after the 18 V plateau (C2), and after electrical breakdown (C3).

Together with electrical measurement, *in situ* LiT observations helped going further in the interpretation. Figure 58C reports the LiT acquisitions associated to the same sample as in Figure 58A: The reference acquisition, i.e. the one performed before stressing the sample, is shown in (C1). The amplitude signal is quite homogeneous all over the sample. Acquisition after the electrical plateau at 18 V, i.e. at the limit between the optimization and early damaging stages, is provided in (C2). The latter is still very homogeneous, and very similar to the one depicted in (C1). There is no apparition of any defects or hot points. After electrical breakdown, the LiT acquisition did not result in any IR signal collection, since no current could be injected through the network anymore. However, in this series, the voltage applied for collecting the LiT acquisition was set very low (0.5 V). In next section, it is shown that by increasing the voltage after breakdown (up to 5 V), the presence of a vertical crack with active conductive bridges could be detected in many samples.

4.2.3.2. *Description of the mechanisms involved in the electrical breakdown of AgNW networks at high voltage*

From a morphological point of view, no visual difference can be detected before and after electrical breakdown. The samples look exactly the same. However, beyond the amplitude and phase acquisitions, the LiT set-up also allows the capture of “pattern” images which consists of emissivity-based contrast mapping of the sample (see **Figure 59A**). By comparing the reference emissivity map (A1), and the one captured after breakdown (A2), a morphological difference can be detected. There is the appearance of a vertical crack through the network after breakdown. Such observation was also confirmed thanks to SEM observations performed after electrical breakdown (see Figure 59B): far from the crack, the huge majority of NWs are safe after breakdown (B1), whereas close to the crack, the NWs are fully or partially spheroidized (B2). Such a crack formation was observed several times on different samples.

The breakdown of the sample via the formation of a physical vertical crack, is coherent with the quickness of the diverging process of electrical resistance depicted in Figure 58B4). When deposited on a metallic chuck, standard AgNW network can sustain a very high voltage charge. The resulting current density is quite homogeneously distributed all over the network (as demonstrated by the homogeneous LiT acquisition reported in Figure 58C), and the corresponding elevation temperature can be sustained by the NWs. Even though the electrical distribution looks well homogeneous, it is likely that in some locations, the temperature of the nanowire is a bit higher than the average elevation temperature. This is inherent to statistical fluctuations in terms of NW coverage. Moreover, due to repeated experiments and as well to potential human practical errors (either during the network fabrication and characterization experiments), some defects might also influence the dynamics of failure (see for instance the scratch in Figure 59A2). From a kinetic point of view, the nanowires that belong to such locations are likely to spheroidize at first in the case the Joule effect-induced temperature reaches the NW sustainable limits, leading to the loss of electrical percolation in the corresponding area. Since the voltage is maintained constant during the experiment, once the first hotspot has reached breakdown (spheroidization), the current density is instantaneously

redistributed and constricted in the very adjacent top and bottom areas. The corresponding NWs overtake the current density limit as well. Hence they get spheroidized in a very short time thereafter, and so does their adjacent NW locations... As a consequence of this thermal runaway mechanism, a vertical crack gets created, leading to the breakdown of the network.

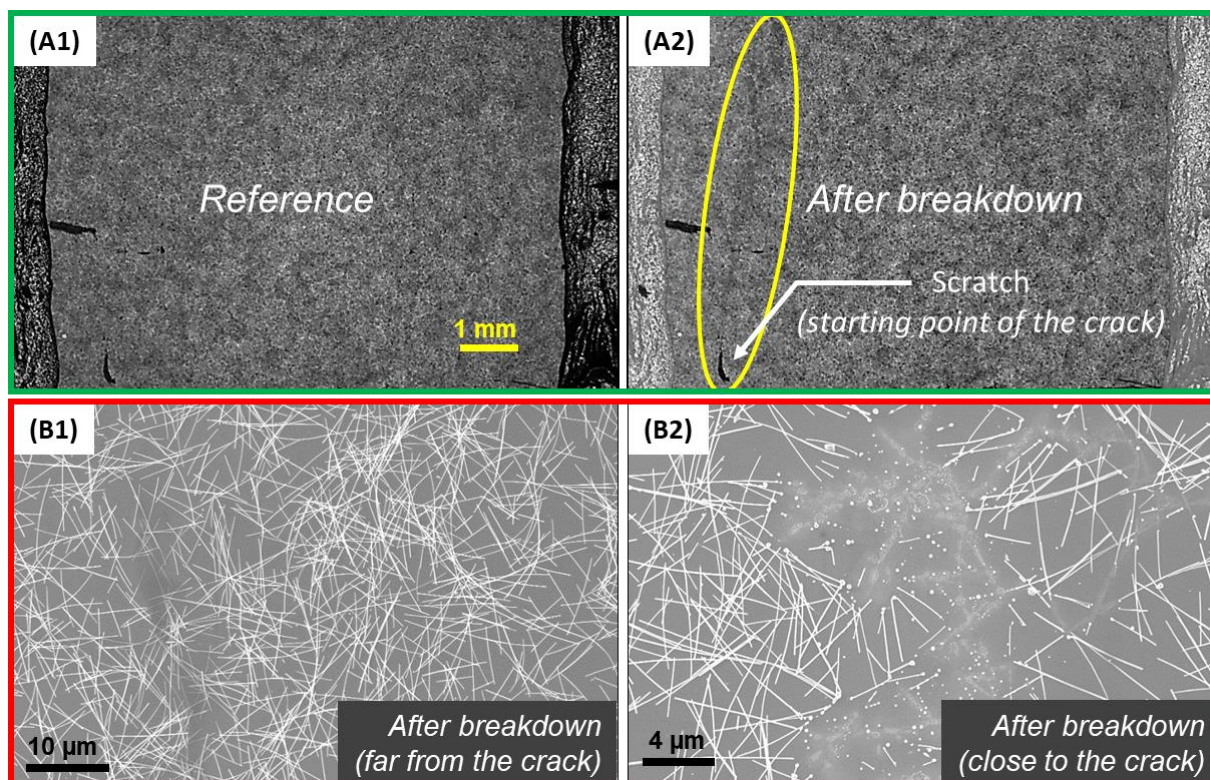


Figure 59. A) Pattern images associated with sample studied in Figure 58A, captured with the LiT set-up. Such pattern images exhibit the emissivity map of the sample before electrical plateaus (A1), and after electrical breakdown (A2). A vertical crack is clearly detectable after breakdown. B) SEM images of the sample after electrical breakdown: far from the crack ((B1), the NWs look non-deteriorated, while close to the crack (B2), the NWs appear fully or partially spheroidized.

In order to check these assumptions, supplementary tests combining electrical and either electrical (1P-mapping) or thermal (LiT) mapping have been performed. An AgNW network ($2.5 \times 2.5 \text{ cm}^2$, deposited on corning glass substrate) associated with an initial resistance of 26Ω was subjected to successive voltage plateaus while 1P-voltage mapping analysis was conducted between each plateau. In this case, the plateau duration was set to 10 min. Voltage value applied to the samples was successively 4, 8, 12, 16, 18, 20 and 22 V (see Figure 60A). Here again, the sample was placed on a metallic-based support. The results depicted in (A) shows that from 4 V up to 16 V, no optimization process of the sample can be detected. The steady-state temperature remains generally constant. A small increase can even be detected during the 8 V and 12 V voltage plateaus. During the 18 V plateau, the steady-state resistance starts decreasing, meaning that the sample is evolving towards a more optimized step. At 20 V, the resistance is not decreasing anymore meaning that the optimization process has been completed (see Figure 60B1). At 22 V the electrical resistance starts increasing slowly during 2 min, and

then much quickly (see Figure 60B2). As a consequence, the plateau was stopped before completion so that intermediate 1P-mapping could be performed to control the electrical distribution. 22 V plateau was then started again twice with early interruption in both cases to control the electrical distribution (see Figure 60B3-B4). It resulted in an accelerated increase of the electrical resistance at each step.

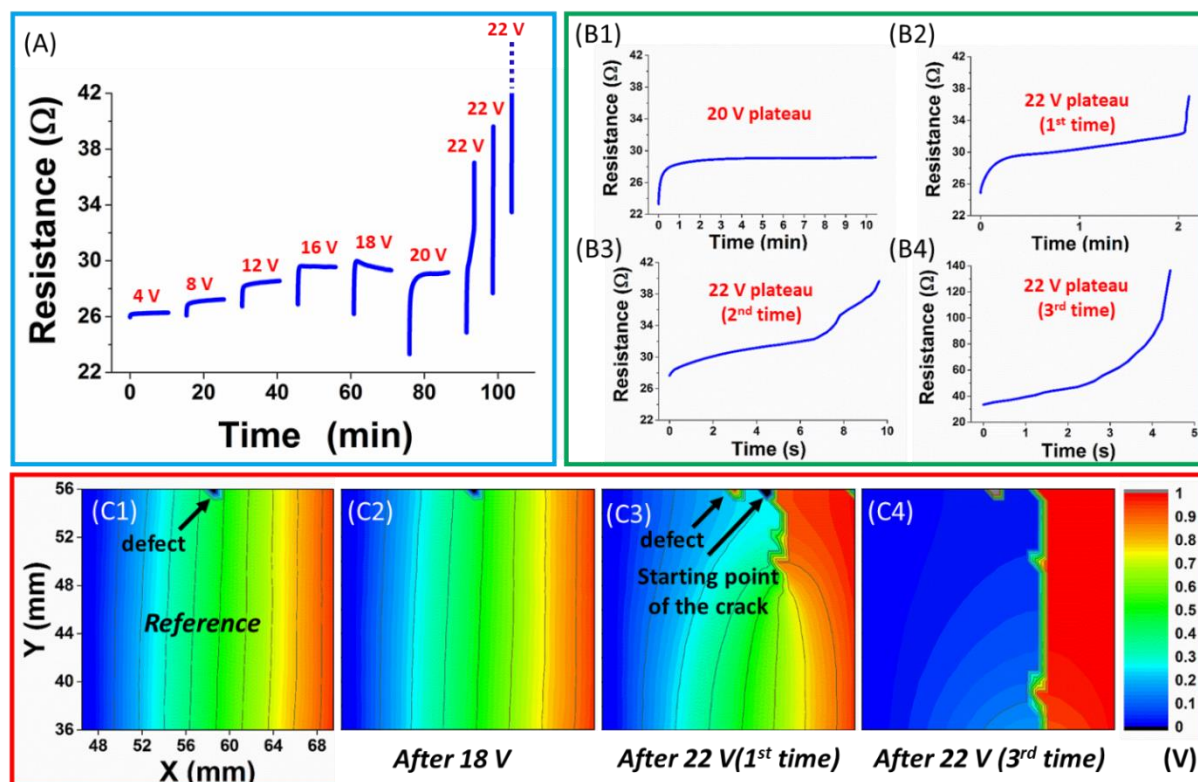


Figure 60. A) Electrical resistance of an AgNW network deposited on a metallic support, measured while voltage plateaus of 10 min each are successively performed from 2 V, up to electrical breakdown at 22 V. From 22 V, the voltage plateaus are stopped after a duration shorter than 10 min due to the quick increase of the electrical resistance. Between each plateau, no bias is applied anymore (except when the sample is subjected to intermediate 1P-Voltage mapping acquisition). B1-B4) Zoom in the 20 V (B1), 22 V-1st time (B2), 22 V-2nd time (B3), and 22V-3rd time (B4) voltage plateaus, respectively. C) Intermediate 1P-voltage mapping of the sample between the voltage plateaus (left electrode is connected to ground while 1 V is applied to right electrode). The images show the electrical equipotential lines against the coordinates (X,Y) of the sample for the following step: (C1) reference, i.e. before any voltage plateau, (C2) after 18 V voltage plateau, (C3) after 22 V - 1st time voltage plateau, and (C4) after 22 V - 3rd time voltage plateau.

1P-mapping revealed very helpful for analyzing and visualizing the mechanisms involved in the electrical breakdown of the sample. The electrical map captured after 18 V plateau (see Figure 60C2) is very similar to the reference map (C1). As already investigated in previous sections, for sample with such a low electrical resistance (26 Ω in the present case), the voltage equipotential lines are very straight. It is the same after the optimization process. At 22 V plateau, after detecting the fast increase of the electrical resistance ($t = 2$ min), the voltage was

immediately stopped. Electrical mapping performed thereafter yielded the detection of a partial “electrical potential crack” (C3). It can be assumed that the first hotspot reaching the spheroidization temperature was located in the top right part of the sample ($X \approx 62$ mm, $Y \approx 56$ mm), and that the thermal (electrical) runaway damaging process started from that point. It can be noticed that contrary to Figure 59A2 where the crack originates from a human-caused physical defect, here the crack does not originate from this type of defect which is clearly visible in the reference image ($X \approx 58$ mm, $Y \approx 56$ mm).

The same type of electrical mapping was performed after the third voltage plateau at 22 V. The latter was stopped in a very short time ($t \approx 5$ s) due to the very fast increase of the network electrical resistance ($R_{\text{final}} = 136 \Omega$). The corresponding electrical mapping (C4) exhibits a complete “electrical potential crack” along the entire width of the sample, in the extension of the previous partial crack (C3). Apart from the crack, in the left and right areas of the samples, the color is either almost fully “blue” or “red”, which means that the electrical potential of all nanowires is either 0 V (left part of the network) or 1 V (right part). This information suggests that apart from the crack, the morphology of the nanowires is safe and not impacted by the electrical breakdown. In the case some spheroidization had happened in some areas, the measurement of the electrical potential would have resulted in nonsensical values (see for instance the black points in Figure 54a, which appear at very low density). In the present case, the value is either 0 or 1, showing that apart from the crack, the network consists of safe and perfectly well interconnected nanowires. This is consistent with the SEM observations depicted in Figure 59B. Finally, Figure 60C4 suggests that the sample has totally “broken down”. The crack seems indeed almost completed. However, the final resistance measured is not so high ($R_{\text{final}} = 136 \Omega$). It means that electrical current is still able to flow through the network. It can be noticed that all the current flow lines are converging on the bottom part of the crack, meaning the huge majority of electrical power is distributed in the bottom part of the crack. More generally, it might exist some safe NW bridges across the crack where current can still flow. The latter are not detectable with 1P-mapping due to the limited probing resolution (0.5 mm).

For the sake of reproducibility, voltage plateaus combined with LiT analysis were also conducted on another AgNW sample associated with an initial resistance of 29Ω . In order to test the impact of the kinetics, the plateau was this time set to 1 h, which is much longer than for the tests reported in Figure 58 and Figure 60. During the first voltage plateau at 10 V, the steady-state electrical resistance remained quite stable (see **Figure 61A**). During the second plateau at 15 V, the latter started decreasing slightly (optimization process), and then increasing faster and faster until early electrical breakdown was achieved (after 15 min, see Figure 61B). As compared with the samples previously studied, the initial resistance of the present sample is the same range of magnitude (29Ω , whereas it was 33Ω and 26Ω in Figure 58 and Figure 60, respectively). However, the breakdown voltage in the present case (15 V), is significantly lower than the one associated with Figure 58 and Figure 60 (20 V and 22 V, respectively). This is very probably related to the extended duration of the voltage plateau in the present case.

Therefore, as expected, the electrical limitation of AgNW networks not only depends on the level of applied voltage but also on the duration of the electrical bias.

LiT acquisitions have also been performed in parallel to the voltage plateaus. Here again, the thermal map after 10 V plateau (C2) look as homogeneous as the reference map (C1). Moreover the acquisition performed immediately after breakdown did not result in any IR signal collection (C3). Unlike the three first LiT acquisitions (C1-C3) for which the applied was set to 0.5 V, another attempt was finally performed after breakdown, but using a much higher acquisition voltage at this time (5 V). Surprisingly, IR signal could be collected leading to the detection of a vertical crack as previously described in Figure 59 and Figure 60C4. Such an unexpected result suggests that the sample is likely to “awaken” after breakdown when subjected to significant voltage. In the same range of idea, it can be noticed in Figure 61B that after breakdown, the electrical resistance starts decreasing back from almost $10^7 \Omega$ down to $27 \text{ k}\Omega$. Such information suggests that contrary to what was firstly expected, the electrical failure of the network is not fully completed after the creation of the crack parallel to the opposite electrodes. More details about the electrical dynamics of the network after breakdown are provided in the next section.

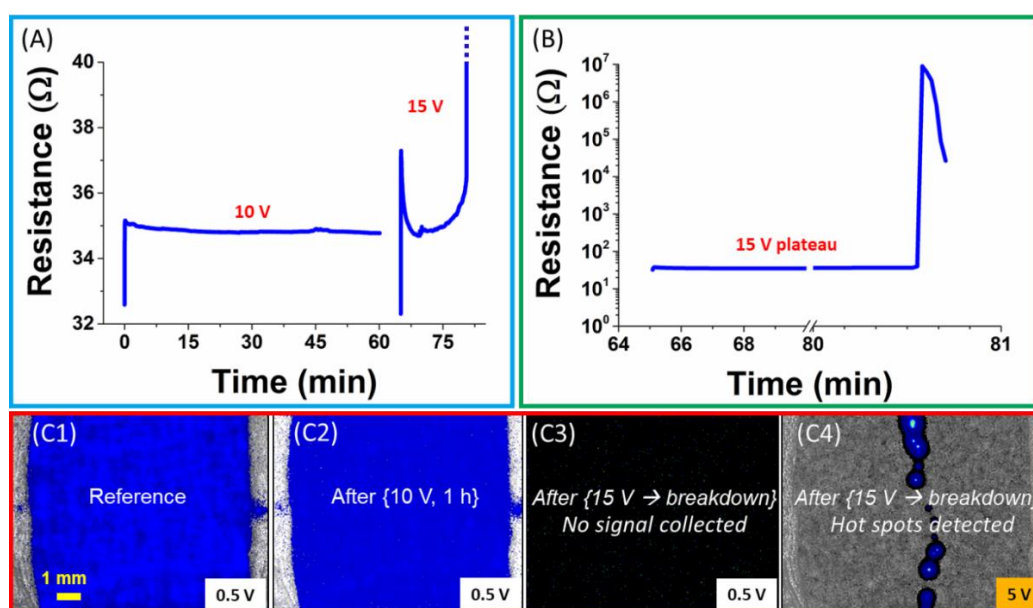


Figure 61. Electrical resistance of an AgNW network deposited on a metallic support, measured while voltage plateaus of 1h each are successively performed from 10 V, up to electrical breakdown at 15 V. Voltage duration at 15 V is much less than 1 h due to the early breakdown of the sample. Between each plateau, no bias is applied anymore (except when the sample is subjected to intermediate LiT acquisitions). B) Zoom in the 15 V voltage plateau. C) Intermediate LiT acquisitions mapping of the sample between the voltage plateaus. The images show the associated amplitude image at the following step: (C1) reference, i.e. before performing any voltage plateau, (C2) after 10 V voltage plateau, (C3) after breakdown (1st try), and (C4) after breakdown (2nd try). The voltage applied during the LiT acquisition was set to 0.5 V (C1-C3) or 5 V (C4).

4.2.3.3. “Life in the crack”

As already mentioned in previous section, even after electrical breakdown, it seems that the sample is still “alive” from an electrical point of view. This implies that the vertical crack is not fully completed. It might exist some AgNW bridges likely to allow current to flow. In order to get more information about the mechanisms taking place after breakdown, the sample depicted in Figure 60 for which breakdown occurred at 22 V (see Figure 60B4-C4) was further subjected to electrical tests. In order to have a live visualization of the electrical/thermal map during the voltage plateaus, an IR camera (FLIR A320G) was placed above the sample. The set-up for applying voltage was exactly the same as in the experiment associated with 1P-mapping described above (same source meter, contact probes, and steel-based support for the sample). At the end of the experiment depicted in Figure 60, the resistance measured under high bias after “preliminary” voltage breakdown was 136 Ω . **Figure 62** reports the electrical resistance measured after preliminary breakdown when either 3 V (A0), 8 V (B0), or 9 V (C0) additional voltage plateaus were successively applied to the sample for a certain duration. Several IR images captured with the IR camera are also provided and shows the thermal map of the sample at a selected time, during the different voltage plateaus at 3 V (A1-A4), 6 V (B1-B4), and 9 V (C1-C4).

First of all, at 3 V, according to the IR images, most of electrical current is flowing through the bottom part of the crack (A1-A4). This is coherent with the shape of equipotential lines depicted in Figure 60C4. Besides, since the applied voltage is not as high as before (3 V instead of 22 V), the electrical behavior of the sample is generally quite stable. It is not diverging anymore, meaning that the sample is not being damaged. On the contrary, some significant and intermittent drops in resistance can be observed in the curve, for example at $t = 12$ s, $t = 24$ s, $t = 29$ s, and $t = 45$ s (see A0). When trying to correlate this with the IR images, some small but clear hot spots (see arrows) can be detected (A3 and A5). Such secondary hot spots can stay either for a very short time (A3) or for several seconds (A5). The time sequences when these hotspots are visible in the IR camera fit exactly with the resistance drops depicted in A0. One reason for the later activation of such secondary bridges could be the prior deterioration of preferential bridges due to high current concentration. However, in the present case, the preferential bridge (at the bottom) does not turn off when secondary bridges get highlighted. Besides, once the secondary bridges turn off, the electrical resistance increases back to its initial value (A0). This means that no deterioration of the bottom bridge has occurred.

During the 8 V plateau, the electrical resistance increased very slightly (from 120 Ω to 162 Ω) until $t = 12$ s, and then increased dramatically (up to 1430 Ω) in a very short time (B0). Hence the experiment was stopped at this stage. On the IR images, it can be seen that the preferential cluster at the bottom is getting hotter and hotter (B1-B5). The Joule-induced deterioration in this area might be responsible for the high increase in resistance at the end. It also has to be noted that at 8 V, several secondary hot bridges can be detected even in the early stage of voltage application. Such bridges “woke up” at higher voltage (8 V) whereas they were inactive at lower voltage.

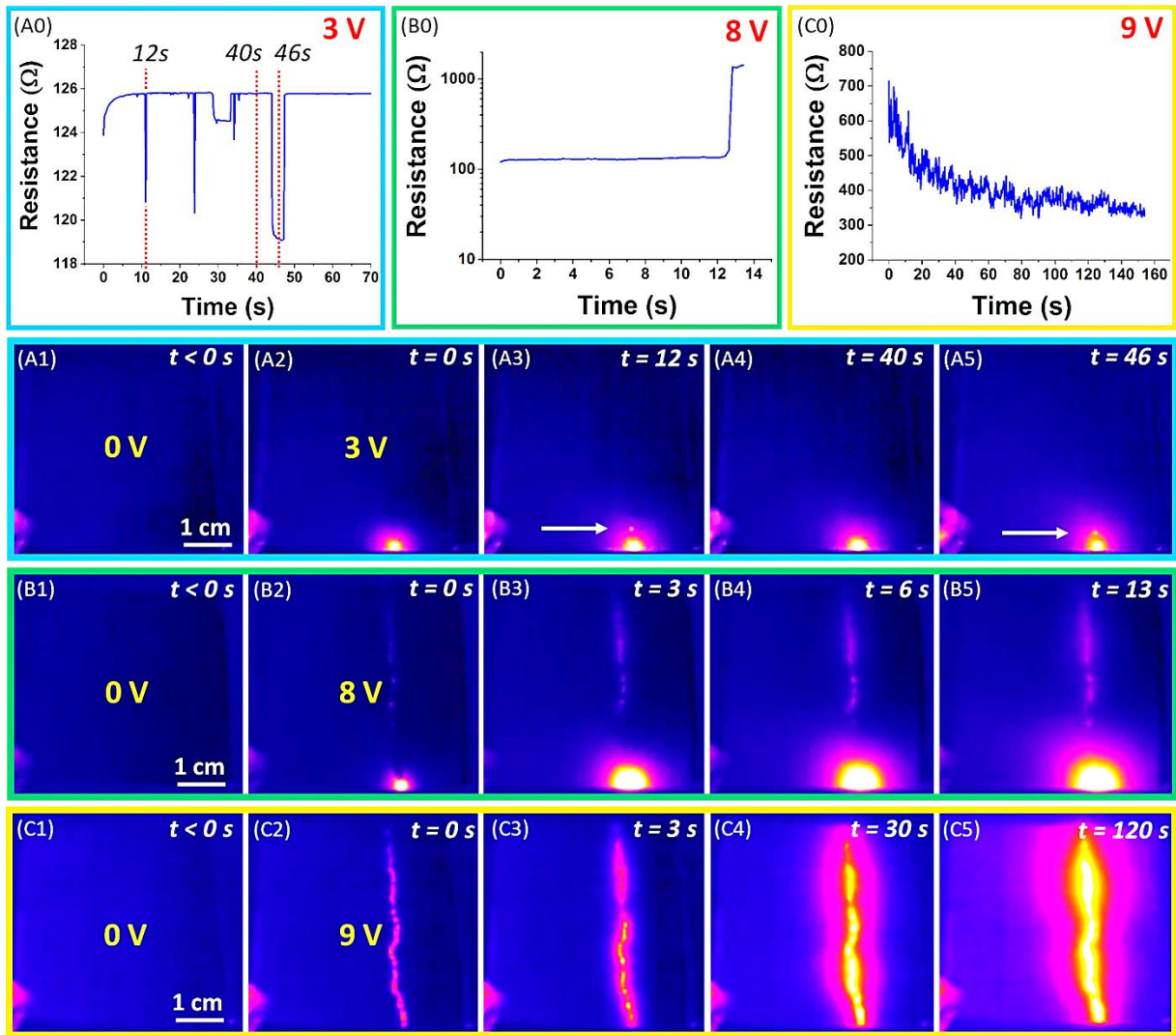


Figure 62. A0-C0) Evolution of the electrical resistance of the same AgNW network as iFigure 60n Figure 60 during additional voltage plateaus at 3 V (A0), 8 V (B0), and 9 V (C0), performed after that preliminary electrical breakdown had occurred. A1-A5). IR images captured with the IR camera during voltage plateau at 3 V: (A1) just before voltage application, (A2) just after voltage was turned on, (A3) at $t = 12$ s, (A4) at $t = 40$ s, (A5) at $t = 46$ s. B1-B5) same as (A1-A5) but with voltage application of 8 V and at different times. C1-C5) same as (A1-A5) but with voltage application of 9 V and at different times.

Surprisingly at 9 V, the resistance starts decreasing back (from 714 Ω down to 334 Ω). On the corresponding IR images (C1-C5), the main hot spot at the bottom is not detectable anymore. Once again, some damage might have taken place in this area inducing the increase of resistance detectable in (B0). On the contrary here, electrical current seems to be much more equivalently distributed in several secondary bridges along the crack. As long as some more bridges “wake up”, more and more conductive paths are available for current, leading to the decrease in resistance.

Beyond the influence on the overall electrical level, such unexpected behavior provides interesting information about how electrical current is able to dynamically redistribute itself

over the network. The secondary hot spots detected first in A3 and A5 and later in C2 indeed consist of NW cluster-based bridges, not preferentially used as conducting pathway by electrical current at the beginning, but likely to be used once other preferential pathways are not suitable anymore. The same kind of observation using LiT was observed when studying further the sample depicted in Figure 61 after breakdown. The reasons to why such bridges are not continuously active, as well as the statistics and probability of activation, remains not yet understood and would require further experiments. Some more SEM investigation were conducted in the area of the vertical crack associated with sample depicted in Figure 61 after breakdown (see **Figure 63**). In some areas, the wires look fully spheroidized (see the red circles in a), while in other areas, the nanowires look only “partially” spheroidized (b, c). Several connections made of very thin metallic filaments can be detected between the wires (see the yellow circles in c), while the wires exhibit much more uneven surface than usually. Such intermediate and local destruction might originates from the high speed associated to the electrical breakdown process. Once the voltage limit is reached, the spheroidization can start. However, due to the creation of the crack and the associated electrical/thermal runaway mechanism, the spheroidization of AgNWs cannot be fully completed in some areas. From an electrical point of view, such filaments are much more resistive as classic NWs. For this reason, such bridges might not be preferentially chosen by current after breakdown. The latter might be associated with the so called “secondary” bridges mentioned above. Here again, these hypothesis require further investigation to be validated.

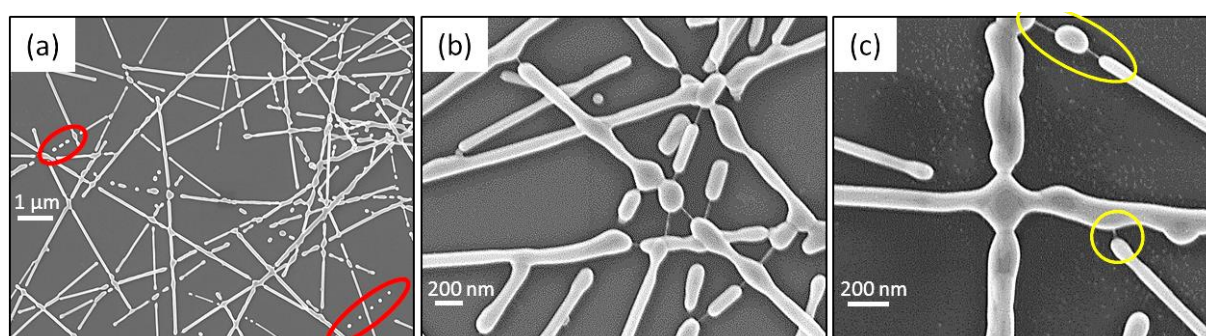


Figure 63. *a-c) SEM images associated with the AgNW network depicted in Figure 61 after electrical breakdown. These three images have been captured along the area of the vertical crack. They show a combination of fully spheroidized nanowires (a) – red circles, together with “partially” spheroidized nanowires (b-c) as well as the presence of small filaments (yellow circles) much smaller than AgNWs themselves.*

4.2.4. Conclusion and outlooks

The influence of several parameters (network density, level of junction optimization, input power) on the electrical and thermal distributions in AgNW networks was deeply studied in this section. 1P-electrical mapping was found very relevant for extracting the voltage equi-potential lines in AgNW networks under bias. Voltage equi-potential lines are found to be substantially straighter when increasing the NW density, leading to a higher electrical homogeneity.

Similarly, LiT analysis confirmed experimentally that the electrical/thermal distribution associated to AgNW networks is much more homogenous after optimization by thermal annealing. Simulations using the Comsol electrical model were also used to evaluate the impact of network density and junction optimization on the network electrical homogeneity, leading to a good correlation with experimental results. In future studies, electrical homogeneity of AgNW networks should be quantified more rigorously, for instance by estimating the tortuosity of voltage equi-potential lines. Moreover, the thermal model developed in Comsol should also be improved to better mimic the thermal behavior of AgNW networks, and even anticipate the parameters influencing their thermal homogeneity.

Such imaging tools were also found very helpful for highlighting the effects of electrically-induced instabilities in AgNW networks at high voltage. More specifically, the formation and propagation of a crack parallel to the bias electrodes could be visually evidenced. However, it seems that many safe AgNW bridges are still available along the crack, allowing electrical current to flow through the network even after breakdown. The origin of such bridges and more generally, the electrical behavior of AgNW networks after breakdown is still under investigation.

In future works, issues about electrical/thermal distribution and stability should also be considered after final encapsulation of AgNW networks, i.e. after deposition of an additional protecting thin layer. Besides, while many efforts focused on electrical mapping at the scale of the electrode (macroscale), one should also devote attention to the characterization of electrical distribution and stability of AgNW networks at the nanoscale. For instance, ongoing project consists of studying *in situ* the local electrical ageing of AgNW networks, using charge contrast imaging technique under SEM (see more details in the thesis conclusion).

Chapter 5. Stretching properties of AgNW-PDMS composites: preliminary results

From a technological point of view, emerging TCMs made of AgNW networks attract intense attention because of their competing optical and electrical properties but also because of their very promising mechanical properties, very convenient for the increasing demand for flexible and even stretchable electronics. Flexibility and stretchability are two specific potential mechanical assets related to some TCMs (and other type of thin films). As already reported in section 1.1.5, an important asset of AgNW networks is their very high level of flexibility. When deposited on polymeric substrates such as PEN or PET, AgNW networks have proved to sustain hundreds of bending cycles to a radius of curvature of 5 mm without having their electrical resistance decreased.^[30] On the contrary, ITO is known for being very brittle. Beyond their flexibility, AgNW deposited onto elastic substrates, such as polydimethylsiloxane (PDMS) have also proved to exhibit interesting stretching capability.

This section focuses on the study of the stretching properties of AgNW-PDMS composites. It constitutes preliminary results ever obtained in the team concerning this topic. A quick state-of-the-art regarding the stretchability of AgNW-based composites is firstly provided (section 5.1). Details related to the fabrication protocols and the stretching tests performed during this thesis are discussed thereafter (section 5.2). Then, the evolution of AgNW network electrical performances while stretching cycles are performed is deeply described. Emphasis is made on the impact of the AgNW network density on the composite stretchability (section 5.3). In order to better understand the stretching limitations and the mechanisms involved in deformation and even failure of such composites, *in situ* SEM observations have also been conducted within the frame of this thesis. The corresponding nano/micro characterization results are presented and discussed in section 5.4.

5.1. Fabrication, properties and applications of AgNW-PDMS stretchable conductors: short state-of-the-art

The proper adhesion or incorporation of AgNWs into elastic substrates is a critical issue. Several techniques have been reported in the literature to fabricate suitable AgNW/Polymer-based stretchable conductors. For example Hu et al. prepared AgNW-crosslinked-polyacrylate composites and used UV irradiation to cure the polymer and separate the AgNW-polymer from the glass substrate.^[221] Another reported technique is the vacuum filtration transfer of AgNWs directly on an elastic PDMS film ^[154,222]. However the most widely reported preparation technique consists of first, depositing liquid PDMS onto a AgNW network, then curing the polymer at certain temperature for certain time, and finally peeling it off so that the NWs can be transferred from the initial substrate (usually glass or silicon) to the polymer.^[222–226] The related schema is presented in **Figure 64**.

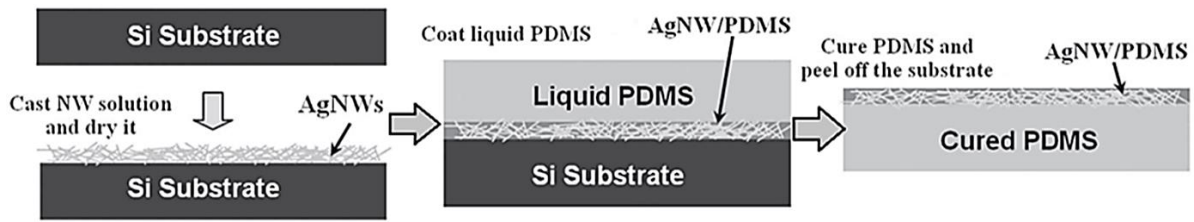


Figure 64. Schematic illustration of the fabrication process of AgNW-PDMS stretchable conductors.^[227]

Other works focused on the enhancement of the electrical stability by pre-straining the polymer substrate prior to the NW deposition and prior to the step of transfer.^[226,228,229] Ho et al. showed that using “wavy” nanowires is suitable for applications requiring large strain since the associated irreversible increase in electrical resistance occurs at larger strains. They fabricated a strain gauge with high sensitivity/gauge factor and tested it on human neck for detection of throat movement.^[229] Huang et al. used a pre-straining and post-embedding process to fabricate AgNW-PDMS nanocomposites for smart clothing that maintains a very stable resistance value up to 80% strain.^[224]

Reversible stretchable transparent conductive coatings were also reported. For example, such coatings exhibited 80% of transparency while maintaining their conductivity safe up to 15% of elongation. On the other hand, other coatings fabricated with a higher quantity of AgNWs exhibited 35% of transparency (\approx opaque films) but could sustain up to 30% of reversible elongation.^[230] This shows that the amount of nanowires plays a critical role in the electrical robustness of AgNW-PDMS under stretching stress. It seems that achieving high reversible elongation requires fabricating a composite made of very dense AgNW network, leading to low value of transparency. As a consequence, a trade-off between the optical transparency and stretchability should be found according to each specific application. Such a trade-off should be assessed in terms of AgNW network density.

Example of stretchable optoelectrical devices integrating AgNW networks, such as elastomeric OLEDs, have already been provided in section 1.2.2 (see Figure 7).^[28] Besides, Hong et al. recently fabricated AgNW-PDMS structures used as transparent and stretchable heater. The resulting device exhibited fast thermal response and was found able to endure repeated large mechanical strain up to 60% with small variance in the resistance. Corresponding IR thermal images at 0% and 60% strain are reported in **Figure 65**.^[154] This shows that stretchable conductors can be suitable for a wide variety of applications, including “thermotherapy”. Another example of applications was investigated by Song et al. They fabricated a class of microstrip patch antennas that are stretchable, mechanically stable and reversibly deformable.^[231]

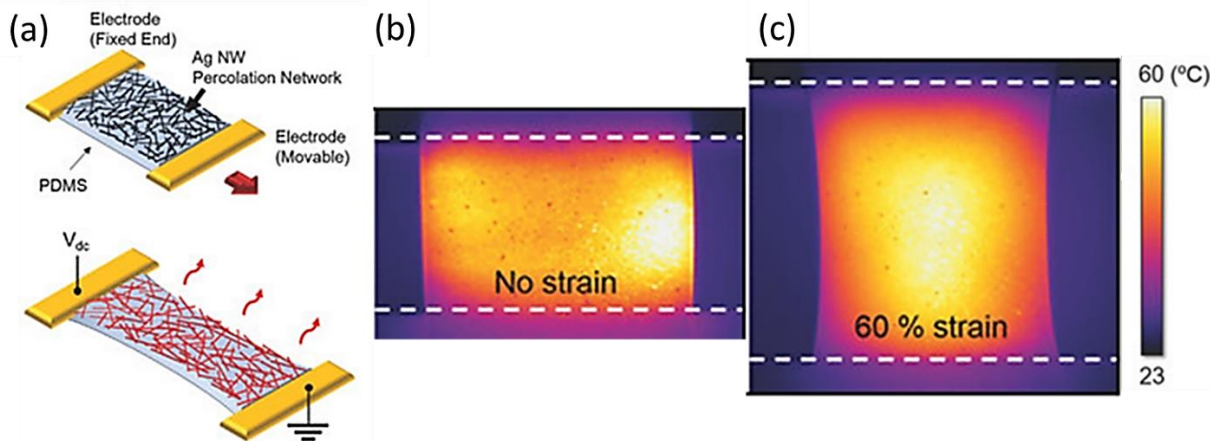


Figure 65. a) Schematic illustration of the stretchable and transparent heater composed of an AgNW percolating network on a PDMS film. b) IR image of an AgNW/PDMS stretchable and transparent heater operating at 60 °C with no strain (b) and at 60% strain condition (c).^[154]

From a fundamental point of view, Xu and Zhu observed *in situ* the surface morphology of the AgNW-PDMS layer during stretching/releasing/re-stretching cycles via optical microscopy and examined its buckled wavy shape further with SEM and cross-sectional SEM imaging (see **Figure 66**).^[227] The weakening and detachment of the NW contacts result in a smaller overall contact area between NWs. Thus it leads to the increase of electrical resistance. It has to be mentioned that such an increase in the observed electrical change is not related to any contribution of the NW plastic deformation under strain, as measured by Zhu et al.^[232]

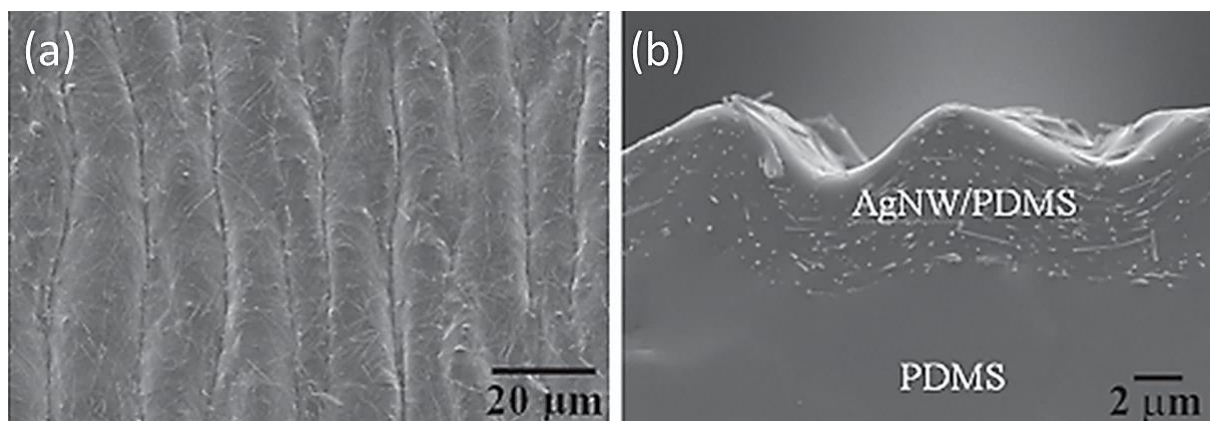


Figure 66. a) SEM image of the AgNW/PDMS surface after the stretching and releasing cycles. The image was taken by tilting the sample at an angle of 20°, b) Cross-sectional SEM image of the AgNW/PDMS layer.^[227]

As demonstrated above, the use of stretchable hybrid composites based on AgNW networks seems very promising for a wide variety of devices. However, a rigorous investigation of the physical mechanisms involved in the stretching properties and limitations of such films is still

missing. Even though the previous paragraph reports some interesting preliminary information, some of this thesis work was dedicated to the analysis of physical mechanisms associated to AgNW-PDMS composite films when subjected to stretching stress. Details about fabrication, stretching set-up, and experiments performed in this frame are provided in next sections.

5.2. Protocols

5.2.1. AgNW-PDMS composites preparation

When fabricating AgNW embedded-PDMS composites, several parameters along each step are likely to influence the performance of the resulting elastic electrode. These are discussed in parallel to the description of the fabrication process. A general schema of the fabrication technique has already been presented in section 5.1 (see Figure 64).

(i) Liquid PDMS preparation

PDMS is one of the most widely used silicon-based organic polymer. When fabricating PDMS dedicated to the mechanical tests of the present study, the base and the cross linking curing agent (Sylgar® 184 silicone elastomer kit) are mixed together in a ratio 10:1. This is the standard ratio used to prepare PDMS as it was reported in several research articles about AgNW-PDMS composites.^[154,223,224,226,227,230,233]

(ii) PDMS deposition on AgNW network and curing

The as-prepared liquid PDMS is then deposited directly onto an AgNW network (glass substrate) by spin coating (1500 rpm for 30 s). The fabricated samples prepared have a relative small size (maximum 5×5 cm²). Thus a large drop of liquid PDMS (around 3-5 ml) is enough to uniformly recover the entire AgNW network. According to other reported protocols, PDMS is sometimes directly cast on the AgNW networks.^[224,227]

After liquid deposition, the PDMS has to be cured. During heat treatment, the curing agent forms cross links in the elastomeric substrate and the PDMS becomes highly elastomeric.^[223] The reported temperature and duration of the treatment vary. In the present study, heating at 160 °C for 30 min in a furnace were the experimental conditions selected, resulting in satisfying performance of the fabricated PDMS. Other studies report 200 °C for 20 min,^[230] 150 °C for 30 min,^[224] 100 °C for 1 h,^[231] 55 °C for 2 h,^[233] 60 °C for 2 h,^[154] 70 °C for 3h,^[226] 65 °C for 12 h,^[227] 120 °C for 12 h.^[223]

(iii) Separation from glass substrate and pre-annealing effect on transfer efficiency

The critical final step consists of successfully and safely transfer the AgNWs, and to do so the AgNW-PDMS adhesion should be favoured compared to the AgNW-glass adhesion. For this purpose, the AgNWs deposited on glass substrate and coated with the cured PDMS are immersed into a heated de-ionised water bath, which is favourable for the AgNW detachment from the substrate. The water is heated up to 50 °C. This water-assisted transfer process was deeply investigated by Kim et al.^[223] According to their experimental investigations, the important factor is not the time of immersion into water but the temperature of the water. The best transfer efficiency was achieved when heating the water bath up to 50 °C. Explanation is based on a thermodynamic approach dealing with the surface tension between the 4 different elements: water, AgNWs, PDMS and glass.^[223]

Pre-annealing treatments of AgNW networks were also tested in order to evaluate the impact of sintering the NW junctions (prior to transfer to PDMS) on the stretching properties of the resulting AgNW-PDMS composite. Pre-annealing of AgNW networks revealed to dramatically influence the transfer process success. In most cases, the pre-sintered AgNW networks were only partially and non-uniformly transferred to the PDMS, in such a remarkable degree that some NW clusters left in the glass substrate could even be visible to the naked eye. It seems that thermal annealing is responsible for increasing the adhesion forces between the AgNWs and the glass substrate so much that the classic protocol is not appropriate for a successful transfer of AgNWs from glass substrate to cured PDMS. However, since it might be really favourable for the resulting electrical properties of the stretchable electrodes to use perfectly sintered AgNWs, further investigation regarding the optimisation of the transfer process is still required. For example, testing different experimental conditions for the steps of PDMS curing and AgNW transfer should be tried in order to succeed in the pre-annealed network transfer onto PDMS.

5.2.2. Stretching tests presentation

To perform stretching tests, the AgNW-PDMS composites are horizontally fixed into two metallic jaws (see **Figure 67a-b**). One of these jaws is motionless while the other can either move away from the other one (stretching) or go back to the starting point (release). Such jaws displacements are driven via physical connections with a motor. The latter is automatically driven by a PC via a LabVIEW program (see the schematic representation of the setup in Figure 67a). Finally, it is possible to measure the electrical resistance behaviour during the mechanical stress. The metallic jaws are indeed electrically connected to a Keithley 2400 sourcemeter, able to input voltage and measure *in situ* the electrical resistance during the experiments.

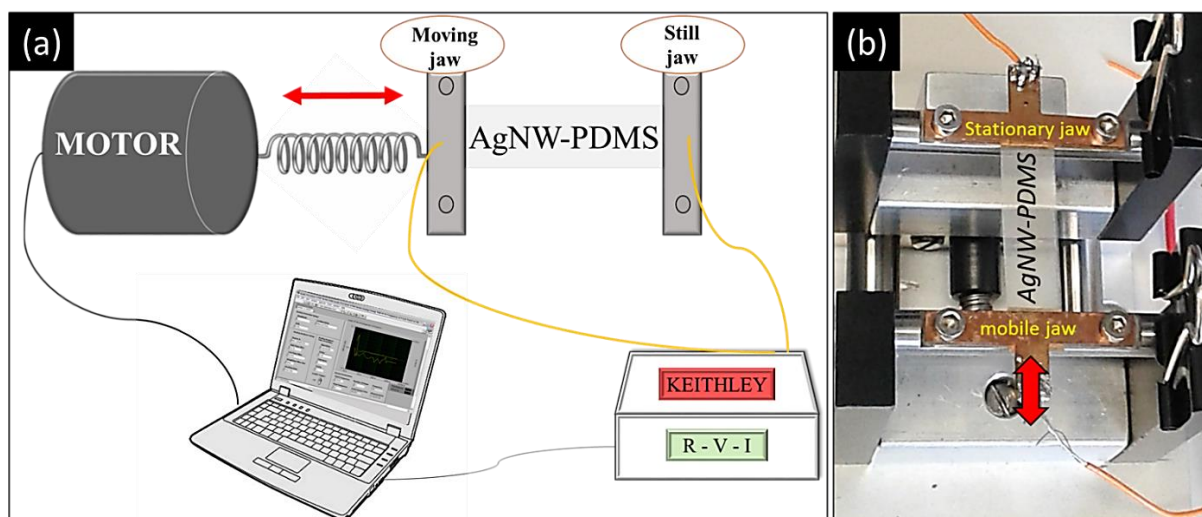


Figure 67. (a) A schematic representation of the mechanical strain set-up. (b) Image showing an AgNW-PDMS sample fixed into the stationary and mobile metallic jaws.

In this study, two different types of stretching tests were performed using the mechanical set-up described above. Generally, the samples are cut in pieces of 1 cm width and 3 cm length between the contacts. The first type of tests (“test n°1”) consists of performing successive series of 100 stretching cycles with increasing elongation: 100 cycles at 5% of elongation, then 100 cycles at 10% of elongation, then 100 cycles at 15% of elongation, and so on... Between each series of 100 cycles, 20 cycles at 0% of elongation (i.e. no strain) are performed as a way to control the electrical properties of the electrode after release. Each cycle is quick: the speed of the moving jaw during a stretching cycle was measured to be close to 1.5 cm s^{-1} . Between each cycle, the electrical resistance is measured thanks to a Keithley source meter (see Figure 67a). Applied voltage when measuring the resistance is set to be 1 V. As a consequence, test n°1 provides information about the electrical stability of AgNW-PDMS released composites, when subjected to successive stretching stress. **Figure 68a** provides an example of experimental results associated with test n°1.

The second type of tests (“test n°2”) consists of performing very slow stretching/releasing cycles while measuring the electrical resistance during the cycles (and not only between the cycles as it is done in test n°1). Applied voltage when measuring the resistance is also set to be 1 V. More specifically for test n°2, a maximum elongation value is carefully selected and 10 cycles of slow stretching (up to the maximum elongation) and releasing (down to 0% elongation) of the elastic AgNW-PDMS composite, are successively performed. Two different speeds values can be used for the stress: 0.004 cm s^{-1} and 0.008 cm s^{-1} . Contrary to test n°1, here the resistance is measured continuously while the sample is under stress (one measurement every second). Hence, test n°2 reveals the electrical behaviour of AgNW-PDMS composites when directly subjected to stretching and releasing stress.

Figure 68b provides an example of results associated with test n°2. In this figure, the tested AgNW-PDMS composite originates from the same sample as the one reported in Figure 68a. The speed used is 0.008 cm s^{-1} .

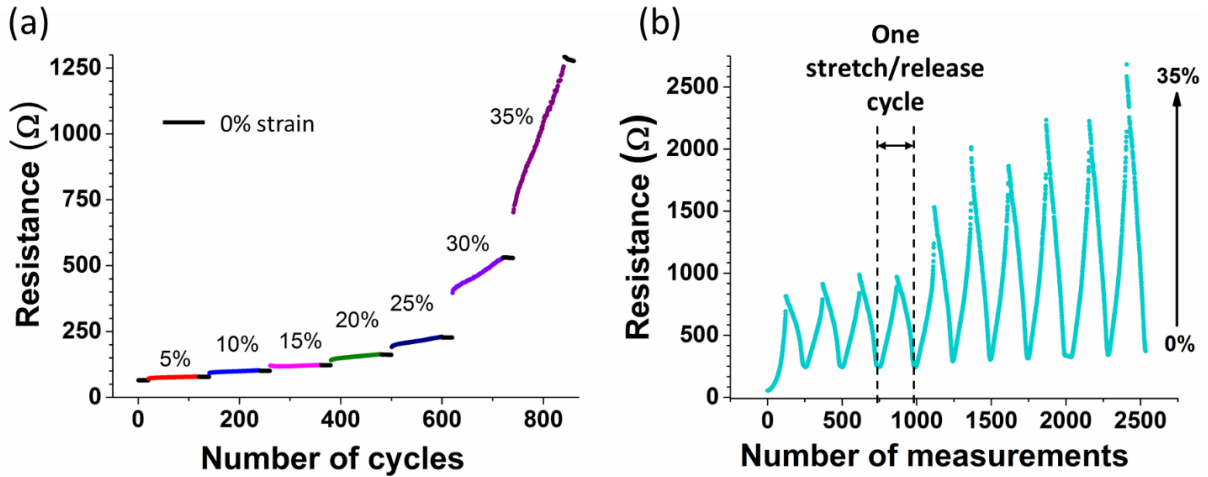


Figure 68. Evolution of the electrical resistance of 2 different pieces originating from the same AgNW-PDMS sample, under two different stretching tests: a) the resistance is measured at the end of each elongation cycle (after release) from 5% to 35%. For each successive value of elongation, 100 cycles are performed. Between each series of 100 cycles, 20 cycles-resistance measurements (at 0% of elongation) are performed. b) The resistance is measured every second during 10 cycles of slow stretching/releasing strain at 35%.

5.3. Impact of the NW density on the stretching properties

Several AgNW-PDMS composites were subjected to test n°1 and test n°2 described above. In order to highlight the impact of AgNW network density on the stretching properties, a series of networks with varying density were fabricated using CEA NWs and spray-coating deposition process. The AgNW-PDMS thin films were fabricated as described in section 5.2.1. Gold contact electrodes were deposited by evaporator. The samples were firstly classified according to the number of spray coatings performed during the deposition process (3 to 6 coatings for the 4 studied samples, respectively). In order to take into account the step of transfer in the estimation of the density of the resulting composite, the geometrical density d_g , and finally the areal mass density (mg m^{-2}) associated to each fabricated samples, were extracted after transfer by capturing SEM images and then by performing ImageJ analysis (see Appendix B).

The order of amd values calculated after transfer of AgNW networks from the glass substrate to the PDMS were different from the expected ones, i.e. not coherent with the number of spray-coatings used for initial AgNW deposition. Probably the AgNWs were not 100% properly transferred to PDMS in some cases (as already mentioned in previous section, the step of transfer still needs to be optimized). However, the initial resistances of each fabricated AgNW-PDMS composites were found to be low, i.e. ranging between 20 and 80 Ω . The samples were finally divided in smaller pieces so that the two specific sorts of test can be performed on each of them. Slight differences in their final sizes could be noticed between the different samples. For comparing properly the impact of the density on the stretching properties, it was then necessary to get rid of the impact of the samples dimensions in the measurement of the electrical resistance. For the sake of comparison, all the measured resistances were “adapted” as follows:

$$R_a = \frac{R_{measured}}{L/W} \quad (5.1)$$

where R_a is the “adapted” resistance, $R_{measured}$ is the resistance measured by the Keithley sourcemeter, L and W are the length and width of the sample, respectively. In this way, the “adapted” resistance is not influenced anymore by the sample dimensions. Furthermore in order to facilitate the comparison, the final results presented in **Figure 69** are the corresponding normalised resistances (% of increased resistance) calculated as follows:

$$\frac{\Delta R}{R_{a,0}} = \frac{R_a - R_{a,0}}{R_{a,0}} \quad (5.2)$$

In Figure 69a, the normalised resistance calculated while test n°1 is performed, is plotted against the number of cycles with increasing elongation values up to 30%. When achieving this maximum elongation value, the electrical resistance of the first three networks reaches the k Ω range. A general trend can be identified: the denser the AgNW network, the more electrically stable the AgNW-PDMS composite under strain. Indeed the electrical resistance associated with the denser network was initially 21 Ω , and remains below 100 Ω until 30% of elongation, while the resistance measured at 30% of elongation for the sparser samples is 500 Ω , 1 k Ω and 1.5 k Ω , respectively. As well, the denser network exceeded 1 k Ω only at 60% elongation. When focusing on the two sparsest samples of the series (60 mg m⁻² and 69 mg m⁻²), at first glance it seems that the results associated with test n°1 do not follow the same tendency regarding the density impact on the stretching properties. Indeed, even though the network with the lowest density had higher initial resistance, it showed lower percent increase during the strain test n°1. This can be attributed to statistical fluctuations and to the fact that their associated values of *amd* are quite close to each other. Anyway, when compared to the other two networks associated with denser networks, the impact of the density on the electrical stability under stretching is significant. It has been further tested and confirmed.

The results associated with test n°2 are presented in Figure 69b. Two samples originating from the same bigger composite as in test 1 were tested under slow stretching/releasing cycles. The networks with *amd* 60 mg m⁻² and 128 mg m⁻² suffered 10 cycles until 30% elongation. Here again, the denser network shows a higher tolerance under strain, which means that the resistance increase induced by stretching is lower. For the denser network, the resistance at 0% after release is also found to be closer to the initial one. Besides, it has to be noticed that the electrical resistance of the two specimen is decreasing while the AgNW-PDMS composite is being released. Even though the electrical resistance reaches very high values (in the range of k Ω and even M Ω) at the maximum of elongation, the resistance decreases to a low value when the sample returns back to 0% elongation. Moreover, once having performed the very first cycle, the samples seem quite stable thereafter since the resistance keeps returning back at the same level after each new cycle. This large difference in the values of the resistance between maximum elongation and 0% elongation should be further investigated. Such electrical behavior suggests that from a mechanical point of view, both destruction and repair process might take place in the AgNW-PDMS composites when either stretched or released. For this purpose, *in situ* characterization by SEM was conducted. The corresponding analysis is presented and discussed in the next section.

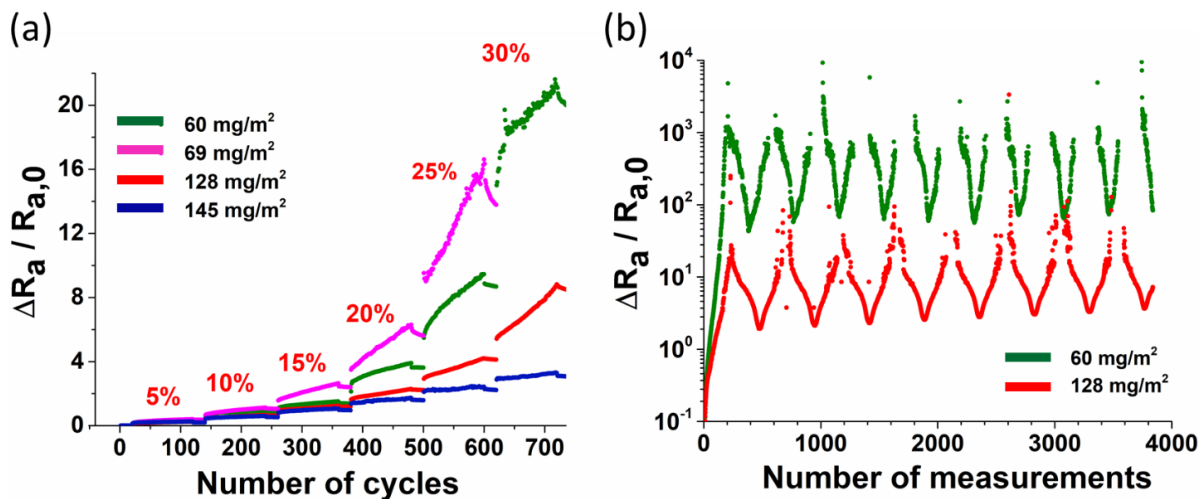


Figure 69. a) Normalized resistance (measured after each stretching/releasing cycle) of AgNW-PDMS composites associated with different network densities and for different elongations. 100 cycles are performed for each elongation, while 20 cycles at 0% are performed before increasing the elongation value. b) Normalized resistance of AgNW-PDMS composites of different network densities under 10 cycles of stretching/releasing until 30% elongation. The resistance is measured every second.

5.4. *In situ* characterization of the mechanical deformations

The nano/micro scale mechanical deformations of AgNW-PDMS composites under strain were observed with the help of Francine Roussel at CMTc. A sample with an AgNW areal mass density of 128 mg m^{-2} was subjected to slow stretching/releasing cycles (like in test n°2), and analysed *in situ* with a SEM (ZEISS Gemini SEM 500) equipped with a traction set-up (see **Figure 70a**). The stretching process was paused in several elongation levels (5%, 10%, 15%, 20%, 25%, 30%, 35%, 40% and back) in order to observe *in situ* the mechanical deformations of the AgNW network and the PDMS substrate. Figure 70b-c depicts the evolution from 0% to 15% of elongation in a certain region. Until 15%, no significant change was observed neither in the polymer nor in the AgNWs.

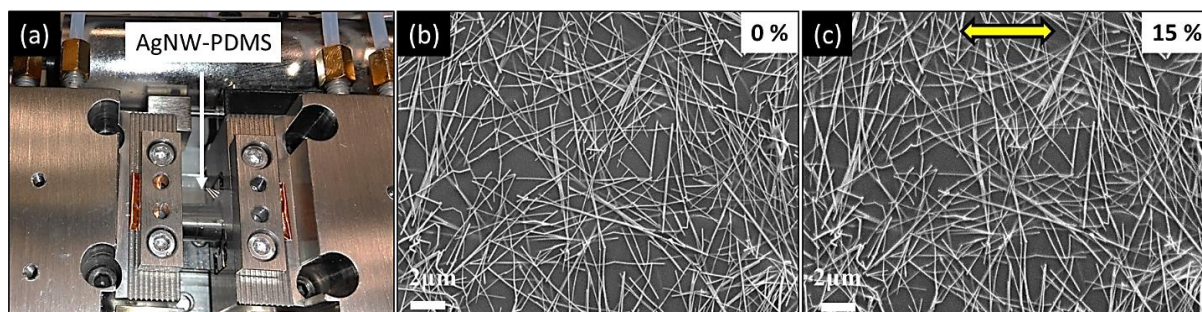


Figure 70. a) Image showing an AgNW-PDMS sample fixed into the jaws of the *in situ* SEM traction set-up. b,c) SEM images of the same region of an AgNW-PDMS composite under stretching: at 0% (a), and at 15% (b) of elongation. No observable changes can be detected. The double arrow indicates the direction of strain.

When focusing on the same area during the strain, a huge crack in the polymer substrate could be detected between 15% and 20% elongation. Another one appeared at 25% elongation (see **Figure 71**). It was first believed that such cracks were induced by strain effects only. However, the latter also revealed to be induced by the extended observation of the same area under SEM. The heat generated by focused electron beam coupled with mechanical strains yielded early damage process via the appearance of huge cracks. The area between the cracks was therefore drastically released. Thus no deformation could be observed between the cracks anymore. Figure 71a-b shows the cracks in polymer, while Figure 71c consists of a zoom in the unaffected (released) region between them. By focusing later on other areas, the general deformation behaviour of the AgNW-PDMS composite could be observed after 20% stretching.

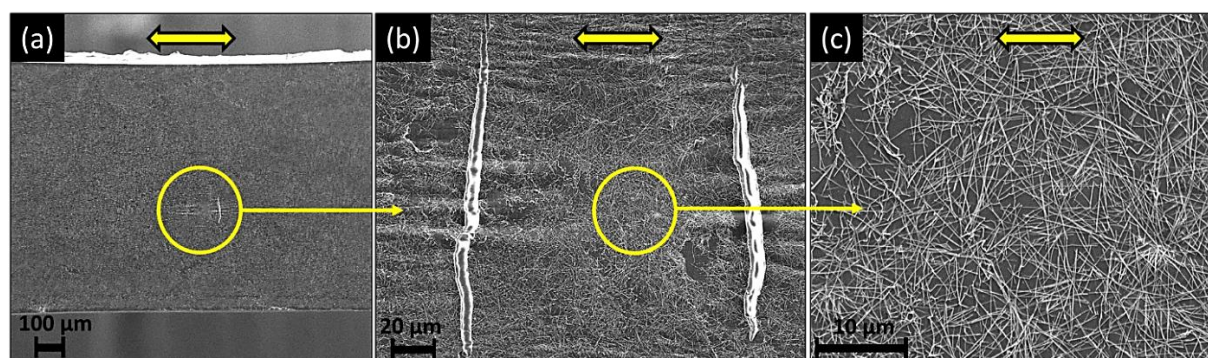


Figure 71. SEM images of an AgNW-PDMS composite under stretching at 25% of elongation: a) general view of the sample, b) zoom in the big cracks on the polymer substrate, induced by the electron beam exposition during an extended time, and c) zoom in the released region between the cracks. The double arrow indicates the direction of strain.

As shown in **Figure 72A1-A2**, at 40% of elongation the surface of the polymer became wavy. Moreover, small cracks could be detected all over its surface, perpendicular to the direction of strain force. Consequently, the NWs were broken and displaced. This can explain the high increase in electrical resistance that was observed during test n°2 at large elongation. The NWs breaking and displacement destroy the percolation paths and the resistance reaches values in the range of MΩ or GΩ. Besides, it justifies the impact of the AgNW network density on the electrical stability under strain: the denser the network, the higher the number of strongly interconnected percolating paths at the surface of the composite, and the higher the probability that some of them stay safe even at very high elongation. In Figure 72A1-A2, some other small deformations can be detected parallel to strain force. However the latter seems to induce much less damage to the AgNW network than the perpendicular cracks.

During the release process, scars in the PDMS are still present but the gaps previously created at maximum elongation get much narrower. This is well depicted in Figure 72B1-B2. It seems that some of the AgNWs previously broken are touching each other again (B2), which is favourable for renewing electrical percolation. This could indeed explain the decrease in electrical resistance when the AgNW-PDMS composites are been released (see test n°2). Electrical current can flow again through the nanowire networks. As a consequence, the

electrical resistance decreases back to relatively low values (see Figure 69b). It does not reach resistance values as low as the initial ones (before stretching) since the junctions between the NWs are not as in intimate contact as before. The contact quality between the NWs is much lower after the first stretching/releasing cycle. As a consequence, the electrical resistance returns to a higher value. Finally, it is important to note that once the very first stretching/releasing cycle has been performed, the increase in electrical resistance after each stress cycle becomes almost negligible (see Figure 69b), meaning that most of the cracks and damages take place only along with the first cycle.

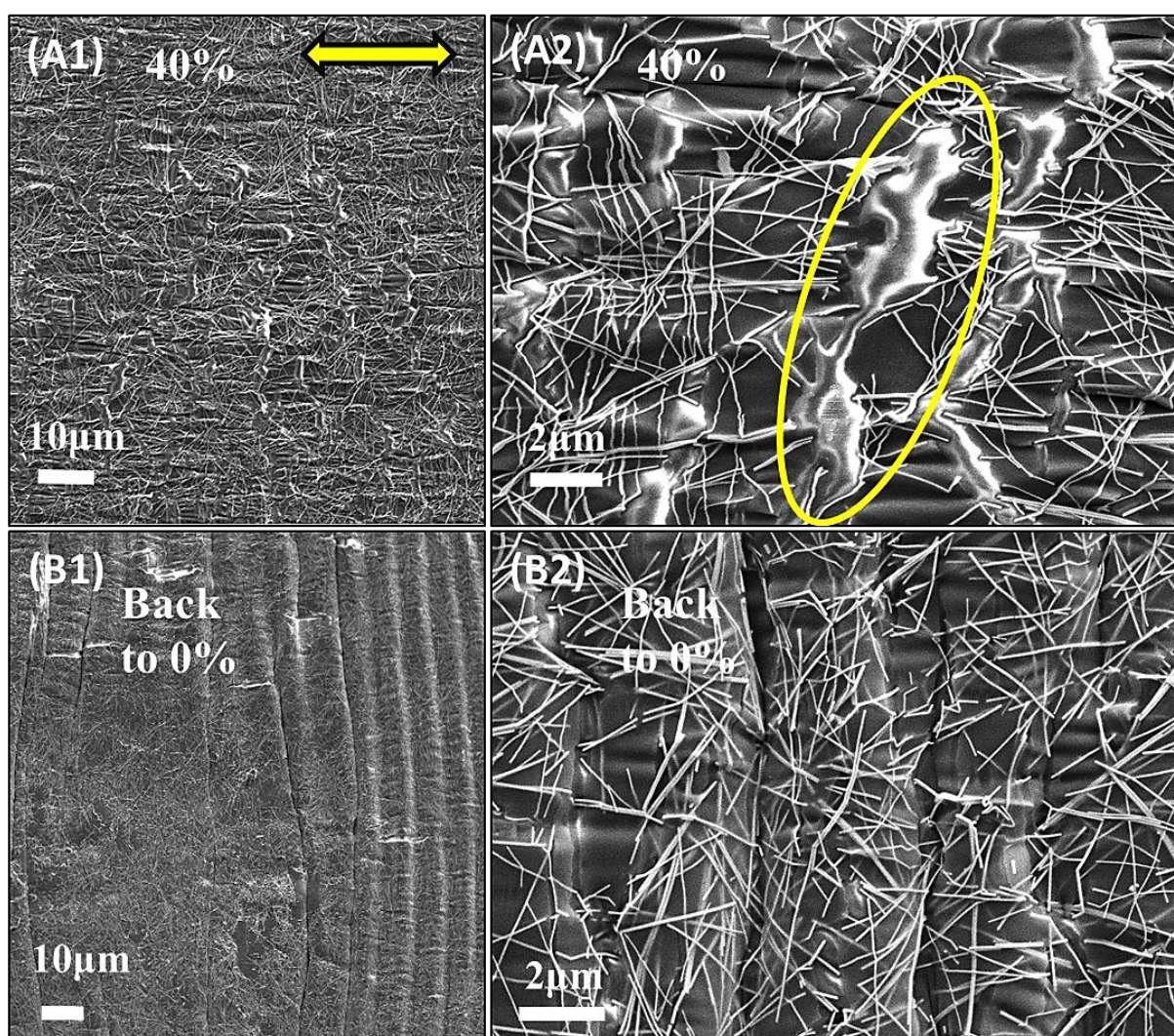


Figure 72. A1) SEM image showing the mechanical deformation of the AgNW-PDMS composite at 40% of elongation. A2) SEM image showing several breaks in the structure, caused by the PDMS substrate deformation at 40% elongation. B1) SEM image of an AgNW-PDMS composite after stretching up to 40% and releasing back to 0% elongation. B2) SEM image after zooming in the areas close to the polymer's cracks that have begun to "heal" after release. The double arrow indicates the direction of strain.

5.5. Outlooks

This study consists of the very first attempt in the laboratory to perform stretching tests on AgNW networks. Some important information could be extracted, especially regarding the impact of the AgNW network density on the stretching properties of AgNW-PDMS composites. However, some of the general physical properties of fabricated composites, such as optical performance, electrical behaviour during thermal annealing, or Young modulus, are still missing. The latter are to be investigated in a close future.

Besides, further investigation is needed in order to reveal better the role of each parameter likely to influence the electrical performance of such composites under strain. The NW dimensions, and especially the NW length, may also strongly influence the stretchability of such composites.^[222,234] From a technical point of view, the use of contacts other than the ones deposited by evaporation is still required. It is indeed necessary to perform such kind of stretching experiments by using contacts which are able to withstand high stretching stress without damage. More specifically, eutectic alloy of Gallium Indium (EGaIn) should be tested. This metallic paste revealed to be highly conductive and elastic at the same time, and was found suitable for several stretchable devices.^[227] Some experiments with EGaIn contacts are being performed at the moment in the laboratory.

Finally, regarding the applications, while AgNW networks on glass or PEN substrate have proved to efficiently shield electromagnetic signals in the radio-frequency range, the shielding effect of AgNW-PDMS under stretching stress has not been reported so far in the literature and would constitute a natural way to pursue the present work. More generally, the trend for portable and wearable devices requires to increase the conformability of integrated materials. For instance, the efficiency of transparent film heaters is intimately related to their ability to conform to the surface about to be heated (helmet visor, windscreen, clothes or human skin for thermotherapy). Due to their high level of flexibility and stretchability, transparent electrodes made of AgNW-PDMS composites might fulfil these conformability requirements.

Chapter 6. Applications

Many efforts during this thesis were devoted to a deep investigation of the literature dealing with the integration of AgNW networks into devices. The resulting state-of-the-art was as exhaustive as possible and gave rise to the publication of a review article in the journal *Small* mostly focused on the wide variety of applications using AgNW-based transparent electrodes.^[30]

From an experimental point of view, most of the work reported and discussed in previous chapters was entirely dedicated and linked with future applicative uses of AgNW-based transparent electrodes. Chapter 2 discussed the best combination of techniques to optimize both electrical and optical properties. Good mastering and knowledge of the physico-chemical mechanisms and limitations involved when such treatments are performed are indeed mandatory for efficient processing and integration of AgNW networks into devices. Chapter 4 discussed the distribution of electrical current into AgNW electrodes according to the AgNW network density, and the junction efficiency. Here again, it is also mandatory for most of the target applications to master the parameters which influence the electrical homogeneity of the network. Chapter 4 also focused on the failure dynamics and its influence on the electrical/thermal distribution at rather high voltage, which is also generally a critical information for fabricating safe, durable, and powerful AgNW-based devices. Finally, preliminary investigations about the stretching properties of AgNW-PDMS composites are also aimed at estimating the potential and limitations of AgNW integration into stretchable devices, for which the market demand is drastically increasing. This is reported in chapter 5.

As a consequence, this final chapter follows on from previous discussions about efficient integration of AgNWs into devices. Before starting this thesis in 2014, several examples of successful integration of AgNW electrodes into devices had already been reported in Grenoble, especially by Simonato group (CEA-Liten), with emphasis on flexible transparent heaters,^[14] capacitive touch sensors,^[26] and organic solar cells.^[30] Within the frame of this thesis, a deep investigation of the mechanism leading to failure in AgNW based-transparent film heaters (TFHs) was performed at LMGP in close collaboration with Mélanie Lagrange, giving rise to a recent publication.^[31] Given that most of experimental work as well as the major part of scientific analysis were conducted by Mélanie Lagrange, the corresponding results are not discussed in detail in the present thesis. In the very first section of this chapter (6.1), the most important results obtained in the team, as well as on-going research and outlooks related to TFH applications are only briefly discussed.

Apart from transparent heaters, most of the applicative work carried out during this thesis focused on trying to open new applicative routes for AgNW networks in the field of radio-frequency (RF) applications, with special emphasis on antennas and electromagnetic shielding. Preliminary investigations and results obtained about these two types of devices are discussed in section 6.2 and 6.3 thereafter.

6.1. AgNW-based transparent film heaters (TFHs)

The principle of AgNW-based TFHs and literature about this field of applications were detailed in section 1.2.3. When applying voltage to the electrode, it consists of taking advantage of Joule effect to heat the surrounding transparent substrate. In order to measure *in situ* the Joule effect-induced elevation temperature, the sample is connected to an external Keithley 2500 sourcemeter driven by a Labview software sending the desired voltage instructions, while a 120 μm thick resistance temperature detector (RTD) is placed underneath the sample (see **Figure 73a**). Figure 73b represents the elevation temperature associated with an AgNW network whose initial resistance is 27 Ω at room temperature, when successive short voltage plateaus (5 min) are applied, up to 5 V.^[31] The elevation temperature can reach almost 90 $^{\circ}\text{C}$ at 5 V, and is associated with a heating rate of about one degree per second in air. When the same experiment is performed under vacuum (see red curve), the resulting elevation temperature is found higher than in normal room conditions. This is due to fact that heat losses by convection are cancelled under vacuum.

Most of the recent works carried out in the team and mostly conducted by Mélanie Lagrange, consisted of understanding the mechanisms leading to failure in AgNW-based TFHs and finding solutions for increasing both electrical and thermal stabilities of such devices.^[24,31] When short voltage plateaus are applied, the heating process seems perfectly reversible at low voltage. The elevation temperature decreases back strictly to its initial value when voltage is decreased (see Figure 73b). However, it was noticed that when longer voltage plateaus are applied (45 min instead of 5 min), the electrical resistance starts increasing linearly during the plateau. This phenomenon is more and more obvious as the voltage value gets higher (see the green dashed lines in Figure 73c). This is attributed to the occurrence of irreversible damaging process across the network (either early spheroidization of AgNWs or electromigration process). As the consequence, when voltage is decreased back, the resistance does not return to its initial value. So does the elevation temperature.^[31] Finally, an efficient solution to enhance the thermal and electrical stability of AgNW-based TFHs was to deposit a very thin (≈ 5 nm) layer of TiO_2 by Atomic Layer Deposition (ALD). As depicted in Figure 73d, coating of TiO_2 layer was responsible for increasing the voltage breakdown limit of devices observed during voltage ramp from about 7 V up to 13 V, without altering optical transmittance of the electrodes.

The fundamental description of AgNW-based TFHs (section 1.2.3) along with all the experiments performed by Mélanie Lagrange was precious for building the thermal simulation model in Comsol (section 3.3.4). In particular, the experimental analysis performed in normal and vacuum conditions were helpful for estimating the convective heat-transfer coefficient h . Generally speaking, the thermal model was developed in order to estimate both the elevation temperature and associated thermal map according to the NW dimensions, network density, nature of the substrate, applied voltage, and any other parameters likely to influence the thermal behavior of AgNW-based TFHs. As already mentioned, the thermal model provides interesting preliminary information but still needs to be improved to complete these requirements.

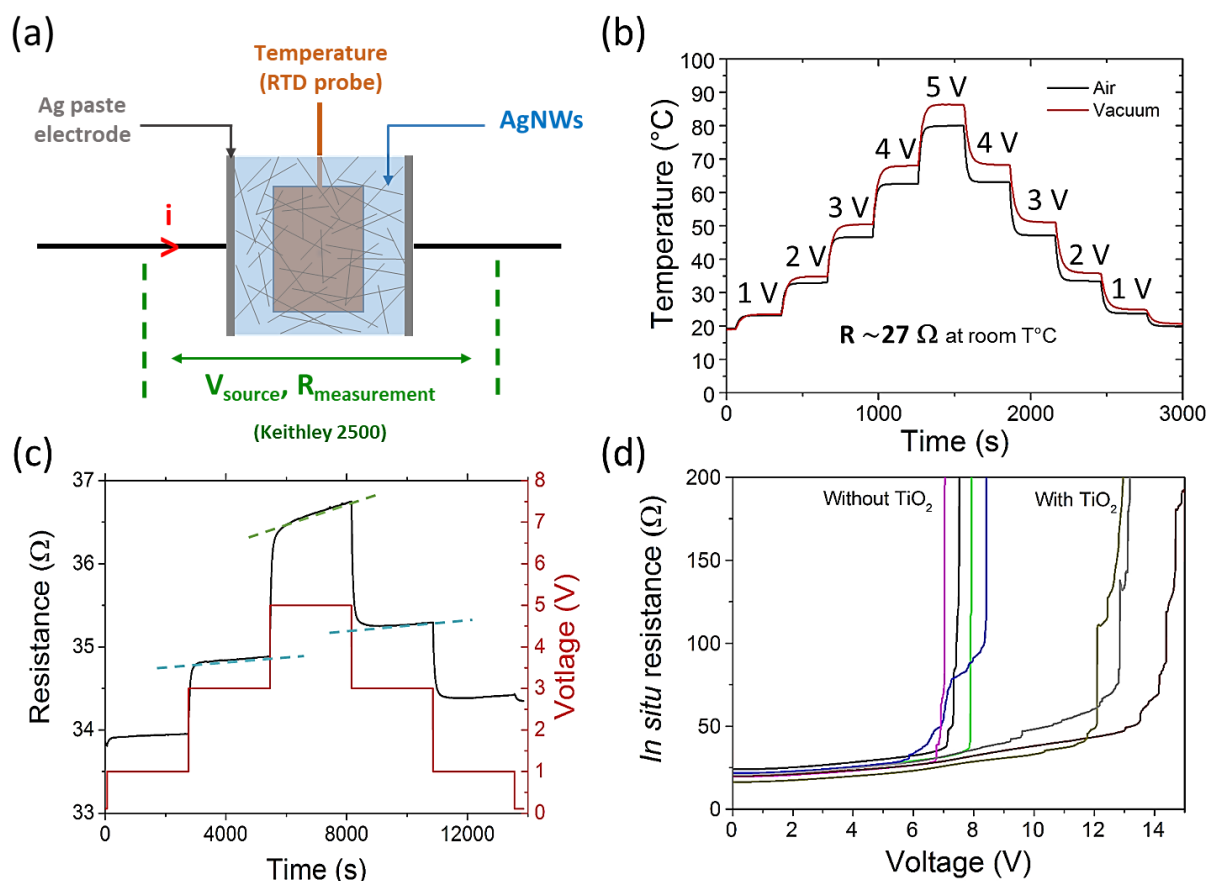


Figure 73. All content extracted or adapted from Mélanie Lagrange thesis.^[24] a) Schematic representation of the set-up used for testing AgNW-based TFHs. b) Temperature elevation of an AgNW network in air and in vacuum, when submitted to increasing and decreasing voltage plateaus (1 V up to 5 V) during 5 min. c) Electrical resistance behavior of AgNW-based TFHs when longer voltage plateaus (45 min) are applied. Electrically-induced irreversible effects can be detected (see dashed lines). d) Effect of 5 nm TiO₂ ALD coating on the electrical resistance of several AgNW networks spray-deposited on glass during a voltage ramp of 0.1 V min⁻¹.

From an experimental point of view, several tests were performed during this thesis to evaluate the impact of environmental conditions on the electrical stability of Liten AgNW-based TFHs. For this purpose, a 5x5 cm² AgNW network with *amd* equal to 115 mg m⁻² was fabricated by spray-coating and cut into four 2.5x2.5 cm² identical samples. Their initial electrical resistance was measured to be very similar, and close to 10 Ω (see the exact values below). Three of them were subjected to similar electrical stress which consisted of successive voltage plateaus (2-4-6 V, etc.) until electrical breakdown of the sample was achieved. The duration of each of the plateau voltage was 10 min, with a 5 min-pause at V = 0 V between 2 successive voltage plateaus. The electrical stability of these three samples was evaluated under different environments described thereafter:

- Sample 1 (R₀ = 11 Ω): ambient atmosphere, no support (the sample is “in the air”)
- Sample 2 (R₀ = 14 Ω): vacuum, no support (the sample is “in vacuum”)
- Sample 3 (R₀ = 12 Ω): ambient atmosphere, sample deposited on a metallic support.

The electrical performances of the networks are expected to be different according to the environment. So is the voltage value at which the networks undergo electrical breakdown, i.e. the voltage limit above which the electrical resistance is diverging. The more the environment conditions facilitate thermal losses, the lower the AgNW network temperature, and the higher the voltage value associated with spheroidization/electromigration and electrical breakdown. In the case of “in air” network, convective losses help reducing the temperature elevation. In the case where the network is deposited onto a metallic chuck (or anything that is highly thermally conductive and having as well a larger thermal inertia than the substrate), then the conduction losses towards the chuck help reducing the elevation temperature as well. As a consequence, it is expected that sample 2 “breaks” before sample 1, and that sample 3 “breaks” at last. Such difference in terms of electrical level and limitation is clearly visible in **Figure 74**.

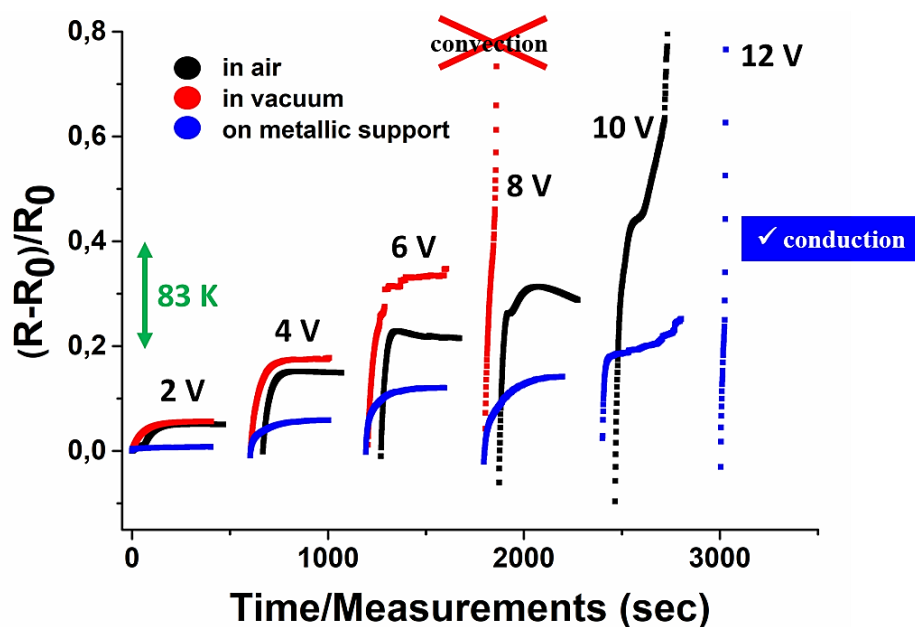


Figure 74. Normalized electrical resistance associated to Liten AgNW networks with same network density and NW dimensions, measured during successive voltage plateaus under 3 different conditions: no support and in atmospheric conditions (black), no support and in vacuum (red), when deposited on a thin metallic support and in atmospheric conditions (blue). The initial resistance of the samples, R_0 , is 11 Ω (black), 14 Ω (red), 12 Ω (blue). For the sake of comparison, the green double arrow indicates the temperature elevation corresponding to an increase of 0.2 in the normalized resistance (when considering a β value of $2.4 \times 10^{-3} \text{K}^{-1}$).

The electrical breakdown occurs at 12 V for sample 3 (blue curve) instead of 10 V for sample 1 (black curve). Moreover the increase in resistance during the bias is less important when the network is deposited on the metallic chuck: due to the faster heat transfer by conduction, the temperature associated to the network is lower and then there is less electron-phonon scattering occurring inside the network. On the other hand, there are no convection losses under vacuum,

thus the temperature of the network and the substrate associated to sample 2 is higher. As a consequence, the increase in resistance against the voltage is more important, leading to the earlier electrical breakdown at 8 V (red curve). In Figure 74, the vertical double arrow indicates what is the temperature elevation (83 K) corresponding to a reversible increase of 0.2 in normalized electrical resistance due to phonon-induced scattering. The calculation is based on Equation 2.1, and by considering that the temperature coefficient of resistivity β is equal to $2.4 \times 10^{-3} \text{ K}^{-1}$ (see section 2.1.2.2).

On-going research performed in the team on AgNW-based TFHs also concerns the study of defects creation across the network, the failure dynamics at both low and high voltages, and finding new routes for protecting final devices from early electrical or thermal instabilities. Research work is aimed at mastering conditions to propose devices as efficient, stable and durable as possible. Regarding the device efficiency, efforts in simulation are pursued in order to optimize the thermal model so that the best combination (trade-off) of experimental parameters leading to the highest overall heating performance and homogeneity can be found. Regarding the stability, it has already been demonstrated that AgNW-based TFH performance is reversible at low voltage (up to 5 V) when only short electrical stress are applied (10 min). However, even at low voltage (5 V), evidence of irreversible damage can be detected when long duration electrical stress (45 min) are applied.^[31] At higher voltage, a thermal/electrical runaway process has been evidenced (**Figure 75a**).

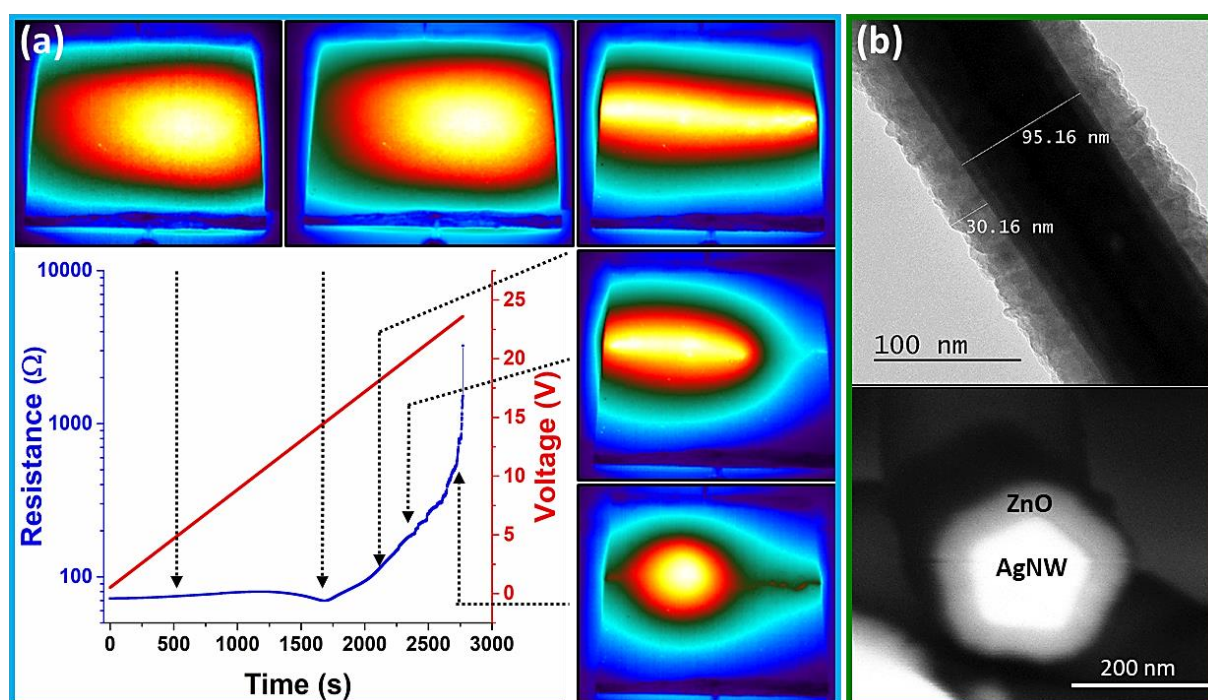


Figure 75. a) Evolution of the electrical resistance of an AgNW network when subjected to a voltage ramp of 0.5 V min^{-1} . Thermal maps captured in situ with a live IR camera are provided at specific times. b) TEM (top) and SEM (bottom) images showing a top view and cross section of an AgNW coated with a ZnO thin layer deposited by SALD.

IR imaging is classically used for assessing the spatial homogeneity of AgNW network based TFH and has been often employed in literature.^[143,235] Live IR thermography can as well be very helpful to describe the failure dynamics at rather high voltage. While the electrode thermal map is very homogenous at the beginning of the voltage ramp, the heat distribution tends to narrow in the central part of the network in parallel to the contact electrodes, resulting in a vertical crack. Successive thermal maps while voltage is increased up to breakdown are provided in Figure 75a. Such process has already been tackled from a fundamental point of view in section 4.2.3. Such phenomenon should be considered here too, when integration AgNW network into real TFH devices.

More generally speaking, the origin of any instability that results in early failure rates, is linked either to silver atomic surface diffusion, electromigration processes, or modification of the surface chemistry. As already mentioned above, TiO₂ coating deposited by temporal ALD was found efficient for improving the stability of AgNW-based TFH devices. However, a new generation ALD technique, called “Spatial ALD” (SALD) appeared lately and a set-up has been recently developed at LMGP by David Muñoz-Rojas.^[236] SALD does not require any vacuum condition and is much faster than conventional ALD. Moreover, the resulting coating have proved to be very conformable, homogenous and reproducible.^[237] LMGP PhD students Viet Huong Nguyen and Sara Aghazadehchors, as well as visitor Dr. Afzal Khan, are currently working on trying to encapsulate AgNWs with various metal oxide-based coatings deposited by SALD such as ZnO (see Figure 75b), Al₂O₃, or TiO₂, to test their protecting properties.

Finally, AgNW-based TFHs will not be commercialized without any encapsulation layer. This is due to both stability considerations (see previous paragraph) and security reasons (to avoid any physical contact between AgNWs and the users). Therefore, the characterization of both performance and stability of AgNW-based TFHs should be achieved considering the entire device, i.e. with the encapsulation layer.

6.2. AgNW-based antennas and transmission lines: preliminary attempts

The literature about RF antennas using AgNW networks is not abundant. The most interesting contributions in this application field were reported in section 1.2.5.2. In the majority of works dealing with AgNW network-based antennas, the main efforts were devoted to reduce as much as possible the return losses, S_{11} , which is used to characterize the amount of incident signal reflected at the entry of the antenna, and expressed in dB as follows:

$$S_{11} = 10 \cdot \log \left(\frac{P_r}{P_i} \right) \quad (6.1)$$

Where P_r is the reflected power and P_i is the incident power. In the case where S_{11} is low enough (generally below -10 or -15 dB), it can be considered that impedance match is completed. The resonant frequency corresponds to the frequency value at which the lowest value of S_{11} is reached, leading the highest radiation performance of the antenna. Several papers showed that S_{11} can be decreased by increasing the smoothness of the surface of the AgNW-based antenna.^[186,187] Other contributions demonstrated that when using an elastomeric substrate such

as PDMS, applying deformation strain to the antenna induces a shift in the resonant frequency, giving rise to potential interest in sensing applications.^[188,189]

However, in most cases the silver content used was too high to ensure optical transparency of the resulting device. Given that the radiation performance of an antenna is directly linked to the electrical conductivity of its radiating element, it is believed that the trade-off usually used for optoelectronic devices (solar cells, LEDs, etc.) between optical transmittance and sheet resistance does not lead to radiation performance high enough in the case of AgNW antennas. To our knowledge, this transparency issue has been overcome in only one case by using wavy AgNWs instead of “straight” AgNWs.^[29]

Generally speaking, the electromagnetic (EM) performances of AgNW networks have never been studied in detail. Several parameters like Joule effect losses or dielectric losses in this frequency range are still missing. In order to better understand the potential and limitations of such AgNW antennas in terms of both radiation efficiency and optical transparency, a collaboration between LMGP, IMEP-LaHC, and CEA-Liten laboratories was started. Each of the RF measurements reported in the present section (as well as in next section about EM shielding) were carried out with the help of Alejandro Niembro, a former PhD student at IMEP-LaHC, as well as Tan Phu Vuong and Philippe Ferrari, Professors at IMEP-LaHC too.

6.2.1. Antenna fabrication and measurement procedure

Radiative elements of the antennas consisted of spray-coated AgNW networks with various electrical performances on Corning glass substrate (1.2 mm thick), with the help of a mechanic mask to ensure that the desired antenna design can be fulfilled (see **Figure 76a**). In very few cases, a thin layer of PEDOT-PSS (Clevios PH1000) thin encapsulation layer was also spray-deposited on top of AgNW networks. In each case, the ground plane of the antennas consisted of a 2×5 cm² very thin {Ti (10 nm), Au (100 nm)} layer deposited at the device’s back-side by Physical Vapor Deposition (PVD), from glass substrate extremity to a distance of 2 mm from the radiating element. The transmission line consisted of a 2 mm-width material connection between the substrate extremity and the radiative element. Some tests were performed using transmission lines made of interconnected AgNWs only. Some other antennas were fabricated using a transmission line coated with additional thin Ti/Au PVD on top of AgNWs. Finally, a connector is fixed at the extremity for transferring incident signals to the antenna (see **Figure 76a**). A small silver paste droplet is added lately to ensure good quality contact between the connector and the transmission line.

S_{11} parameter and corresponding bandwidth frequencies are firstly measured using a vector network analyzer (see **Figure 76b**). Then the antenna’s radiation efficiency, defined as the ratio of the radiated power to the input power of the antenna, can be measured in the anechoic chamber (**Figure 76c**). For this purpose, the antenna is vertically fixed as shown in **Figure 76c**. The distance between the studied antenna (emission) and reception standard antenna is around 4 m. In a specific direction and for a specific frequency, the gain can be defined as the ratio of the radiation intensity in that direction to the mean radiation intensity of a perfectly efficient

isotropic antenna. Such parameter is expressed in dBi (“i” standing for “isotropic”). The gain can be measured in every space directions (θ, φ) thanks to the automatic motion of the antenna inside the anechoic room, giving rise to the “radiation pattern” of the antenna.

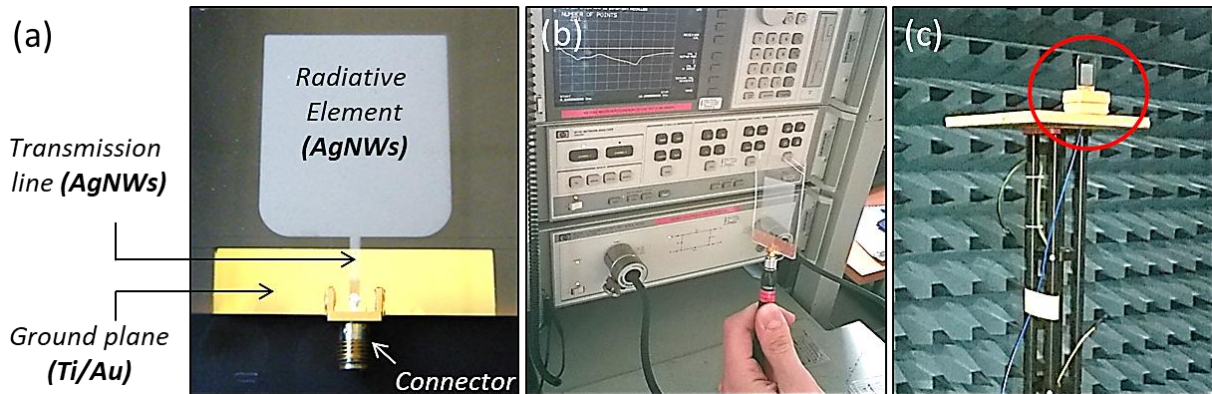


Figure 76. a) Image of an AgNW-based antenna showing the radiative element, transmission line, ground plane, and connector. b) Vector network analyzer (VNA) used for measuring antenna’s S -parameters. c) Image showing an AgNW-based antenna (red circle) in an anechoic room for measurement of the EM radiating pattern.

The S_{11} parameter and radiation pattern of the “reference” antenna, in which every elements are made only of Ti (10 nm) / Au (100 nm) thin layer deposited by PVD, were first calculated using the “CST Microwave studio” 3D electromagnetic simulator. The corresponding results are reported in **Figure 77** thereafter. The expected resonant frequency is close to 2 GHz. The radiation pattern exhibits quite an isotropic distribution. Its theoretical radiation efficiency was measured to be -0.06 dB, while the highest gain value is obtained in the direction ($\varphi = 0, \theta = 0$) and equals +2.4 dBi.

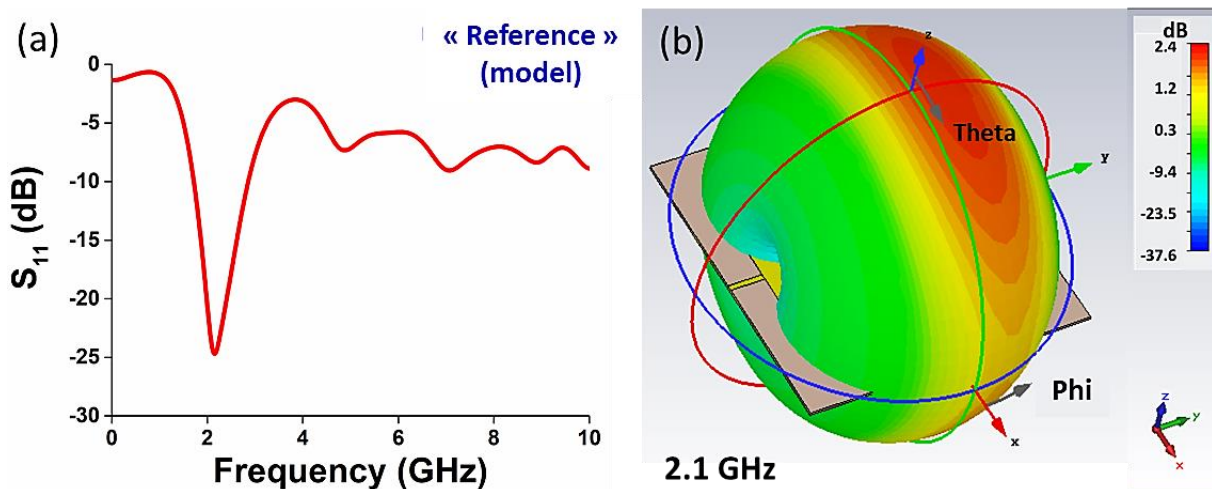


Figure 77. a) Simulated results showing S_{11} parameter against frequency for the reference antenna. b) Simulated 3D radiation pattern calculated at the resonant frequency (2.1 GHz) associated with the reference antenna.

6.2.2. Performance of AgNW-based antennas

For the sake of comparison, S_{11} parameters associated with the real “reference” antenna, as well as with an AgNW antenna (corresponding to “antenna 2” in **Table 4**), are reported in **Figure 78**. First, the resonant picks around 2 GHz is well visible in both types of antennas (“reference” and “AgNW” antenna), as expected from the simulation. However, in any case, a secondary resonant pick is also detected in the range 7-9 GHz, which is not predicted by the simulation. The origin of this secondary resonant pick is still mysterious. The gain value measured for the real “reference” antenna is +0.61 dB which is slightly less than in the fictive simulated reference antenna. However, according to Alejandro Niembro, the measurement mistake associated to a real gain measurement in an anechoic chamber is about 1 dB, even without taking into account alignment mistakes ($\varphi \approx 0$, $\theta \approx 0$) likely to increase slightly the error.

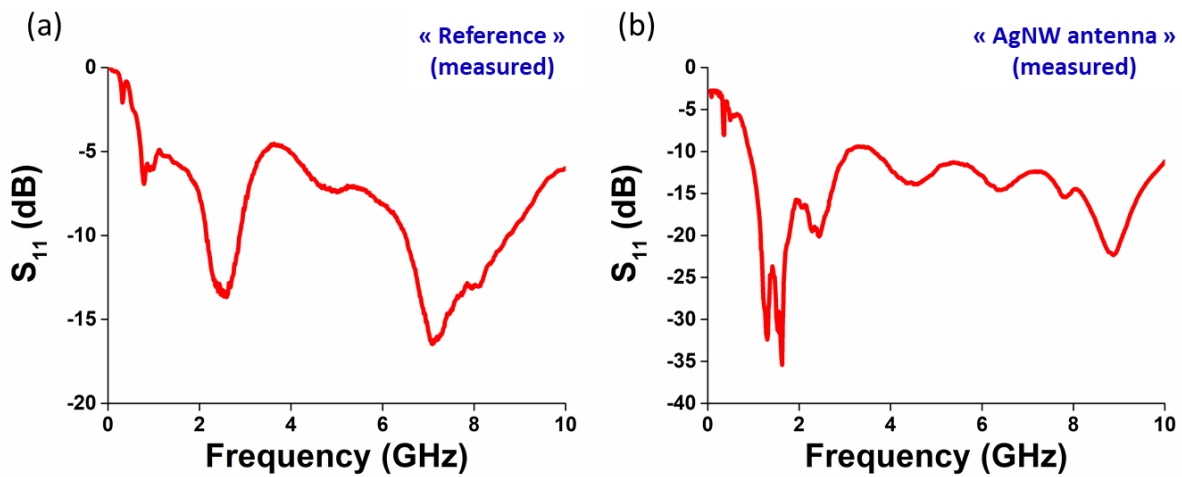


Figure 78. a) S_{11} parameter against the frequency associated with the real “reference” antenna (every elements in Ti/Au). b) S_{11} parameter against the frequency for an AgNW antenna (corresponding to “antenna 2” in Table 4).

The gain in the $\{\varphi \approx 0, \theta \approx 0\}$ direction was also measured on several AgNW-based antennas. The most significant results are reported in Table 4. Gain values are provided along with the electro-optical performances of the antennas (sheet resistance, and optical transmittance without substrate contribution). “Antenna 1” is entirely made of AgNWs while “Antenna 2” and “Antenna 3”, have their transmission line made of an additional Ti (10 nm)/Au (100 nm) layer deposited on top of AgNWs, as a way to test the influence of the nature of the transmission line. Besides, a very thin layer of PEDOT-PSS was finally deposited on top of “Antenna 3” in order to increase the smoothness of the resulting antenna.

According to the very low sheet resistance associated with the radiating element of “Antenna 1” ($R_{sh} \approx 3 \Omega \text{ sq}^{-1}$), the gain measured for this antenna ($G_1 \approx -3 \text{ dB}$) is quite disappointing. Surprisingly, the gain value of “Antenna 2”, associated with a higher sheet resistance ($R_{sh} \approx 7.5 \Omega \text{ sq}^{-1}$), is consistently higher than G_1 ($G_2 \approx -1.6 \text{ dB}$). It seems that the nature of the transmission

line plays a critical role in the overall performance of the antenna. More specifically, adding a thin metallic layer (Ti/Au) on top of AgNWs was proven very efficient for improving the performance of the antenna. Finally, the sheet resistance of “Antenna 3” ($R_{sh} \approx 7.3 \Omega \text{ sq}^{-1}$) is very similar to the one of “Antenna 2”. However, due to the presence of PEDOT-PSS on top and between AgNWs, the gain value was increased up to $G_3 \approx -1.1 \text{ dB}$, which is the highest gain value obtained in the team so far.

Table 4. Characteristics and performances of the reference and AgNW-based antennas. (NR: “not relevant”)

Characteristics	Reference Antenna	Reference Antenna	Antenna 1	Antenna 2	Antenna 3
Method	Simulated	Measured	Measured	Measured	Measured
Radiative element	{Ti/Au}	{Ti/Au}	{AgNWs}	{AgNWs}	{AgNWs, PEDOT PSS}
Transmission line	{Ti/Au}	{Ti/Au}	{AgNWs}	{AgNWs, Ti/Au}	{AgNWs, Ti/Au, PEDOT PSS}
Sheet resistance $\Omega \text{ sq}^{-1}$	NR	NR	3.2	7.5	7.3
Tranmittance % , $\lambda = 550 \text{ nm}$, <i>without substrate contribution</i>	NR	NR	66	81	63
Resonant frequency GHz	2.1	2.5	2.4	2.5	2.5
Gain $f = f_r, \theta = 0, \varphi = 0$	+2.4	+0.61	-3.07	-1.63	-1.14

However, adding PEDOT-PSS as a way to increase the smoothness has a critical impact on the transparency at the same time. The optical transmittance at $\lambda = 550 \text{ nm}$ of Antenna 3 was indeed measured to be 63% (without substrate contribution), making it not compatible with RF applications for which optical transparency is required. On the contrary, the optical transmittance of “Antenna 2” is still acceptable (81%). Given that the design of the antenna yields quite isotropic radiation distribution, the gain values obtained for Antenna 2 and 3 are not high, but still acceptable. In order to increase the gain of AgNW-based antenna, it would be necessary to work on designs leading to more directive radiation patterns.

In order to get further information about the electromagnetic behavior of AgNW network in the radio-frequency range, a study was finally devoted to transmission lines made of AgNW networks. Such work is necessary for measuring the propagation constant $\gamma = \alpha + j\beta$ (α is the attenuation constant and β the phase constant), and the characteristic impedance Z_c , which are critical parameters for assessing the assets and limitations of AgNW networks in RF devices.

6.2.3. Transmission lines

A transmission line is made of a single strip and a ground plane, on opposite faces of a sheet of dielectric material. In the present study, several AgNW microstrip lines were fabricated on PEN substrate, whose dielectric constant is around 2.9. The width of the lines were selected using the Wheeler formula,^[238,239] and according to the desired characteristic impedance: 840 μm , 320 μm , 160 μm , and 86 μm , for impedance values of 25 Ω , 50 Ω , 75 Ω , and 100 Ω , respectively. The connecting pads, as well as ground plane were made of {Ti (10 nm), Au (100 nm)} deposited by PVD. Prior to any measurement, TRL calibrations^[240] (“THRU”, “REFLECT”, “LINE”) were systematically performed using reference lines also made of {Ti (10 nm), Au (100 nm)}, deposited by PVD. The entire architecture of an AgNW lines series associated with a length of 1 cm each is provided in **Figure 79a** as example.

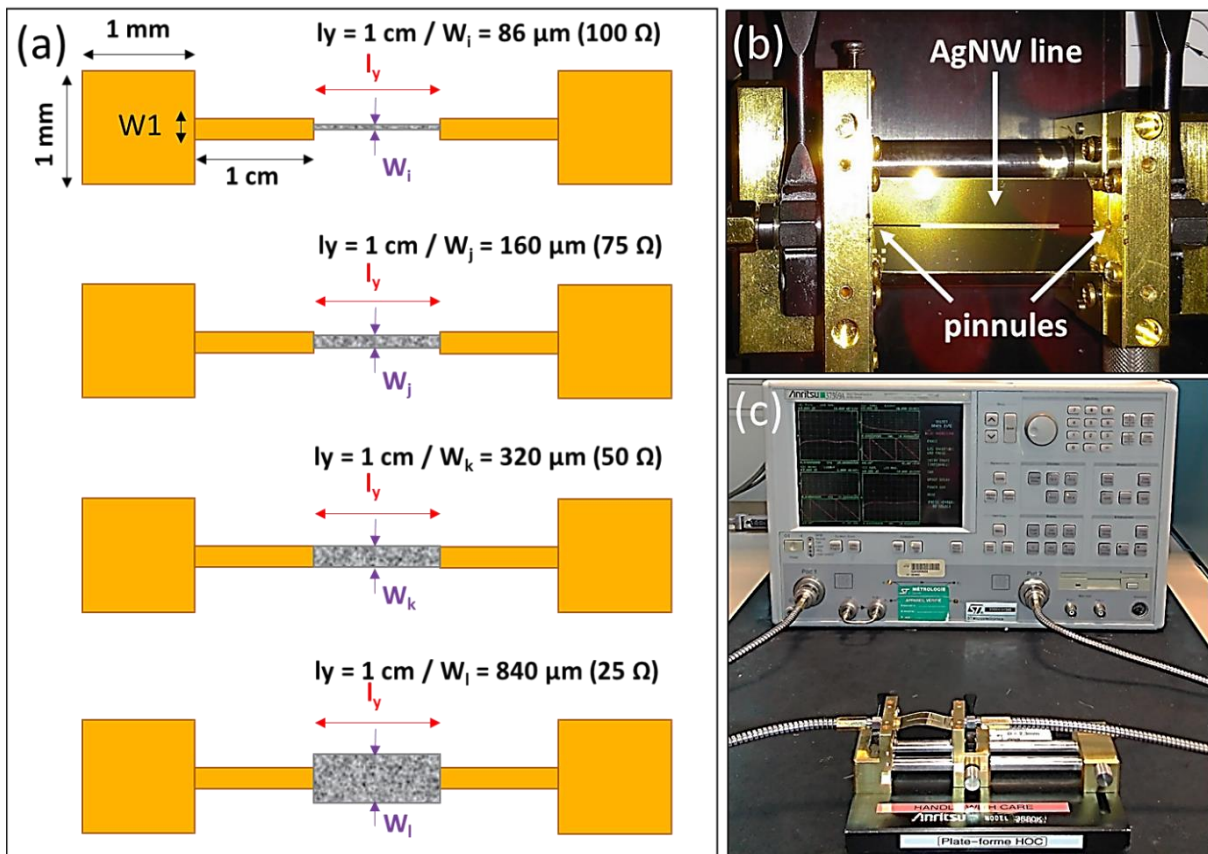


Figure 79. (a) Schematic representation of AgNW lines with various widths (86 μm , 160 μm , 320 μm , and 840 μm) corresponding to the various impedance values targeted (25 Ω , 50 Ω , 75 Ω , 100 Ω). Connecting pads are made of {Ti (10 nm), Au (100 nm)}, deposited by PVD. So is the ground plane. (b) Image showing a real AgNW line fixed in the measurement set-up. (c) Image showing an AgNW line connected to a vector network analyzer (VNA) measuring S parameters of the line in the range 0-20 GHz.

Three different length values were tested for the lines (4 mm, 1 cm, and 2 cm). Contrary to a monopole antenna which contains by definition only one entry port, a transmission line contains two ports: port 1 is where the incident signal gets into the line, while port 2 is where the transmitted signal is collected. After calibration, the S parameters of the lines were measured using a vector network analyzer (see Figure 79b-c): As already mentioned in previous part, S_{11} is expressed as $S_{11} = 10 \cdot \log(P_{r,1}/P_{i,1})$, with $P_{i,1}$ and $P_{r,1}$ the incident and reflected power to port 1, respectively. Similarly, S_{21} is expressed as $S_{21} = 10 \cdot \log(P_{t,2}/P_{i,1})$, with $P_{t,2}$ the power transmitted to port 2 (coming from port 1), and $P_{i,1}$ the incident power emitted from port 1.

Lines with two different AgNW network densities (“standard” and “dense”) were tested. The electrical and optical performances of blank samples, fabricated at the same time and in the same conditions as the AgNW lines, were measured to be $\{R_{sh} = 27 \Omega \text{ sq}^{-1}, T_r = 92 \%\}$ and $\{R_{sh} = 7 \Omega \text{ sq}^{-1}, T_r = 82 \%\}$, in the “standard” case, and “dense” case, respectively. T_r values are provided at $\lambda = 550 \text{ nm}$, without substrate contribution. The DC impedance of the lines are reported in **Table 5** thereafter. Due to the very low width of the lines fabricated, their electrical resistance was very high in many cases. In most cases, only the 25 Ω and 50 Ω lines (which correspond to the lines with the highest width), exhibited a measurable DC resistance.

When decreasing the width, the increase in DC resistance for continuous conductive materials is straight forward considering the Pouillet’s resistance formula, $R = \rho \cdot \frac{L}{e \cdot W}$, with ρ the resistivity, and with L , e , and W the length, thickness, and width of the conductive material, respectively. However, in the case of AgNW networks, such an increase in resistance might be even more critical due to the non-continuous architecture of the network. Even when using AgNW networks with low sheet resistance, the number of available conductive paths is indeed critically decreased when lowering the width of the networks, leading to an accelerated process of the resistance increase as compared with common conductive materials. Such an issue has to be seriously taken into account when trying to integrate AgNW networks in devices with low-size architecture.

Table 5. DC impedance of the AgNW lines fabricated with various lengths, widths, and NW densities (O.R.: “Out of Range”, DM: “damaged”).

Length (cm)	L₁ (0.4 cm)				L₂ (1 cm)				L₃ (2 cm)			
Width (μm)	840	320	160	86	840	320	160	86	840	320	160	86
Z_c (Ω)	25	50	75	100	25	50	75	100	25	50	75	100
R_{DC} (Ω) “Standard”	209	1800	O.R	O.R	DM	66000	O.R	O.R	13000	O.R	O.R	O.R
R_{DC} (Ω) “Dense”	76	338	O.R	O.R	DM	621	22000	O.R	192	812	O.R	O.R

In every cases, the S parameters measured for AgNW lines yielded very low value of transfer coefficient S_{21} , meaning that the EM losses were found very high along the lines. S_{11} and S_{21} parameters measured for the line series with the lowest length (0.4 cm) and sheet resistance

(“dense”), are reported in **Figure 80a-b**. For the sake of comparison, S parameters associated with the calibration lines in Ti/Au are also reported on the same figure.

In this example, S_{11} value obtained for the AgNW lines are between -5 and -15 dB (see Figure 80a, green and blue curves), meaning that the contact between the connector and the line is correct, and that the impedance match is acceptable. As expected, S_{11} parameter associated to the reference line (red curve) is much lower, and corresponds to the one expected. Regarding parameter S_{21} , the measured values are {-8 dB; -11.7 dB; -12.6 dB; -15.2 dB} and {-13 dB; -15.2 dB; -16.7 dB; -18.2} at 5, 10, 15, and 20 GHz, and for the 25 Ω and 50 Ω AgNW lines, respectively (see Figure 80b). This means that only {15.8%; 6.8%; 5.5%; 3%} and {5%; 3%; 2.1%; 1.5%} of the incident power is transmitted to port 2 at these frequencies, and for the two AgNW lines, respectively. Electromagnetic losses are then substantial when considering the AgNW lines. On the other hand {85.1%; 83.2%; 81.3%; 83.2%} of the incident power is transmitted when considering the Ti/Au line depicted in Figure 80b).

The attenuation of a microstrip line may consist of conductor (ohmic) losses, dielectric (substrate) losses, radiation (antenna effect) and propagation of surface waves and higher order modes. As already mentioned, due to the very thin width of the fabricated lines, the DC resistance was already very high, despite the high network density. Apart from this issue, the most contribution to EM losses is likely to be linked to the ohmic losses induced by the presence of numerous AgNW junctions across the lines, as compared with a standard continuous conductive material.

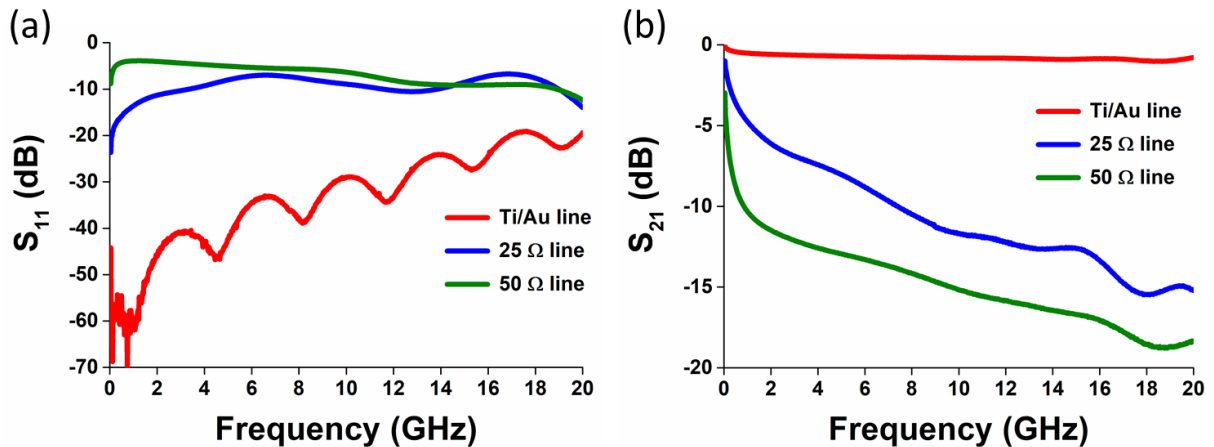


Figure 80. S parameters measured for the 25 Ω and 50 Ω AgNW lines, as well as for the Ti/Au line used for the TRL calibration: a) S_{11} parameter for each line. b) S_{21} parameter for each line. All the lines have the same length (0.4 cm). The width of the lines is either 320 μm (for the 50 Ω AgNW line and Ti/Au line) or 840 μm for the 25 Ω AgNW line.

Due to the very high EM losses measured in this first series of experiments, this study about AgNW transmission lines and especially the extraction of the parameters of interests has not been completed yet. Further prospects may consist of reproducing the same kind of experiment, but using much larger lines. In that way, one could discriminate the origin of the losses as a

“dimension effect” or as a property intrinsically linked to the nature of the material. Finally, performing simulations based on real interconnected random networks instead of fictive continuous material would be much more beneficial for determining the scope and limitations of such lines in terms of density, and dimensions. Transferring realistic network architectures generated using Matlab software (see section 3.3.1) to dedicated RF softwares such as HFSS, or CST, has been successfully completed. However the influence of the junction resistance is not taken into account when using such softwares, leading to an underestimation of EM losses. By using Comsol RF module instead of HFSS or CST, the junction resistance could be taken into account (see section 3.3.3) leading potentially to more realistic simulations. Effort should be pushed in this direction to pursue this preliminary investigation.

6.3. AgNW networks for transparent electromagnetic shielding

As introduced in section 1.2.5.1, AgNW percolating networks show great potential for electromagnetic (EM) shielding applications. The physical parameter used to characterize the shielding performance of a material is called shielding effectiveness (SE) and is defined as:

$$SE = 10 * \log\left(\frac{P_{in}}{P_{trans}}\right) = 20 * \log\left(\frac{E_{in}}{E_{trans}}\right) = -S_{21} \quad (6.2)$$

with P_{in} and E_{in} the incident electromagnetic power and field (respectively), P_{trans} and E_{trans} the transmitted electromagnetic power and field, respectively, and S_{21} the transmission coefficient. The higher the SE value, the better the shielding performance. More precisely, the total SE consists of the combination between reflection losses, absorption losses, and the multiple-reflection losses, as illustrated in **Figure 81**.

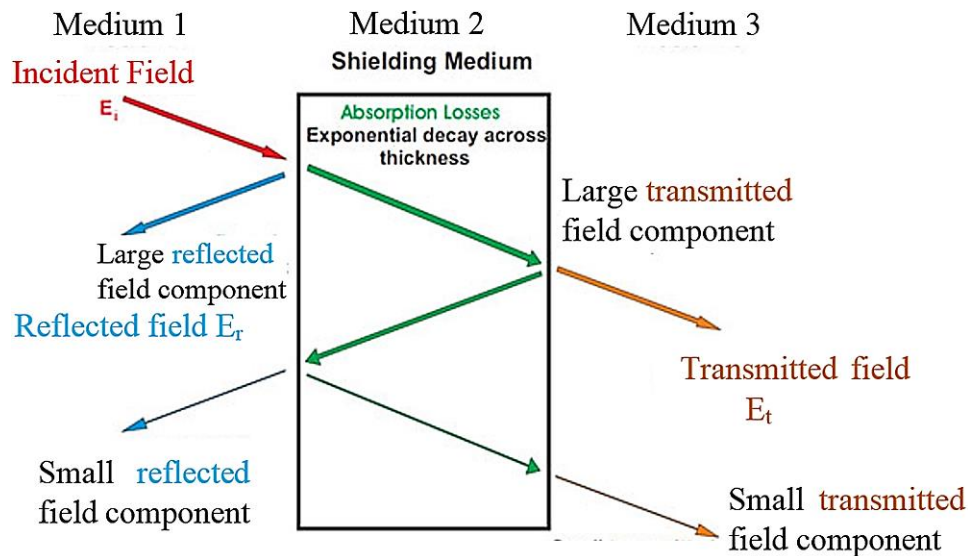


Figure 81. A schematic illustration of the three losses mechanisms (reflection, absorption, and multiple-reflection losses) responsible for the shielding properties of materials.

The reflection losses largely depend on the relative mismatch between the incoming wave and the surface impedance of the material. The absorption losses are caused by the eddy “Foucault” current generated inside the shielding material, responsible for disturbing and making the EM incident field decrease exponentially (evanescent wave) across the material (for a given frequency). After a distance of several δ , which is defined as the skin depth of the material, the EM field is absent. Finally, the multi-reflection term is a correction factor for the multiple signal reflections that might occur in the material. As the skin depth of silver is in the order of several μm in the 800 MHz to 20 GHz frequency range, far larger than the diameter of the silver nanowires used in the experiment (60 nm), the influence of the absorption and multi-reflection losses should be insignificant. Hence the reflection of energy is the major loss mechanism involved in the AgNWs EM shielding.

6.3.1. Measurement of the shielding effectiveness of AgNW networks

6.3.1.1. Description of the experimental setup

The SE of the AgNW networks was measured in collaboration with Alejandro Niembro (IMEP LaHC laboratory) within an anechoic chamber, whose top view is shown in **Figure 82a**. The transmission antenna is placed outside the chamber. Conversely, the reception antenna is located inside the anechoic room so that all the reflective and environment-coming signals cannot disturb the measurement. A metallic wall is placed at the interface of the anechoic chamber. An A4 format aperture is created in the middle of the metallic wall as a placeholder for the material under test (see Figure 82b). The SE is measured between 800 MHz and 20 GHz. EM signals are emitted, collected and treated thanks to a vector network analyser (VNA).

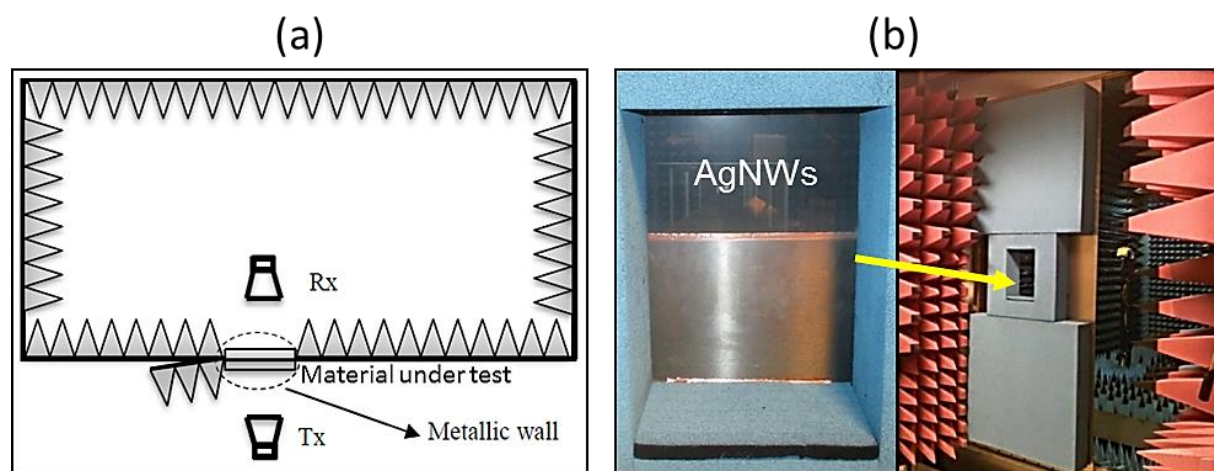


Figure 82. a) A schematic top view of the anechoic chamber used for measuring the EM shielding effectiveness of AgNW networks. b) Picture of the metallic wall panel. The hole where the studied specimen is positioned has a size corresponding to A4 paper. It can be reduced to A5 size by adding a copper plates (as illustrated in the image here).^[241]

Several large (A5 format) AgNW networks made of Liten AgNWs were fabricated by spray-coating. The reason for fabricating large-size networks when focusing on the shielding properties is that in the RF frequency range studied here, the wavelength of the incident waves varies between 37.5 cm (@ 800 MHz) and 1.5 cm (@ 20 GHz). To avoid the sample being considered as negligible to the incident light wavelength, its dimensions have to be at least similar to the half wavelength.

6.3.1.2. Impact of the AgNW network density on the shielding properties

In order to evaluate the impact of AgNW network density on shielding effectiveness of AgNW networks, three different samples “AgNW-1”, “AgNW-2”, “AgNW-3” with increasing network densities were fabricated. Their electrical and optical properties were measured to be $\{R_{sh} = 23 \Omega \text{ sq}^{-1}, T_r = 93\%\}$, $\{R_{sh} = 8 \Omega \text{ sq}^{-1}, T_r = 90\%\}$, $\{R_{sh} = 4 \Omega \text{ sq}^{-1}, T_r = 76\%\}$, respectively. The corresponding S_{21} parameters are provided in **Figure 83** in the range of 800 MHz – 20 GHz. It is around 18 dB, 25 dB, and 30 dB, respectively, in most of the frequency range. More specifically, for the sample exhibiting the highest transparency ($T_r = 93\%$), the shielding efficiency is close to 20 dB, which means that about 99% of the incident signal power is shielded by AgNWs, while keeping a very high level of optical transparency at the same time.

As the network density is increased, the NW surface coverage increases too, leading to higher reflectivity level of the AgNW electrodes. Hence, the shielding efficiency measured for the two other samples is higher (see red and blue curves). The shielding efficiency values associated to the three samples are very promising. The trade-off achieved in this thesis in terms of shielding level and optical transparency of AgNW networks is very similar to state-of-the-art values provided in literature (see section 1.2.5.1).^[179]

Deep shielding peaks can be detected near 10 GHz and also 17 GHz for the red curve. They are very deep for the two denser networks, while they are hardly detectable for the sparsest network. Thermal annealing of the sample did not help removing these peaks (see **Figure 84b**). Shielding measurements performed one year later yielded again the same type of shielding peaks. When using plastic substrates like PEN or PET instead of glass, the corresponding S_{21} signals are much more flattened (see **Figure 85**). It is then believed that the nature of the substrate is likely to influence the appearance of shielding peaks. However, when measuring the shielding effectiveness of glass substrate alone, no specific peaks can be detected (see Figure 84a, pink curve). As a consequence, the origin of these peaks remains unexplained.

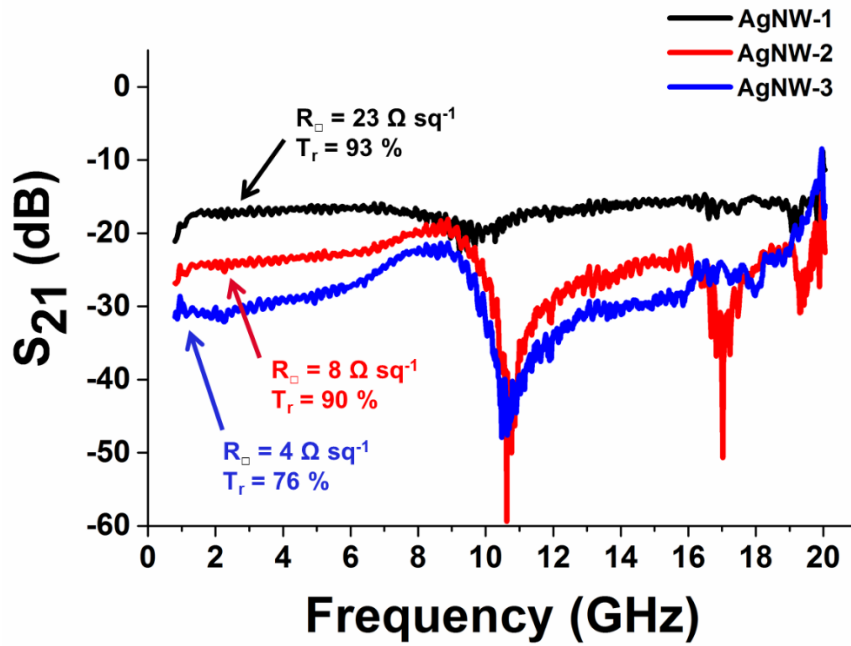


Figure 83. Transfer coefficient S_{21} as a function of signal frequency for AgNW networks deposited on glass substrate, with increasing AgNW network densities. The samples are associated with an optical transparency ($\lambda = 550$ nm, without substrate contribution) of 93%, (black curve), 90% (red curve), and 76% (blue curve).

6.3.1.3. Impact of environmental ageing, thermal annealing, substrate, and deposition technique

The samples reported in the previous section were studied further. First, their shielding efficiency was measured again after having been stored in “normal” conditions (i.e. day light, in air) for one year, to check whether the shielding performance of AgNW networks is affected by “normal” environmental ageing. Then the samples were placed on a hot plate, heated at 150°C for 15 min, and measured one more time to see whether thermal annealing can be beneficial to the shielding properties of AgNW networks. Finally shielding tests associated with AgNW networks deposited on substrates other than glass, and by using deposition technique other than spray-coating were performed.

The stability of the AgNWs in air is outstanding. As shown in Figure 84a, the SE was not changed significantly after having been stored in normal conditions (day light, in air) for one year. This ageing resistance feature might be due to the fact that silver is a noble metal. Hence it is not likely to react a lot with oxygen at room temperature. Moreover, the PVP shell surrounding the wires may also help preserving the network from oxidation and any other degrading chemical reactions. It has been reported by Mayousse et al., that AgNW networks are very stable when stored under ambient atmosphere up to, at least, two and a half years.^[111] However, AgNW networks are likely to be covered by a protecting layer when integrated in an EM shielding transparent windows, or any other real device. Therefore, the ageing behavior of AgNW networks should also be investigated after encapsulation in final product.

In order to evaluate whether thermal annealing can be beneficial the EM SE of AgNW networks, the previous samples were heated at 150 °C during 15 min. The shielding performance is indeed intimately linked to the surface resistance of the shielding material. By creating well sintered junctions, the overall resistance of the latter might decrease significantly according to the type of AgNWs used (see section 2.1.2). However in the present case, the difference before and after annealing was not obvious since AgNW networks used for the present were made with Liten NWs, which already offer very low sheet resistance of the resulting networks after deposition. It can be noticed that thermal annealing has a larger positive impact in the 2-8 GHz range, considering the sample showing the highest sheet resistance (see black and green curves in Figure 84b). However, its overall influence on shielding effectiveness is almost insignificant when using high density networks made with Liten AgNWs.

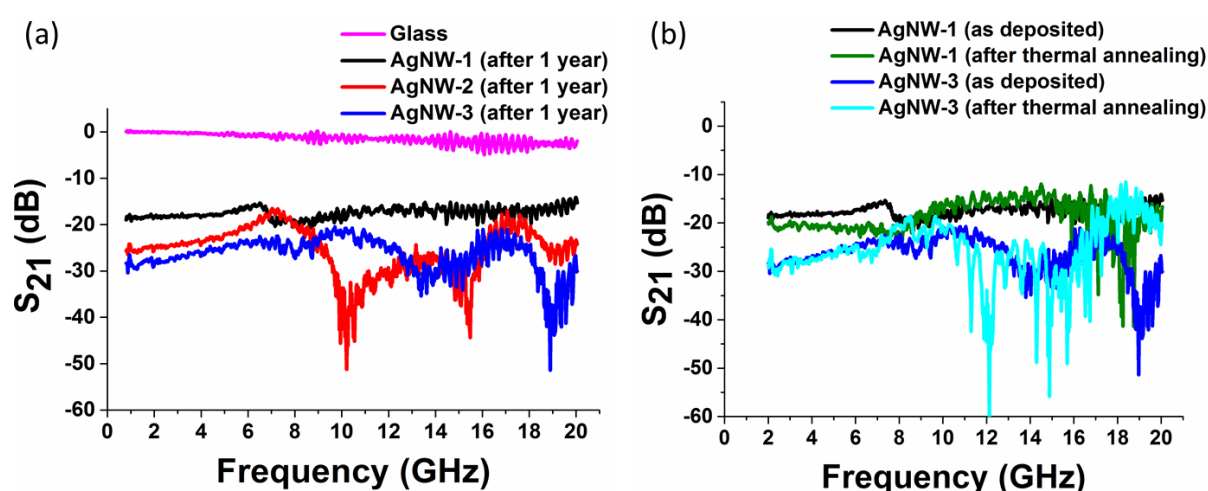


Figure 84. a) Transfer coefficient S_{21} as a function of signal frequency for glass substrate (pink) and for the three AgNW networks depicted in Figure 83, after one year storage in ambient conditions. b) Transfer coefficient S_{21} as a function of signal frequency for two of the sample studied “AgNW-1” and “AgNW-3”, as-deposited (black and blue curves), and after annealing at 150 °C during 15 min (green and cyan curves).

Finally, shielding tests with AgNW networks deposited on substrates other than glass and using deposition methods other than spray-coating were also performed (see Figure 85). The shielding effectiveness associated to the AgNW network deposited on PEN substrate (green curve) is consistent with the shielding level of samples deposited on glass. With a sheet resistance of $18 \Omega \text{ sq}^{-1}$, the latter exhibits a SE close to 21 dB at low frequencies, just between “AgNW-1” ($23 \Omega \text{ sq}^{-1}$) and “AgNW-2” ($8 \Omega \text{ sq}^{-1}$) samples, respectively associated with a SE of 18 dB and 25 dB. “AgNW-2” and the present sample deposited on PEN exhibit the same optical transparency (90%), and therefore, should be associated to a very similar AgNW surface coverage. However, the sheet resistance is higher in the case of the sample deposited on PEN, resulting in a lower SE, as compared to “AgNW-2”. Hence, the substrate, and especially the adhesion of the NWs to the substrate might influence the shielding effectiveness via a change in the network sheet resistance. Finally, two samples were fabricated by Mayer rod coating on PET substrates,

yielding results consistent with the electrical performance of AgNW networks. As a consequence, the sheet resistance of AgNW networks is definitely the most critical parameter influencing the shielding effectiveness of AgNW networks.

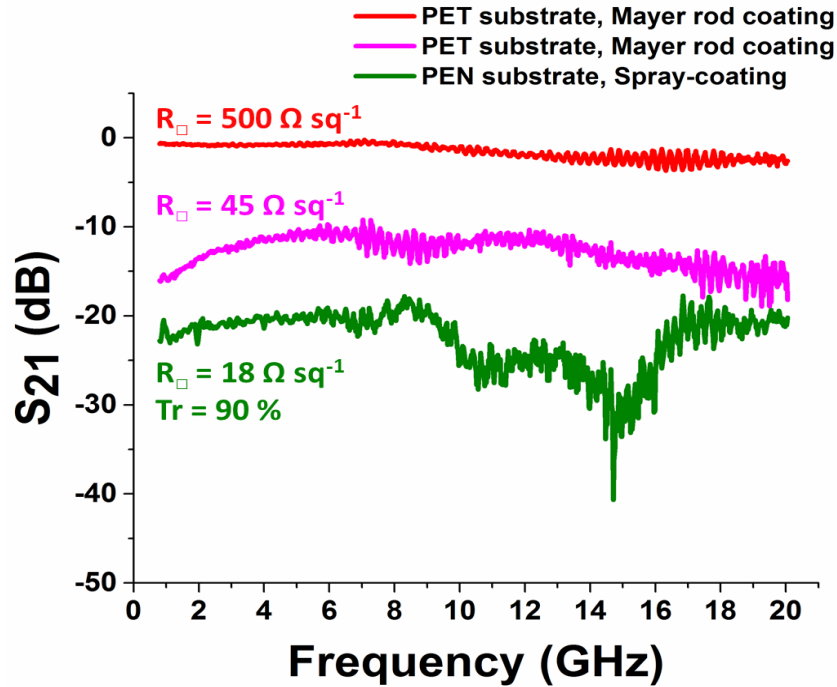


Figure 85. Transfer coefficient S_{21} as a function of signal frequency for two AgNW networks deposited by Mayer rod coating on PET substrate associated with a sheet resistance of $500 \Omega \text{ sq}^{-1}$ and $45 \Omega \text{ sq}^{-1}$, respectively, as well as for an AgNW network deposited by spray coating on PEN substrate and associated with a sheet resistance of $18 \Omega \text{ sq}^{-1}$.

6.3.1.4. Comparison with thin silver films and thin silver wire mesh screens

In order to compare the shielding performance of AgNW networks with other types of silver based-materials, theoretical shielding efficiencies of thin silver films and silver wire meshes were calculated.

(i) The case of thin silver films

By considering the schematic representation of electromagnetic field from medium 1 to medium 3 in Figure 81, the ratio between the transmitted and incident magnetic or electric fields can be written as follows:

$$\frac{E_t}{E_i} = \frac{H_t}{H_i} = (1 + R)(1 - R) * e^{-\frac{l}{\delta}} * [1 + R^2 e^{-2\frac{l}{\delta}} + R^4 e^{-4\frac{l}{\delta}} + \dots] \quad (6.3)$$

Which can be simplified as:

$$\frac{E_t}{E_i} = \frac{H_t}{H_i} = 4 \frac{Z_s * Z_{air}}{(Z_s + Z_{air})^2} * e^{-\frac{l}{\delta}} * \frac{1}{1 - R^2 e^{-2\frac{l}{\delta}}} \quad (6.4)$$

R is the reflection coefficient expressed as $R = \frac{Z_s - Z_{air}}{Z_s + Z_{air}}$, with Z_s and Z_{air} the impedances of the shielding material and air, respectively. l is the thickness of the shielding material, and δ is the skin depth, expressed as $\delta = 1/\sqrt{\pi\mu\sigma f}$ where μ , and σ are the permeability and the conductivity of the shield while f is the frequency of the incident wave.

According to the definition of the shielding efficiency (see Equation 6.2):

$$SE = 20. \log \left(\frac{E_i}{E_t} \right) = 20. \log \left(\frac{(Z_s + Z_{air})^2}{4. (Z_s * Z_{air})} \right) + 20. \log \left(e^{\frac{l}{\delta}} \right) + 20. \log \left(1 - R^2 e^{-2\frac{l}{\delta}} \right) \quad (6.5)$$

The first term in Equation 6.5 indicates the shielding efficiency related to the reflection (SE_R) of incident waves. By considering $Z_{air} \gg Z_s$, knowing that $Z_{air} = \sqrt{\frac{\mu_0}{\epsilon_0}} = 377 \Omega$ and finally by expressing Z_s as $Z_s = \sqrt{\frac{j\omega\mu}{\sigma + j\omega\epsilon}}$, SE_R can be simplified as follows:

$$SE_R = 20. \log \left(\frac{Z_{air}}{4.Z_s} \right) = 31.5 + 10. \log \left(\frac{\sigma}{\mu f} \right) \quad (6.6)$$

The values calculated for SE_R in the case of silver at $f = 1$ GHz and $f = 20$ GHz are 78.5 dB and 65.5 dB, respectively. This is the main contribution to the overall shielding effectiveness of Ag thin films.

The second term in Equation 6.5 indicates the shielding efficiency related to the absorption (SE_A) of incident waves and can be simplified as follows:

$$SE_A = 8.69 \frac{l}{\delta} \quad (6.7)$$

In the case of a 2 μm thick Ag film (very close to the skin depth value), SE_A is calculated to be 8.67 dB and 39.8 dB, at 1 GHz and 20 GHz, respectively. In order to make the comparison with AgNW networks, very thin AgNW films should be considered. In the case where the thickness is reduced to 100 nm, SE_A is then calculated to be either 0.4 dB or 1.9 dB, at 1 GHz and 20 GHz, respectively, far less than SE_R . As already mentioned, when the thickness is much lower than the skin depth, absorption losses are negligible: this is coherent with the previous calculation.

Finally, the third term in Equation 6.5 indicates a correction coefficient related to the multiple reflection (SE_{MR}) occurring at the two boundaries of the shield. Considering that $Z_{air} \gg Z_s$, R^2 is close to 1. Hence, SE_{MR} can be simplified as follows:

$$SE_{MR} = 20. \log \left(1 - e^{-2\frac{l}{\delta}} \right) \quad (6.8)$$

In the case of a 2 μm thick Ag film, SE_{MR} is calculated to be -1.3 dB and 0.0 dB, at 1 GHz and 20 GHz, respectively. On the other hand, for a 100 nm thick Ag film, SE_{MR} drastically decreases down to -20.5 dB and -8.9 dB, at 1 GHz and 20 GHz, respectively. When the thickness of the shielding material is the same order of magnitude than the skin depth, the signal amplitude is already very low before reaching the second extremity. Hence, the multiple reflection

phenomenon is negligible. However it should be taken into account when using materials much thinner than the skin depth, as demonstrated by the values reported above.

(ii) *The case of thin silver wire mesh screens*

The theory of electromagnetic shielding efficiency associated to wire mesh screens has been deeply investigated by K.F. Casey.^[242] The architecture of such screens consists of a perfectly regular mesh screens wherein the individual meshes are square and the wire junctions are assumed to be perfectly bounded (no contact resistance). According to Casey, when finite conductivity is ascribed to the mesh wires, it does exist a frequency limit ω_{min} below which the shielding efficiency is essentially constant and equal to SE_{lim} . In the case of normal incidence, these two parameters can be expressed as follows:^[242]

$$\omega_{min} = \frac{R_S}{L_S} \quad \text{and} \quad SE_{lim} = 20 \cdot \log \left(1 + \frac{Z_{air}}{2R_S} \right) \quad (6.9)$$

R_S is the equivalent DC sheet resistance of wire mesh expressed as $R_S = \frac{a}{\pi r^2 \sigma}$,^[242] with a the side of one individual square mesh, r the wire radius, and σ the wire conductivity. L_S is the sheet inductance parameter expressed as $L_S = -\frac{\mu_0 a}{2\pi} \cdot \ln \left(1 - e^{-\frac{2\pi r}{a}} \right)$. Z_{air} is the intrinsic impedance of free space expressed as $Z_{air} = \left(\frac{\mu_0}{\epsilon_0} \right)^{1/2}$ ($Z_{air} = 377 \Omega$). The calculations performed in the case of a silver wire mesh screens with a radius of 60 nm (which corresponds to the average NW diameter used for measuring the shielding effectiveness of AgNW networks in the present thesis) are reported in **Table 6**.

Table 6. Electrical performance, shielding efficiency, and areal mass density associated with a 60 nm thick silver wire mesh screen when the side of individual square mesh is either 10 μm or 1 μm .

a (μm)	f_{min} (GHz)	R_S (Ω)	SE_{lim} (dB)	amd (mg m^{-2})
10	1122	56	12.8	11.8
1	2536	5.6	30.8	109

For the sake of comparison with AgNW networks (see Figure 84), the level of theoretical shielding efficiency (SE) of both Ag thin films and thin Ag wire mesh screens against the silver areal mass density (amd) was investigated. In the case of Ag thin film of thickness l , the amd can be simply expressed as: $amd_{thin\ film} = d_{Ag} \cdot l$. In the case of wire mesh screen, the areal mass density can be expressed as $amd_{mesh} = 4\pi d_{Ag} \left[\frac{r^2(a+r)}{(a+2r)^2} \right] \approx_{a \gg r} 4\pi d_{Ag} \left(\frac{r^2}{a} \right)$ which yields $amd_{mesh}^{a=10\ \mu\text{m}} = 11.8\ \text{mg m}^{-2}$ and $amd_{mesh}^{a=1\ \mu\text{m}} \approx 109\ \text{mg m}^{-2}$ (see Table 6). When considering $a \gg r$, $amd_{mesh}^{a=10\ \mu\text{m}} \approx 11.9\ \text{mg m}^{-2}$ and $amd_{mesh}^{a=1\ \mu\text{m}} \approx 119\ \text{mg m}^{-2}$. Such an approximation can therefore be considered as valid in the range of amd considered. Therefore, the SE as a function of the amd for these two types of material can be expressed as:

$$SE_{thin\ film} \approx 31.5 + 10 \cdot \log\left(\frac{\sigma}{\mu f}\right) + 8.69 \frac{amd}{d_{Ag} \delta} + 20 \cdot \log\left(1 - e^{-2 \frac{amd}{d_{Ag} \delta}}\right) \quad (6.10)$$

$$SE_{wire\ mesh} \approx 20 \cdot \log\left[1 + amd \left(\frac{377\sigma}{8d_{Ag}}\right)\right]$$

The theoretical SE values associated with Ag thin films and Ag wire mesh screens was plotted against the amd in the range 0-300 mg m^{-2} (see blue and red curves in **Figure 86**). The values provided are considered as valid with a good approximation for low amd values, for $a \gg r$ in the case of wire meshes, and in the frequency range 1-10 GHz. In these conditions, the changes in frequency do not involves any changes in $SE_{wire\ mesh}$ (see Equation 6.10). Similarly in this range of amd (very thin films), changes in frequency induce almost insignificant changes in $SE_{thin\ film}$. The SE values measured for AgNW networks in this thesis are also reported in Figure 86 (green triangles). The amd values provided for AgNW networks indicate only a tendency and should further confirmed using ImageJ script.

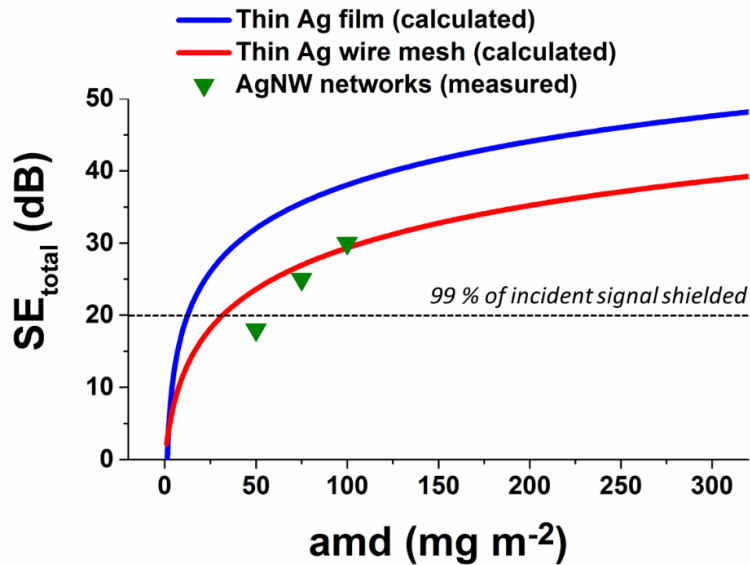


Figure 86. Total shielding efficiency (SE) in the range [1-10 GHz] as a function of Ag areal mass density, for thin Ag film (blue, calculated), thin Ag wire mesh screens (red, calculated), and AgNW networks (green, measured). For thin Ag wire meshes, SE is independent on the frequency (Equation 6.9). For thin Ag films, SE should depend on the frequency (see Equations 6.6, 6.7, 6.8). However, for such low amd values (i.e. low thicknesses), the changes in SE between $f=1$ GHz and $f=10$ GHz are almost insignificant. The amd values corresponding to the three AgNW networks reported here (green triangle), and previously described (Figure 83) indicates only a tendency and should be further confirmed.

In the range 50-100 mg^{-2} , the shielding efficiency associated to the three different types of Ag materials is close or higher than 20 dB, which is the standard level targeted in most shielding devices. As expected, the highest SE is achieved in the case of a continuous thin film. The SE associated with wire mesh screen is slightly higher than the one of AgNW networks in this amd range, although the difference decreases as the amd increases and is almost insignificant at 100

mg m⁻². As a consequence, it can be considered that AgNW networks can compete with Ag wire mesh screen in terms of raw material content required. However, another very important asset for the target application is the level of transparency of the resulting shielding device. The transmittance level corresponding to the *amd* values discussed above should be rigorously investigated for the three types of materials, in order to complete the comparison. It is likely that AgNW networks and Ag wire mesh grids offer a much better compromise than Ag thin film in terms of shielding properties, optical transmittance, and raw materials needs. Finally, one major advantage of AgNW networks over Ag wire mesh screens is that they involve much lower costs of fabrication and are entirely compatible with solution process.

6.3.2. EM shielding outlooks

AgNW networks have proved to exhibit very promising EM shielding properties. The measured SE were as high as 20 dB for networks associated with an optical transmittance around 90%. The impact of the network density on the shielding performances was demonstrated: the higher the density, the higher the surface coverage, and the higher the reflectivity of the network leading to higher SE values. The latter values were found to be quite stable in 0-20 GHz frequency range, except the presence of several peaks, whose origin is still not completely explained so far. The shielding level of AgNW networks was not substantially modified after thermal annealing nor after one year storage in light and in air.

Future prospects may concern the investigation of AgNW-PDMS composites shielding properties under stretch. When performing stretching cycles, the local areal mass density might be slightly modified, leading to a modification of the reflectivity level too. Moreover, the impact of changing the NW dimensions on the overall shielding properties of AgNW networks should also be investigated. Similarly to AgNW-based antennas, simulations of the shielding properties of AgNW networks using realistic random network architecture would be very beneficial to anticipate the parameters influencing the shielding efficiency, as well as the expected shielding level.

Finally, preliminary tests using more complex AgNW architectures and aimed at optimizing RF signal transmission through double glazed windows with reinforced thermal insulation were performed during this thesis.^[185] Such study should be continued and completed in the future. More specifically, the design of the architecture needs to be adapted using simulation models, and according to the scope and limitations of AgNW networks. More generally, the integration of AgNW networks in more complex shielding devices should be further investigated in close future.

Conclusion and future works

The technology of transparent electrodes based on silver nanowire (AgNW) networks is gaining increasingly in maturity. The present thesis aimed at investigating important assets – unexplored (or not explored enough) so far – in order to increase the robustness, reliability, and industrial compatibility of such technology. Here are some of the main conclusions and outlooks related to this thesis work.

The influence of several optimization techniques on the reduction of AgNW network electrical resistance was investigated considering either commercial AgNWs (Seashell) or AgNWs synthesized at CEA-Liten. Acid treatment proved to be very efficient in reducing the sheet resistance of networks fabricated with both sources of AgNWs. TEM observation of NW-NW junction cross-sections prepared by ultramicrotomy revealed that acid treatment is helpful to enhance better intimate contact between AgNWs. However the exact origin of the physical or chemical mechanisms involved in the decrease of the junction resistance is still the subject of on-going work. Acid treatment is a simple and low energy activation technique, compatible with solution process. However, it was demonstrated that performing additional thermal ramp annealing can optimize further AgNW networks, as well as improving their electrical homogeneity. Thermal annealing is indeed responsible for activating silver atomic diffusion near the junctions, leading to well sintered junctions. Such process is helpful for further decreasing the overall network resistance. From a statistical point of view, it is also helpful for minimizing the amount of inactive junctions throughout the network, which leads to a better electrical homogeneity. As a consequence, efficient and quick activation of AgNW networks can be achieved by performing acid treatment, while combination of acid treatment and thermal ramp annealing is beneficial to further optimize the electrical performance of AgNW networks.

To better understand and control the local mechanisms involved in either acid or thermal treatments, more efforts have to be devoted in exploring the internal structure of the junctions (by ultramicrotomy). Besides, the impact of the NW dimensions (diameter and length) on the AgNW network overall performances should also be investigated. Fabricating AgNW-based transparent electrodes with desired NW dimensions and network density is essential to fulfill the technical requirements of the target applications (high transparency, low haziness, etc.). Control of the AgNW dimensions during the synthesis consists of on-going work headed by PhD student Djadidi Toybou (CEA-Liten, 2016-2019). Simulation tools developed during the present thesis might also be helpful to anticipate the influence of the NW dimensions and network density and make correlation with real AgNW networks fabricated with different couples of NW dimensions.

Within this simulation work, we succeeded in transferring randomly generated AgNW network architectures from Matlab to Comsol. Most of the work was then dedicated to the construction of realistic models of AgNW networks, in order to extract some of their critical electrical and thermal properties. For instance, SEM and TEM based observations of the junctions' shapes helped modeling properly the NW-NW junctions. Moreover, the selection of the physical parameters such as the single nanowire conductivity, the contact impedance (grain boundary

resistance at the junctions), and the constriction thermal conductance, were meticulously implemented to the models thanks to experimental data recently obtained in the team as well as theoretical models extracted from the literature. To our knowledge, this work constitutes the first attempt to simulate the AgNW networks physical properties using the FEM numerical method.

The electrical model constructed using Comsol revealed to be efficient and helpful for extracting global information (electrical resistance) and local information (electrical distribution, current density), as well as for testing the influence of several parameters such as the network density, the NW dimensions, and the electrical junction efficiency. However, the model does not fit the percolation theory at very low density. It overestimates the conduction level of networks close to the percolation threshold. A possible route for overpassing this drawback may consist of assigning the efficiency level of the junctions according to a Gaussian distribution. Besides, increasing the system size would be beneficial for increasing the reliability of the model. Finally, the value used for estimating the contact impedance in the model only relies on experiments performed by other research teams.^[202] Here again, it would be beneficial for the reliability of our electrical model to perform measurements of the electrical resistance of single AgNW junctions before and after optimization, using AgNW synthesized in the lab. On the other hand, our thermal model provides interesting information but cannot yet be considered enough realistic. Efforts have to be continued to improve the description of losses mechanisms, especially with external part of the circuit and at the lateral faces of the substrate. This should results in more realistic simulated temperature distribution.

Other prospects may concern the simulation of AgNW network optical properties, which is a mandatory aspect for applicative purpose. For instance, anticipating the influence of the NW dimensions or network density on the total or diffused (haze) transmittance would indeed be very helpful for fabricating adapted AgNW-based electrodes. Ongoing simulation work also concerns the mimicking of collection efficiency when using AgNW networks for solar cell applications. Such work is currently carried out by PhD student Sara Aghazadehchors (LMGP and Univ. Liège, 2015-2018), and may be incorporated in Comsol model for characterizing both the assets and limitations associated with AgNW-based transparent electrodes when integrated in solar cells.

The heart of the present thesis work was the investigation of the electrical distribution in AgNW networks. At the scale of the entire network, our ability to distinguish NW areas taking part in the electrical conduction from potentially inactive areas is a critical point for the applications. Several mapping techniques, such as LiT and 1P-voltage mapping, revealed to be very helpful for investigating electrical distribution in AgNW networks. By combining experimental and numerical studies, a discrete activation process of efficient percolating pathways through the network was evidenced, giving rise to a geometrical quantized percolation phenomenon. In the case where the network density is close to the percolation threshold and when low voltage is applied, individual “illuminated” pathways can be detected throughout the network while new branches get activated as soon as the voltage is increased. From an applicative point of view, it was shown than the thermal and electrical distributions associated to the onset of electrical percolation in AgNW networks can be controlled by the voltage application level and by the

shape of the electrodes as well. Such phenomenon also proved to be highly influenced by the average NW diameter.

More generally, the electrical distribution in AgNW networks is highly dependent on the network density and on the level of junction optimization. Voltage equi-potential lines – experimentally extracted using the 1P-mapping technique – were found to become substantially straighter when increasing the NW density, leading to a higher electrical homogeneity. Similarly, LiT analysis confirmed experimentally that the electrical/thermal distribution associated to AgNW networks is much more homogenous after optimization by thermal annealing. In future study, electrical homogeneity of AgNW networks should be quantified more rigorously, for instance by estimating the tortuosity of voltage equipotential lines. Experimental results showing the influence of both the network density and junction optimization could be confirmed and correlated with Comsol models developed in this thesis.

Finally, such imaging tools were found very helpful for characterizing the mechanisms responsible for instabilities and failures in AgNW networks when subjected to electrical stress. The effects of such instabilities on the AgNW networks electrical map could also be highlighted. More specifically, an electrically-induced thermal runaway mechanism could be evidenced, leading to the growth of a crack parallel to the bias electrodes. Ongoing research (in close collaboration with LEPMI) focuses on the development of “dynamic” simulations to mimic such a failure mechanism. Very preliminary simulation results are depicted in **Figure 87**, and are compatible with experimental observations reported in this thesis.

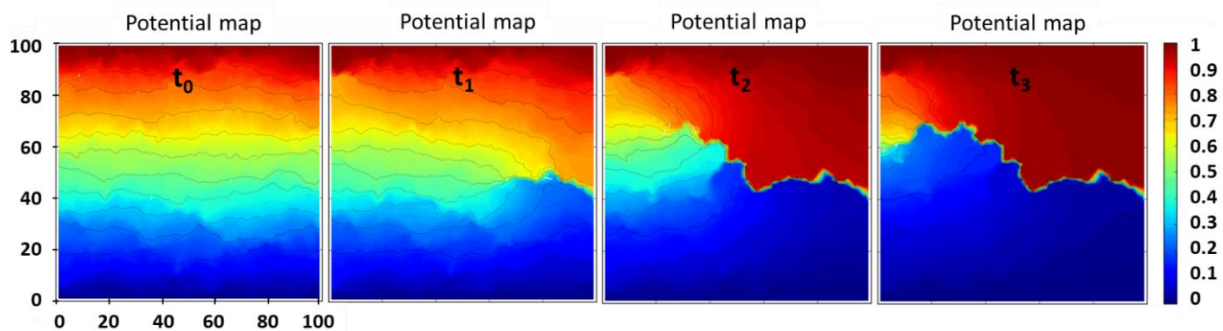


Figure 87. Dynamic simulation performed using SPICE software, showing the evolution of an electrical potential map while voltage limit is applied to the network. In each run the current density flowing in each of the individual nanowires is calculated and compared to the experimentally estimated sustainable current limit. Any nanowire carrying an electrical current higher than the limit is set as “inactive” in future runs. Simulations performed by Nicolas Charvin (LEPMI).

In future works, issues about electrical/thermal distribution and stability should be considered after final encapsulation of AgNW networks. It should be kept in mind that in most of the target applications, AgNW networks will have to be protected by an encapsulation layer, for both safety and performance considerations. For instance, depositing a protecting thin layer by SALD (TiO_2 , Al_2O_3 , ZnO) might be beneficial for overstepping some of the AgNW networks stability limitations. Therefore, the influence of such an additional thin layer on the electrical/thermal homogeneity and stability of the resulting hybrid electrode should also be

cautiously investigated. Besides, while many efforts focused on electrical mapping at the scale of the electrode, one should also devote attention to the characterization of electrical distribution and stability of AgNW networks at the nanoscale. For instance, ongoing project consists of studying *in situ* electrical ageing of AgNW networks, using charge contrast imaging technique under SEM. AgNWs are deposited on a silicon microchip between an Au-based-two electrode system (see **Figure 88a**), allowing electrical connection with external part of the SEM. When AgNWs are physically connected to the bias electrodes, electrons from incident beam can be easily drained off by AgNWs through the external circuit. Hence, no secondary electrons are sent back to the detector: the corresponding nanowires appear “black” (see Figure 88b). On the other hand, some percolating pathways might be destroyed when increasing voltage due to early spheroidization and/or electromigration process, inducing charge effects in the disconnected wires and pathways. The latter appear “white” since a huge amount of secondary electrons are sent back to the detector in that case (see Figure 88b). Such study might lead to *in situ* nanoscale live visualization of failure dynamics of AgNW networks under bias.

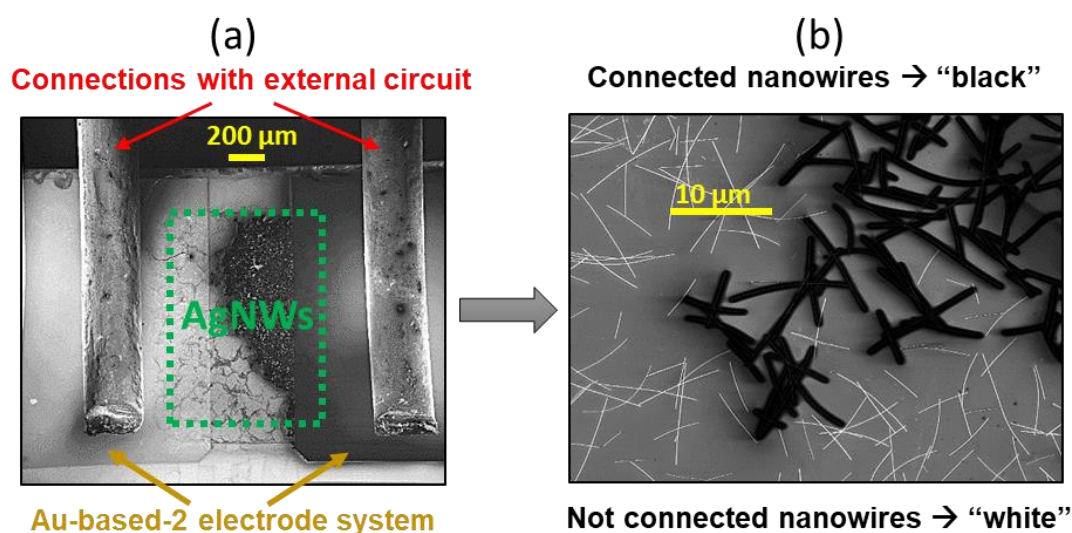


Figure 88. a) Image captured under SEM showing the silicon microchip, Au-based-two electrode system, and connections with external circuits, used for charge contrast *in situ* imaging analysis. b) SEM images showing either black or white silver nanowires, according to their physical connection with Au electrodes. In order to achieve satisfying charge contrast under SEM, it is required to use an “In Lens” detector.

This thesis work also briefly explored the mechanical properties of AgNW networks. Due to the increasing demand for portable and wearable electronic, research for flexible and conformable conductive materials is required. From a technological point of view, the flexibility of AgNW network-based electrodes is a major advantage over ITO-based electrodes, and has been demonstrated for several years.^[30] On the contrary, the literature about their stretching properties is still poor. In this context, the stretchability of AgNW-PDMS composites was investigated in this thesis via a dual approach combining *in situ* electrical measurements of the electrical resistance when performing stretching/releasing cycles, and *in situ* nanocharacterization (SEM) of the mechanical deformations of such composites under strain.

More precisely, the nanowires appear to show damages only above a relatively high percentage of elongation ($\approx 30\text{-}40\%$) because of mechanical deformations (cracks) that firstly occur in the nearby polymer substrate. Such cracks are responsible for a high increase in the electrical resistance at high strain. However, when the AgNW-PDMS composites are released back, some cracks start healing and several nanowires are likely to touch each other again, leading to the rebuilding of percolation paths through the network.

Many details regarding the physical properties of AgNW-PDMS composites (mechanical, optical, electrical, thermal, etc.) are still under investigation. For instance, the electrical mapping techniques used in this thesis may be suitable for imaging the potential distortion of electrical distribution in such strained-composites. Moreover, the impact of the NW dimension, and especially the NW length on the stretching limitations should be investigated. For instance, using longer NWs might indeed be beneficial for extending the stretchability of these composites. From an applicative point of view, it was evidenced that PDMS is subject to buckling at high strain, which might be restrictive for applications requiring transparent electrodes with very smooth surface. The origin of this phenomenon is still unclear and should therefore be further investigated. The use of elastic substrates other than PDMS may also be investigated. However, these preliminary results are very promising for future integration of AgNWs into stretchable devices. Future applicative prospects may concern the analysis of the mechanical and thermal performances of stretchable transparent films heaters (TFHs) made of AgNW-PDMS composites. The influence of stretching on the electromagnetic shielding behavior of such composites appears also as an interesting investigation route.

Finally, some of this thesis work was directly dedicated to the integration of AgNW networks in functional devices. Much of the study about AgNW-based TFHs focused on stability issues: deep analysis of the mechanisms leading to failure was headed by former PhD student Mélanie Lagrange (LMGP, 2012-2015). It was also evidenced that such devices exhibit very promising heating capability, and good reliability when not subjected to aggressive electrical stress. At higher voltage and for long stress duration, some irreversible damages might appear, due to early spheroidization or electromigration process. Electrical mapping techniques and especially IR thermography (“live” imaging) or LiT (“semi-live” imaging) used during this thesis would also be beneficial to monitor the evolution of electrical and thermal distributions under aggressive electrical stress. Similarly, efforts to increase the device stability, especially by adding thin conformal encapsulation layer by SALD have to be continued. This is on-going research carried out by PhD student Sara Aghazadehchors.

Apart from TFHs, some of the applicative work was also dedicated to electromagnetic (EM) applications, with special emphasis on Radio-Frequency (RF) antennas and EM shielding. Several antennas entirely or partly made of interconnected AgNWs were fabricated. While impedance match at the entrance of the antenna (S_{11}) revealed to be coherent with the simulation results, the radiation performances of the AgNW-based antennas were found slightly lower than expected. In particular, antennas associated with transmission lines made of only AgNWs exhibited lower gain values than those associated with a hybrid transmission lines (AgNWs-Au, AgNWs-PEDOT PSS). The low width of the transmission line, as well as the percolating nature of AgNW networks might be responsible for inefficient signal transmission from

incident port to radiating element of the antennas. This was further confirmed by preliminary studies specifically dedicated to transmission lines made of AgNW networks. In order to get deeper information regarding the required NW density and device dimensions, as well as for anticipating the overall performance of the resulting devices (signal losses, radiation efficiency, etc.), it would be desirable to build a RF simulation model using realistic AgNW network architectures.

On the other hand, the EM shielding properties of AgNW networks revealed very promising. The shielding efficiency (SE) was found to be as high as 20 dB in the 1-20 GHz range, for samples exhibiting a very high optical transparency ($\approx 90\%$) at the same time. The influence of the network density was also investigated: the higher the network density, the higher the shielding efficiency, as a result of the increase of sample reflectivity with the AgNW surface coverage. As already mentioned, future works may focus on the investigation of the AgNW network shielding behavior under mechanical stress (stretching, bending, twisting). Besides, fabricating more complex architecture dedicated to specific shielding applications such as transparent Frequency Selective Surfaces (FSS)^[185] may be tested. For instance, preliminary tests aimed at optimizing RF signal transmission through double glazed windows with reinforced thermal insulation were performed during this thesis. Here again, RF simulation based on realistic interconnected AgNWs architectures would be very beneficial for anticipating the limitations of fabricated EM shielding devices, as well as for optimizing their design. More generally, efforts have to be continued so that the simulation tools developed in this thesis can be helpful for RF applications.

Another important aspect that should be developed is the potential risk that could arise from industrial use of AgNWs. Although it can be anticipated that there are many societal and individual benefits from AgNW-enabled technology, safety aspects are to be tackled. There are already existing studies on the toxicity of the nanomaterials themselves^[243–246] and others are ongoing. Furthermore, potential exposure to AgNWs as a result of release from commercial products is also currently under investigation, in particular at Grenoble within the thesis of Djadidi Toybou.

As already mentioned above, there are still many outlooks and challenges to tackle regarding the science and technology related to AgNW networks. This thesis helped overcoming several fundamental issues about the physical phenomena taking place at the scales of both the network (macroscale) and the NW-NW junctions (nanoscale). Other advances concerned more applicative aspects, either to increase the robustness of already existing AgNW-based applications, or to open new applicative routes for this technology. The intrinsic performance of AgNW networks proved to fit with industrial requirements in many cases. These percolating networks consists of a promising low-cost, indium-free, high performance, and flexible alternative solution to commonly used TCO-based transparent electrodes. In order to encourage such technology replacement, efforts should be continued to make it more stable and reliable: this requires to keep going on studying the fundamental mechanisms responsible for local instabilities, while offering solutions to fabricate more robust and more resistant AgNW-based electrodes without altering their intrinsic properties. With some of the original contributions presented above, may this thesis contribute even modestly to go in this direction...

Appendix A: physical equations solved in Comsol simulations using the finite element method

1. Ohm's law

$$\nabla \cdot \mathbf{J} = Q_j, \quad \mathbf{J} = \sigma \mathbf{E} + \mathbf{J}_e, \quad \mathbf{E} = -\nabla V$$

Where \mathbf{J} is the current density, \mathbf{J}_e is the outside current source, Q_j is the total amount of charge in the system, σ is the material conductivity, \mathbf{E} is the electrical field and V is the voltage.

2. Electrical contact impedance

$$\mathbf{n} \cdot \mathbf{J}_1 = \frac{1}{\rho_s} (V_1 - V_2), \quad \mathbf{n} \cdot \mathbf{J}_2 = \frac{1}{\rho_s} (V_2 - V_1)$$

Where \mathbf{n} is the normal vector of the contact face, ρ_s is the surface resistance and indices 1 and 2 refer to two sides of the boundary.

3. Heat transfer at steady state

$$\rho C_p \mathbf{u} \cdot \nabla T + \nabla \cdot \mathbf{q} = Q, \quad \mathbf{q} = -k \nabla T$$

Where ρ is the material density, C_p is the specific heat capacity at constant pressure, T is the absolute temperature, \mathbf{u} is the velocity vector, \mathbf{q} is the heat flux by conduction, Q is the heat source and k is the thermal conductivity.

4. Heat transfer in time-dependent case

$$\rho C_p \frac{\partial T}{\partial t} + \rho C_p \mathbf{u} \cdot \nabla T + \nabla \cdot \mathbf{q} = Q, \quad \mathbf{q} = -k \nabla T$$

With t the time.

5. The thermal convective equation

$$q_0 = h * (T_{ext} - T)$$

With q_0 the heat losses, h the heat transfer coefficient and T_{ext} the external temperature.

6. The thermal radiation equation

$$-\mathbf{n} \cdot \mathbf{q} = \varepsilon \sigma (T_{amb}^4 - T^4)$$

With ε the surface emissivity, σ the Stefan–Boltzmann constant and T_{amb} the ambient temperature.

Appendix B: calculation of the AgNW network areal mass density

The areal mass density amd of AgNW networks is a critical parameter, giving a basis from which we can predict other properties like electrical resistance and transparency. It is therefore crucial to be able to estimate precisely the amd values. The method previously developed in the team^[24] used the software ImageJ to count pixels in binarised SEM images. The amd was calculated by estimating the ratio ξ of Ag-covered surface S_{Ag} against total surface S_{tot} . This method revealed efficient but was subjected to a relatively high margin of error, especially in the estimation of ξ that may be substantially overestimated when looking at a SEM image.

To get rid of these uncertainties, a new method was recently developed in collaboration with LEPMI (Nicolas Charvin), where the equivalent total length of AgNWs L_{eq} is directly calculated by image analysis. We still use ImageJ to analyse SEM images of AgNW networks (see **Figure 89a**). However, we now use a ridge detection algorithm to identify the nanowires directly. Starting from a raw SEM image, we first need to crop off the data bar. Then, we use the ImageJ plugin “Ridge Detection”, with the algorithm developed by Steger.^[247] The algorithm is sensitive to bright features in front of a dark background and can detect line segments (see Figure 89b-c).

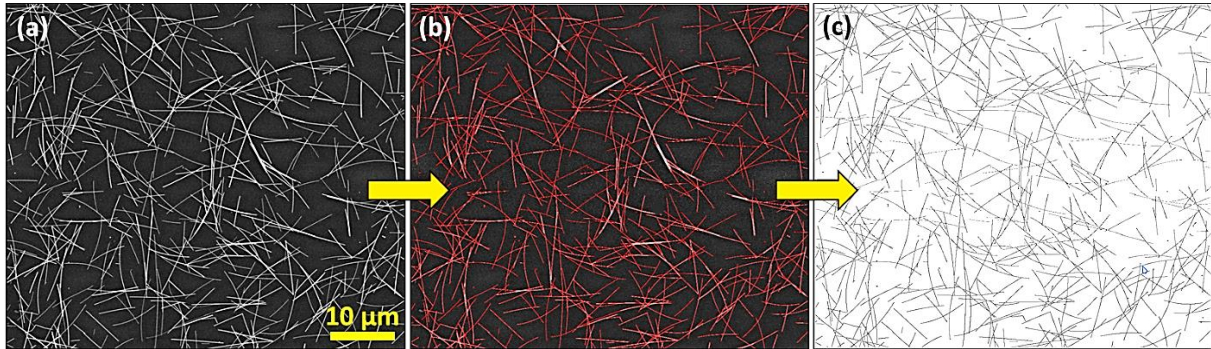


Figure 89. a) Captured SEM image of an AgNW network, about to be analyzed using ImageJ. b-c) Detection of NWs using the plugin “Ridge Detection”, and reconstruction of virtual networks.

The plugin then lists the lengths of all detected segments, in units of pixels. The scale factor for the conversion from pixels to nm can be extracted from the TIFF image metadata. By taking the sum, we estimate with a good approximation the total length L_{eq} of all nanowires together. The geometrical density d_g , defined as $d_g = \frac{L_{eq}}{S_{tot}}$ is extracted. Assuming the NWs to be cylindrically shaped, the amd is finally calculated as follows:

$$amd = n * m_{NW} = \frac{d_g}{L_{NW}} * m_{NW} = d_g * \left(\frac{\pi d_{Ag} D_{NW}^2}{4} \right)$$

Where n is the number of NWs per unit area, m_{NW} is the mass of individual NWs, D_{NW} and L_{NW} the average AgNW diameter and length, respectively, and d_{Ag} is the density of silver.

References

- [1] D. S. Ginley, H. Hosono, D. C. Paine, *Handbook of Transparent Conductors*, Springer, New York, NY, USA, **2010**.
- [2] D. S. Hecht, L. Hu, G. Irvin, *Adv. Mater.* **2011**, *23*, 1482.
- [3] T. M. Barnes, M. O. Reese, J. D. Bergeson, B. A. Larsen, J. L. Blackburn, M. C. Beard, J. Bult, J. van de Lagemaat, *Adv. Energy Mater.* **2012**, *2*, 353.
- [4] C. G. Granqvist, *Sol. Energy Mater. Sol. Cells* **2007**, *91*, 1529.
- [5] J. van de Groep, P. Spinelli, A. Polman, *Nano Lett.* **2012**, *12*, 3138.
- [6] Y. H. Kim, C. Sachse, M. L. Machala, C. May, L. Müller-Meskamp, K. Leo, *Adv. Funct. Mater.* **2011**, *21*, 1076.
- [7] M. V. Fabretto, D. R. Evans, M. Mueller, K. Zuber, P. Hojati-Talemi, R. D. Short, G. G. Wallace, P. J. Murphy, *Chem. Mater.* **2012**, *24*, 3998.
- [8] K. Ellmer, *Nat. Photonics* **2012**, *6*, 809.
- [9] D. Langley, G. Giusti, C. Mayousse, C. Celle, D. Bellet, J.-P. Simonato, *Nanotechnology* **2013**, *24*, 452001.
- [10] S. Ye, A. R. Rathmell, Z. Chen, I. E. Stewart, B. J. Wiley, *Adv. Mater.* **2014**, *26*, 6670.
- [11] S. Yao, Y. Zhu, *Adv. Mater.* **2015**, *27*, 1480.
- [12] X. Xiong, C.-L. Zou, X.-F. Ren, A.-P. Liu, Y.-X. Ye, F.-W. Sun, G.-C. Guo, *Laser Photonics Rev.* **2013**, *7*, 901.
- [13] C. F. Guo, Z. Ren, *Mater. Today* **2015**, *18*, 143.
- [14] C. Celle, C. Mayousse, E. Moreau, H. Basti, A. Carella, J.-P. Simonato, *Nano Res.* **2012**, *5*, 427.
- [15] S. De, T. M. Higgins, P. E. Lyons, E. M. Doherty, P. N. Nirmalraj, W. J. Blau, J. J. Boland, J. N. Coleman, *ACS Nano* **2009**, *3*, 1767.
- [16] S. Sorel, D. Bellet, J. N. Coleman, *ACS Nano* **2014**, *8*, 4805.
- [17] S. Ji, W. He, K. Wang, Y. Ran, C. Ye, *Small* **2014**, *10*, 4951.
- [18] T. Rai, P. Dantes, B. Bahreyni, W. S. Kim, *IEEE Electron Device Lett.* **2013**, *34*, 544.
- [19] L. Song, A. C. Myers, J. J. Adams, Y. Zhu, *ACS Appl. Mater. Interfaces* **2014**, *6*, 4248.
- [20] Y.-H. Yu, C.-C. M. Ma, C.-C. Teng, Y.-L. Huang, S.-H. Lee, I. Wang, M.-H. Wei, *Mater. Chem. Phys.* **2012**, *136*, 334.
- [21] M. Hu, J. Gao, Y. Dong, K. Li, G. Shan, S. Yang, R. K.-Y. Li, *Langmuir* **2012**, *28*, 7101.
- [22] Céline Mayousse, Elaboration d'électrodes transparentes souples à base de nanofils métalliques, PhD thesis: Grenoble Alpes University, **2014**.
- [23] Daniel Langley, Silver Nanowire Networks: Effects of Percolation and Thermal Annealing on Physical Properties, PhD thesis: Grenoble Alpes University, Université de Liège, **2014**.
- [24] M. Lagrange, Physical Analysis of Percolating Silver Nanowire Networks Used as Transparent Electrodes for Flexible Applications, PhD thesis: Grenoble Alpes University, **2015**.
- [25] J. Colegrove, *ITO-Replacement Report*, Touch Display Research Inc, Santa Clara, CA, USA, **2016**.
- [26] C. Mayousse, C. Celle, E. Moreau, J.-F. Mainguet, A. Carella, J.-P. Simonato, *Nanotechnology* **2013**, *24*, 215501.
- [27] M. S. Miller, J. C. O'Kane, A. Niec, R. S. Carmichael, T. B. Carmichael, *ACS Appl. Mater. Interfaces* **2013**, *5*, 10165.
- [28] J. Liang, L. Li, X. Niu, Z. Yu, Q. Pei, *Nat. Photonics* **2013**, *7*, 817.
- [29] B. S. Kim, K.-Y. Shin, J. B. Pyo, J. Lee, J. G. Son, S.-S. Lee, J. H. Park, *ACS Appl. Mater. Interfaces* **2016**, *8*, 2582.

- [30] T. Sannicolo, M. Lagrange, A. Cabos, C. Celle, J.-P. Simonato, D. Bellet, *Small* **2016**, *12*, 6052.
- [31] M. Lagrange, T. Sannicolo, D. Muñoz-Rojas, B. G. Lohan, A. Khan, M. Anikin, C. Jiménez, F. Bruckert, Y. Bréchet, D. Bellet, *Nanotechnology* **2017**, *28*, 055709.
- [32] Y. Sun, B. Gates, B. Mayers, Y. Xia, *Nano Lett.* **2002**, *2*, 165.
- [33] Y. Sun, Y. Xia, *Adv. Mater.* **2002**, *14*, 833.
- [34] B. Wiley, Y. Sun, B. Mayers, Y. Xia, *Chem. – Eur. J.* **2005**, *11*, 454.
- [35] Y. Shi, H. Li, L. Chen, X. Huang, *Sci. Technol. Adv. Mater.* **2005**, *6*, 761.
- [36] A. R. Rathmell, S. M. Bergin, Y.-L. Hua, Z.-Y. Li, B. J. Wiley, *Adv. Mater.* **2010**, *22*, 3558.
- [37] S. Coskun, B. Aksoy, H. E. Unalan, *Cryst. Growth Des.* **2011**, *11*, 4963.
- [38] D. Zhang, R. Wang, M. Wen, D. Weng, X. Cui, J. Sun, H. Li, Y. Lu, *J. Am. Chem. Soc.* **2012**, *134*, 14283.
- [39] A. R. Rathmell, M. Nguyen, M. Chi, B. J. Wiley, *Nano Lett.* **2012**, *12*, 3193.
- [40] I. E. Stewart, S. Ye, Z. Chen, P. F. Flowers, B. J. Wiley, *Chem. Mater.* **2015**, *27*, 7788.
- [41] S. De, T. M. Higgins, P. E. Lyons, E. M. Doherty, P. N. Nirmalraj, W. J. Blau, J. J. Boland, J. N. Coleman, *ACS Nano* **2009**, *3*, 1767.
- [42] D. P. Langley, M. Lagrange, G. Giusti, C. Jiménez, Y. Bréchet, N. D. Nguyen, D. Bellet, *Nanoscale* **2014**, *6*, 13535.
- [43] W. Cao, J. Li, H. Chen, J. Xue, *J. Photonics Energy* **2014**, *4*, 040990.
- [44] S. Ye, A. R. Rathmell, I. E. Stewart, Y.-C. Ha, A. R. Wilson, Z. Chen, B. J. Wiley, *Chem. Commun.* **2014**, *50*, 2562.
- [45] C. Mayousse, C. Celle, A. Carella, J.-P. Simonato, *Nano Res.* **2014**, *7*, 315.
- [46] S. Li, Y. Chen, L. Huang, D. Pan, *Inorg. Chem.* **2014**, *53*, 4440.
- [47] A. Tao, F. Kim, C. Hess, J. Goldberger, R. He, Y. Sun, Y. Xia, P. Yang, *Nano Lett.* **2003**, *3*, 1229.
- [48] K. E. Korte, S. E. Skrabalak, Y. Xia, *J. Mater. Chem.* **2008**, *18*, 437.
- [49] I. E. Stewart, A. R. Rathmell, L. Yan, S. Ye, P. F. Flowers, W. You, B. J. Wiley, *Nanoscale* **2014**, *6*, 5980.
- [50] M. Lagrange, D. P. Langley, G. Giusti, C. Jiménez, Y. Bréchet, D. Bellet, *Nanoscale* **2015**, *7*, 17410.
- [51] V. Scardaci, R. Coull, P. E. Lyons, D. Rickard, J. N. Coleman, *Small* **2011**, *7*, 2621.
- [52] M. Reinhard, R. Eckstein, A. Slobodskyy, U. Lemmer, A. Colmann, *Org. Electron.* **2013**, *14*, 273.
- [53] W. Gaynor, G. F. Burkhard, M. D. McGehee, P. Peumans, *Adv. Mater.* **2011**, *23*, 2905.
- [54] T. Tokuno, M. Nogi, M. Karakawa, J. Jiu, T. T. Nge, Y. Aso, K. Suganuma, *Nano Res.* **2011**, *4*, 1215.
- [55] J. Krantz, M. Richter, S. Spallek, E. Spiecker, C. J. Brabec, *Adv. Funct. Mater.* **2011**, *21*, 4784.
- [56] S. B. Sepulveda-Mora, S. G. Cloutier, *J. Nanomater.* **2012**, *2012*, 7.
- [57] A. R. Rathmell, B. J. Wiley, *Adv. Mater.* **2011**, *23*, 4798.
- [58] L. Hu, H. S. Kim, J.-Y. Lee, P. Peumans, Y. Cui, *ACS Nano* **2010**, *4*, 2955.
- [59] C.-H. Liu, X. Yu, *Nanoscale Res. Lett.* **2011**, *6*, 75.
- [60] F. Guo, X. Zhu, K. Forberich, J. Krantz, T. Stubhan, M. Salinas, M. Halik, S. Spallek, B. Butz, E. Spiecker, T. Ameri, N. Li, P. Kubis, D. M. Guldi, G. J. Matt, C. J. Brabec, *Adv. Energy Mater.* **2013**, *3*, 1062.
- [61] T. Stubhan, J. Krantz, N. Li, F. Guo, I. Litzov, M. Steidl, M. Richter, G. J. Matt, C. J. Brabec, *Sol. Energy Mater. Sol. Cells* **2012**, *107*, 248.
- [62] H. Guo, N. Lin, Y. Chen, Z. Wang, Q. Xie, T. Zheng, N. Gao, S. Li, J. Kang, D. Cai, D.-L. Peng, *Sci. Rep.* **2013**, *3*, DOI 10.1038/srep02323.

- [63] P. Lee, J. Lee, H. Lee, J. Yeo, S. Hong, K. H. Nam, D. Lee, S. S. Lee, S. H. Ko, *Adv. Mater.* **2012**, *24*, 3326.
- [64] J.-W. Lim, D.-Y. Cho, Jihoon-Kim, S.-I. Na, H.-K. Kim, *Sol. Energy Mater. Sol. Cells* **2012**, *107*, 348.
- [65] S.-B. Kang, Y.-J. Noh, S.-I. Na, H.-K. Kim, *Sol. Energy Mater. Sol. Cells* **2014**, *122*, 152.
- [66] M. Majumder, C. Rendall, M. Li, N. Behabtu, J. A. Eukel, R. H. Hauge, H. K. Schmidt, M. Pasquali, *Chem. Eng. Sci.* **2010**, *65*, 2000.
- [67] C. Mayousse, C. Celle, E. Moreau, J.-F. Mainguet, A. Carella, J.-P. Simonato, *Nanotechnology* **2013**, *24*, 215501.
- [68] A. Bid, A. Bora, A. K. Raychaudhuri, *Phys. Rev. B* **2006**, *74*, 035426.
- [69] T. Araki, J. Jiu, M. Nogi, H. Koga, S. Nagao, T. Sugahara, K. Suganuma, *Nano Res.* **2014**, *7*, 236.
- [70] C. Preston, Y. Xu, X. Han, J. N. Munday, L. Hu, *Nano Res.* **2013**, *6*, 461.
- [71] E.-J. Lee, Y.-H. Kim, D. K. Hwang, W. K. Choi, J.-Y. Kim, *RSC Adv* **2016**, *6*, 11702.
- [72] J. H. Lee, P. Lee, D. Lee, S. S. Lee, S. H. Ko, *Cryst. Growth Des.* **2012**, *12*, 5598.
- [73] E.-J. Lee, M.-H. Chang, Y.-S. Kim, J.-Y. Kim, *APL Mater.* **2013**, *1*, 042118.
- [74] J. Jiu, T. Araki, J. Wang, M. Nogi, T. Sugahara, S. Nagao, H. Koga, K. Suganuma, E. Nakazawa, M. Hara, H. Uchida, K. Shinozaki, *J. Mater. Chem. A* **2014**, *2*, 6326.
- [75] B. Li, S. Ye, I. E. Stewart, S. Alvarez, B. J. Wiley, *Nano Lett.* **2015**, *15*, 6722.
- [76] J. W. Borchert, I. E. Stewart, S. Ye, A. R. Rathmell, B. J. Wiley, K. I. Winey, *Nanoscale* **2015**, *7*, 14496.
- [77] P. N. Nirmalraj, A. T. Bellew, A. P. Bell, J. A. Fairfield, E. K. McCarthy, C. O’Kelly, L. F. C. Pereira, S. Sorel, D. Morosan, J. N. Coleman, M. S. Ferreira, J. J. Boland, *Nano Lett.* **2012**, *12*, 5966.
- [78] A. T. Bellew, H. G. Manning, C. Gomes da Rocha, M. S. Ferreira, J. J. Boland, *ACS Nano* **2015**, *9*, 11422.
- [79] Q. Nian, M. Saei, Y. Xu, G. Sabyasachi, B. Deng, Y. P. Chen, G. J. Cheng, *ACS Nano* **2015**, *9*, 10018.
- [80] S. Coskun, E. Selen Ates, H. Emrah Unalan, *Nanotechnology* **2013**, *24*, 125202.
- [81] J. Lee, P. Lee, H. Lee, D. Lee, S. S. Lee, S. H. Ko, *Nanoscale* **2012**, *4*, 6408.
- [82] S. Han, S. Hong, J. Ham, J. Yeo, J. Lee, B. Kang, P. Lee, J. Kwon, S. S. Lee, M.-Y. Yang, S. H. Ko, *Adv. Mater.* **2014**, *26*, 5808.
- [83] E. C. Garnett, W. Cai, J. J. Cha, F. Mahmood, S. T. Connor, M. Greyson Christoforo, Y. Cui, M. D. McGehee, M. L. Brongersma, *Nat. Mater.* **2012**, *11*, 241.
- [84] T. Kim, A. Canlier, G. H. Kim, J. Choi, M. Park, S. M. Han, *ACS Appl. Mater. Interfaces* **2013**, *5*, 788.
- [85] S. De, J. N. Coleman, *MRS Bull.* **2011**, *36*, 774.
- [86] G. Haacke, *J. Appl. Phys.* **1976**, *47*, 4086.
- [87] M. Göbelt, R. Keding, S. W. Schmitt, B. Hoffmann, S. Jäckle, M. Latzel, V. V. Radmilović, V. R. Radmilović, E. Spiecker, S. Christiansen, *Nano Energy* **2015**, *16*, 196.
- [88] H. Kim, C. M. Gilmore, A. Piqué, J. S. Horwitz, H. Mattoussi, H. Murata, Z. H. Kafafi, D. B. Chrisey, *J. Appl. Phys.* **1999**, *86*, 6451.
- [89] C. J. M. Emmott, A. Urbina, J. Nelson, *Sol. Energy Mater. Sol. Cells* **2012**, *97*, 14.
- [90] K. Ghaffarzadeh, R. Das, *Transparent Conductive Films (TCF) 2016-2026: Forecasts, Markets, Technologies*, IDTechEx Ltd, Boston, MA, USA, **2016**.
- [91] S. Bae, H. Kim, Y. Lee, X. Xu, J.-S. Park, Y. Zheng, J. Balakrishnan, T. Lei, H. Ri Kim, Y. I. Song, Y.-J. Kim, K. S. Kim, B. Özyilmaz, J.-H. Ahn, B. H. Hong, S. Iijima, *Nat. Nanotechnol.* **2010**, *5*, 574.
- [92] U. Kim, J. Kang, C. Lee, H. Y. Kwon, S. Hwang, H. Moon, J. C. Koo, J.-D. Nam, B. H. Hong, J.-B. Choi, H. R. Choi, *Nanotechnology* **2013**, *24*, 145501.

- [93] T. Sun, Z. L. Wang, Z. J. Shi, G. Z. Ran, W. J. Xu, Z. Y. Wang, Y. Z. Li, L. Dai, G. G. Qin, *Appl. Phys. Lett.* **2010**, *96*, 133301.
- [94] D. S. Hecht, A. M. Heintz, R. Lee, L. Hu, B. Moore, C. Cucksey, S. Risser, *Nanotechnology* **2011**, *22*, 075201.
- [95] L. Hu, H. Wu, Y. Cui, *MRS Bull.* **2011**, *36*, 760.
- [96] H. Wu, D. Kong, Z. Ruan, P.-C. Hsu, S. Wang, Z. Yu, T. J. Carney, L. Hu, S. Fan, Y. Cui, *Nat. Nanotechnol.* **2013**, *8*, 421.
- [97] A. Madaria, A. Kumar, F. Ishikawa, C. Zhou, *Nano Res.* **2010**, *3*, 564.
- [98] D.-S. Leem, A. Edwards, M. Faist, J. Nelson, D. D. C. Bradley, J. C. de Mello, *Adv. Mater.* **2011**, *23*, 4371.
- [99] H. Lee, D. Lee, Y. Ahn, E.-W. Lee, L. S. Park, Y. Lee, *Nanoscale* **2014**, *6*, 8565.
- [100] G. Giusti, V. Consonni, E. Puyoo, D. Bellet, *ACS Appl. Mater. Interfaces* **2014**, *6*, 14096.
- [101] T. Chih-Hung, H. Sui-Ying, H. Tsung-Wei, T. Yu-Tang, C. Yan-Fang, Y. H. Jhang, L. Hsieh, W. Chung-Chih, C. Yen-Shan, C. Chieh-Wei, L. Chung-Chun, *Org. Electron.* **2011**, *12*, 2003.
- [102] Y. Chiba, A. Islam, R. Komiya, N. Koide, L. Han, *Appl. Phys. Lett.* **2006**, *88*, 223505.
- [103] Z. Tang, W. Tress, O. Inganäs, *Mater. Today* **2014**, *17*, 389.
- [104] M.-H. Chang, H.-A. Cho, Y.-S. Kim, E.-J. Lee, J.-Y. Kim, *Nanoscale Res. Lett.* **2014**, *9*, 330.
- [105] G. Khanarian, J. Joo, X.-Q. Liu, P. Eastman, D. Werner, K. O'Connell, P. Trefonas, *J. Appl. Phys.* **2013**, *114*, 024302.
- [106] S. Mehra, M. G. Christoforo, P. Peumans, A. Salleo, *Nanoscale* **2013**, *5*, 4400.
- [107] Y. Atwa, N. Maheshwari, I. A. Goldthorpe, *J. Mater. Chem. C* **2015**, *3*, 3908.
- [108] H. H. Khaligh, I. A. Goldthorpe, *Nanoscale Res. Lett.* **2013**, *8*, 1.
- [109] H. Li, J. M. Biser, J. T. Perkins, S. Dutta, R. P. Vinci, H. M. Chan, *J. Appl. Phys.* **2008**, *103*, 024315.
- [110] T.-B. Song, Y. Chen, C.-H. Chung, Y. (Michael) Yang, B. Bob, H.-S. Duan, G. Li, K.-N. Tu, Y. Huang, Y. Yang, *ACS Nano* **2014**, *8*, 2804.
- [111] C. Mayousse, C. Celle, A. Fraczkiewicz, J.-P. Simonato, *Nanoscale* **2015**, *7*, 2107.
- [112] J. Jiu, J. Wang, T. Sugahara, S. Nagao, M. Nogi, H. Koga, K. Suganuma, M. Hara, E. Nakazawa, H. Uchida, *RSC Adv.* **2015**, *5*, 27657.
- [113] N. Weiß, L. Müller-Meskamp, F. Selzer, L. Bormann, A. Eychmüller, K. Leo, N. Gaponik, *RSC Adv.* **2015**, *5*, 19659.
- [114] L. Xu, Y. Yang, Z.-W. Hu, S.-H. Yu, *ACS Nano* **2016**, *10*, 3823.
- [115] Y. C. G. Kwan, Q. L. Le, C. H. A. Huan, *Sol. Energy Mater. Sol. Cells* **2016**, *144*, 102.
- [116] I. N. Kholmanov, S. H. Domingues, H. Chou, X. Wang, C. Tan, J.-Y. Kim, H. Li, R. Piner, A. J. G. Zarbin, R. S. Ruoff, *ACS Nano* **2013**, *7*, 1811.
- [117] F. S. F. Morgenstern, D. Kabra, S. Massip, T. J. K. Brenner, P. E. Lyons, J. N. Coleman, R. H. Friend, *Appl. Phys. Lett.* **2011**, *4*, 183307.
- [118] T.-B. Song, Y. S. Rim, F. Liu, B. Bob, S. Ye, Y.-T. Hsieh, Y. Yang, *ACS Appl. Mater. Interfaces* **2015**, *7*, 24601.
- [119] K. Zilberberg, F. Gasse, R. Pagui, A. Polywka, A. Behrendt, S. Trost, R. Heiderhoff, P. Görrn, T. Riedl, *Adv. Funct. Mater.* **2014**, *24*, 1671.
- [120] P. Lee, J. Ham, J. Lee, S. Hong, S. Han, Y. D. Suh, S. E. Lee, J. Yeo, S. S. Lee, D. Lee, S. H. Ko, *Adv. Funct. Mater.* **2014**, *24*, 5671.
- [121] D. Muñoz-Rojas, X. Moya, *Materials for Sustainable Energy Applications: Conversion, Storage, Transmission and Consumption*, Pan Stanford, Singapore, **2016**.
- [122] S. Fonash, *Solar Cell Device Physics*, Elsevier, **2012**.
- [123] A. Klein, *J. Am. Ceram. Soc.* **2013**, *96*, 331.

- [124] D. P. Langley, G. Giusti, M. Lagrange, R. Collins, C. Jiménez, Y. Bréchet, D. Bellet, *Sol. Energy Mater. Sol. Cells* **2014**, *125*, 318.
- [125] L. J. Andrés, M. F. Menéndez, D. Gómez, A. L. Martínez, N. Bristow, J. P. Kettle, A. Menéndez, B. Ruiz, *Nanotechnology* **2015**, *26*, 265201.
- [126] F. Guo, N. Li, V. V. Radmilović, V. R. Radmilović, M. Turbiez, E. Spiecker, K. Forberich, C. J. Brabec, *Energy Environ. Sci.* **2015**, *8*, 1690.
- [127] D. Angmo, T. R. Andersen, J. J. Bentzen, M. Helgesen, R. R. Søndergaard, M. Jørgensen, J. E. Carlé, E. Bundgaard, F. C. Krebs, *Adv. Funct. Mater.* **2015**, *25*, 4539.
- [128] Y.-J. Noh, S.-S. Kim, T.-W. Kim, S.-I. Na, *Sol. Energy Mater. Sol. Cells* **2014**, *120*, Part A, 226.
- [129] J.-W. Lim, D.-Y. Cho, K. Eun, S.-H. Choa, S.-I. Na, J. Kim, H.-K. Kim, *Sol. Energy Mater. Sol. Cells* **2012**, *105*, 69.
- [130] J.-Y. Lee, S. T. Connor, Y. Cui, P. Peumans, *Nano Lett.* **2008**, *8*, 689.
- [131] J. H. Yim, S. Joe, C. Pang, K. M. Lee, H. Jeong, J.-Y. Park, Y. H. Ahn, J. C. de Mello, S. Lee, *ACS Nano* **2014**, *8*, 2857.
- [132] J.-Y. Lee, S. T. Connor, Y. Cui, P. Peumans, *Nano Lett.* **2010**, *10*, 1276.
- [133] F. Guo, P. Kubis, T. Przybilla, E. Spiecker, A. Hollmann, S. Langner, K. Forberich, C. J. Brabec, *Adv. Energy Mater.* **2015**, *5*, n/a.
- [134] C.-C. Chen, L. Dou, R. Zhu, C.-H. Chung, T.-B. Song, Y. B. Zheng, S. Hawks, G. Li, P. S. Weiss, Y. Yang, *ACS Nano* **2012**, *6*, 7185.
- [135] G. A. dos R. Benatto, B. Roth, M. Corazza, R. R. Søndergaard, S. A. Gevorgyan, M. Jørgensen, F. C. Krebs, *Nanoscale* **2015**, *8*, 318.
- [136] X.-Y. Zeng, Q.-K. Zhang, R.-M. Yu, C.-Z. Lu, *Adv. Mater.* **2010**, *22*, 4484.
- [137] Z. Yu, Q. Zhang, L. Li, Q. Chen, X. Niu, J. Liu, Q. Pei, *Adv. Mater.* **2011**, *23*, 664.
- [138] L. Li, Z. Yu, W. Hu, C. Chang, Q. Chen, Q. Pei, *Adv. Mater.* **2011**, *23*, 5563.
- [139] L. Li, Z. Yu, C. Chang, W. Hu, X. Niu, Q. Chen, Q. Pei, *Phys. Chem. Chem. Phys.* **2012**, *14*, 14249.
- [140] W. Gaynor, S. Hofmann, M. G. Christoforo, C. Sachse, S. Mehra, A. Salleo, M. D. McGehee, M. C. Gather, B. Lüssem, L. Müller-Meskamp, P. Peumans, K. Leo, *Adv. Mater.* **2013**, *25*, 4006.
- [141] H.-G. Im, S.-H. Jung, J. Jin, D. Lee, J. Lee, D. Lee, J.-Y. Lee, I.-D. Kim, B.-S. Bae, *ACS Nano* **2014**, *8*, 10973.
- [142] J. Song, J. Li, J. Xu, H. Zeng, *Nano Lett.* **2014**, *14*, 6298.
- [143] R. Gupta, K. D. M. Rao, S. Kiruthika, G. U. Kulkarni, *ACS Appl. Mater. Interfaces* **2016**, *8*, 12559.
- [144] S. M. Lee, J. H. Lee, S. Bak, K. Lee, Y. Li, H. Lee, *Nano Res.* **2015**, *8*, 1882.
- [145] M. Kamalisarvestani, R. Saidur, S. Mekhilef, F. S. Javadi, *Renew. Sustain. Energy Rev.* **2013**, *26*, 353.
- [146] P. Liu, L. Liu, K. Jiang, S. Fan, *Small* **2011**, *7*, 732.
- [147] R. G. Gordon, *Mrs Bull.* **2000**, *25*, 52.
- [148] J. J. Bae, S. C. Lim, G. H. Han, Y. W. Jo, D. L. Doung, E. S. Kim, S. J. Chae, T. Q. Huy, N. Van Luan, Y. H. Lee, *Adv. Funct. Mater.* **2012**, *22*, 4819.
- [149] Y.-H. Yoon, J.-W. Song, D. Kim, J. Kim, J.-K. Park, S.-K. Oh, C.-S. Han, *Adv. Mater.* **2007**, *19*, 4284.
- [150] D. Kim, L. Zhu, D.-J. Jeong, K. Chun, Y.-Y. Bang, S.-R. Kim, J.-H. Kim, S.-K. Oh, *Carbon* **2013**, *63*, 530.
- [151] X. Zhang, X. Yan, J. Chen, J. Zhao, *Carbon* **2014**, *69*, 437.
- [152] T. Kim, Y. W. Kim, H. S. Lee, H. Kim, W. S. Yang, K. S. Suh, *Adv. Funct. Mater.* **2013**, *23*, 1250.
- [153] S. Wang, X. Zhang, W. Zhao, *J Nanomater.* **2013**, *2013*, 3:3.

- [154] S. Hong, H. Lee, J. Lee, J. Kwon, S. Han, Y. D. Suh, H. Cho, J. Shin, J. Yeo, S. H. Ko, *Adv. Mater.* **2015**, 27, 4744.
- [155] J. Li, J. Liang, X. Jian, W. Hu, J. Li, Q. Pei, *Macromol. Mater. Eng.* **2014**, 299, 1403.
- [156] M. M. Menampambath, K. Yang, H. H. Kim, O. S. Bae, M. S. Jeong, J.-Y. Choi, S. Baik, *Nanotechnology* **2016**, 27, 465706.
- [157] R. J. Mortimer, D. R. Rosseinsky, P. M. S. Monk, Eds. , *Electrochromic Materials and Devices*, John Wiley & Sons, Weinheim, **2015**.
- [158] C. G. Granqvist, *Thin Solid Films* **2014**, 564, 1.
- [159] V. Vorflusev, S. Kumar, *Science* **1999**, 283, 1903.
- [160] C. M. Lampert, *Mater. Today* **2004**, 7, 28.
- [161] C.-G. Granqvist, *Nat. Mater.* **2006**, 5, 89.
- [162] J. Remmele, D. E. Shen, T. Mustonen, N. Fruehauf, *ACS Appl. Mater. Interfaces* **2015**, 7, 12001.
- [163] S. Radhakrishnan, S. Unde, A. . Mandale, *Mater. Chem. Phys.* **1997**, 48, 268.
- [164] C. Yan, W. Kang, J. Wang, M. Cui, X. Wang, C. Y. Foo, K. J. Chee, P. S. Lee, *ACS Nano* **2014**, 8, 316.
- [165] H. Hosseinzadeh Khaligh, K. Liew, Y. Han, N. M. Abukhdeir, I. A. Goldthorpe, *Sol. Energy Mater. Sol. Cells* **2015**, 132, 337.
- [166] K. Ghaffarzadeh, Y. Yamamoto, H. Zervos, *Conductive Ink Markets 2016-2026: Forecasts, Technologies, Players*, IDTechEx Ltd, Boston, MA, USA, **2016**.
- [167] C. Chen, E. A. Dorjgotov, M. Kuwabara, W. Choi, M. P. Grunthaler, A. Lin, J. Z. Zhong, W. Chen, S. P. Hotelling, L. R. Youngs (Apple Inc), *US 20140016043A1*, **2014**.
- [168] Y. Jeon, H. B. Jin, S. Jung, H. Go, I. Lee, C. Lee, Y. K. Joo, K. Park, *J. Opt. Soc. Korea* **2015**, 19, 508.
- [169] Y. Kim, C.-H. Song, M.-G. Kwak, B.-K. Ju, J.-W. Kim, *RSC Adv* **2015**, 5, 42500.
- [170] M. Cann, M. J. Large, S. J. Henley, D. Milne, T. Sato, H. Chan, I. Jurewicz, A. B. Dalton, *Mater. Today Commun.* **2016**, 7, 42.
- [171] J. Li, J. Liang, L. Li, F. Ren, W. Hu, J. Li, S. Qi, Q. Pei, *ACS Nano* **2014**, 8, 12874.
- [172] S. Hong, J. Yeo, J. Lee, H. Lee, P. Lee, S. S. Lee, S. H. Ko, *J. Nanosci. Nanotechnol.* **2015**, 15, 2317.
- [173] A. Fried, X. Zhang, J. Abrahamson, C. Wang, J. Luo, R. Monson, P.-S. Shih, H.-L. Pan, T.-L. Chang, in *Nanotechnol. IEEE-NANO 2015 IEEE 15th Int. Conf. On, IEEE*, **2015**, pp. 1186–1189.
- [174] J.-H. Chang, K.-M. Chiang, H.-W. Kang, W.-J. Chi, J.-H. Chang, C.-I. Wu, H.-W. Lin, *Nanoscale* **2015**, 7, 4572.
- [175] M. Mol Menampambath, C. Muhammed Ajmal, K. Hee Kim, D. Yang, J. Roh, H. Cheol Park, C. Kwak, J.-Y. Choi, S. Baik, *Sci. Rep.* **2015**, 5, 16371.
- [176] G. A. Gelves, M. H. Al-Saleh, U. Sundararaj, *J. Mater. Chem.* **2010**, 21, 829.
- [177] C. Yang, H. Gu, W. Lin, M. M. Yuen, C. P. Wong, M. Xiong, B. Gao, *Adv. Mater.* **2011**, 23, 3052.
- [178] Y.-H. Yu, C.-C. M. Ma, C.-C. Teng, Y.-L. Huang, S.-H. Lee, I. Wang, M.-H. Wei, *Mater. Chem. Phys.* **2012**, 136, 334.
- [179] M. Hu, J. Gao, Y. Dong, K. Li, G. Shan, S. Yang, R. K.-Y. Li, *Langmuir* **2012**, 28, 7101.
- [180] M. Jalali, S. Dauterstedt, A. Michaud, R. Wuthrich, *Compos. Part B Eng.* **2011**, 42, 1420.
- [181] O. Breuer, U. Sundararaj, *Polym. Compos.* **2004**, 25, 630.
- [182] Y. Yang, M. C. Gupta, K. L. Dudley, R. W. Lawrence, *Nano Lett.* **2005**, 5, 2131.
- [183] N. Li, Y. Huang, F. Du, X. He, X. Lin, H. Gao, Y. Ma, F. Li, Y. Chen, P. C. Eklund, *Nano Lett.* **2006**, 6, 1141.

- [184] J. Liang, Y. Wang, Y. Huang, Y. Ma, Z. Liu, J. Cai, C. Zhang, H. Gao, Y. Chen, *Carbon* **2009**, *47*, 922.
- [185] B. A. Munk, *Frequency Selective Surfaces: Theory and Design*, Wiley, Hoboken, NJ, USA, **2000**.
- [186] N. Komoda, M. Nogi, K. Suganuma, K. Kohno, Y. Akiyama, K. Otsuka, *Nanoscale* **2012**, *4*, 3148.
- [187] N. Komoda, M. Nogi, K. Suganuma, K. Otsuka, *ACS Appl. Mater. Interfaces* **2012**, *4*, 5732.
- [188] T. Rai, P. Dantes, B. Bahreyni, W. S. Kim, *IEEE Electron Device Lett.* **2013**, *34*, 544.
- [189] L. Song, A. C. Myers, J. J. Adams, Y. Zhu, *ACS Appl. Mater. Interfaces* **2014**, *6*, 4248.
- [190] D.R. Lide, *CRC Handbook of Chemistry and Physics 2004-2005: A Ready-Reference Book of Chemical and Physical Data*, CRC Press, **2004**.
- [191] J.-P. Simonato, C. Celle, C. Mayousse, T. Lescouet, *Procédé de Purification de Nanofils Métalliques. Brevet*, **2014**.
- [192] M. del P. Buera, G. Levi, M. Karel, *Biotechnol. Prog.* **1992**, *8*, 144.
- [193] Y. Gao, P. Jiang, D. F. Liu, H. J. Yuan, X. Q. Yan, Z. P. Zhou, J. X. Wang, L. Song, L. F. Liu, W. Y. Zhou, G. Wang, C. Y. Wang, S. S. Xie, J. M. Zhang, D. Y. Shen, *J. Phys. Chem. B* **2004**, *108*, 12877.
- [194] J. Lee, I. Lee, T.-S. Kim, J.-Y. Lee, *Small* **2013**, *9*, 2887.
- [195] D. Stauffer, A. Aharony, *Introduction to Percolation Theory, 2nd Revised Ed.*, Taylor And Francis, London, **1994**.
- [196] I. Balberg, N. Binenbaum, C. H. Anderson, *Phys. Rev. Lett.* **1983**, *51*, 1605.
- [197] B. Vigolo, C. Coulon, M. Maugey, C. Zakri, P. Poulin, *Science* **2005**, *309*, 920.
- [198] M. Žeželj, I. Stanković, *Phys. Rev. B* **2012**, *86*, 134202.
- [199] M. E. J. Newman, R. M. Ziff, *Phys. Rev. Lett.* **2000**, *85*, 4104.
- [200] M. E. J. Newman, R. M. Ziff, *Phys. Rev. E* **2001**, *64*, 016706.
- [201] Z. Cheng, M. Han, P. Yuan, S. Xu, B. A. Cola, X. Wang, *RSC Adv* **2016**, *6*, 90674.
- [202] A. T. Bellew, H. G. Manning, C. Gomes da Rocha, M. S. Ferreira, J. J. Boland, *ACS Nano* **2015**, DOI 10.1021/acsnano.5b05469.
- [203] G. R. McGEE, M. H. Schankula, M. M. Yovanovich, *Nucl. Eng. Des.* *86 1985 369-381* **1985**.
- [204] J. N. Reddy, *An Introduction to the Finite Element Method*, **2014**.
- [205] T. Sannicolo, D. Muñoz-Rojas, N. D. Nguyen, S. Moreau, C. Celle, J.-P. Simonato, Y. Bréchet, D. Bellet, *Nano Lett.* **2016**, *16*, 7046.
- [206] S. Coskun, E. Selen Ates, H. Emrah Unalan, *Nanotechnology* **2013**, *24*, 125202.
- [207] A. Kim, Y. Won, K. Woo, C.-H. Kim, J. Moon, *ACS Nano* **2013**, *7*, 1081.
- [208] D. A. Wharam, T. J. Thornton, R. Newbury, M. Pepper, H. Ahmed, J. E. F. Frost, D. G. Hasko, D. C. Peacock, D. A. Ritchie, G. a. C. Jones, *J. Phys. C Solid State Phys.* **1988**, *21*, L209.
- [209] B. van Wees, H. van Houten, C. Beenakker, J. Williamson, L. Kouwenhoven, D. van der Marel, C. Foxon, *Phys. Rev. Lett.* **1988**, *60*, 848.
- [210] A. Sattar, S. Fostner, S. A. Brown, *Phys. Rev. Lett.* **2013**, *111*, 136808.
- [211] R. Landauer, *J. Math. Phys.* **1996**, *37*, 5259.
- [212] C. Durkan, M. . Welland, *Ultramicroscopy* **2000**, *82*, 125.
- [213] U. Landman, W. Luedtke, B. Salisbury, R. Whetten, *Phys. Rev. Lett.* **1996**, *77*, 1362.
- [214] S. R. Das, A. M. S. Mohammed, K. Maize, S. Sadeque, A. Shakouri, D. B. Janes, M. A. Alam, *Nano Lett.* **2016**, *16*, 3130.
- [215] O. Breitenstein, W. Warta, M. Langenkamp, *Lock-in Thermography: Basics and Use for Evaluating Electronic Devices and Materials*, Springer Science & Business Media, **2010**.

- [216] C. Schmidt, F. Altmann, O. Breitenstein, *Mater. Sci. Eng. B* **2012**, *177*, 1261.
- [217] J. A. Fairfield, C. Ritter, A. T. Bellew, E. K. McCarthy, M. S. Ferreira, J. J. Boland, *ACS Nano* **2014**, *8*, 9542.
- [218] A. Bid, A. Bora, A. Raychaudhuri, *Phys. Rev. B* **2005**, *72*, DOI 10.1103/PhysRevB.72.113415.
- [219] H. Wong, *J. Appl. Phys.* **2012**, *111*, 103509.
- [220] H. S. Shin, J. Yu, J. Y. Song, *Appl. Phys. Lett.* **2007**, *91*, 173106.
- [221] W. Hu, X. Niu, L. Li, S. Yun, Z. Yu, Q. Pei, *Nanotechnology* **2012**, *23*, 344002.
- [222] P. Lee, J. Lee, H. Lee, J. Yeo, S. Hong, K. H. Nam, D. Lee, S. S. Lee, S. H. Ko, *Adv. Mater.* **2012**, *24*, 3326.
- [223] J. Kim, J. Park, U. Jeong, J.-W. Park, *J. Appl. Polym. Sci.* **2016**, *133*, n/a.
- [224] G.-W. Huang, H.-M. Xiao, S.-Y. Fu, *Sci. Rep.* **2015**, *5*, 13971.
- [225] M. Amjadi, A. Pichitpajongkit, S. Ryu, I. Park, in *2014 IEEE 27th Int. Conf. Micro Electro Mech. Syst. MEMS*, **2014**, pp. 785–788.
- [226] X. Ho, J. Nie Tey, W. Liu, C. Kweng Cheng, J. Wei, *J. Appl. Phys.* **2013**, *113*, 044311.
- [227] F. Xu, Y. Zhu, *Adv. Mater.* **2012**, *24*, 5117.
- [228] X. Ho, C. K. Cheng, J. N. Tey, J. Wei, *J. Mater. Res.* **2014**, *29*, 2965.
- [229] X. Ho, C. K. Cheng, J. N. Tey, J. Wei, *Nanotechnology* **2015**, *26*, 195504.
- [230] T. Akter, W. S. Kim, *ACS Appl. Mater. Interfaces* **2012**, *4*, 1855.
- [231] L. Song, A. C. Myers, J. J. Adams, Y. Zhu, *ACS Appl. Mater. Interfaces* **2014**, *6*, 4248.
- [232] Y. Zhu, Q. Qin, F. Xu, F. Fan, Y. Ding, T. Zhang, B. J. Wiley, Z. L. Wang, *Phys. Rev. B* **2012**, *85*, DOI 10.1103/PhysRevB.85.045443.
- [233] X. Yue, Y. Xi, C. Hu, X. He, S. Dai, L. C. and G. Wang, *RSC Adv* **2015**, *5*, 32566.
- [234] J. R. Greer, J. T. M. De Hosson, *Prog. Mater. Sci.* **2011**, *56*, 654.
- [235] M. C. Larciprete, A. Albertoni, A. Belardini, G. Leahu, R. Li Voti, F. Mura, C. Sibilina, I. Nefedov, I. V. Anoshkin, E. I. Kauppinen, A. G. Nasibulin, *J. Appl. Phys.* **2012**, *112*, 083503.
- [236] D. Muñoz-Rojas, J. MacManus-Driscoll, *Mater. Horiz.* **2014**, *1*, 314.
- [237] V. H. Nguyen, J. Resende, C. Jiménez, J.-L. Deschanvres, P. Carroy, D. Muñoz, D. Bellet, D. Muñoz-Rojas, *J. Renew. Sustain. Energy* **2017**, *9*, 021203.
- [238] H. A. Wheeler, *IEEE Trans. Microw. Theory Tech.* **1965**, *13*, 172.
- [239] H. A. Wheeler, *IEEE Trans. Microw. Theory Tech.* **1977**, *25*, 631.
- [240] G. F. Engen, C. A. Hoer, *IEEE Trans. Microw. Theory Tech.* **1979**, *27*, 987.
- [241] A. Niembro-Martin, E. Pistono, P. Lemaitre-Auger, T.-P. Vuong, G. E. P. Tourtollet, in *2014 IEEE Conf. Antenna Meas. Appl. CAMA*, **2014**, pp. 1–3.
- [242] K. F. Casey, *IEEE Trans. Electromagn. Compat.* **1988**, *30*, 298.
- [243] L. D. Scanlan, R. B. Reed, A. V. Loguinov, P. Antczak, A. Tagmount, S. Aloni, D. T. Nowinski, P. Luong, C. Tran, N. Karunaratne, D. Pham, X. X. Lin, F. Falciani, C. P. Higgins, J. F. Ranville, C. D. Vulpe, B. Gilbert, *ACS Nano* **2013**, *7*, 10681.
- [244] D. E. Gorka, J. S. Osterberg, C. A. Gwin, B. P. Colman, J. N. Meyer, E. S. Bernhardt, C. K. Gunsch, R. T. DiGulio, J. Liu, *Environ. Sci. Technol.* **2015**, *49*, 10093.
- [245] R. M. Silva, J. Xu, C. Saiki, D. S. Anderson, L. M. Franzi, C. D. Vulpe, B. Gilbert, L. S. Van Winkle, K. E. Pinkerton, *Part Fibre Toxicol* **2014**, *11*, 52.
- [246] S. Sweeney, I. G. Theodorou, M. Zambianchi, S. Chen, A. Gow, S. Schwander, J. (Jim) Zhang, K. F. Chung, M. S. P. Shaffer, M. P. Ryan, A. E. Porter, T. D. Tetley, *Nanoscale* **2015**, *7*, 10398.
- [247] C. Steger, *IEEE Trans. Pattern Anal. Mach. Intell.* **1998**, *20*, 113.

